



**Network of European Research Infrastructures for
Earthquake Risk Assessment and Mitigation**

Report

**Analysis of relative contribution of source, scattering and
local site effects to ground motion**

Activity:	<i>Near fault ground motion</i>
Activity number:	<i>JRA3, Task 13.1, 13.2 13.4, 13.5, 13.6</i>
Deliverable:	<i>Analysis of relative contribution of source, scattering and local site effects to ground motion</i>
Deliverable number:	<i>13.4</i>
Responsible activity leader:	<i>Luis Angel Dalguer</i>
Responsible participant:	<i>INGV</i>
Authors:	<i>Antonella Cirella and Alessio Piatanesi</i>

**Seventh Framework Programme
EC project number: 262330**



The following partners contributed to this deliverable:

ETHZ (*Luis Angel Dalguer, Seok Goo Song, Cyrill Baumann*)

INGV (*Antonella Cirella, Alessio Piatanesi, Elena Spagnuolo, Elisa Tinti*)

CNRS-ISTerre (*Cécile Cornou, Fabrice Cotton, Afifa Imtiaz, Mathieu Causse*)

KOERI (*Eser Çakti, Mustafa Erdik, Ebru Harmandar, Karin Sesetyan, Esra Zengin*)

AMRA (*Sergio Del Gaudio, Gaetano Festa, Ernestina Lucca, Antonio Scala, Antonio Emolo, Aldo Zollo*)

METU (*Aysegul Askan, Sinan Akkar, Gabriele Ameri, Fatma Nurten Sisman, Shaghayegh Karimzadeh, Onur Pekcan*)

TABLE OF CONTENTS

Summary	5
1. Source Complexity	
1.1. Kinematic Modeling: Spatial and Temporal Heterogeneity Analyses through Kinematic Source Inversions: The Case of 2009 L'Aquila Earthquake (INGV team).....	7
1.2. Kinematic Modeling: Rupture process of the 2007 Niigata-ken Chuetsu-oki earthquake by non-linear joint inversion of strong motion and GPS data (INGV team).....	15
1.3. Kinematic Modeling: Multiple Point Source and Finite Fault Inversions for 2011 Van earthquake (METU team).....	21
1.4. Dynamic Modeling: Kink Fault Modeling, Damage Models (AMRA team).....	31
1.5. Dynamic Modeling: Dynamic Parameters Distributions Computed from Finite Fault Kinematic Models (INGV team).....	40
1.6. Source Statistic Modeling: Constraining 1-point and 2-point source statistics (ETHZ team).....	44
2. Ground Motion Simulations	
2.1. On the magnitude and distance dependency of ground motion variability (ISTerre team).....	47
2.2. Constraining the variability of source parameters for physics-based ground-motion predictions (ISTerre team).....	54
2.3. Sets of Ground motion Simulations based on 360 Rupture Scenarios (ETHZ team).....	58
2.4. Statistical Analysis: The effect of 1-point and 2-point source statistics on ground motions (ETHZ team).....	66
2.5. Case Studies	
2.5.1. <i>Broadband simulations of 2009 L'Aquila earthquake (AMRA team)</i>	72
2.5.2. <i>Intra-event ground motion variability of the 2009 L'Aquila earthquake (INGV team)</i>	81
2.5.3. <i>Stochastic Finite Fault Ground Motion Simulation of the 2009 L'Aquila Earthquake (METU team)</i>	85
2.5.4. <i>Broadband (HIC Model) Ground motion Simulation of the 2009 L'Aquila earthquake (METU team)</i>	94

<i>2.5.5. Broadband (HIC Model) Ground Motion Simulation of the 2011 Van Earthquake (METU team).....</i>	<i>101</i>
<i>2.5.6. Stochastic Finite Fault Ground motion Simulation of the 2011 Van earthquake: Mainshock and Aftershock Modeling (KOERI team).....</i>	<i>111</i>
<i>2.5.7. Low and High Frequency Ground motion Simulation of the 1999 Kocaeli earthquake (KOERI team).....</i>	<i>131</i>

3. Scattering and Locale Site Effects

3.1. Spatial Variability of the Ground motion and its effect on the Structural Behavior based on NERA Argostoli experiment (ISTerre team).....	141
3.2. Statistical Analyses of the Kappa Factor of Soils: Application on the Marmara Dataset (METU team).....	148
3.3. Assessment of Nonlinear Dynamic Building Response to Simulated Ground Motions (METU team).....	156
3.4. Modeling of Spatial Variation of Ground Motion: A case study for Istanbul (KOERI team).....	164
3.5. Development of Coherency Models (KOERI team).....	174

4. Conclusions.....

References.....

Summary

NERA JRA3 brings together competences in numerical modelling, waveform simulation and earthquake source dynamics in order to study the variability of strong-ground shaking near the fault. In particular, JRA3 activities are focused on the analysis of the relative contributions of source complexity, scattering and local site effects to the near-field ground motion spatial variability.

This report consists of three main chapters (see the list of contents for details) and contains most of the scientific results obtained during the first 3 years of activity by the different research' teams (AMRA, ETHZ, INGV, ISTerre, KOERI, METU) involved in WP13 of the NERA project.

In the first chapter, we investigate the source complexity through kinematic and dynamic modelling approaches. In particular, kinematic descriptions of the rupture process of three earthquakes (the 2009 Mw 6.1 L'Aquila, the 2007 Niigata-ken Chuetsu-oki, the 2011 Van earthquakes) are produced. The associated rupture histories are obtained from the inversion of real data. For the L'Aquila earthquake we also provide a dynamic modelling inferred from the associated kinematic model. We develop a suite of earthquake dynamic models with heterogeneous stress distributions consistent, in a statistical sense, with past earthquakes. Each suite tests a particular set of assumptions about friction laws, fault-zone rheology, geological structures, initial stress and fault geometry (fault kinks).

The second chapter contains the results of ground motion simulations. In particular we investigate specific effects produced by source complexity, such as ground motion differences between buried and surface-rupturing earthquakes, directivity pulses induced by sub-shear rupture, velocity pulses induced by super-shear rupture propagation, the effect of fault zones on the ground motion and the role of fault geometry (investigating the frequency content emitted by the fault kinks). We address the

problem of estimating the ground motion variability by generating a large number of source models, by varying initial conditions (nucleation point, rupture velocity, slip distribution). Probability Density Functions (pdf) of some relevant ground motion parameters (PGA, PGV, PSA, etc.) are produced at the sites of interest. We also examine the magnitude and distance dependency of ground motion variability and we perform a statistical study by analysing the effect of 1-point and 2-points source statistics on ground motions. Three different case studies are investigated (the 2009 L'Aquila, the 2001 Van and the 1999 Kocaeli earthquakes).

The third chapter collects the results obtained from the analysis of the ground motion spatial variability due to scattering and local site effects. In particular we analyse the effect of the ground motion spatial variability on structural behaviour (NERA Argostoli experiment); we perform a statistical analysis of the *kappa* factor of soils (application on the Marmara dataset); we assess non-linear dynamic building response to simulated ground motion. Moreover, we develop a coherency model for Istanbul, that can be used for the assessment and simulation of spatially variable ground motion.

1. Source Complexity

1.1 Kinematic Modeling: Spatial and Temporal Heterogeneity Analyses through Kinematic Source Inversions: The Case of 2009 L'Aquila Earthquake (INGV team)

The M_w 6.1 L'Aquila main shock is one of the best-recorded normal faulting earthquakes worldwide and has allowed the collection of an extremely interesting observational data set. It occurred on April 6th 2009 (01:32 UTC) and struck the Abruzzi region in central Italy (see Figure 1) causing more than 300 fatalities in the L'Aquila city and nearby villages. The availability of high quality data set (including strong motion accelerograms, GPS, CGPS and Differential Synthetic Aperture Radar Interferometry - DInSAR - measurements) promoted numerous studies to constrain the rupture process. Different studies have pointed out the complexity of the earthquake nucleation (Lucente *et al.* 2010), the initial stages of the rupture history (Ellsworth and Chiaraluce 2009; Di Stefano *et al.* 2011) and the subsequent coseismic rupture propagation (Cirella *et al.* 2009). Despite its moderate magnitude, the rupture process of the L'Aquila main shock is surprisingly complex. The analysis of the closest strong motion accelerograms shows an initial emergent P-wave signal (hereinafter EP) followed by an impulsive onset (IP) after few tenths of second (Michelini *et al.* 2009). This suggests that the initial stages of the rupture are characterized by a relatively small moment release (initiated by the EP) followed ~ 0.9 s later by a high moment release (beginning with the impulsive phase, IP) located nearly 2 km up-dip from the hypocenter (Di Stefano *et al.* 2011). The rupture history imaged by Cirella *et al.* (2009) also displays this initial up-dip propagation. These observations and modeling results together with the interpretation of fluid involvement in the foreshock activity and the earthquake nucleation process (Lucente *et*

al. 2010) corroborate the heterogeneity of the rupture process during the L'Aquila main shock. The aim of the INGV team in the present study is to further investigate these issues by imaging the rupture history through the non-linear inversion of strong motion, GPS and DInSAR data (inverted either separately or jointly). To address the problem of the heterogeneity of the rupture process, we give particular attention to the variability of model parameters and we attempt to better constrain the local rupture velocity on the fault plane. A detailed description of the adopted technique is given in the deliverable D13.3 (New Simulation Scheme) of this JRA3 WP.

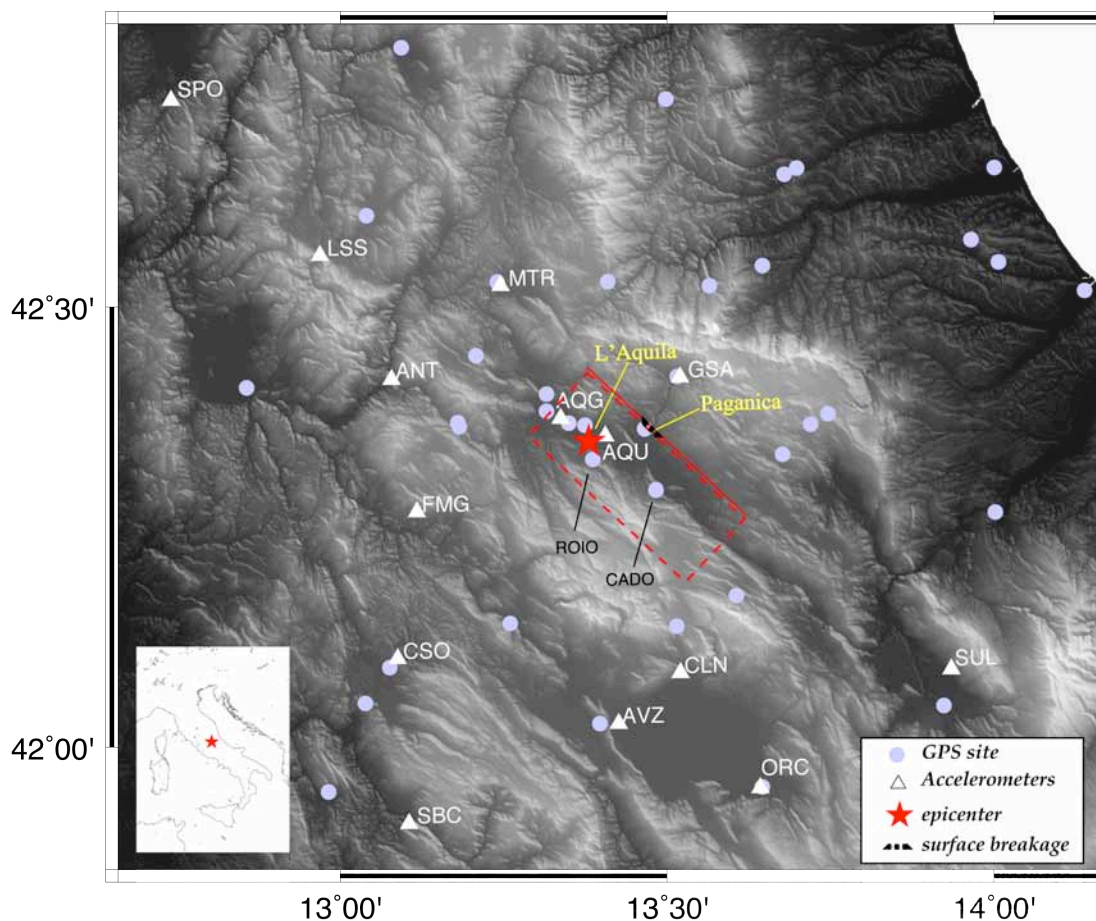


Figure 1. Map of the fault geometry of the 2009 L'Aquila earthquake. The red box represents the surface projection of the fault plane adopted in this study. White triangles represent the selected strong motions stations. Violet dots represent the GPS sites, The red star indicates the epicenter. In yellow are displayed the location of the L'Aquila town and Paganica village.

DATA

In this study we have selected 13 three-component digital accelerometers of the RAN Network (“Rete Accelerometrica Nazionale”, managed by the Italian Civil Protection, <http://itaca.mi.ingv.it/ItacaNet>) and the AQU (MedNet network, <http://mednet.rm.ingv.it/data.php>) accelerogram (see Figure 1). They were integrated to obtain ground velocity time histories and band-pass filtered between 0.02 and 0.5 Hz with a two-pole and two-pass Butterworth filter. We do not model higher frequencies because of difficulties in computing appropriate Green’s Functions and to reduce bias caused by site effects, that are affecting ground motion time histories at frequencies higher than 0.6 Hz (De Luca *et al.* 1998). In order to image the details of the slip distribution through the inversion of GPS data, we have considered 36 three-component GPS displacements inferred from measurements at the closest receivers (see Figure 1). These horizontal and vertical coseismic displacements represent a sub-set retrieved from the analysis of the 43 GPS measurements published by Cheloni *et al.* (2010). We have applied the DInSAR technique to the Envisat and ALOS SAR satellite data. The ENVISAT pair has been acquired on April 27th, 2008 and April 12th, 2009 from the descending orbit with a look angle of 23° and a perpendicular baseline of 41m; whilst the ALOS pair has been taken on July 20th, 2008 and April 22th, 2009 from the ascending orbit with a look angle of 36° and a perpendicular baseline of 322m. Both interferograms have been generated at ~ 300 m resolution, in order to achieve a sufficient spatial resolution and an acceptable signal to noise ratio. Moreover, the 90 m SRTM digital elevation model is used to subtract the topographic contribution. In the resulting ENVISAT C-band differential interferogram (Figure 2a) each color cycle (fringe) corresponds to a ground displacement of ~ 2.8 cm along the Line of Sight (LoS) of the satellite, while in the ALOS L-band each fringe corresponds to a ~ 11.8 cm in LoS (Figure 2b).

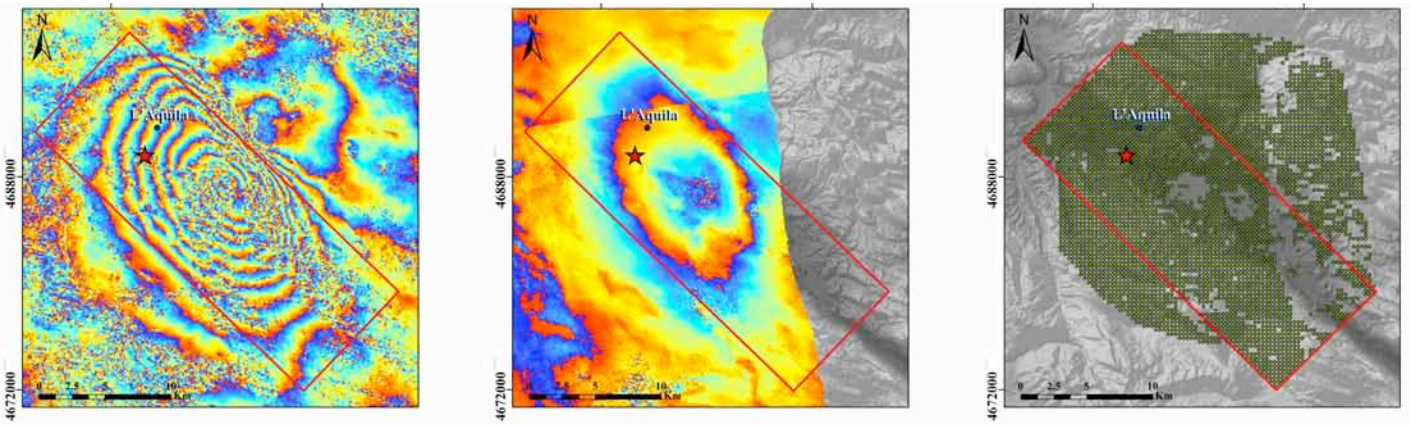


Figure 2. a) Envisat wrapped interferogram; b) ALOS wrapped interferogram; c) Green color shows the 4599 resampled pixels (size 300m), from both interferograms, selected in this study. The red rectangle represents the surface projection of the fault plane fixed for this study, while the red star represent the epicenter.

MODEL SETUP

Crustal Structure

For computing the Green's functions, we have assumed for all recording stations (except for AQU and AQG) the 1D velocity model (nnCIA.mod) proposed by Herrmann *et al.* (2011), and calibrated during the sequence through the analysis of surface wave dispersion. For AQU and AQG seismic stations we have adopted a 1-D velocity model specific for these receivers obtained by the analysis of receiver functions (Bianchi *et al.* 2010). The kinematic tractions on the fault plane are calculated using the Discrete Wavenumber - Finite Element (DWFE) integration technique (Spudich and Xu, 2003), which allows the computation of the complete response of a 1D layered.

Fault Model

The adopted fault plane, striking N133°E and dipping 54° to the SW (Cirella *et al.* 2009), is 28 km long and 17.5 km wide with the shallow top border located at 0.5 km depth just below the surface breakage observed along the Paganica fault (EMERGEO WG, 2010; see Figure 1). We assume the INGV hypocenter (Chiarabba *et al.* 2009). The strike of the fault is well constrained by DInSAR data. We invert for slip direction, assuming a dominant normal fault mechanism consistent with moment tensor solutions and aftershocks focal mechanisms and allowing the rake angle to

vary in the range $270^\circ \pm 40^\circ$. We invert simultaneously for all the parameters at nodal points equally spaced (3.5 km) along strike and dip directions. During the inversion, we fix a given range of variability for each model parameter. In particular, in this study we adopt the following variability intervals: peak slip velocity values can range between 0 and 3.5 m/s at 0.25 m/s interval; the rise time between 0.75 and 3 sec at 0.25 sec interval and the rake angle from 230° to 310° in steps of 10° . The rupture time at each grid node is constrained by the arrival time from the hypocenter of a rupture front having a speed comprised between 1.4 and 4 km/s.

JOINT INVERSION

Both the separate and joint inversion solutions reveal a complex rupture process and a heterogeneous slip distribution (Cirella et al., 2012). The average rupture model, inferred from the joint inversion, is shown in Figure 3a. The three panels on the left display the computed slip distribution, the inverted rise time and peak slip velocity distributions, respectively. The black arrows on the top-left panel show the slip direction, the white contour lines display the rupture time distribution on the fault plane. The three panels on the right (Figure 3b) display the distribution on the fault plane of the coefficient of variation for the rupture times (top panel), the rise time (middle panel) and the peak slip velocity (bottom panel). In each of these three panels the white contour lines display the spatial distribution of the associated model parameter. The obtained solution reveals a heterogeneous slip distribution characterized by two main asperities; a smaller shallow patch of slip located up-dip from the hypocenter and a second deeper and larger asperity located south-east wards along-strike direction. The distributions of the coefficient of variation for rupture times, rise time and peak slip velocity shown in Figure 3b reveal a small dispersion of model parameters in the fault portions that slipped during the L'Aquila earthquake. This suggests that the average model contains stable features of the rupture history and

allows the identification of the relevant properties. The main outcome emerging from our modeling is the evident and somewhat surprising complexity of the rupture process, in particular considering its moderate magnitude and the small dimension of the fault area. The source complexity is characterized by: (i) the heterogeneous distribution of model parameters on the fault plane, (ii) the variability of the rupture velocity and (iii) the peculiar spatial evolution of the rupture front. In order to better discuss these features we have plotted in Figure 4a both the local rupture velocity imaged from rupture times and the rupture velocity vector. Figure 4b displays the distribution on the fault plane of the rupture mode coefficient proposed by Pulido and Dalguer (2009).

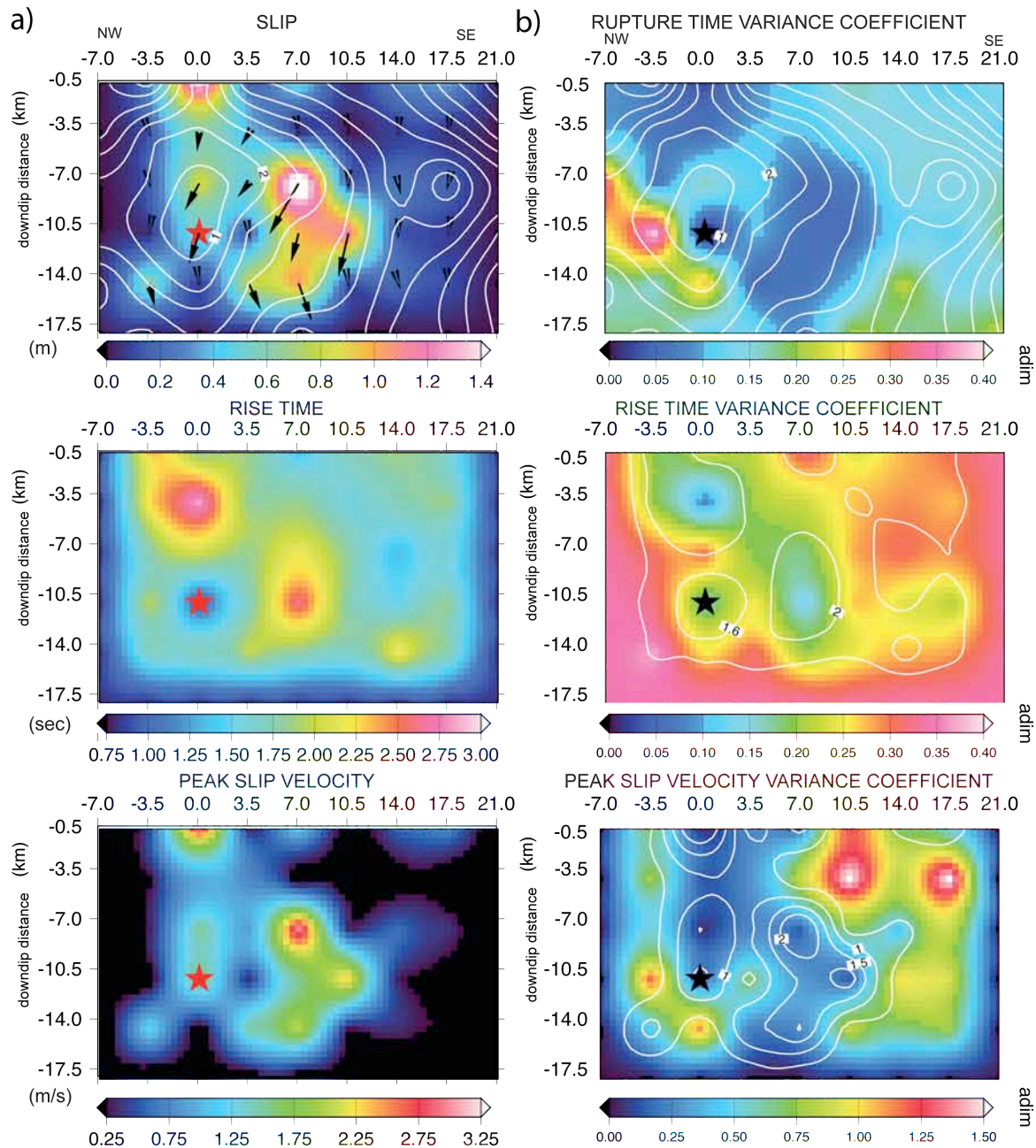


Figure 3. a) Inverted rupture model (average model from ensemble inference) of the 2009 L'Aquila earthquake. Upper, middle and bottom panels show total slip, rise time and peak slip velocity distributions, respectively. The rupture time is shown by contour lines in white color at 1s intervals; the black arrows displayed in top panel represent the slip vector; b) Coefficient of variation (CV). Top, middle and bottom panels display the rupture times, the rise time and the peak slip velocity spatial distributions of the CV, respectively. White contour lines in each panel display the spatial distribution of the associated model parameter.

The key feature of the source process emerging from these plots concerns the rupture history, which is characterized by two distinct stages. The first stage begins with rupture nucleation and with up-dip propagation at

relatively high (~ 4.0 km/s), but still sub-shear, rupture velocity (Figure 4a). The second stage starts nearly 2.0–2.5 s after nucleation and it is characterized by the along-strike rupture propagation. The largest and deeper asperity fails during this stage of the rupture process. The rupture velocity is larger in the up-dip than in the along-strike direction. The up-dip and along-strike rupture propagation are separated in time and associated with a Mode II and a Mode III crack, respectively (Figure 4b).

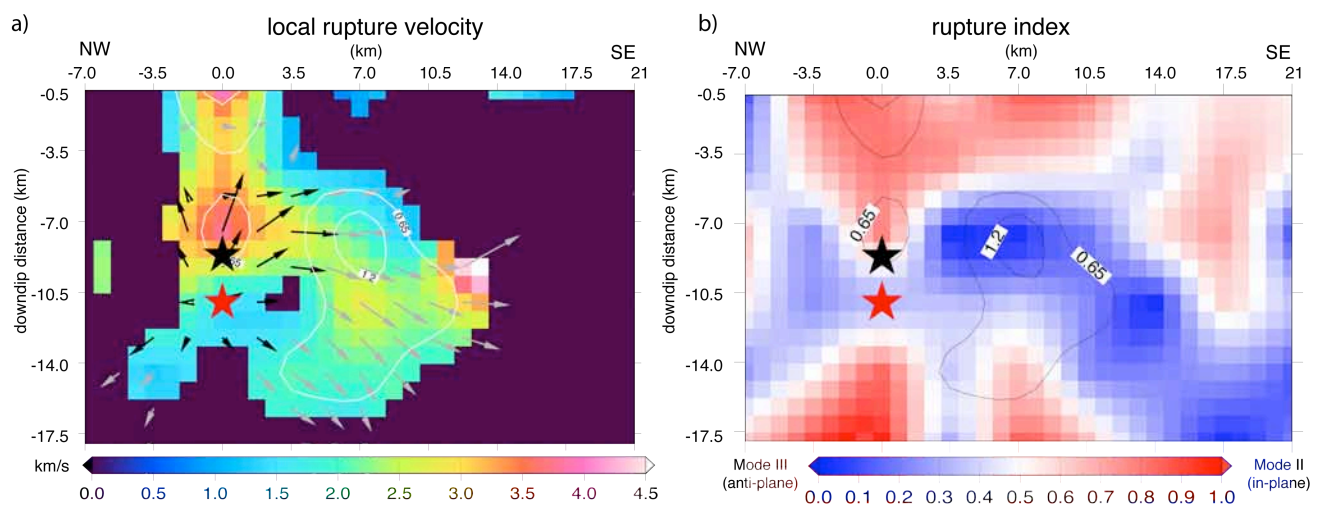


Figure 4. a) Local rupture velocity distribution on the fault plane for the 2009 L'Aquila main shock overlapped by the slip contour (white line, in m) and by the rupture velocity vectors (black and gray arrows show the rupture velocity vector for rupture times between 0 sec and 2.0 sec and over 2.0 sec, respectively). b) Rupture index displaying the rupture mode across the fault plane for the 2009 L'Aquila earthquake. Values toward 1 correspond to a pure mode II (inplane) rupture, values toward 0 to a pure mode III (antiplane) rupture. Values in between correspond to a mixed rupture mode.

Our results show that the L'Aquila earthquake featured a very complex rupture, with strong spatial and temporal heterogeneities suggesting a strong frictional and/or structural control of the rupture process.

1.2 Kinematic Modeling: Rupture process of the 2007 Niigata-ken Chuetsu-oki earthquake by non-linear joint inversion of strong motion and GPS data (INGV team)

The 2007 Niigata-ken Chuetsu-oki earthquake (M_w 6.6) occurred near the west coast of Honshu, Japan, on July 16th at 01:13 UTC (Figure 5). The epicenter has been located at 37.557°N, 138.608°E (Japan Meteorological Agency). This earthquake caused severe damages and fatalities around the source region. In particular, the earthquake struck the Kashiwazaki-Kariwa nuclear power plant (KKNPP), placed on the hanging wall of the causative fault, where a peak ground acceleration (PGA) associated with surface motions exceeding 1200 gals has been recorded (Irikura *et al.*, 2007). The 2007 Niigata-ken Chuetsu-oki earthquake is one of the few large events whose causative fault extends beneath a nuclear power plant; for this reason it attracts the attention of both the geophysical and engineering communities.

In this work, we investigate the rupture process of the 2007 Niigata-ken Chuetsu-oki earthquake, by jointly inverting strong-motion seismic data and GPS measurements. The goal is to constrain the rupture history to better understand the mechanics of the causative fault as well as the observed ground shaking at the nuclear power plant.

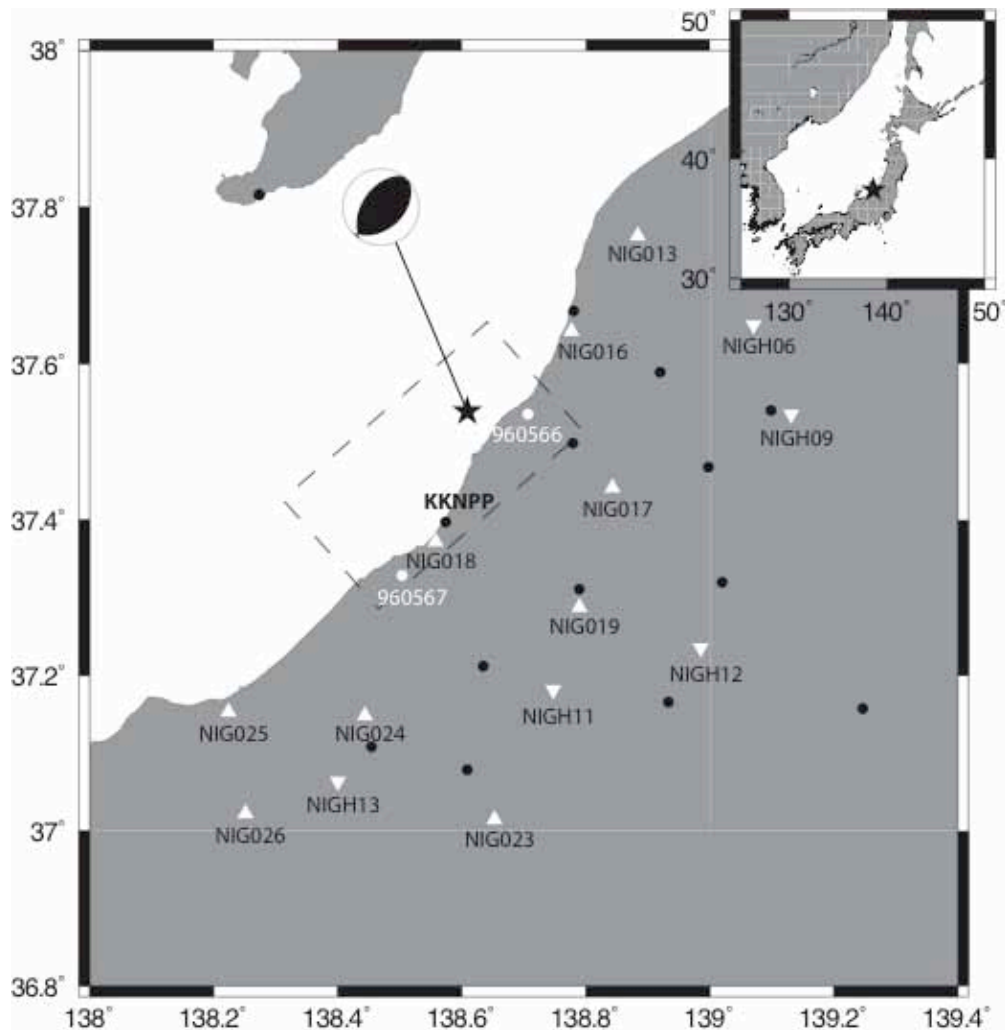


Figure 5. Map of the fault geometry of the 2007 Niigata-ken Chuetsu-oki, Japan earthquake. The dashed black line represents the surface projection of the fault plane adopted in this study. Black star indicates the epicenter. White triangles and inverted triangles represent K-NET (surface sensor) and KiK-net (borehole sensor) strong motion stations respectively. Black dots represent GPS stations. White dots are GPS stations not used in this study. KKNPP indicates the site of Kashiwazaki-Kariwa nuclear power plant.

Data and fault model

Strong motion data from 13 stations of KiK-net (<http://www.kik.bosai.go.jp>) and K-NET (<http://www.k-net.bosai.go.jp>) and 14 GPS (deployed by the Geographical Survey Institute) records of the co-seismic surface displacement are used in our modeling attempts. Their focal distances are less than 70 km and their locations are displayed in Figure 5. We have also plotted in this figure the location of two GPS benchmarks (960566, 960567) and one

accelerograph (NIG018) that are not used in the inversion presented in this study. These GPS data have been excluded because the instrumentation and/or the corrected coseismic displacements might have problems (S. Aoi and K. Koketsu, personal communications). Moreover, we have not used the waveforms recorded at the NIG018 site, which is the closest to the KKNPP power plant, because it is strongly affected by non-linear site effects. However, we have verified that including or excluding these data does not change the inverted source model. Original acceleration recordings are integrated to obtain ground velocity time histories. The resulting velocity waveforms are band-pass filtered between 0.02 and 0.5 Hz using a two-pole and two-pass Butterworth filter. We invert 60 seconds of each waveform, including body and surface waves. The hypocenter location by H-net data is 37.54°N , 138.61°E with 8.9 km depth. We perform the inversion assuming a rupture starting point at the hypocenter located at 8 km depth and on the south-east dipping fault (Figure 5), striking $\text{N}49^{\circ}\text{E}$ and dipping 42° (F-net solution). According to aftershocks distribution we assume a fault model with a length of 38.5 km and a width of 31.5 km; the top of the fault is located at 0.5 km depth. All kinematic parameters are simultaneously inverted at nodal points every 3.5 km equally spaced along strike and dip. During the inversion, the peak slip velocity is allowed to vary between 0 and 4 m/s with 0.25 m/s step increment and the rise time between 1 and 4 sec with 0.25 step increment. The rake angle ranges between 71° and 131° with 5° step increment (the rake angle of the moment tensor solution of F-net is 101°); the rupture time distribution is constrained by a rupture velocity ranging between 2 and 4 km/s. To calculate the Green's functions, we adopt a 1D- crustal model referring to the velocity structure proposed by Kato *et al.* (2005). A detailed description of the adopted methodology can be found in the deliverable D13.3 (New Simulation Scheme) of this JRA3 WP.

Inversion results

The adopted algorithm explores about 2 millions rupture models to build up the model ensemble. Figure 6-a shows the inverted source model obtained by averaging a subset of the model ensemble (nearly 300.000 rupture models), corresponding to those models having a cost function exceeding by 2.5% the minimum value of the cost function reached during the inversion. Left panel in Figure 6-a displays the final slip distribution, middle and right panels show the rise time and the peak slip velocity distributions on the fault plane, respectively. The left panel also shows the slip direction at each grid node. The retrieved model is characterized by two principal patches of slip: a small patch near the nucleation point and a larger one located at 10÷15 km south-west from the nucleation. The larger asperity is characterized by a rise time ranging between 2.5 and 3.5 sec and a peak slip velocity of 2.0÷3.5 m/s, corresponding to 1.5÷2.5 m of slip. The slip direction, shown in the left panel of Figure 6-a (black arrows), is consistent with a nearly pure reverse faulting mechanism. The total rupture duration is about 10 sec. In correspondence of the larger asperity, the rupture front rapidly accelerates from 2.3 km/s to 3.5 km/s. The rupture acceleration occurs in the south-western portion of the fault plane, very close to KKNPP. The adopted inversion methodology has the advantage to provide both the best fitting and the average source models with the corresponding standard deviations of model parameters. Figure 6-b shows the standard deviations of rupture time, rise time and peak slip velocity. We point out that the imaged acceleration of the rupture front is a stable feature and it is associated with relatively small standard deviations. As expected, standard deviations of rise time are larger in the areas of small or negligible slip. Moreover, the absolute values of peak slip velocity display a larger variability in the high slip patches.

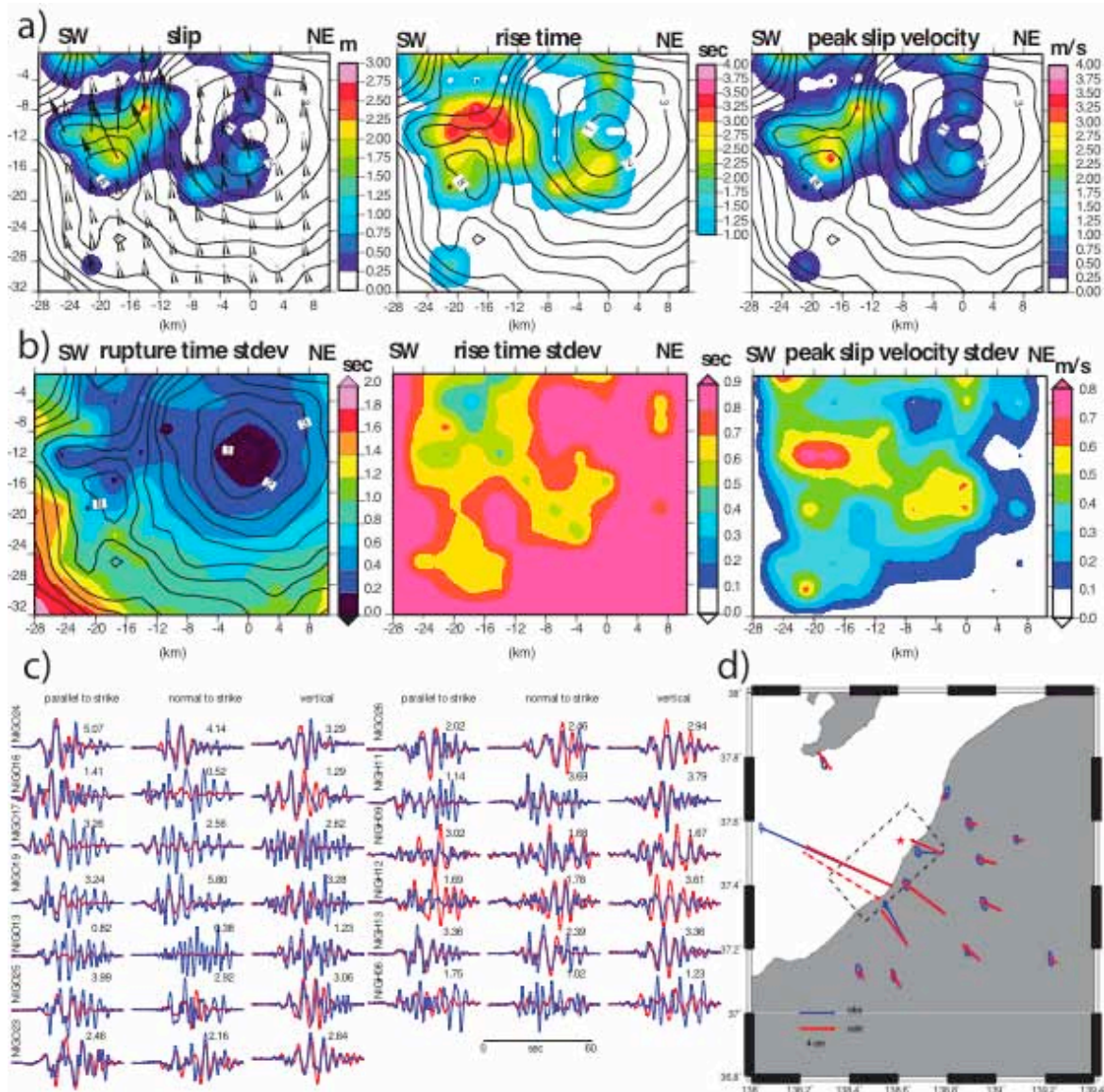


Figure 6. a) Inverted rupture model (average model from ensemble inference) of the 2007 Niigata-ken Chuetsu-oki earthquake. Left, middle and right panels show total slip, rise time and peak slip velocity distributions, respectively. White color in middle panel represents the areas of small or negligible slip. Rupture time shown by contour lines (in seconds); black arrows displayed in left panel represent the slip vector. b) Standard deviation of rupture time, rise time and peak slip velocity for the average rupture model computed through ensemble inference. c) Comparison of recorded strong motions (blue lines) with predicted waveforms computed from the inverted rupture model of Figure 6-a (red lines). Numbers with each trace are peak amplitude of the synthetic waveforms in cm/s. d) Comparison of observed (blue arrows) with synthetic (red arrows) horizontal GPS displacements.

Rupture Directivity Effects

The most peculiar feature of this earthquake is the presence of a nuclear power plant in the hanging wall of the causative fault. As

shown in the previous section, the inferred source model is characterized by a non-uniform slip distribution and a heterogeneous rupture propagation. Slip velocity is concentrated in two patches relatively close to the nuclear power plant (KKNPP), with a slip velocity peak of nearly (3.50 ± 0.75) m/s. The maximum observed PGA, among the accelerograms available to the authors, is 813 cm/s^2 recorded at K-NET Kashiwazaki station (NIG018), which is the closest site to KKNPP. In order to quantitatively assess the source contribution to the ground shaking observed at the nuclear power plant, we have performed a forward estimate of predicted ground motions. By using the inverted rupture model, we have simulated ground velocity time histories at a virtual dense array of seismic stations (889 sites, see Figure 7-a), 14 of which correspond to the actual recording sites mapped in Figure 5. In this way we get a good azimuthal coverage and a dense sampling of the near source area. Figure 7 shows the distributions of the simulated PGV values for the fault-parallel, fault-normal and vertical components. PGV is measured from synthetic seismograms filtered in the same frequency bandwidth adopted for waveform inversion.

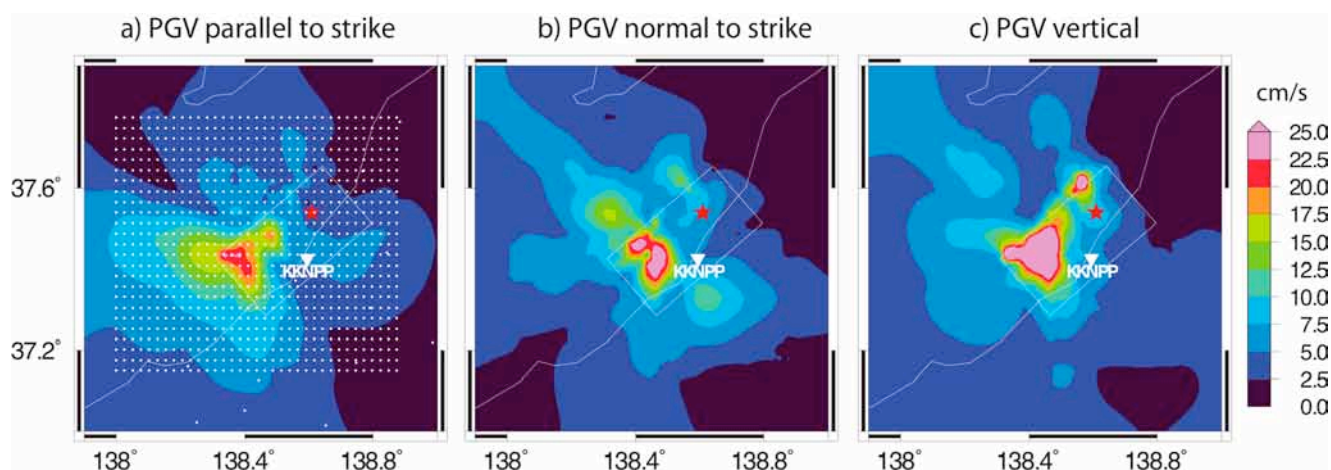


Figure 7. Predicted PGV distribution for the inverted model shown in Figure 6-a. Maps a), b) and c) display the parallel to strike, normal to strike and vertical component, respectively. White circles in panel a) indicate the grid of sites and the white label shows the location of the Kashiwazaki Kariwa nuclear power plant (KKNPP).

The pattern of peak ground velocity reflects the fault geometry, the heterogeneous slip distribution and rupture SW acceleration, revealing

clear directivity effects. The high values of PGV predicted southwestward of the hypocenter are mostly due to the slip distribution and source-to-receiver geometry. Despite this relevant rupture directivity effect, the predicted PGV at NIG018 underestimates the observed value (filtered in the same frequency bandwidth as synthetics) by nearly a factor 10. This result confirms that other effects associated with complex propagation paths and site amplifications contributed to explain the severe ground motion recorded at KKNPP. Worthy of note is the observation that recorded PGA at KKNPP is much larger (nearly two times) than the adopted design value (Sugiyama, 2007). We emphasize that the average rupture model proposed in this study by inverting GPS and strong motion data includes the most relevant features of roughly 300.000 models, which yield a reasonable fit to the observed data. In particular, the adopted inversion procedure allows us to analyze the standard deviations of model parameters and to conclude that the rupture acceleration as well as the directivity effects are stable features of the causative earthquake rupture. We believe that this approach is of relevance to constrain the variability of kinematic model parameters, and it represents an important step towards the performing of reliable predictions of ground motion time histories.

1.3 Kinematic Modeling: Multiple Point Source and Finite Fault Inversions for 2011 Van earthquake (METU team)

On October 23, 2011, M_w 7.1 earthquake occurred in Eastern Turkey, close to Van and Erciş towns, causing more than 600 casualties and a widespread structural damage. The earthquake ruptured a 60-70 km long NE-SW fault with a thrust mechanism, in agreement with regional tectonic stress regime. In this work package, we studied the fault process of the

event and the recorded ground motions using different sets of data. We present the hierarchic modeling of the source mechanism herein step by step. We note that whenever needed, full wavefield Green's functions are calculated by the discrete wavenumber method (Bouchon, 1981). The 1D layered crustal model used herein is based on the study by Gök et al. (2011).

Step 1. Regional data: centroid moment tensor

Table 3 summarizes centroid moment tensor (CMT) solutions of the event provided by international agencies, employing teleseismic data. The spread in the reported horizontal position of centroid is as large as ~ 30 km (even up to ~ 100 km when including the USGS CMT), and very large are also differences between the reported strike, dip (up to 30°) and rake angles (up to 50°). To better constrain the CMT solution we use broadband (BB) data from 12 regional stations (Figure 8) and perform full waveform inversion in ISOLA software [Sokos and Zahradnik, 2008]. The epicentral distances range from ~ 330 to 1290 km, and complete waveforms are inverted in frequency range 0.005 to 0.010 Hz. Deviatoric solution provides a strongly dominant single point source, with a very high double-couple (DC) percentage, $DC > 90\%$. Grid search over depth has almost no resolution. The horizontal grid search (10×10 km) provides the formally optimal source position at 38.689°N , 43.351°E , with the strike/dip/rake angles = 246° , 52° , 75° (Figure 8).

Step 2. Near-regional data: hypocenter relocation and major subevent

In the aftermath of the earthquake, various institutions provided hypocenter locations (Table 4 reports the locations given by the main Turkish and International institutions) showing a significant variability for such a large magnitude event. In order to clarify this aspect, we attempted a relocation of the hypocenter using 20 P-wave and 7 S-wave readings obtained from the stations shown in Figure 9. Four alternative

HYPO [Lee and Valdés, 1989] relocations considering different subsets of the data (e.g., P and S, only P, only near stations, or with a fixed depth) are shown by stars in Figure 10. The hypocenter depth varies from 8 to 15 km. Dots in Figure 10 are the relocation by NonLinLoc method [Lomax et al., 2000] (preferred depths were <10km). As a reference hypocenter solution for the further study we adopt the location from P and S waves (see Table 4). Note that the variability of the epicenter positions in Table 4 is much smaller (~ 10 km) than among the centroid positions (Table 3). Nevertheless, the subsequent modeling (except the high-frequency HIC method) is fully independent of the hypocenter position.

Strong-motion (SM) data from 6 near-regional stations (triangles in Figure 9) are used for the finite-extent source modeling. From the set of stations we had to exclude stations 6503 and 4902 because of the missing absolute time information. The retained stations are in the distance range 120-220 km from the epicenter. In this step we increase frequency band to 0.05-0.10 Hz with respect to the CMT analysis in order to obtain a better spatial resolution of the source and also because the waveform inversion (ISOLA) already requires a few subevents. We concentrate on the major subevent. The deviatoric inversion cannot be used, because now it produces a very large ($> 50\%$) non-DC component due to the finite-extent source effect. Keeping fixed the double-couple focal mechanism from the BB solution (step 1), and making a grid search over depth, we arrive at a clear preference of the depths greater than 10km, but the depths 10-20 km are almost equally likely. The horizontal grid search (5x5 km) maximizes correlation between observed and synthetic waveforms for the major subevent at 38.734°N , 43.351°E (where the 'beachball' is attached in Figure 10). Elongation of the correlation isolines in the NW-SE direction is due to limited azimuthal coverage of the SM stations (worse than in the hypocenter location, where more stations were available). The same horizontal grid search was also repeated in the DC-constrained mode. It confirmed the same optimal position of the major subevent.

Table 3. CMT parameters obtained by global agencies (in italics) and in this study.

CMT	Lat [°N]	Lon [°E]	Depth [km]	Origin time	Mo [*10 ¹⁹ Nm]	Strike [°]	Dip [°]	Rake [°]
<i>Global CMT</i>	38.67	43.42	15.4	10:41:30 .6	6.4	248	36	60
<i>USGS CMT</i>	39.45 1	43.35 4	16.0	10:41:44 .5	9.9	272	19	101
<i>USGS FF (*)</i>	38.62	43.48	15	10:41:21 .6	5.16	241	51	50-70
<i>USGS W-phase</i>	38.85 2	43.84 0	13	10:41:21 .6	5.6	241	51	58
<i>SCARDEC</i>	38.62 7	43.53 5	16-23	10:41:21	6.86	248	53	64
This study regional data (†)	38.68 9	43.35 1	15	10:41:22 .4	7.4	246	52	75
This study near-reg. data (‡)	38.73 4	43.35 1	15	10:41:24 .3	2.1	246	52	75

(*) Finite-fault inversion; location corresponds to the hypocenter, rake varies along the fault.

(†) Fixed depth (poorly resolved, but with basically no change of the focal mechanism).

(‡) Parameters correspond to major subevent. Depth is fixed; it is not shallower than 10km but cannot be resolved in greater detail. Mechanism was fixed at the values of the previous row.

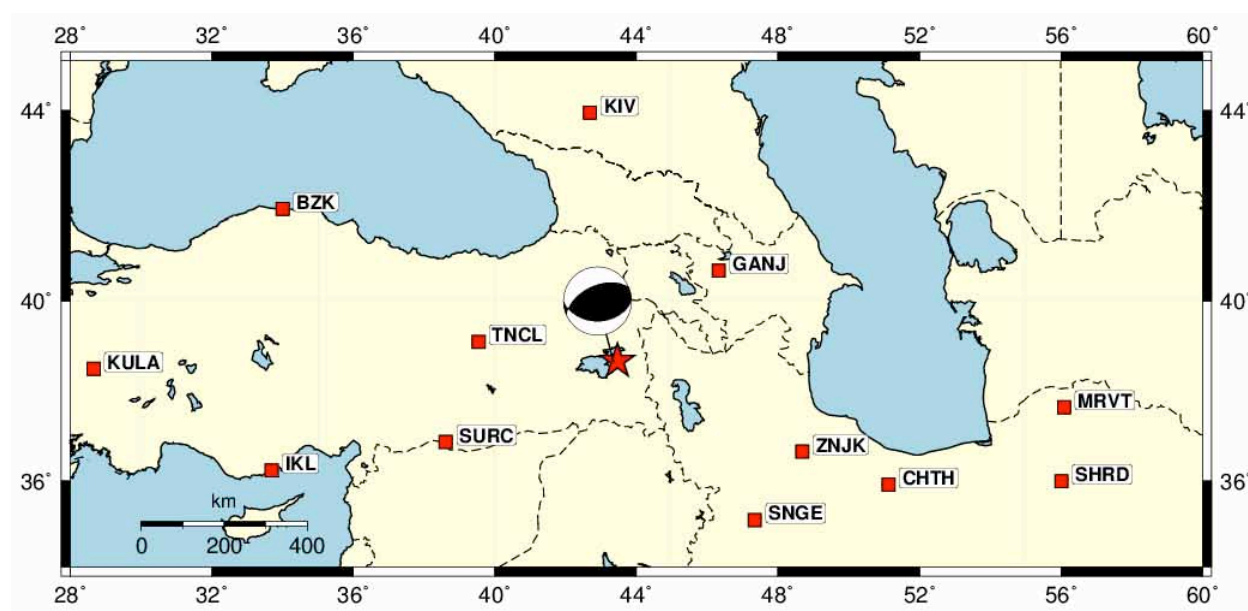


Figure 8. Map of the area with the CMT solution (beachball) calculated for the 2011 Van earthquake using regional broad-band seismograms in the frequency range 0.005 - 0.010 Hz. The used stations are shown by squares.

Table 4. Hypocenter parameters obtained by global agencies (in italics) and in this study.

Hypocenter	Lat [°N]	Lon [°E]	Depth [km]	Origin time UTC
<i>USGS</i>	38.691	43.497	16	10:41:21
<i>EMSC</i>	38.78	43.40	10	10:41:23.4
<i>AFAD</i>	38.689	43.466	19	10:41:18.26
<i>KOERI</i>	38.76	43.36	5	10:41
This study	38.716	43.405	8	10:41:21.2

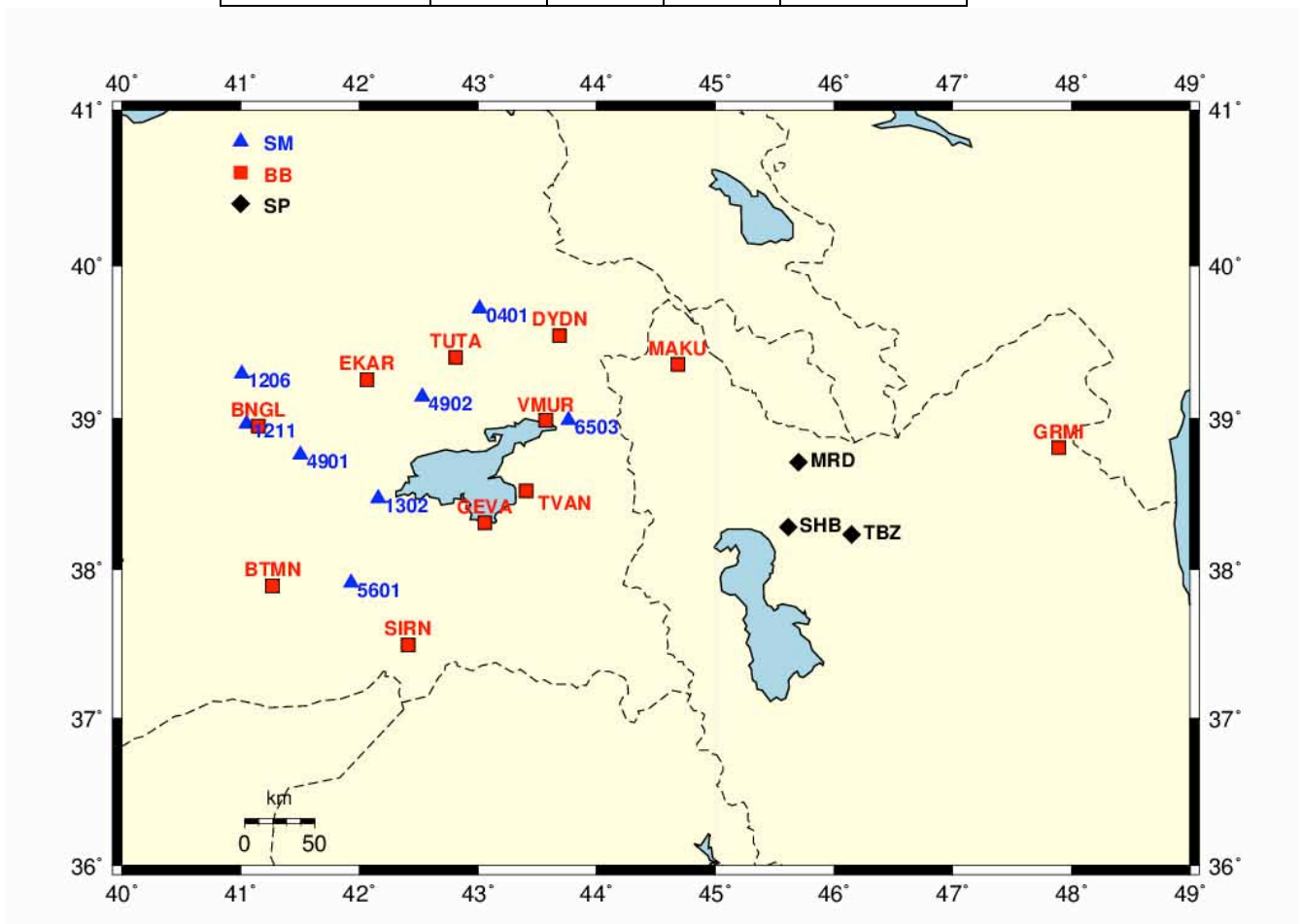


Figure9. Near-regional strong-motion(SM), broad-band (BB) and short-period(SP) stations used in this study.

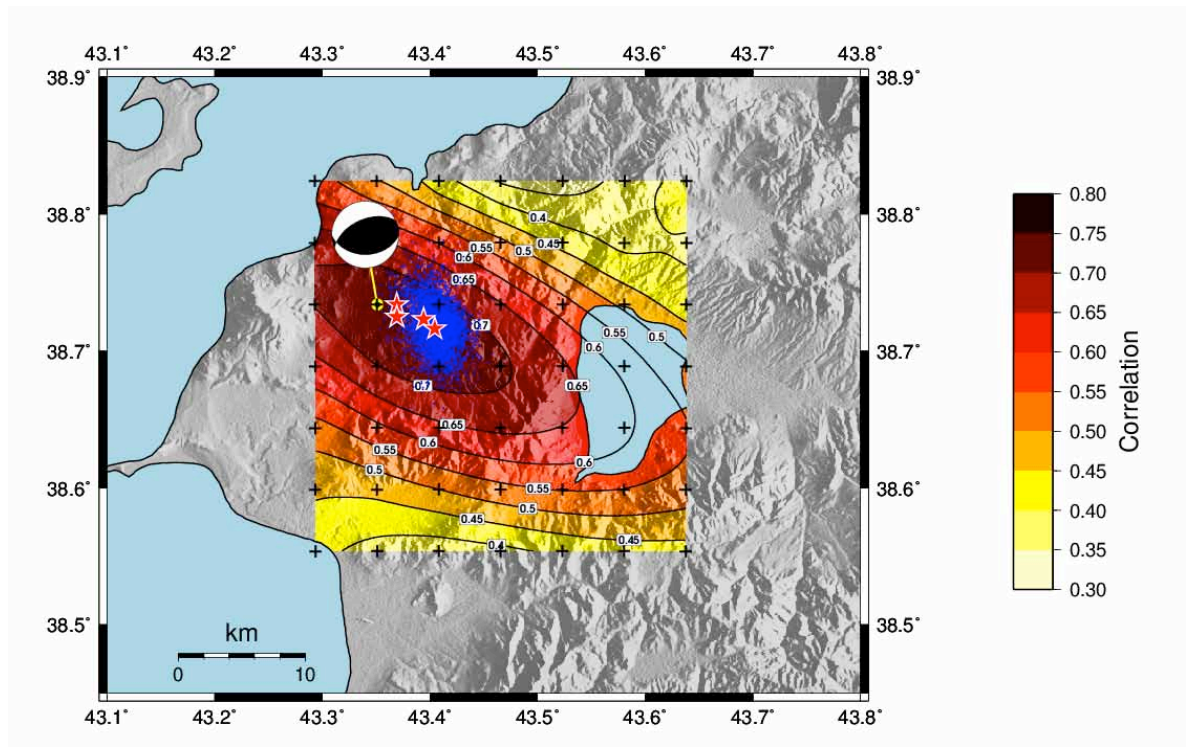


Figure 10. Four alternative hypocenter locations by HYPO (asterisks) and NonLinLoc location (dots) from all stations in Figure 9. The beach ball corresponds to the major subevent inferred from near-regional strong-motion data (see Figure 9), except stations 6503 and 4902, in frequency range 0.05-0.10 Hz by maximizing correlation (isolines) between the observed and synthetic waveforms.

Step3: Near-regional data and GPS: finite-extent source inversion

At this stage, we invert the near-regional strong-motion (SM) data in the frequency range 0.05-0.15 Hz to get a deeper insight into the rupture process. First we use the Multiple Point Source (MPS) inversion. Then the MPS inversion is used to set-up the Multiple Finite-Extent (MuFEx) model. The MPS solution is constructed by iteratively deconvolving individual subevent contributions from complete waveforms (ISOLA code). In order to prevent concentration of the seismic moment release in the first subevent, which is a typical drawback of the free iterative deconvolution, we use a modified iterative deconvolution providing a smoother distribution of the moment on the fault plane: if a subevent requires moment m to fit the data, we permit only $m/4$, and increase the number of searched subevents 4-times [Zahradnik and Galovic, 2010]. The strike, dip and rake of the subevents are kept fixed according to the CMT solution

of step 1. The moment rate of each subevent is a triangle of duration of 10 s. We use a fault plane passing through the point defined by the coordinates of the major subevent assuming its strike and dip parameters, see step 2 above (Table 3), while the depth is fixed at 15 km. This fault plane approximately satisfies the H-C consistency condition [Zahradnik et al., 2008]; indeed, the fault plane encompasses the reference hypocenter if we increase our hypocenter depth (Table 4) by just 2 km. The DC subevents (position, rupture time and scalar moments) were searched in a grid along the fault plane. The MPS solution converged with total moment magnitude M_w 7. Figure 11 shows the space-time distribution of the moment release, projected onto the horizontal plane. The waveforms are matched with variance reductions $VR=0.53$. The MPS solution was repeated with altered parameters to find out its common (stable) features: (i) the moment distribution is relatively compact, (ii) the largest subevents are close to the epicenter (red star in Figure 11), (iii) the smaller subevents are always delayed by ~ 3 s, and situated south-west from the main patch. Very late small subevents (>12 s after the main subevent) also exist, but their position is unstable. The MPS solution exhibits a more-or-less unilateral rupture propagation in the SW direction. As explained in the introduction section, this might be merely an artifact due to the poor azimuthal station coverage. All stations but one are situated west of the epicenter, i.e., the direction of the apparent rupture propagation, and only one station (0401) is located in the perpendicular direction (north of the epicenter). Moreover, without stations closer to the fault, the inverse problem solution might lack important features of the rupture propagation, such as partial propagation in the NE direction. To overcome this issue, we setup a Multiple Finite Extent (MuFEX) source model that allows for a general rupture propagation including possible rupture propagation complexities (rupture jumps and delays). In the MuFEX inversion the source is parameterized by finite-extent subsources, similarly to the approach by Vallée and Bouchon (2004). In the present application we assume three rectangular subsources with constant slip and

rupture velocity. Their position (Figure 12) is based on the MPS inversion, with trial-and-error adjustments to obtain the best waveforms match. Rise time is assumed smaller than the reciprocal of the maximum frequency considered (0.15Hz), thus the delta function is considered. Each subsource has its individually ascribed set of trial nucleation positions, rupture velocities and nucleation times [Galovič and Zahradník, 2012]. We grid-search all combinations of the subsource parameters, while simultaneously solving the least-squares problem for the subsource slip in each tested model. All models are eventually characterized by their fit with observed data (in terms of variance reduction VR). Neglecting all models with negative slip values, and considering models whose variance reduction is at least 95% of the best VR value (0.45), we arrive at a database of plausible models. The GPS data are also used to constrain the features of the slip model. Coseismic displacement is simulated in the forward modeling and compared with the observed one in order to reduce the number of plausible models. The database of plausible MuFEx models (representing uncertainty of the slip inversion) is relatively rich due to unfavorable station distribution with all stations situated at large distances and almost exclusively in a single quadrant. Finally, we select three scenarios with very different styles of the rupture propagation (Figure 12): Model M1 – rupture of subsource n.2 is delayed by ~ 10 s; M2 – subsource n.1 ruptures first and then shallow subsources are activated; M3 – regular rupture propagation from a single nucleation point (no multiple nucleation points, no rupture delays). Rupture velocity (V_r) is 3km/s for all models. The fit with observed data and the GPS vectors is shown in Figure 13. Note that despite the very different style of rupture propagation the fit with the observed waveforms is practically the same for all three models. The differences in fit of the GPS data are given mostly by the slip value of subsource n.2.

Conclusions

Our comprehensive study of the event starts with hypocenter relocation, CMT analysis by means of the full-waveform inversion using the ISOLA package, and the multiple-point source inversion. The latter is then extended to the inversion of the event considering multiple finite-extent (MuFEx) source model, grid-searching for possible values of parameters of the subsources, namely nucleation times, nucleation point positions and rupture velocities. Due to the unfavorable station locations (stations situated at large distances and almost exclusively in a single quadrant), the uncertainty of the source model is very large. We present three selected models to illustrate a broad variability in possible rupture propagation. Broadband simulations with these final source models can be found in Section 2.5.5.

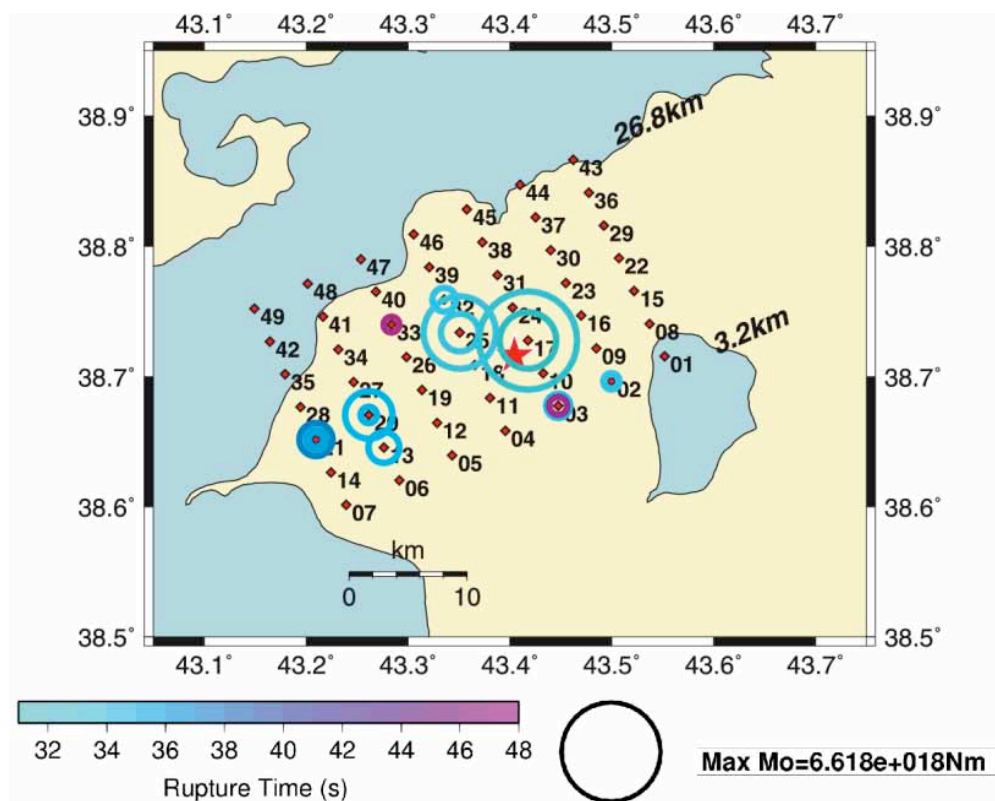


Figure 11. Multiple point source inversion (frequency 0.05-0.15 Hz; VR=0.53) based on the data from near-regional strong-motion stations (see Figure 9) except stations 6503 and 4902. Radii of the circles are proportional to moment of the subevents. The rupture time scale is formally increased by +30s with respect to the origin time. The bottom right circle shows the moment scale. The epicenter of this study is shown by asterisk. The numbers to the right of the fault plane indicate the depth of its top and bottom edges.

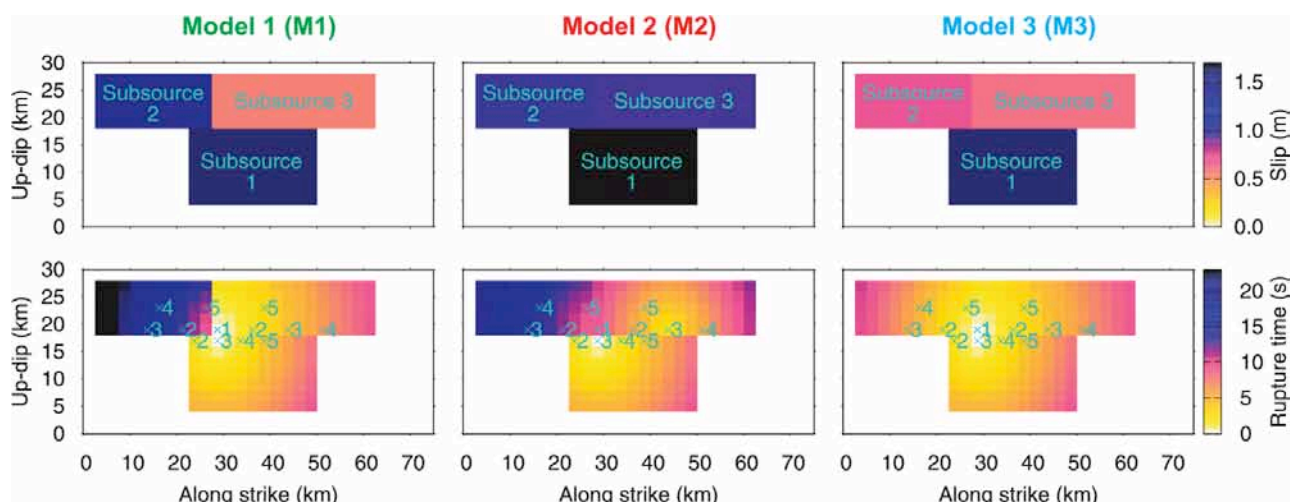


Figure 12. Three alternative Multiple Finite-Extent source models almost equally well fitting the data of near-regional strong motion stations

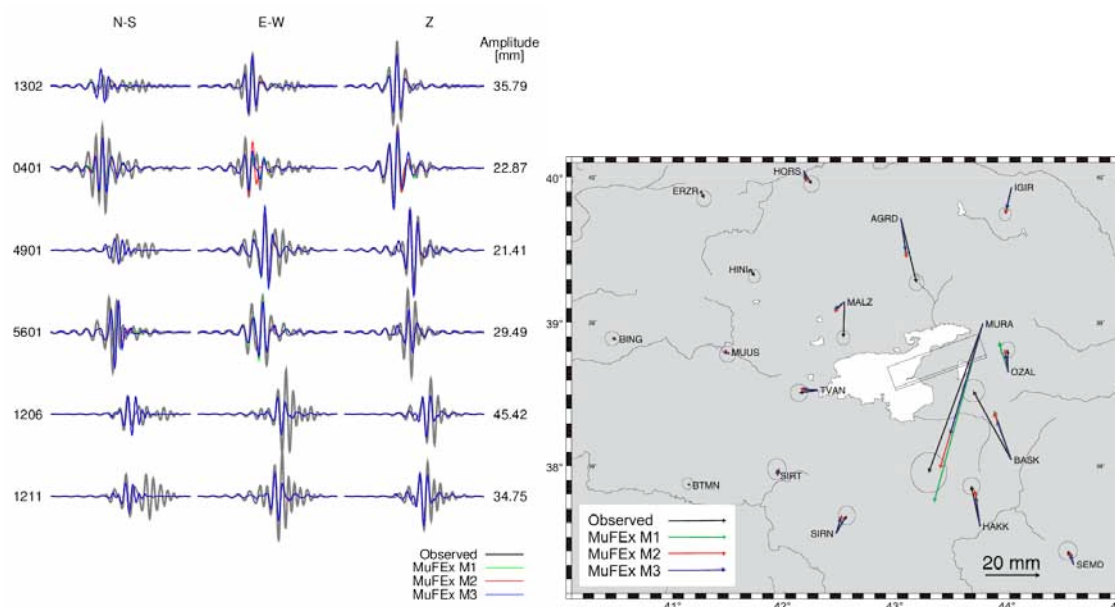


Figure 13. Left: Comparison of complete observed and synthetic displacement waveforms of near-regional strong motion stations (see Figure 9, $VR=0.43-0.45$, duration 100 s) used in the MuFEX source inversion. Note that the seismograms for the models M1-M3 are almost the same although the rupture models differ significantly (see Figure 12). Numbers refer to the peak displacements. Right: Comparison of observed GPS vectors with synthetic ones for models M1-M3. The surface projection of the fault is displayed.

The results shown in this contribution can be found in the following paper: F. Gallovič, G. Ameri, J. Zahradník, J. Janský, V. Plicka, E. Sokos, A. Askan, M. Pakzad (2013). Fault process and broadband ground-motion simulations of the 23 October 2011 Van (Eastern Turkey) earthquake, *in press* at *Bulletin of the Seismological Society of America*.

1.4 Dynamic Modeling: Kink Fault Modeling, Damage Models (AMRA team)

Effect of the kink on the rupture propagation and radiation

Faults are segmented at all scales, with rupture paths characterized by kinks, bends, jogs and jumps. Complexity in the geometry results into a rough profile for the initial stress even for a uniform remote charge and generates local stress concentration and off-fault dissipation as damage in the surrounding volume. Numerical studies, laboratory experiences, observations on natural faults and inversion of seismological data point to these geometrical discontinuities as critical regions for rupture propagation and near fault radiation: they can control the rupture speed up to arrest the faulting process and can generate directional high frequency waves. With this study, we investigated by numerical simulations the role of the geometry on both the propagation of the rupture and the high-frequency radiation pattern in the fault vicinity. We simplified the problem to the case of a single kink, that is a fault which instantaneously changes its slope. Even tackling this simple problem with numerical methods is difficult. Rapid slope changes of the fault surface require adaptive non Cartesian grids, with an accurate approximation of the energy balance between the elastodynamic flux and the dissipation in the process zone. Moreover, the kinematic incompatibility of the slip at the kinks should result into an energy integrable singular static stress field which has to be taken into account by the numerical models. We investigated here recent advances in numerical approximation of dynamic rupture using the non-smooth spectral element method that allows to model the geometrical complexity of the fault interface together with a spectral accuracy in the solution of the radiated wavefield. The non smooth contact and friction conditions are locally solved in terms of traction, slip and slip rate. We assumed a simple 2D in-plane rupture propagation with uniform remote stress distribution and we investigated

the role of rapid variations in the fault geometry on the rupture velocity, the radiated energy, the wave amplitude and the stress distribution in the volume surrounding the fault as a function of the kinking angle, the initial conditions and the fracture energy. As compared to a straight rupture, we found that a sudden change in the rupture velocity occurs when the rupture turns at the kink. Increase or reduction of the rupture speed only depends (for low angles up to 25°) on the extensional or compressional branch. Hence, the rupture velocity is mainly driven by the sudden change in the dynamic normal stress, which decreases on the extensional branch and increases on the compressional branch (see Figure 14). In the extensional branch, the variation in the rupture velocity is more important when the rupture impact at low speeds as compared to the Rayleigh wave velocity. The opposite occurs in the compressional branch. In this case, the rupture velocity is significantly reduced, and for high angles (20° to 25°) the rupture stops at the kinks.

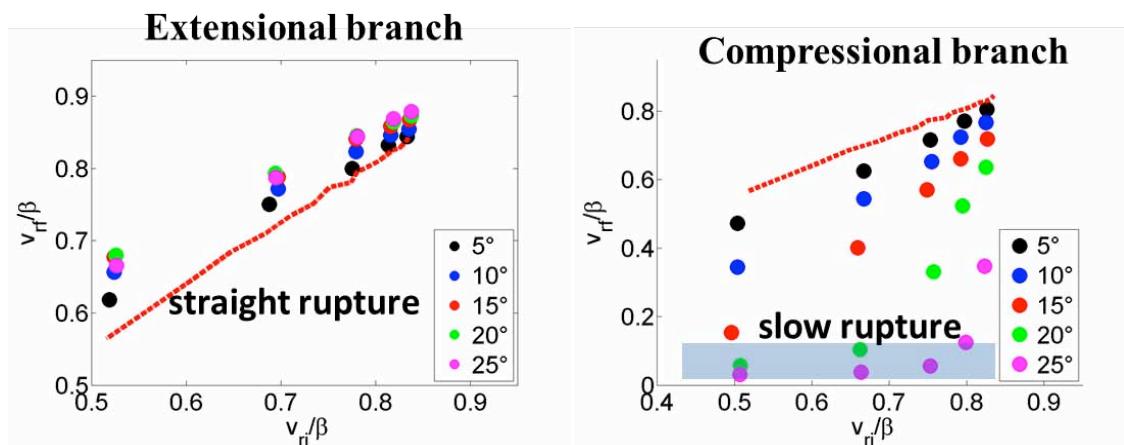


Figure 14. Sudden change in the rupture velocity when the rupture goes beyond the kink

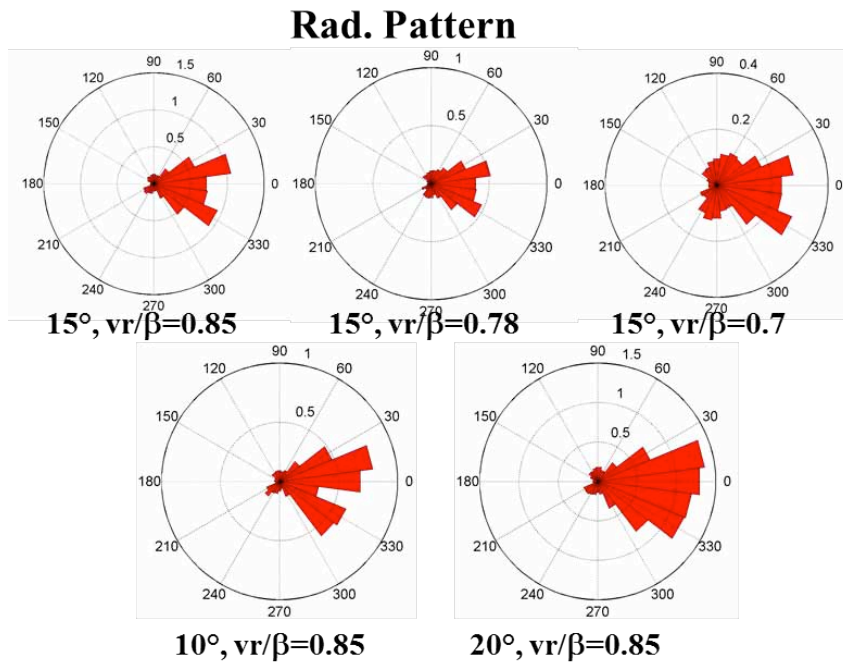


Figure 15: Radiation pattern for different kink angles and rupture velocities.

It is pretty interesting to observe that, depending on the initial stress condition, the kink can speed up a rupture at supershear velocities while a rupture advancing at a supershear speed can preserve its velocity when crossing a kink even if static conditions would not allow to develop the supershear (s parameter larger than 2). As for the radiation, when the dynamic rupture impacts against a kink a strong S wave is emitted, coming from the unbalanced stress conditions on the two branches of the faults. This phase looks like a directional stopping phase, because a part of this is absorbed by the rupture that nucleates on the new branch. In Figure 15 we plotted the relative amplitude as a function of the azimuth for different kink angles and rupture velocities. We observed that the amplitude of the radiation is poorly sensitive to changes in the rupture velocity while it strongly depends on the kink angle. Specifically large accelerations are expected in the direction between the two branches and up to 40° , while the amplitude in the antidirective region is smaller than one order of magnitude. This difference is even more enhanced for supershear rupture propagation.

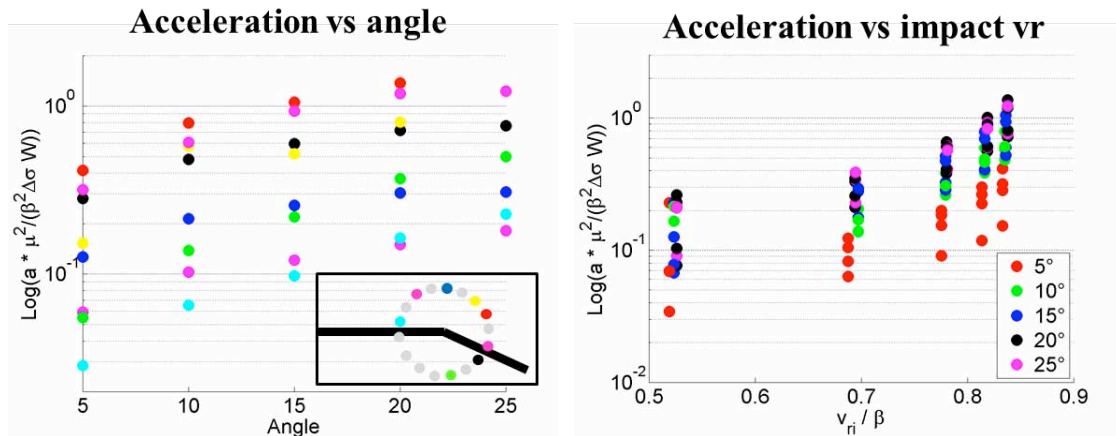


Figure 16: Normalized PGA as a function of the kink angle, at different locations and as a function of the impact rupture velocity.

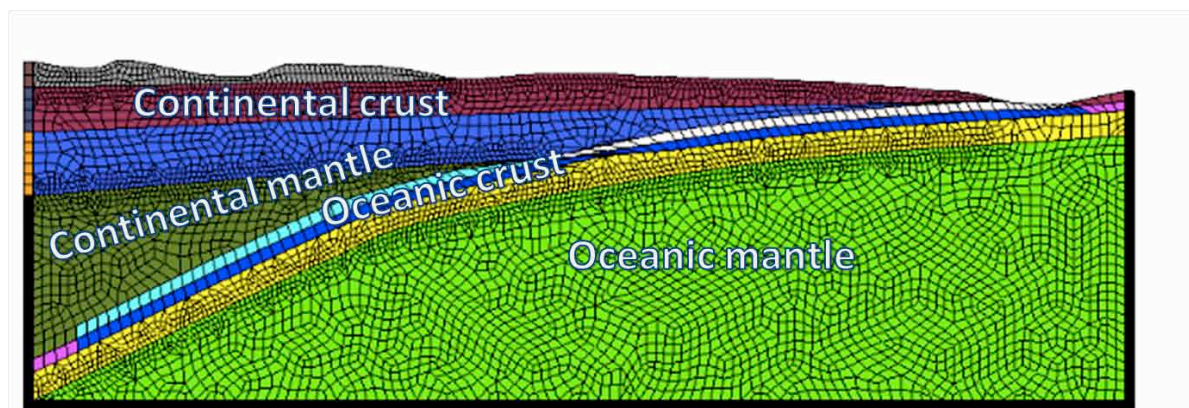


Figure 17: Numerical mesh of the Tohoku area.

When looking finally to the peak acceleration as a function of the kink angle or the impact velocity (Figure 16), we observe almost one order of magnitude in the PGA when moving around the kink from directive to antidirective region for all angles, with a maximum in the PGA for a kink angle of 20° . The PGA is strongly sensitive to the velocity at which the rupture impacts against the kink and increases linearly in a logarithmic scale as a function of the rupture speed. For high speeds the PGA strongly decreases of one order of magnitude when the kink angle is reduced to 5° . Finally the ground motion in the near fault region is also sensitive to the frictional properties of the fault and as expected the acceleration decreases as the characteristic slip length increases. This happens

because a larger amount of energy is spent by the friction and is not available to radiate high frequency waves.

Geometrical control on the radiation and rupture propagation for the Tohoku earthquake

The Tohoku earthquake $M=9.0$, occurred off the east coast of Japan on March 2011 and generated a huge tsunami that ravaged the east coast of North Japan. The East-Japan seismogenic area represents a typical example of subduction zone with a nearly horizontal plate in the shallow part close to the trench and a steepest one at depth. In this specific case, the subduction plate presents some geometrical complexities, that can be modeled as a series of kinks going from near to grazing incidence at the free surface up to 25 degrees at the continental mantle-oceanic crust interface: this makes the event suitable to infer interesting information about the influence of the geometry on the rupture propagation and radiation. Additionally, Tohoku earthquake was recorded by a large amount of seismic stations and marine buoys. Inversion of local and teleseismic data indicates a complex frequency dependent rupture with low frequency radiation generated near the trench, where the tsunami wave was triggered, and the largest slip (30 to 80 m) was observed while the high frequency contribution, responsible for the ground shaking on the coast, originated in the deepest part. Since geometrical features mainly appears in the up-dip direction, where the rupture was confined during its first stage, a large number of 2-D spectral element dynamic rupture simulations was performed. In all the simulations the geometry of the subduction interface and the velocity model were fixed, resulting into a single 2D mesh for the area (Figure 17). We point out that the Tohoku earthquake nucleated in a particular crustal area of the plate, where according to the theory of bimaterial interfaces, the rupture should be favored to propagate bilaterally. Many rupture models were generated by changing the nucleation point, the stress distribution and remote stress orientation, the friction conditions, by including in the stress field possible

effects due to large pore pressure near the trench or to asperities in the continental mantle, as indicated by kinematic inversions.

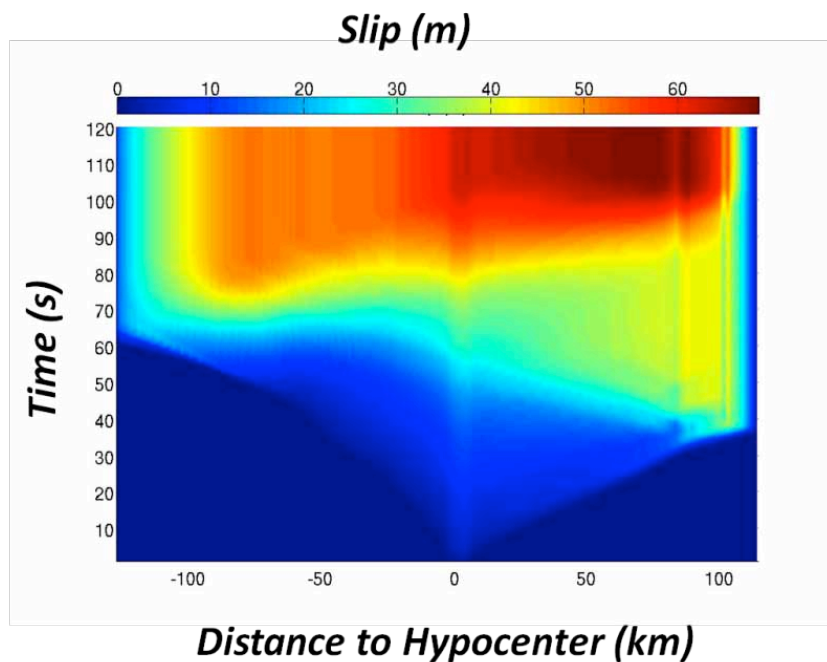


Figure 18: Slip map from preferred model

As a general feature, we observed a different behavior of the rupture as a function of the direction of propagation: upwards the rupture goes faster and the dynamics is mostly controlled by the changes in the slope of the interface. In some cases it stops near the trench where it is not statically favored; nevertheless sometimes it restarts, boosted by trapped surface waves generated and amplified below the oceanic floor. For downward propagation we obtained a slow rupture in its initial stage followed by a sudden acceleration at the entrance in the mantle in correspondence with a sharp change of slope. For some specific stress conditions (according to the s value) the rupture accelerates up to supershear speeds. From inspection of all models, our preferred one fairly well represents all the features of the initial stage of the Tohoku earthquake. We obtained a bilateral rupture faster upward and a large patch of slip at the trench as an effect of both low normal traction and stationary surface waves. We also retrieved a second asperity between the hypocenter and the shallow

part; although the strength parameter was still consistent with a supershear condition ($1 < s < 1.4$) the rupture proceeds to the generalized Rayleigh wave speed at least until a few kilometers before the start of the healing (Figure 18). Inside the mantle the rupture accelerates and this acceleration behaves as a high frequency radiator. Since the location of the geometrical and structural discontinuities are not collocated, we can recognize that the geometrical variations are more important than structural ones. When comparing the strong motion at the station MYG011 of the *K-Net* network, we retrieved only the first high-frequency burst while the second wave train is likely to be associated to a complex 3-D effect of the rupture. We retrieve also a high-frequency signal from the trench, that could be due to a lack of anelastic attenuation near the surface which could be needed for a more realistic model.

Damage Modeling

Geological observations of fault zones reveal that a seismic rupture does not only provide localization of slip along a very thin interface of few centimeters of thickness, but creates damage in a deeper region, the thickness of which can reach several hundreds of meters. Since the wavelengths at which we investigate the rupture are generally larger than the thickness of fault zones, we renounce to the description of the microscopic/mesoscopic processes occurring within the fault zones and simplify the geometrical description of the problem by replacing the layer with an interface of zero thickness. As a consequence of remote stress, the boundary condition should firstly reproduce the elastic deformation of the layer up to a given strength level and later, when the irreversible rupture occurs, the two competing mechanisms of the layer damaging and the friction mobilization. To build up the model we assumed that, during the interseismic period, the fault layer is elastically deformed as the effect of remote tectonic load and accumulates strain energy with time. This energy is reversible and could be in principle released if the remote load

were removed. The layer can sustain the load until the fracture threshold is reached. After that point, the rupture starts and damage is produced inside the layer dissipating energy in competition with the friction along the main interface. We assumed a thermodynamic description of the rupture, a Dupré form for the damage dissipation energy and an internal state parameter that describes the evolution of the damage, the parameter ranging between 0 (completely damaged interface) and 1 (no damage). We came out with a new constitutive law, with three parameters, the dynamic friction coefficient, the elastic stored energy, that can be related to the fault strength and the elastic stiffness of the interface, which is directly linked to the elastic properties homogeneized in the damaged layer surrounding the interface. The constitutive law is a non linear relationship with a minimum, when plotting the traction as a function of the slip. Within this friction law, we investigated the behavior of the nucleation, the dynamic rupture and the radiation in a 2D inplane geometry. As for the nucleation size, this is controlled by the slope of the interface law at zero slip. For the damaged interface we did not observe a critical length smaller than the equivalent linear slip weakening length with the same slope. We argue that this is because of the convexity of the interface laws, that results in a decrease of the slope along the curve as the slip increases. Hence, the interface can accommodate smaller stress drops by large slip. However, when assuming a large thickness of the damage layer, we also observe a stable solution according to which the traction can increase until the zero mode becomes itself unstable. Finally, from a general point of view, there is not a large variability in the critical length also close to the transition unstable regime/definitely stable regime.

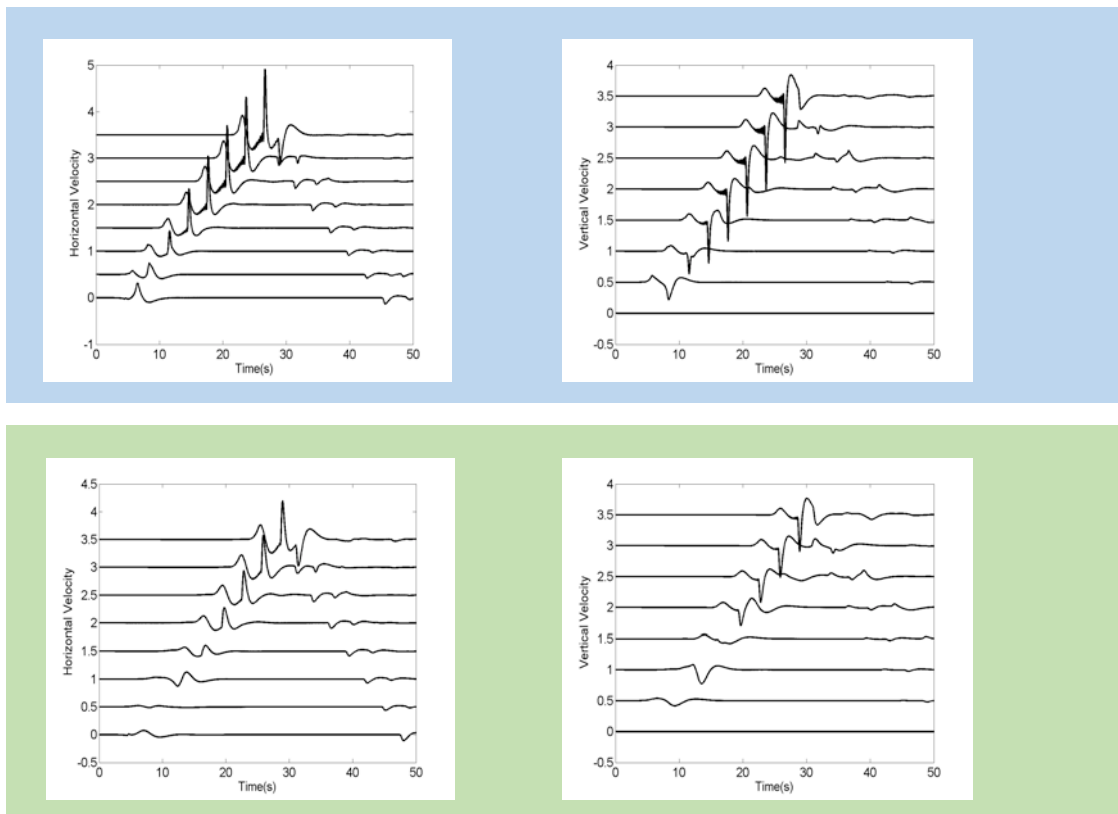


Figure 19: Velocity seismograms for linear slip weakening and friction-damage interface laws.

Looking at the dynamic simulations we observed a generally slower rupture, as compared to interface frictional models. We indeed need a larger distance to reach asymptotic rupture speeds (Rayleigh or P wave speed). Pulse and crack modes for supershear propagation still hold and transition occurs for the same values of s and k parameters as compared to the linear slip weakening model. Anyhow, since the distance at which the supershear changes of about one order of magnitude we can conclude that the presence of the damage inhibits the supershear acceleration. Finally, we compared the linear slip weakening model with the coupled friction-damage interface law on the radiated field, by recording the fault high frequency radiation at a series of receivers. As a conclusion, we found as significant reduction in the high frequency content in the near-fault records, as shown in Figure 19. Specifically this implies that the peak-ground acceleration can be reduced of one order of magnitude in the fault vicinity because of the extended damage, independently of the azimuth of the station. On the other way around, we can also include

artificial damage on the fault itself to stabilize and limit the high frequency pollution generated by numerical simulations.

1.5 Dynamic Modeling: Dynamic Parameters

Distributions computed from Finite Fault

Kinematic Models (INGV team)

In order to compute the dynamic traction evolution on the fault plane corresponding to a specific kinematic model, we solve the elasto-dynamic equation by using the slip velocity history as a boundary condition on the fault plane (Day et al., 1998; Tinti et al., 2005a). We employ a 3-D finite difference dynamic code based on traction-at-split-nodes to compute the dynamic traction time history on the earthquake fault plane (Andrews, 1999). The fault is represented by a surface containing double nodes and the stress is calculated through the fundamental elasto-dynamic equation (Ide and Takeo, 1997, Bouchon, 1997). The algorithm computes stress variations, and the absolute value of shear traction is obtained after assigning the amplitude and the direction of initial stress (see Tinti et al., 2005a, for details).

Fukuyama and Madariaga (1998) have proposed an analytical expression relating the shear traction change on the fault plane to the slip velocity

$$\tau(\vec{x}, t) = \frac{\mu}{2V_s} \dot{S}(\vec{x}, t) + \int_{\Sigma} \int_0^t K(\vec{x} - \vec{\xi}; t - t') \dot{S}(\vec{\xi}, t') dt' d\Sigma \quad (1.1)$$

where $\dot{S}(\vec{x}, t)$ represents the slip velocity, V_s the S-wave velocity, μ the rigidity, K the dynamic load associated to those points that are still slipping at a given time t and Σ is the fault area. Equation (1.1) shows that the total dynamic traction in each fault position is calculated by the sum of two contributions: the instantaneous term depending on the slip velocity at the same position and the dynamic load related to the previous slip history (including the contributions of those grid points

within the cone of causality). If we use this equation to interpret our numerical algorithm, we can state that each node of the fault plane is forced to move with a prescribed slip velocity time history, and the stress change is determined as the sum of the instantaneous contribution of this slip velocity and the contribution of those points on the fault that are still slipping at the prescribed time. This approach does not require specifying a constitutive law and the dynamic traction evolution is a result of calculations. Equation (1.1) further corroborates the link between slip velocity and shear traction change. The traction evolution allows the calculation of different dynamic source parameters such as the breakdown work W_b (Tinti et al., 2005a, Cocco et al., 2006), breakdown and dynamic stress drop and strength excess (see Figure 20) on the assumed fault plane as well as the estimate of the critical slip weakening distance D_c (see Cocco et al., 2009).

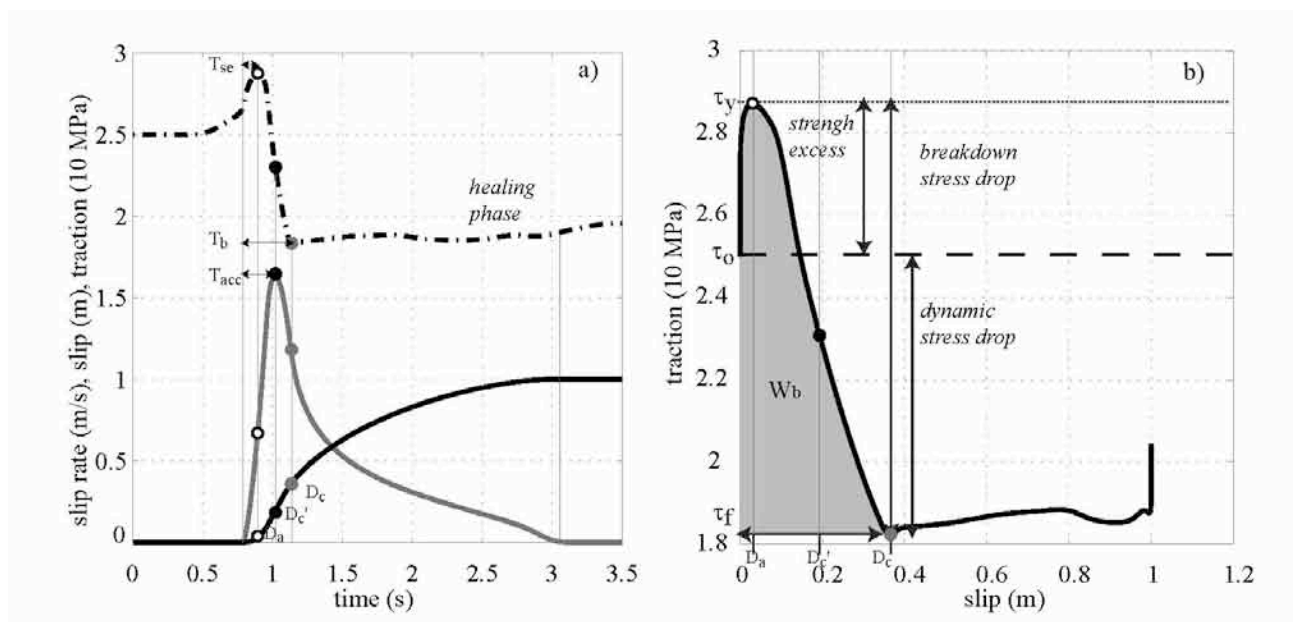


Figure 20: (a) Comparison of slip velocity, slip and traction time histories at a target point on a fault plane using a smoothed Yoffe function as a source time function (Tinti et al 2005b). Black solid circle indicates the time of peak slip velocity (T_{acc}) and the grey solid circle indicate the end of weakening (T_b); (b) corresponding traction versus slip behavior; the same circles of panel a are indicated in term of slip with D_a , D'_c and D_c parameters, respectively. The grey area represents the breakdown work (W_b).

We applied this methodology to the 2009 L'Aquila M_w 6.1 earthquake. The input kinematic model used to retrieve the corresponding dynamic source parameters derived from Cirella et al 2012. This kinematic model is inferred through a joint inversion of strong motion, GPS and InSAR data (see Cirella et al 2012 and Section 1.1 for details). Because this model has a heterogeneous rake distribution (even if the earthquake is a prevalent dip slip fault), the dynamic parameters are inferred accounting for both the along-dip and along-strike slip velocity components. Details for the computation of dynamic parameters with heterogeneous rake on the fault plane are explained on Tinti et al (2005a). In Figure 21a we show the slip distribution inferred from Cirella et al (2012) and interpolated to have the minimum resolution needed to compute dynamic parameters. The spatial discretization and the time step of this dynamic model are 350 m and 0.02 s, respectively. In Figure 21b we show traction change evolution versus slip for some subfaults of the fault plane (the subfaults are indicated in Figure 21a with grey dots). Figure 21b highlights the heterogeneous evolution of the traction on the fault plane. However, all the subfaults having significant slip show a clear slip-weakening behaviour (not imposed a priori).

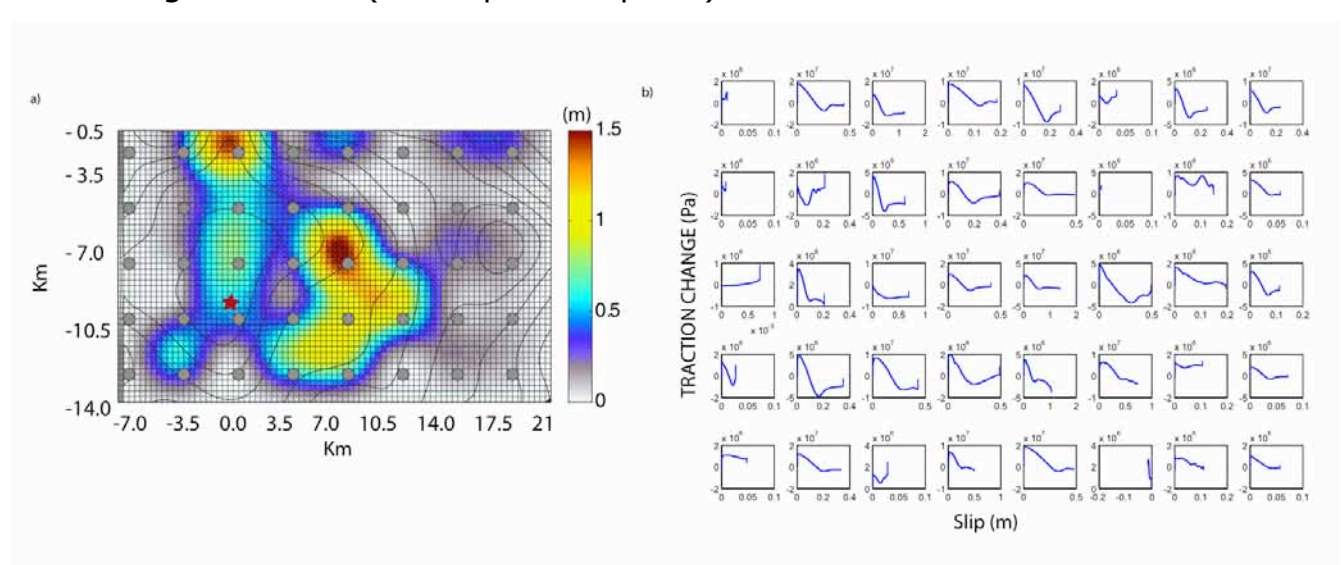


Figure 21: (a) Slip distribution of 2009 L'Aquila earthquake. Star indicates the hypocenters, contours indicate rupture time; (b) Traction change versus slip evolutions (for simplicity only dip components for both the parameters are showed) for several subfaults highlighted through grey dots on panel a.

The knowledge of traction evolution and slip time history allows the computation of D_c as well as all the other dynamic fundamental parameters at each gridpoint on the fault plane.

The D_c distribution inferred from this plot is heterogeneous on the fault plane but strongly dependent on total slip (Tinti et al., 2009). Indeed, the inferred ratio D_c/D_{tot} is quite constant, it ranges between 0.5-0.6 and strongly depends on the a priori assumption of T_{acc} parameter imposed during the kinematic inversion (Tinti et al 2009). Tinti et al. (2005a) defined the breakdown work (W_b) as an alternative measure of seismological fracture energy. W_b is defined as the excess of work over the minimum traction level achieved during slip. Figure 22 shows the distribution of breakdown work as defined by Tinti et al 2005a.

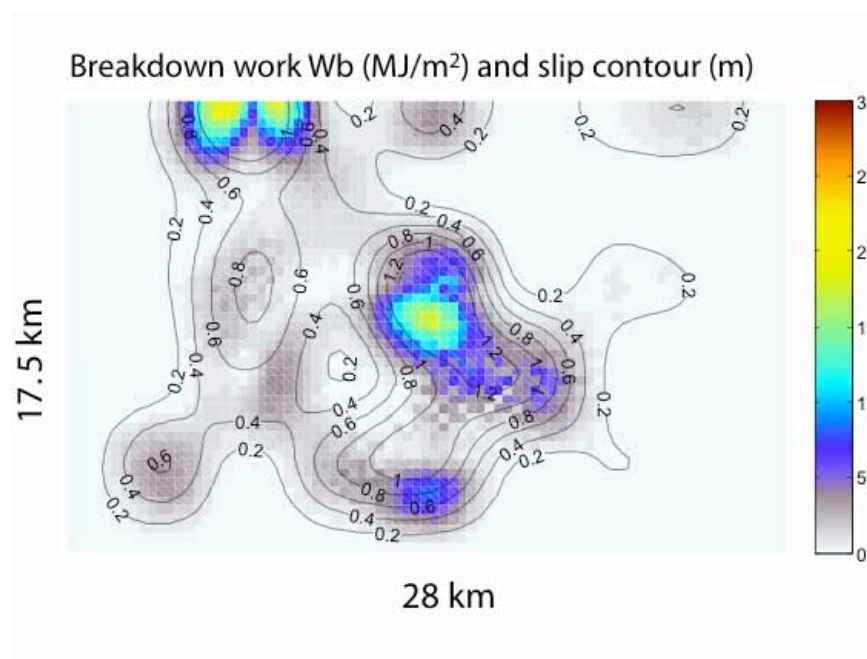


Figure 22: Breakdown work distribution and contours of slip distribution.

The contours represent the slip distributions superimposed on the W_b values. We observe that breakdown work density is strongly correlated with the corresponding slip distribution: W_b is concentrated in high slip patches. The correlation between W_b and the slip distributions is due primarily to the correlation of D_c with slip but also secondarily to the correlation of stress drop with total slip.

Starting from this distribution it is possible to compute average estimates of W_b over the whole fault or relative only to the contribution of the part of fault that slipped more than a percentage of the average slip or maximum slip. These values can be useful to infer information on scaling relation between breakdown work and seismic moment or breakdown work and slip.

1.6 Source Statistic Modeling: Constraining 1-point and 2-point source statistics (ETHZ team)

In this study, we constrain 1-point and 2-point statistics of kinematic source parameters derived from dynamic rupture modeling, following the method proposed by Song et al. (2009) and Song & Somerville (2010). Figure 23 shows an example of both auto- and cross-correlation structures estimated from three spontaneous dynamic rupture models (Song & Dalguer 2013). The three rupture models are obtained by dynamic modeling under the slip weakening friction law by perturbing the standard deviation of input stress drop distributions. As shown in Figure 23, both auto- and cross-correlation structures are significantly and systematically perturbed by the perturbation of the standard deviation. In particular, both cross-correlation maximum and response distance (i.e., offset distance of the cross-correlation maximum) decrease with the standard deviation increasing. This study clearly demonstrates that the standard deviation of input dynamic parameters may play a dominant role in determining the characteristics of source statistics in derived kinematic motions although they are not explicitly considered in many dynamic rupture-modeling studies.

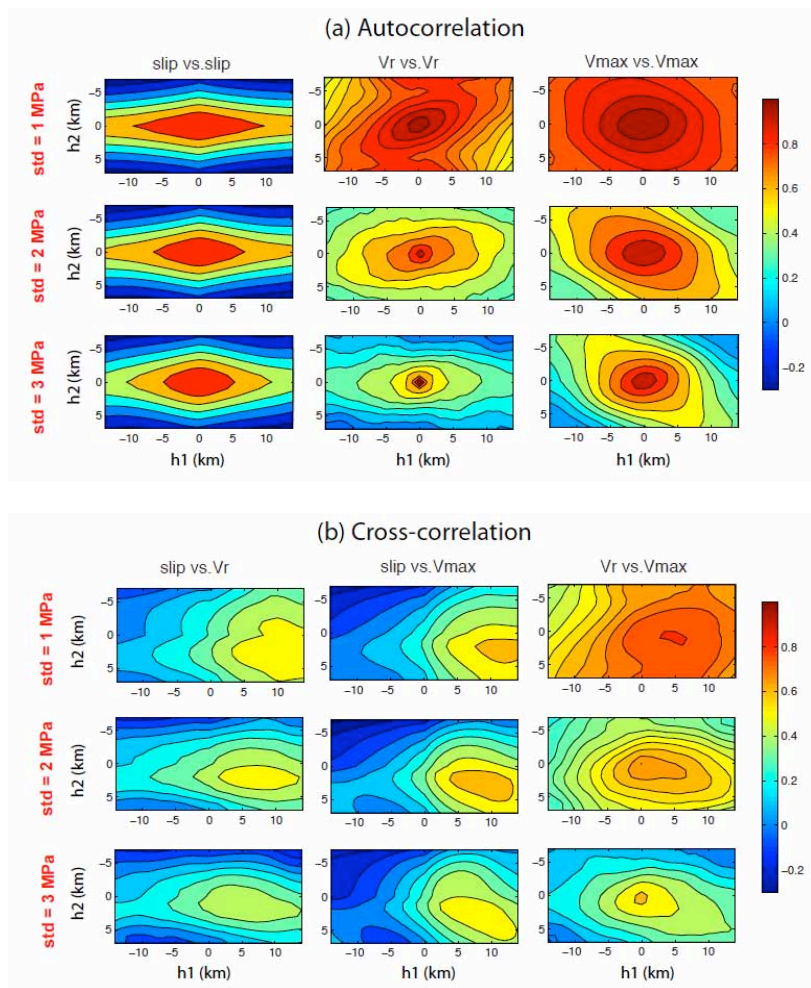


Figure 23. 2-point correlation structures extracted from a dynamic rupture model. (a) autocorrelation, (b) cross-correlation (Song & Dalguer 2013).

We also investigated 2-point correlation structures by analyzing a number of dynamically derived rupture models (~ 200), developed by Dalguer & Mai (2011; 2012). Figure 24 shows distributions of maximum cross-correlation coefficients between different pairs of source parameters. We observe strong correlations between all pairs of source parameters and especially stronger correlations are observed between slip and peak slip velocity. The histograms of the maximum cross-correlation coefficients generally follow the slightly skewed Gaussian distribution. The response distance estimates are relatively small (mostly smaller than 3 km) for rupture models in the database. Figure 25 shows the distributions of correlation lengths both in the along-strike (ax) and along-dip directions. The diagonal and off-diagonal blocks represent correlation length estimates from auto- and cross-correlations, respectively. Note that the

cross-correlation also has its own correlation length estimates since we consider non-zero offset correlation as well. The histograms generally follow the exponential distribution.

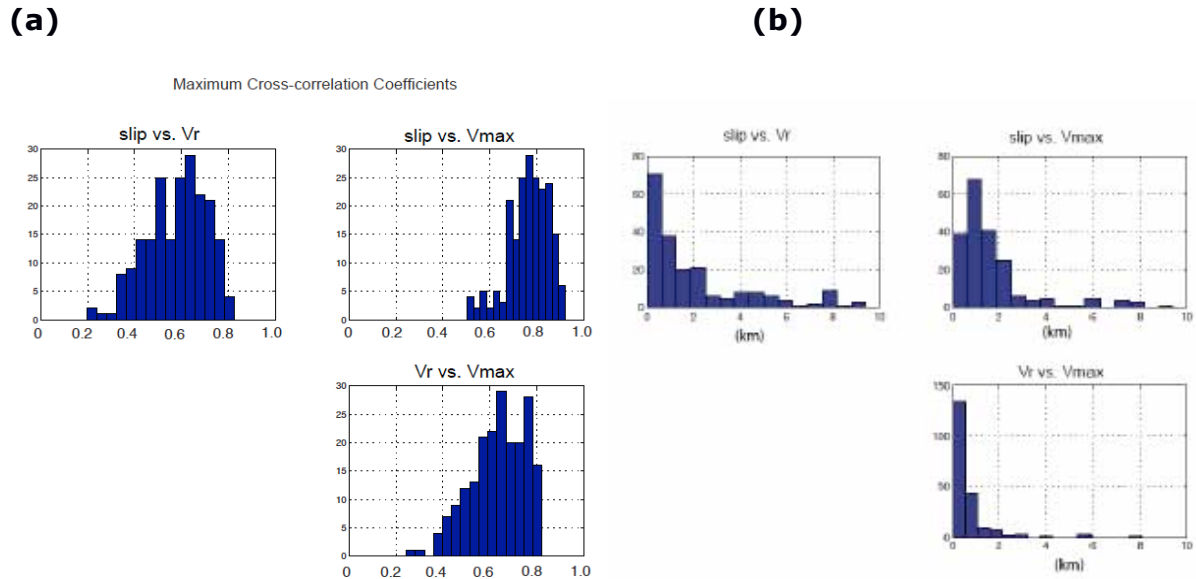


Figure 24. Maximum cross-correlation coefficients (a) and response distances (b) extracted from about 200 events in the dynamic rupture model database (Song et al. 2013). The magnitude ranges between 6.5 and 7.0. The histograms of the maximum cross-correlation coefficients generally follow the slightly skewed Gaussian distribution. The database includes various types of events such as strike-slip vs. dip-slip, surface vs. subsurface rupture, and depth-dependent vs. independent stress field in dynamic modeling.

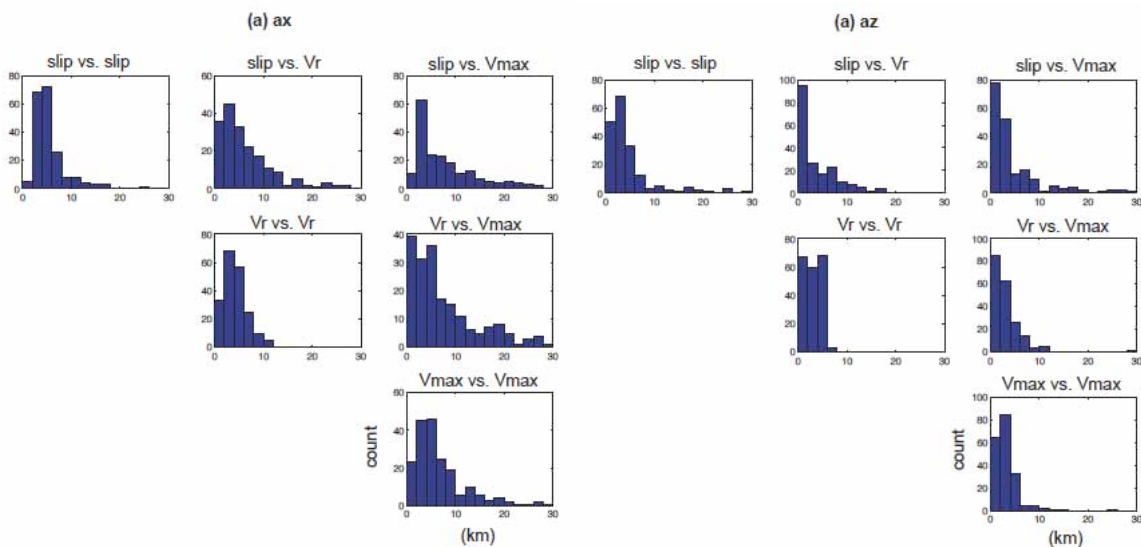


Figure 25. The distribution of correlation length estimates both in the along-strike (ax) and along-dip (az) directions. The diagonal and off-diagonal blocks represent correlation length estimates from auto- and cross-correlations, respectively. The histograms generally follow the exponential distribution.

2. Ground Motion Simulations

2.1 On the magnitude and distance dependency of ground motion variability (ISTerre team)

Empirical Ground-Motion Prediction Equations (GMPEs) are developed by means of regression techniques from recorded strong motion data, generally based on very simple parameterization with magnitude (M), distance (d) and site category (s). The distribution of ground motion for a given M, d and s is then represented in terms of a median and a standard deviation, referred to as the aleatory variability “sigma”, which is a fundamental component in Probabilistic Seismic Hazard Assessment (PSHA). It strongly controls the seismic hazard level, especially for long return periods. It is therefore imperative to accurately constrain sigma to improve seismic hazard analyses.

Ideally, sigma should represent the aleatory ground-motion variability obtained from repeated events on the same fault and recorded at the same station, and then include only the natural variability of the source rupture process on a given fault (Anderson and Brune 1999).

Nevertheless present practices in GMPEs assume that the variability in ground motion at a single site-source combination is the same as the variability in ground motion observed in a more global dataset, using records at multiple stations from different earthquakes in various tectonic contexts. This is known as the “ergodic assumption” (Anderson and Brune 1999).

This means that the total sigma estimated from GMPEs mixes the source variability and site variability while the former could be treated as predictable (e.g. epistemic) and reduced by acquiring additional data. Some recent studies have been undertaken to split sigma into various component (e.g. Al-Atik et al., 2010; Chen and Tsai, 2002). The variability can then be expressed as:

$$\sigma = \sqrt{\sigma_A^2 + \sigma_E^2} \quad (2.1)$$

where σ_A refers to the within-event variability (variability of site conditions and path effects for a given event recorded at various stations) and σ_E refers to the between-event variability (essentially due to the natural source randomness). The variability σ can further be refined by extracting the contribution of site-specific effects from the within-event variability. It is then referred to as “single station sigma” (i.e. without the ergodic assumption). A very recent work done by Rodriguez-Marek et al (2011) brings light on the issue of the variation of single station sigma, by analyzing the Japanese KiK-net database. One of the most significant conclusions is that the single station sigma depends on magnitude and distance. The authors propose a new model for the single station sigma, including distance and magnitude dependency, to be used in PSHA studies. The outcome of the study of Rodriguez-Marek et al. (2011), based on accelerometric data analysis, serves as a motivation to understand the physical phenomena affecting the ground motion variability, especially in the near field region, where the variability is poorly constrained due to the lack of available records. A possible approach is then to study the ground-motion variability from synthetic data (e.g. Ripperger et al. 2007). The contribution of different source features, such as the complexity of the final slip distribution on the fault plane, the directivity effects or the radiation pattern effects can then be carefully examined. In order to capture some physical explanation on the origin of the ground motion variability in the near-field, we evaluate single station sigma from synthetic data, as a function of distance and magnitude. Different kinematic models are considered to describe the slip history on the fault. The slip functions are next convolved with numerically computed Green’s functions for a 1D velocity structure, using a discrete wavenumber technique (Bouchon et al., 1981). The single station sigma values are finally compared to the study of Rodriguez-Marek et al (2011).

Synthetic ground motion computation

We perform synthetic velocity time series (up to 3 Hz) for a simple station layout on a 1D velocity structure, using a kinematic description of the source. We assume strike slip events on a vertical fault plane. A suite of source models for $M_w=6.7$ was generated using the database of finite-source rupture models (<http://www.seismo.tehz.ch/static/srcmod>) and k^{-2} kinematic source model (Causse et al. 2009) in order to account for different slip roughness. $M_w=5$ source models were also generated by using k^{-2} source model and also simple source points, so as to compare the effects of extended and punctual sources on the ground-motion variability. We end up with a suite of 8 source models.

Following Ripperger et al. (2008), a network of 50 hypothetical stations at various azimuths and distances have been built, based on the Joyner-Boore distance (r_{jb}) definition, which is the closest distance to the surface projection of the fault. The receiver configuration was set up for the r_{jb} distances 1, 3, 10, 30 and 60 km. The receivers have been positioned along the lines parallel to the fault at the specified distances as well as beyond the ends of the fault extending radially outward with azimuths of 0° , 30° and 60° . The medium of propagation chosen is considered to be a 1D layered velocity structure. Green's functions are computed using the discrete wavenumber simulation code AXITRA (Coutant, 1989).

Synthetic ground-motions are computed by convolving the Green's functions with the slip history of all the sub-faults. The assumed source velocity function is a smooth ramp (Cotton and Campillo 1995). Synthetics are next low-pass filtered using a second order Butterworth filter with a cutoff frequency of 3 Hz.

Finally 3-components velocities time series are obtained at each receiver location for the respective fault models. We adopt the GMRotD50 as a measure for PGV (Boore et al. 2006), which is an orientation-independent geometric mean, using period-dependent rotation angles and is

determined as the 50th percentile of the value which correspond to the median value of the PGV.

The two orthogonal components of the synthetic time series have been rotated from 0° to 90° in 1° steps and the geometric mean for each pair of rotated time series are next stored.

Finally the median value of all the 91 values of the geometric means is taken as the PGV value for the model at a particular station.

PVG attenuation with distance

Figure 26 shows mean (and standard deviation error bar) of ground motion in terms of natural log of PGV averaged over the different azimuths and along the r_{jb} distances from the faults.

At close distance from the fault, the profile of PGV shows an initial gradual increase in amplitude and then rapidly decreases with increasing distance to the fault.

Furthermore, the deeper the hypocentre the farther the maxima of PGV in the near field. This can be simply explained by the contribution of radiation pattern effect and ground motion attenuation with distance (the area located right at the top of the vertical fault corresponds to a node of the S-wave).

Finally it can also be noted that PGV values are higher for the simulated $M_w 6.7$ Fukuoka events using k^{-2} source models. This is due to the use of a shorter rise time (1 s) compared to the inverted model (~ 3 s).

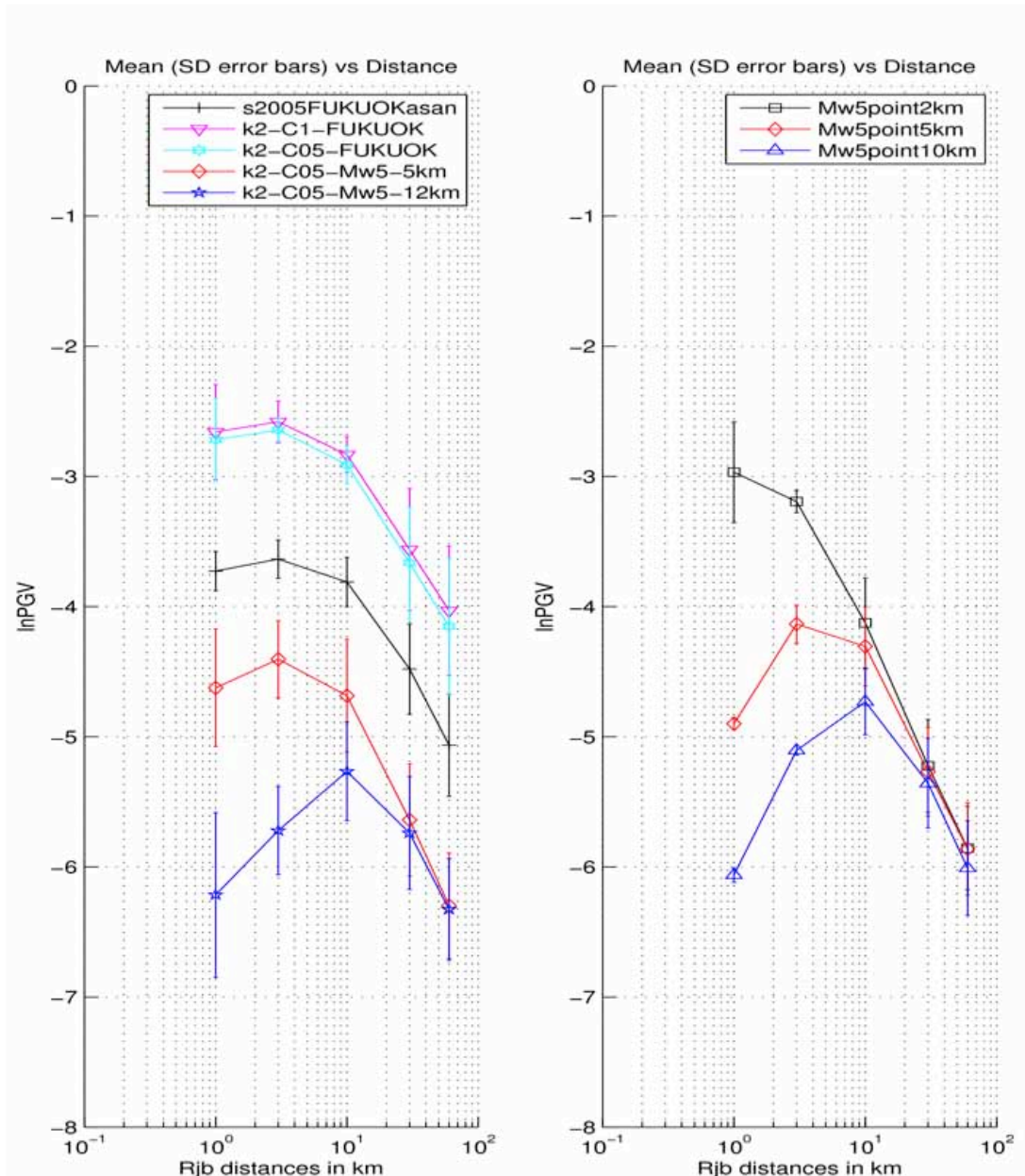


Figure 26. PGV attenuation with distance for the 8 compiled source models.

PGV variability

Figure 27 shows the standard deviation of the ground motion (between-event component of the PGV variability) for the different source models. The first striking observation is that the variability is highly dependent on magnitude and distance.

More precisely it seems that: (1) the variability decreases with distance

for smaller magnitudes; (2) the variability decreases with magnitude at short distances. In far-field conditions (distance larger than the rupture length), the variability has only slight dependence on magnitude.

A simple explanation will be that in the far field extended sources behave like point sources, and accordingly, the variability is dominated by the radiation pattern variability. We observe also only slight dependency with focal depth, simply because the sensitivity of the radiation pattern is lower in far-field.

The variability is significantly lower for $M_w = 6.7$, which seems to indicate that smaller event have higher intra event variability at short distances. Note that point sources have significantly lower variability, indicating that the variability is dominated by the source complexity. The rough k^{-2} model (k2-C1-Fukuoka) results in larger variability than that of the other two models but the difference is small.

This is probably because at this distance range of the station network is not dense enough to catch the small scale variability of the slip distribution on the fault plane. For extended sources ($M_w = 5$ and $M_w = 6.7$) the variability is observed to be smaller between 3 and 10 km. Indeed, in this distance range the impact of the source complexity vanishes and the distance is too small for the variability to be dominated by the radiation pattern effects.

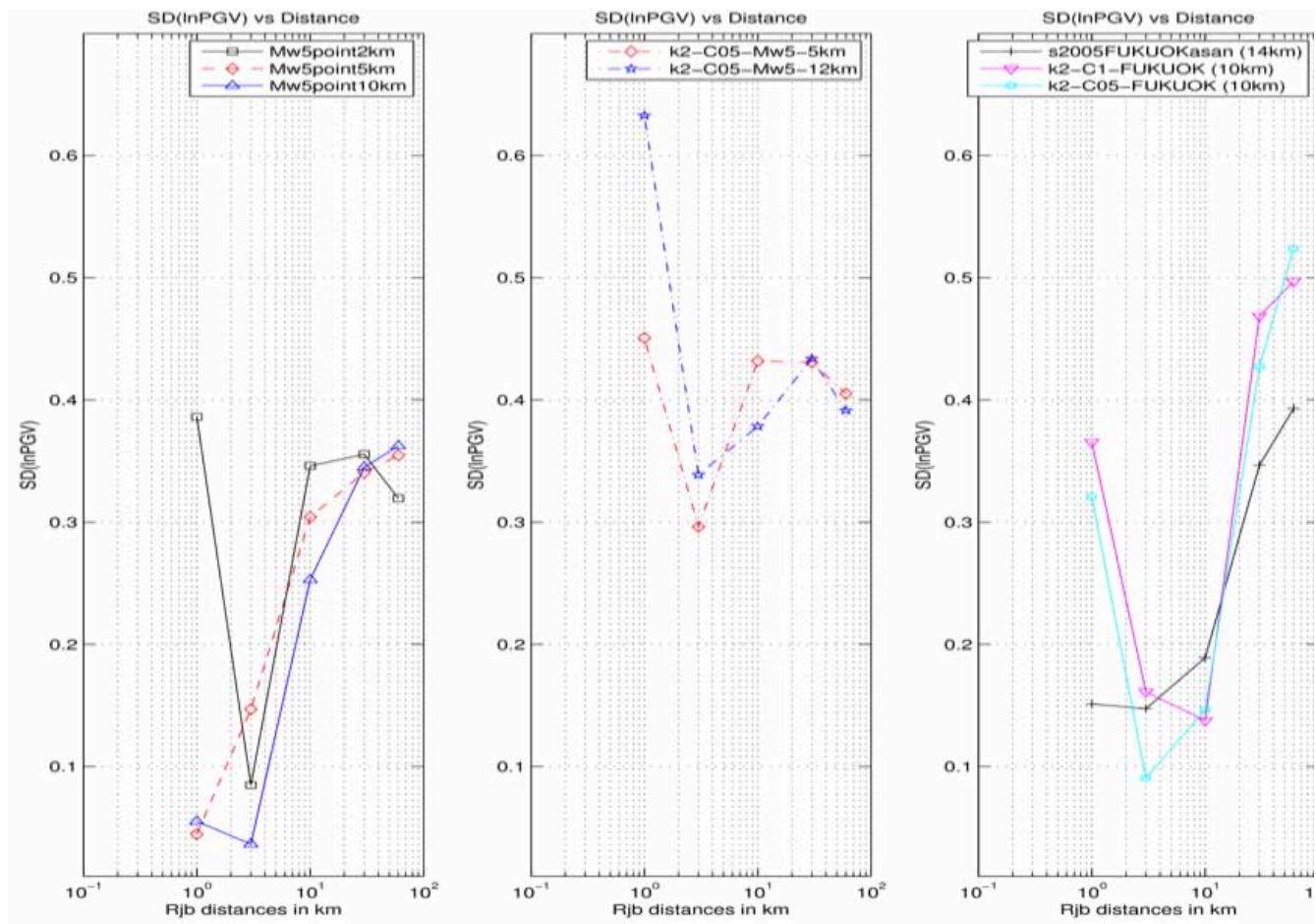


Figure 27. PGV variability vs. distance for the 8 source models generated in this study. Left and middle: Mw=5 and various focal depths. Right: Mw=6.7.

Perspectives

We have analysed the magnitude, and distance dependency of sigma, through numerical ground-motion simulations. Our results suggest that the PGV variability: (1) decreases with distance for small magnitudes and (2) decreases with magnitude at short distances from the source. This tendency is also observed in a recent independent study from real data analysis (Rodriguez-Marek et al., 2011). Nevertheless this study needs to be expanded to confirm these tendencies by conducting sensitivity studies to check the influence of the station layout on the variability values, and to expand it to a larger set of “realistic” kinematic models, all extracted from the database of finite-source rupture models. This will allow the analysis of both the within-event and the between event components of the variability.

2.2 Constraining the variability of source parameters for physics-based ground-motion predictions (ISTerre team)

The prediction of ground-motion due to a future hypothetical earthquake is a fundamental stage in seismic hazard and risk mitigation. A key issue for performing physics-based ground-motion predictions (*i.e.* including the basics principle of the earthquake source physics) is the a priori choice of the parameters describing the source process, such as the stress drop, the rupture velocity, etc ... Such parameters remains poorly constrained, though they strongly affect ground-motion. There is thus a real need to better characterize the distributions of source parameters. Those distributions will not only control the mean level of the ground-motion, but also the variability of the predictions. Within the NERA project we have carried out two different studies. The first one takes advantage of a suite of finite-source rupture models of past earthquakes, from which we have analyzed the distribution of some parameters describing the source dynamics (stress drop and fracture energy). The proposed distributions may be useful to constrain the initial conditions in spontaneous dynamic rupture calculations for earthquake source studies, and physics-based near-source ground-motion prediction. The second study focuses on the stress drop, a key parameter that controls the high-frequency ground-motion. This study is based on the recent observations on the ground-motion variability, within the framework of ground-motion prediction equations. From the variability of peak ground acceleration, we have constrained the variability of stress drop.

Variability of dynamic source parameters inferred from kinematic models of past earthquakes

The earthquake rupture process distributes accumulated strain energy into fracture energy, radiated seismic energy and heat. In this context, the

term “fracture energy” is a mesoscopic parameter that characterizes energy dissipation phenomena involved in the rupture expansion. Quantifying the energy balance for the dynamic rupture process remains a crucial issue in earthquake seismology, as it strongly affects ground-motion estimation and seismic hazard assessment, because rupture dynamics control the radiated seismic energy. The goal of this study is to constrain average, and global dynamic source properties, and to examine their distribution and potential scaling with seismic moment. We assessed fracture energy, static and dynamic stress drops, as well as apparent stress drop from a set of past earthquakes for which finite-source rupture models are available. We carried out several tests showing that kinematic inversion models of limited resolution may still carry useful information on the scaling of dynamic source properties. We took advantage of a large earthquake rupture model database (now at <http://equake-rc.info/srcmod/>), and we analyzed a suite of 31 rupture models from 21 crustal events with various styles of faulting, with M_w ranging from 5.7 to 7.7. We proposed empirical models defining the distribution of fracture energy, static stress drop and dynamic stress drop that may be useful in advanced source modelling for ground-motion simulation, such as “pseudo-dynamic” models or spontaneous rupture simulations (Figure 28). Our results indicate that fracture energy, static and dynamic stress drop, and apparent stress drop tend to increase with magnitude. The epistemic uncertainty due to uncertainties in kinematic inversions remains small ($\phi \sim 0.1$ in \log_{10} units), showing that kinematic source models provide robust information to analyze the distribution of average dynamic source parameters.

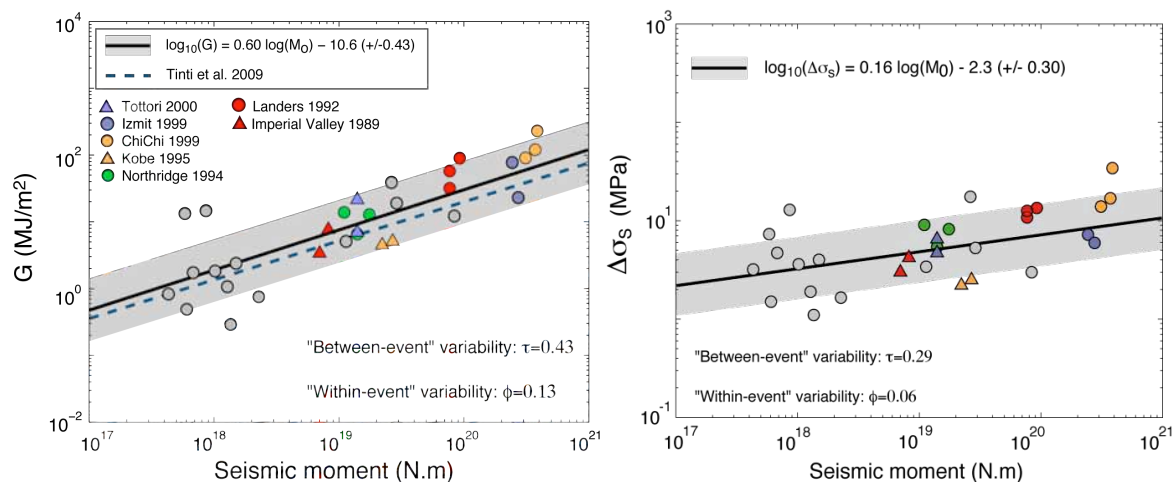


Figure28 Empirical models proposed for fracture energy and stress drop with respect to seismic moment. The circles in color indicates event for which many published source models have been used. The between-event variability refers to the aleatory variability and the within-event variability refers to the epistemic uncertainty (both expressed in log10 units).

What is the variability of stress drop?

There are many methods for simulating ground-motion. Each has particular strengths, and each can provide estimates of ground-motion. However, all the simulation methods depend, directly or indirectly, on the selected stress drop and on its distribution. Stress drop determines the position of the corner frequency and hence the level of the high-frequency ground motion. The problem is not with the average stress drop, which can vary from region to region; it is with the standard deviation (σ) of the stress drop. As we use ground-motion simulations to guide our understanding of earthquake hazard, it is imperative to know what standard deviation (σ) should be used for the stress-drop distribution. Ground-motion variability is usually divided into between-event variability and within-event variability (e.g., Al Atik et al., 2010; Rodriguez-Marek et al. 2013). The between-event variability can be interpreted as the combined ground-motion variability resulting from event-specific factors (e.g., randomness in the source process) that have not been included in the predictive model. The within-event variability, on the other hand, represents the combined ground-motion variability coming from path- and site-specific factors (e.g., randomness in the site amplification for a given

site class). Within the framework of ground-motion prediction equation (GMPE) development, source effects are, in general, accounted for only by magnitude and a term characterizing the fault mechanism in a simplified form. The between-event variations of stress-drop values are then one of the key factors of GMPE's between-event variability. Recent ground-motion predictive equations developments give the opportunity to compare and analyze the values of between-event variabilities. Using the theory of stationary Gaussian random functions and a simple source (Brune's model), we use the results of McGuire and Hanks (1980) showing that there is a proportionality relation between peak ground acceleration (PGA) and the stress drop to constrain the stress-drop variability. The stress-drop variabilities derived from those observed between-event ground-motion variabilities are around 0.5 (in natural log units), whereas those derived from source-parameter studies, that is, corner frequency analysis, are around 1.5 (Figure 29). This strong disagreement may be due to large uncertainties in the corner frequency estimations.

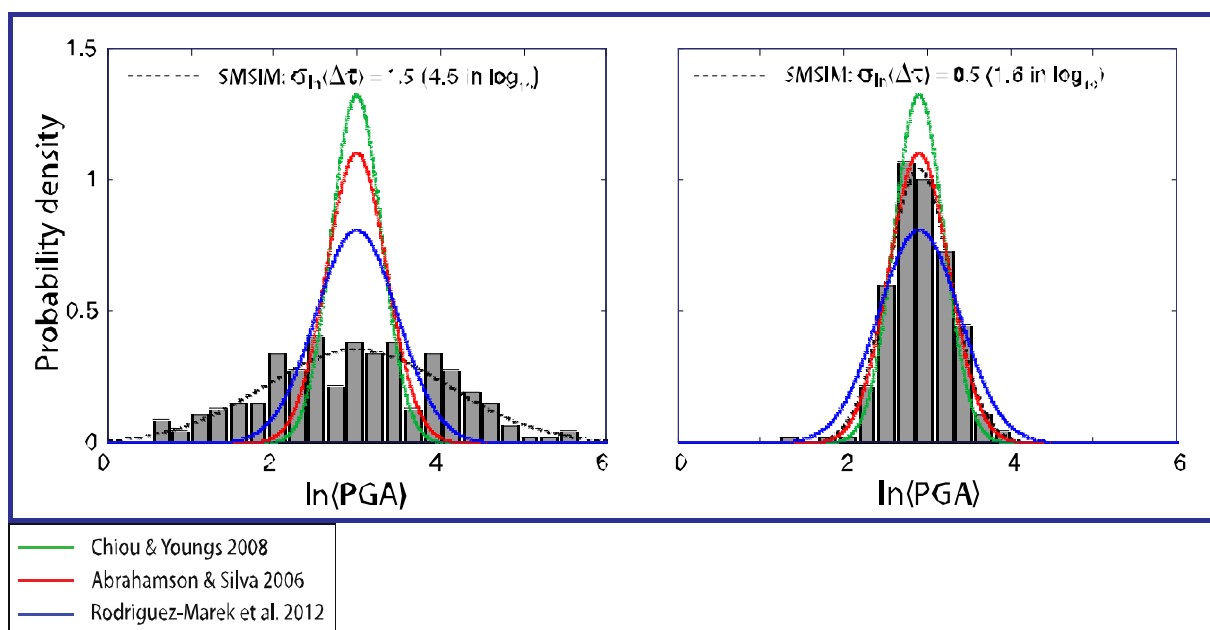


Figure 29 The result of computing PGA with two different values of variability on the natural log of stress drop. Histograms are from 200 runs of SMSIM (Boore, 2003) with a lognormal distribution of stress drop with a sigma of 1.5 (typical value from seismic results) and 0.5 (typical value inferred from GMPEs). As expected, the GMPEs produce a good fit to the histogram because the inferred sigma was deduced from the GMPEs.

2.3 Sets of Ground motion Simulations based on 360 Rupture Scenarios (ETHZ team)

We investigate earthquake source characteristics and near-source ground motion using spontaneous dynamic rupture simulations. For that purpose we have developed 360 dynamic rupture models (Dalguer and Mai, 2011, 1012) in the range of $M_w \sim 5.5-7.0$. The models are for three classes of faulting (thrust, normal and strike slip) for buried and surface-rupturing earthquakes. Stress and frictional strength consider two extreme cases of normal stress, 1) depth-dependent, and 2) depth-independent. This diversity of rupture models generates a broad range of scenarios for evaluating near-source ground motion variability and for identifying the causes of extreme ground motion. Comparing PGV and PSA of our simulation with empirical GMPE, we find an increased variability in the near-field of the rupture. The consistent saturation of these quantities predicted by GMPE is not obvious in our calculations. Rather, there are significant ground-motion reductions near the source for buried faults, but considerable increase for surface rupturing earthquakes. Extreme ground motions appear to be correlated with faulting that breaks the free surface, with largest shaking levels for strike-slip ruptures. For buried ruptures, thrust faulting earthquakes generate the strongest ground motion, normal faulting the weakest. Baumann and Dalguer (2013) verified the consistency of the synthetic ground motion with empirical GMPEs. In general, simulated ground motion are consistent with GMPE's at distance $>5\text{km}$, but not at short distance. The methodology to generate dynamic rupture models is explained in deliverable D13.3 (New simulation schemes) of this JRA3 WP. But also it can be found in published paper Dalguer and Mai (2011,2012). The database of the 360 dynamic rupture models will be available through the implementation report (Deliverable 13.5).

But it can also be download from:

<http://www.seg2.ethz.ch/dalguer/download/DynaModels360.html> or ask directly to Dr. Luis A. Dalguer (dalguer@sed.ethz.ch). Calculations were developed using the Support Operator Rupture Dynamics code (SORD). The SORD code (Ely et al., 2008, 2009) is based on a generalized Finite Difference scheme that can utilize meshes of arbitrary structure and incorporate irregular geometry, with the capability to model general fault geometry and topography. The code is freely available in the internet (<http://gely.github.io/coseis/www/index.html>).

MODEL PARAMETRIZATION OF DYNAMIC RUPTURE MODELS

The list below summarizes the modeling parameters adopted in our dynamic rupture simulations:

- strike-slip faulting: dip=90° fault length = 30km fault width=12km;
- thrust faulting: dip=45° fault length = 24km fault width=15km;
- normal faulting: dip=60° fault length = 24km fault width=15km;
- for ruptures that are not allowed to break the surface, the faults are buried at 5km depth;
- static friction coefficient = 0.6 dynamic friction coefficient = 0.56 cohesion force = 1.0×10^6 Pa;
- dynamic overshoot coefficient = 1.5 critical slip distance = 0.2;
- critical slip distance smoothly increases from 0.3 m to 5 m at fault boundaries in a 3 km-wide buffer zone that surrounds the above defined fault areas; this approach ensures that rupture propagation stops smoothly at the borders of the fault;
- loading under compression (trust/ strike slip fault), unloading under extension (normal fault) = 50×10^6 Pa. The loading is applied at 15km depth;
- strike-slip faults have the principal stress σ_2 equal to the average between σ_1 and σ_3 , and the angle θ is 45° (fault plane angle measured with the σ_3 axes) ;

- initial stress stochastic field realizations based on von Karman distribution with correlation length of 8.0 km in along-strike and along-dip direction, Hurst number $H = [0, 0.25, 0.5]$; resulting stress distribution are hence compatible to seismological observations (Mai and Beroza, 2002);
- normal stress = 120 MPa, for model with non-depth dependent stress;
- layered 1D velocity-density structure, derived as the average model of available models in Switzerland (Figure 30);
- numerical setup uses 8 grid element per wavelength; a conservative estimate yields that we accurately resolve a maximum frequency of ~ 3 Hz, given the chosen velocity structure and grid size of 100 m; domain-size 100 km x 100 km x 30 km;
- simulations were carried out on "Rosa", a Cray XT5 at the Swiss National Supercomputing Center (CSCS), on 4096 CPUs.

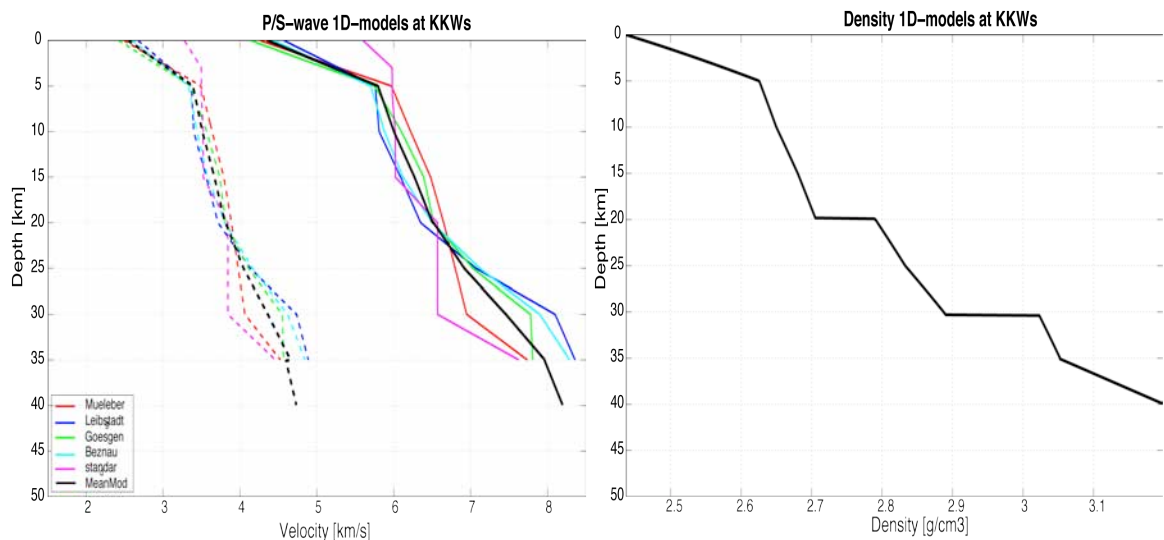


Figure 30. 1D velocity structure model (left) and density (right) used for dynamic rupture simulations.

NUMERICAL RESULTS

Dynamic Rupture Solutions. From the total of 360 models, that include buried and surface rupture with normal stress depth and non depth

dependent models for three classes of faulting (strike, reverse and normal-slip), a diversity of rupture scenarios has been simulated in a range of M_w 5.5 – 7.0. Figure 31 shows representative models for strike-slip faults. The rupture propagation, slip, peak slip velocity and stress drop distribution evolve in a diverse manner. For each case of rupture (buried and surface-rupturing) models with non-depth dependent stress parameterization results in solutions with larger stress drop, but earthquake size is larger for depth dependent stress models. Surface rupturing model with depth dependent stress predicts the largest size earthquake, but the non-dependent stress model results in the largest peak slip rate values.

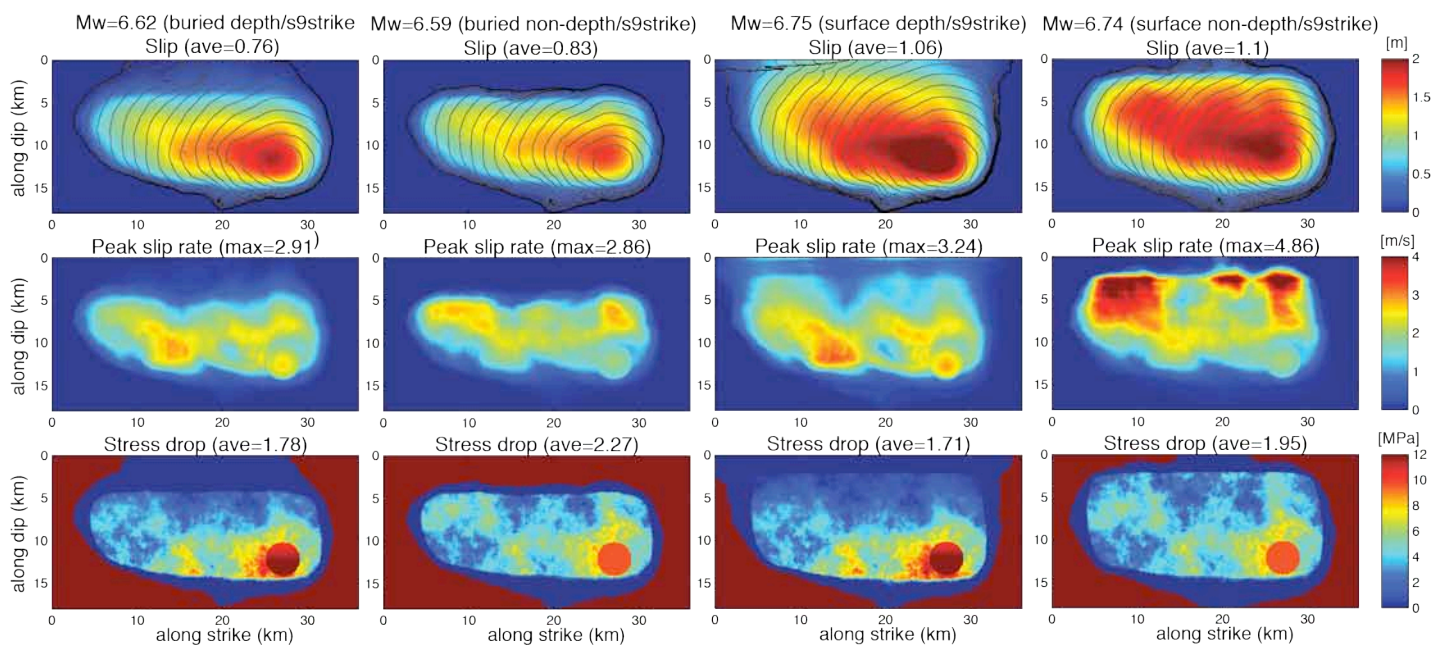


Figure 31. Dynamic rupture solutions for a strike-slip rupture with the identical stochastic stress parameterization, for depth and non-depth dependent stress and for buried and surface-rupturing models. Top panels show slip distribution, contour line is the rupture time each 0.5 sec. Middle panels show peak-slip distribution, and bottom is stress drop distribution.

Ground Motion Solutions. We compare the resulting ground motions of all 360 models to common ground-motion prediction equations (GMPE) and observations, focusing on the maximum ground motion generated by these models. Site-amplification corrections using the period-dependent

amplification coefficient of Borchardt (1994, 2002) are applied to scale computed ground motions to $V_{s30}=1500\text{m/s}$ from the minimum shear-wave velocity in our simulations ($V_{s30}=2500\text{m/s}$). This correction is needed to facilitate the comparison with the GMPE's that are based on V_{s30} -values less than 1500 m/s. Synthetic ground motions are filtered using a band pass Butterworth filter from 0.01 to 3.0 Hz. Figure 32 displays PGV and PGA (for waveforms up to $f_{\text{max}} = 3$ Hz) for all models. We find that surface rupturing models predict stronger ground motion than buried rupture, with the strongest corresponding to non-depth dependent stress models, acceleration exceeding in some case gravity. Strike slip models predict the strongest ground motion, followed by reverse-slip rupture models. Maximum ground motion levels is constant up to $M_w \sim 6.3$ for strike slip fault, and up to $M_w \sim 6.7$ for reverse and normal faults. Differences in ground-motions between buried ruptures with depth and non-depth dependent stress are indistinguishable.

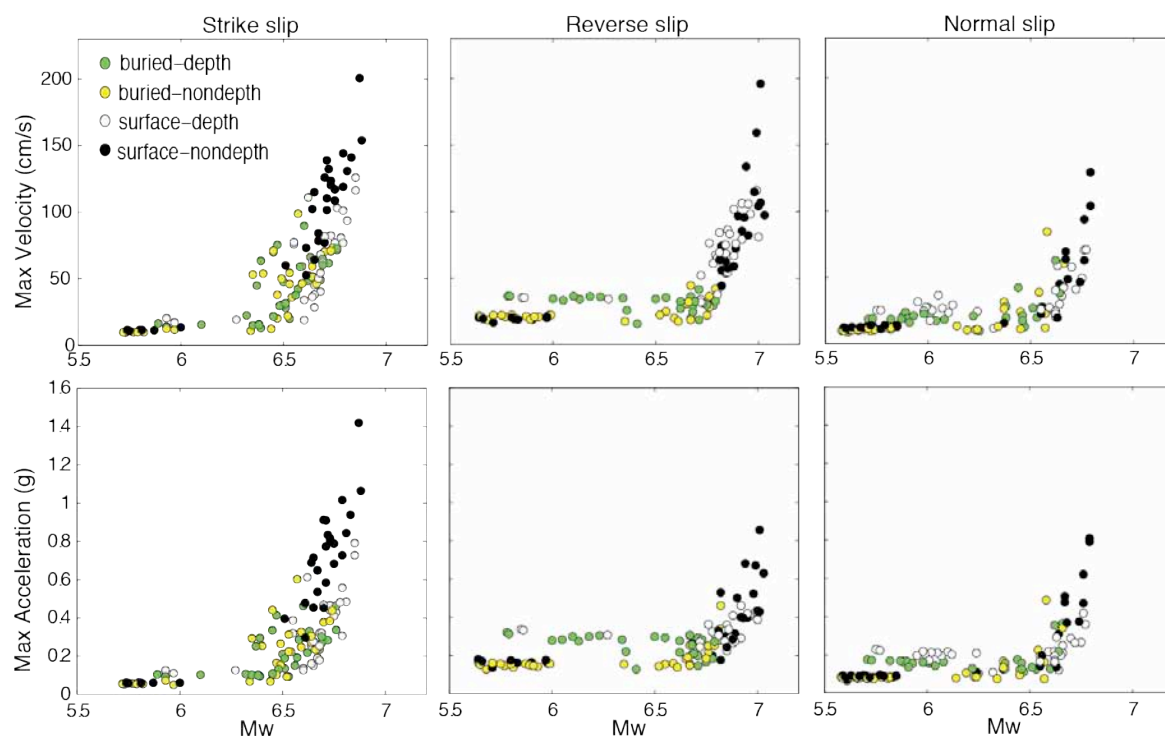


Figure 32. Maximum horizontal ground motion of velocity (top) and acceleration (bottom) for strike, reverse and normal faults of buried and surface rupturing with depth and non-depth dependent stress for a total of 360 models.

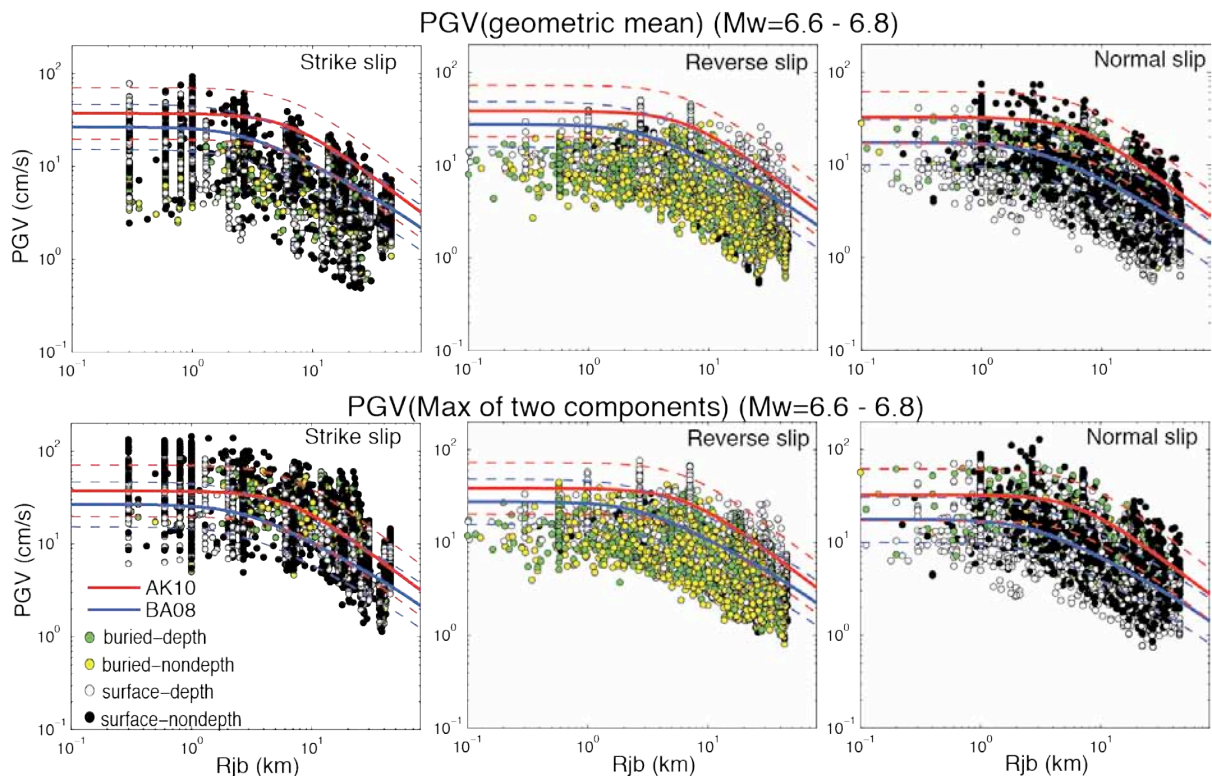


Figure 33. Horizontal PGV comparisons with GMPE from AK10 (Akkar and Bommer, 2010) and BA08 (Boore and Atkinson, 2008) and for strike, reverse and normal faults of buried and surface rupturing with depth and non-depth dependent stress, for models in the magnitude range M_w 6.6 – 6.8. Top shows comparison using the classic geometric and bottom correspond to the maximum of the two horizontal components.

Figure 33 compares PGV with GMPE from Akkar and Bommer (2010) hereafter AK10 and Boore and Atkinson (2008) here after BA08, for a range of magnitude of M_w 6.6 – 6.8. We use Joyner-Boore distance (R_{jb}). The PGV estimates from our simulations are calculated assuming two criteria, the geometric mean of the two maximum horizontal components (top of Figure 33) and the maximum value of the two maximum horizontal components (bottom of Figure 33). In general PGV is consistent with GMPE, with better fitting at distance R_{jb} larger than about 3-7 km than at very close distances to the fault. Estimates using the maximum criterion provide better comparison than the geometric mean criterion. We find an increased variability in the near-field of the rupture. The consistent saturation of these quantities as predicted by GMPE is not obvious in our calculations. Rather, there are significant ground-motion reductions near the source for buried faults and for dip-slip ruptures, but considerable

increase for strike slip surface rupturing earthquakes. Similar pattern is observed for simulate PSA up to 1.0Hz (not shown here). Extreme ground motion appears to be correlated with faulting that breaks the free-surface with the strongest for strike-slip rupture, predicting acceleration ground motion exceeding the gravity. Figure 34a shows a representative of PSA exceeding the gravity predicted by surface rupturing of strike, reverse and normal-faulting models with non-depth dependent normal stress. As seen in this figure, gravity is exceeded at frequencies in the range of 1.0 – 2.5 Hz ($T = 0.4 - 1.0$ s). For reference, Figure 34b displays PSA at several stations exceeding gravity during the 2011 M_w 6.3 Christchurch, New Zealand earthquake, in which extreme ground motion were observed in the same frequency range.

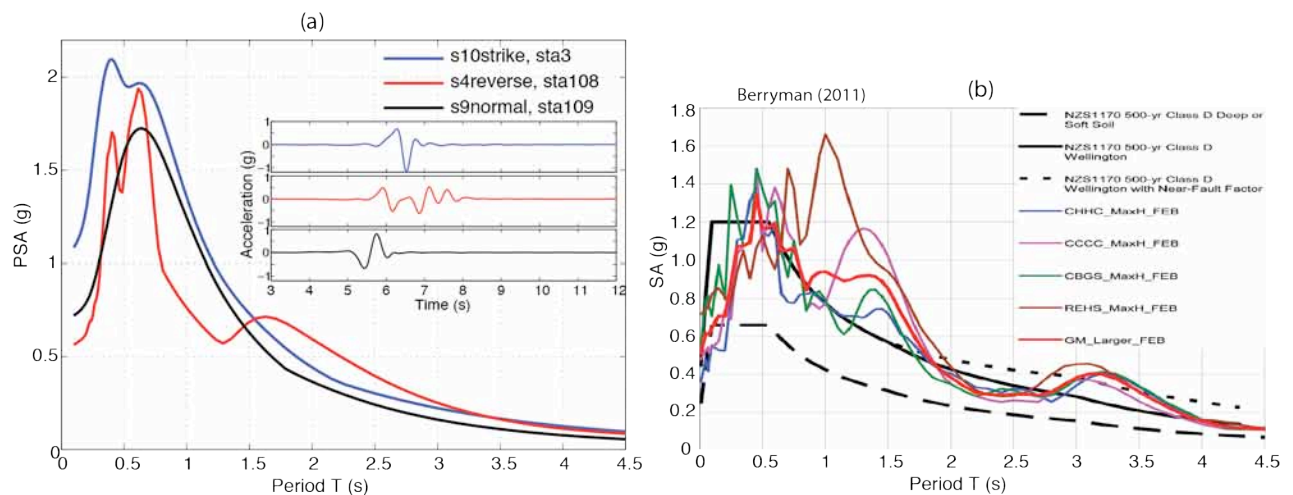


Figure 34. Left (a) PSA at selected station very near the source for strike, reverse and normal faulting with surface rupturing and non-depth dependent stress; the inset figure displays the corresponding acceleration time histories. Right (b), Spectral Acceleration at several stations exceeding gravity during the 2011 M_w 6.3 Christchurch, New Zealand earthquake (After Berryman, 2011). Solid and dashed black line are design spectral motions.

CONCLUSIONS

We have developed a suite of rupture dynamic simulation to evaluate ground-motion variability generated by those events, with a particular focus on extreme ground motion acceleration exceeding 1g in earthquake in the range of $M_w \sim 5.5 - 7.0$. A total of 360 source models for strike, reverse and normal faulting with buried and surface rupturing features as well as depth and non-depth dependent stress parameterization have been generated and their resulting near-field ground-motions have been examined. This diversity of rupture models creates a broad range of scenarios for evaluating near-source ground motion variability and for identifying the causes for extreme ground motion. Surface rupturing events predict the stronger ground motion than buried rupture, with the strongest for surface rupturing models with non-depth dependent stress. In general, simulated ground motion are consistent with GMPE's at distance greater than 5km, but not at short distance. The consistent saturation, very close to the source, of ground motion quantities as predicted by GMPE is not obvious in our calculations, rather, there are significant ground-motion reductions near the source, particularly for buried faults, and considerable variability for surface rupturing earthquakes. There is an increased variability in the near-field considering all the rupture models. Extreme ground motion appear to be correlated with faulting that breaks the free-surface with the strongest for strike-slip rupture. We found ground motion at some stations very near to the source that exceed the gravity acceleration at frequencies range 1.0 to 2.5Hz, those extreme ground motions resemble the ground motion recorded during the 2011 M_w 6.3 Christchurch, New Zealand earthquake that occurs at such as frequency range.

2.4 Statistical Analysis: The effect of 1-point and 2-point source statistics on ground motions (ETHZ team)

The effect of dynamic source parameters on ground motions

In this study, we investigate the effect of dynamic source parameters on near-source ground motions characteristics in the framework of 1-point and 2-point statistics. Figure 35 shows three different input stress drop distributions in dynamic rupture modeling. They all follow the same spectral decay rate (k^{-1} , 2-point autocorrelation), but have three different standard deviation values (1-point statistics). We perform spontaneous dynamic rupture modeling with them under the slip weakening friction law, and found that the standard deviation of the input stress drop strongly affects near-source ground motions as shown in Figure 36. Although the input stress drop has the same mean values and same spectral decay rate, we observe significant changes in the near-source ground motion intensity (peak ground velocity), depending on the standard deviation. The larger standard deviation produces stronger ground motions in particular in the forward rupture directivity region. This study strongly implies that we need to more explicitly consider 1-point statistics of input source parameters in dynamic rupture modeling in physics-based ground motion simulation.

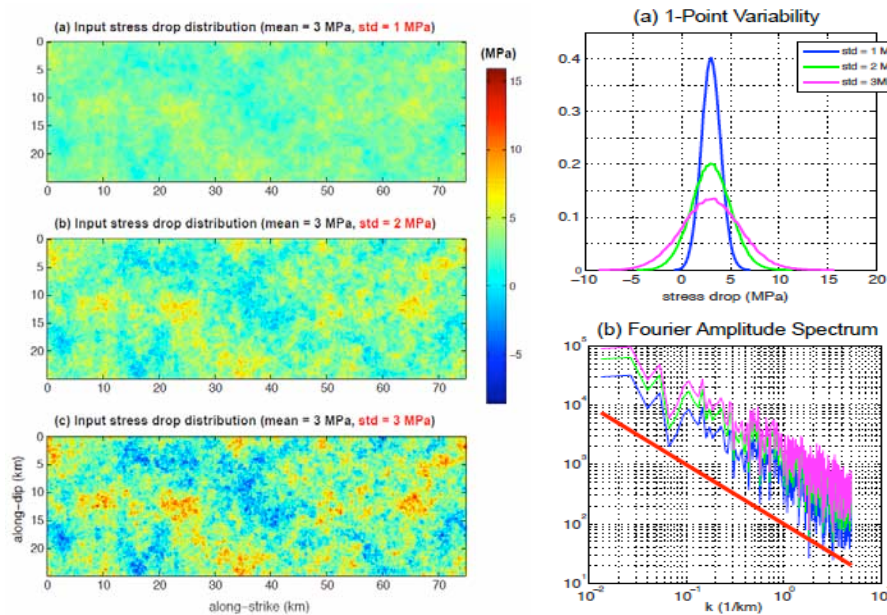


Figure 35. [left] Input stress drop distribution with the same Gaussian 1-point statistics, but different standard deviations, i.e., (a) 1 MPa, (b) 2 MPa, (c) 3 MPa. All three distributions have the same mean stress drop (= 3 MPa) and follow the same spectral decay rate (k^{-1}). [right] 1-point probability density function (a) and Fourier amplitude spectrum (b) of three input stress drop distributions on the left. Note that they all have the same spectral decay rate (k^{-1}) although the standard deviation varies from 1 MPa to 3 MPa. The red solid line in (b) shows a reference spectral decay rate (k^{-1}) (Song & Dalguer, 2013).

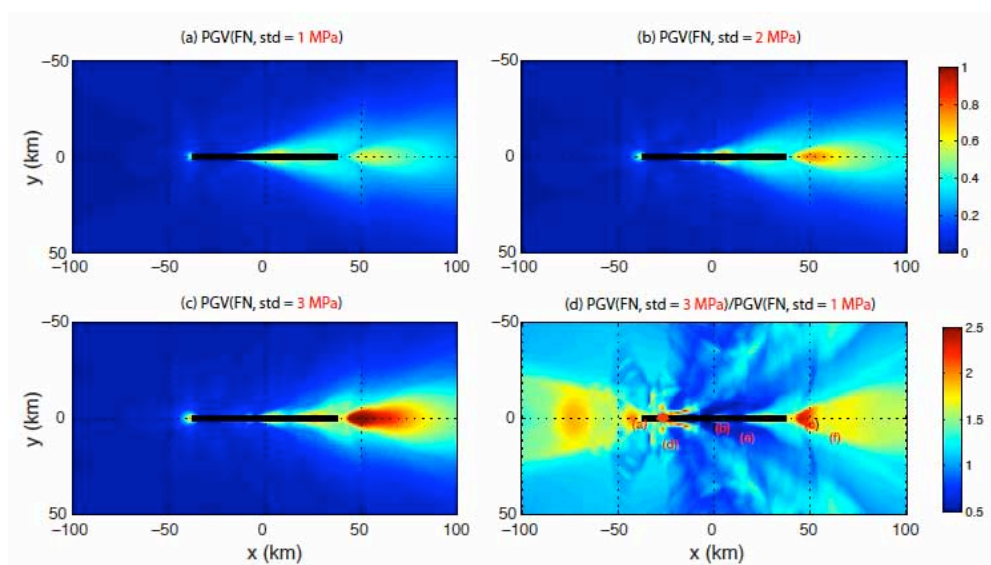


Figure 36. The distribution of peak ground velocity (PGV, fault normal component) with three different standard deviation values of input stress drop, (a) 1 MPa, (b) 2 MPa, and (c) 3 MPa. The bottom right (d) panel shows the ratio of PGV(std = 3MPa) to PGV (std = 1 MPa). PGV values increase significantly with standard deviation, especially in the forward and backward rupture directivity region. The solid black line and red star indicates the surface projection of the faulting plane and nucleation point, respectively (Song & Dalguer 2013).

The effect of kinematic source parameters on ground motions

The effect of 1-point statistics

In this study, we investigate the effect of kinematic source parameters on near-source ground motion characteristics in the framework of 1-point and 2-point statistics. We first develop a new pseudo-dynamic rupture model generator using 1-point and 2-point statistics of key kinematic source parameters such as slip, rupture velocity, and peak slip velocity (Song & Somerville 2010; Song et al. 2013), and test how each component in kinematic source statistics affects near-source ground motions. Figures 37 and 38 show how the perturbation in 1-point statistics affects ground motions. The depth-dependent standard deviations of both rupture velocity and peak slip velocity are perturbed as shown in Figure 37. In other words, the standard deviations are stretched out by a factor of 2, or compressed by a factor of 2, keeping the same depth-dependent mean profile. We observe that the larger standard deviations produce much strong near-source ground motions. Given the fact that the standard deviation of kinematic source parameters are not explicitly considered in most finite source modeling studies, this study clear shows the importance of 1-point statistics in finite source characterization for simulating ground motions.

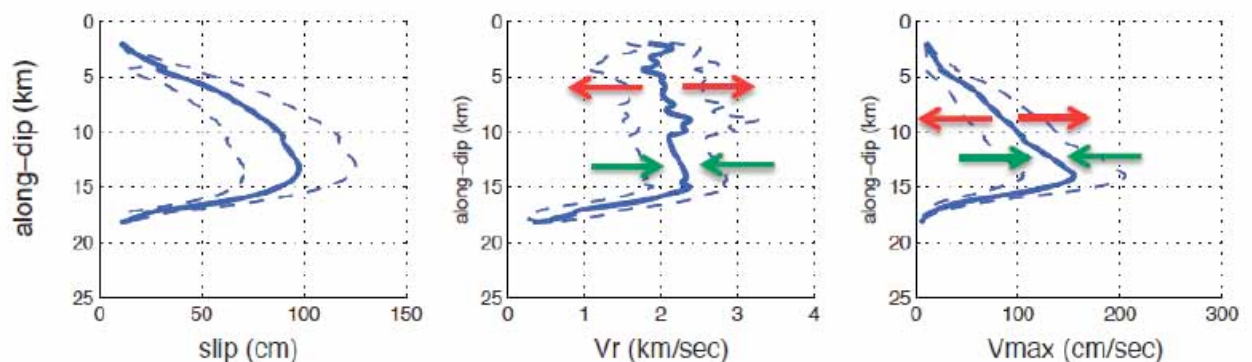


Figure 37. Depth-dependency of 1-point statistics. The solid and dashed blue lines denote mean and 1-sigma range at the given depth, respectively. The arrows indicate the perturbation of 1-point statistics in ground motion modeling. The red arrows indicate that the 1-sigma range (dashed-lines) are stretched by a factor of 2 with respect to the solid blue line. The dark green lines indicate that it is compressed by half (Song et al. 2013).

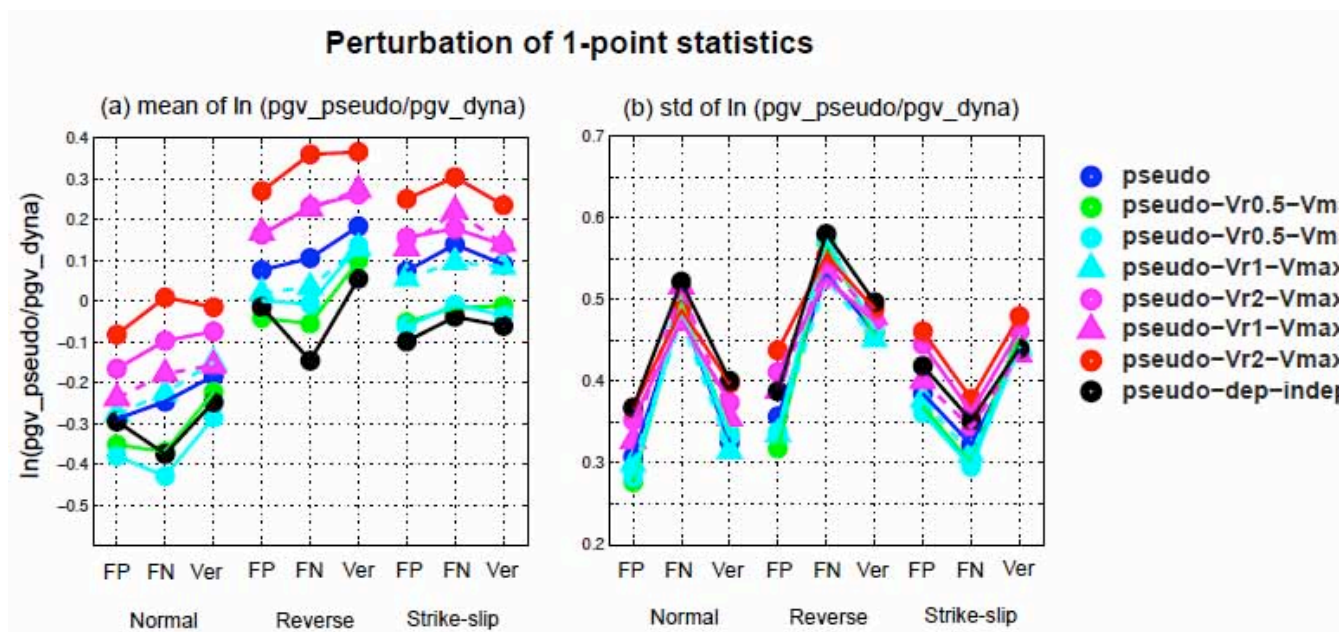


Figure 38. Comparison of pseudo-dynamically generated ground motions against dynamically generated ground motions after perturbing a certain element of 1-point statistics in pseudo-dynamic source models. (a) Mean of $\ln(\text{pgv_pseudo}/\text{pgv_dyna})$ for 168 stations, (b) Standard deviation of $\ln(\text{pgv_pseudo}/\text{pgv_dyna})$ for 168 stations. Mean and standard deviation are also averaged for 30 randomly simulated events by stochastic modeling (Song et al. 2013).

The effect of 2-point statistics

In the new pseudo-dynamic source modeling, we can perturb a certain element of 2-point statistics and directly investigate its effect on near-source ground motions. Figure 39 shows one example of the perturbation of 2-point statistics. In Figure 39(a), all components of both auto- and cross-correlation structures between kinematic source parameters are included in the covariance matrix while all cross-correlation structures (off-diagonal components) are removed in Figure 39(b). Figure 40 shows that correlations between source parameters produce stronger ground motions in general. In particular, correlation between slip and rupture velocity plays a dominant role in determining near-source ground motion intensities. In addition, if we consider appropriate correlations in finite source modeling, simulated ground motions contain less randomness. This study clearly demonstrates the efficiency of pseudo-dynamic source

modeling in the framework of 1-point and 2-point statistics. We observe that both 1-point and 2-point statistics of kinematic source parameters significantly affect near-source ground motions. We also emphasize that we need to consider both 1-point and 2-point statistics more explicitly in finite source modeling for simulating ground motions.

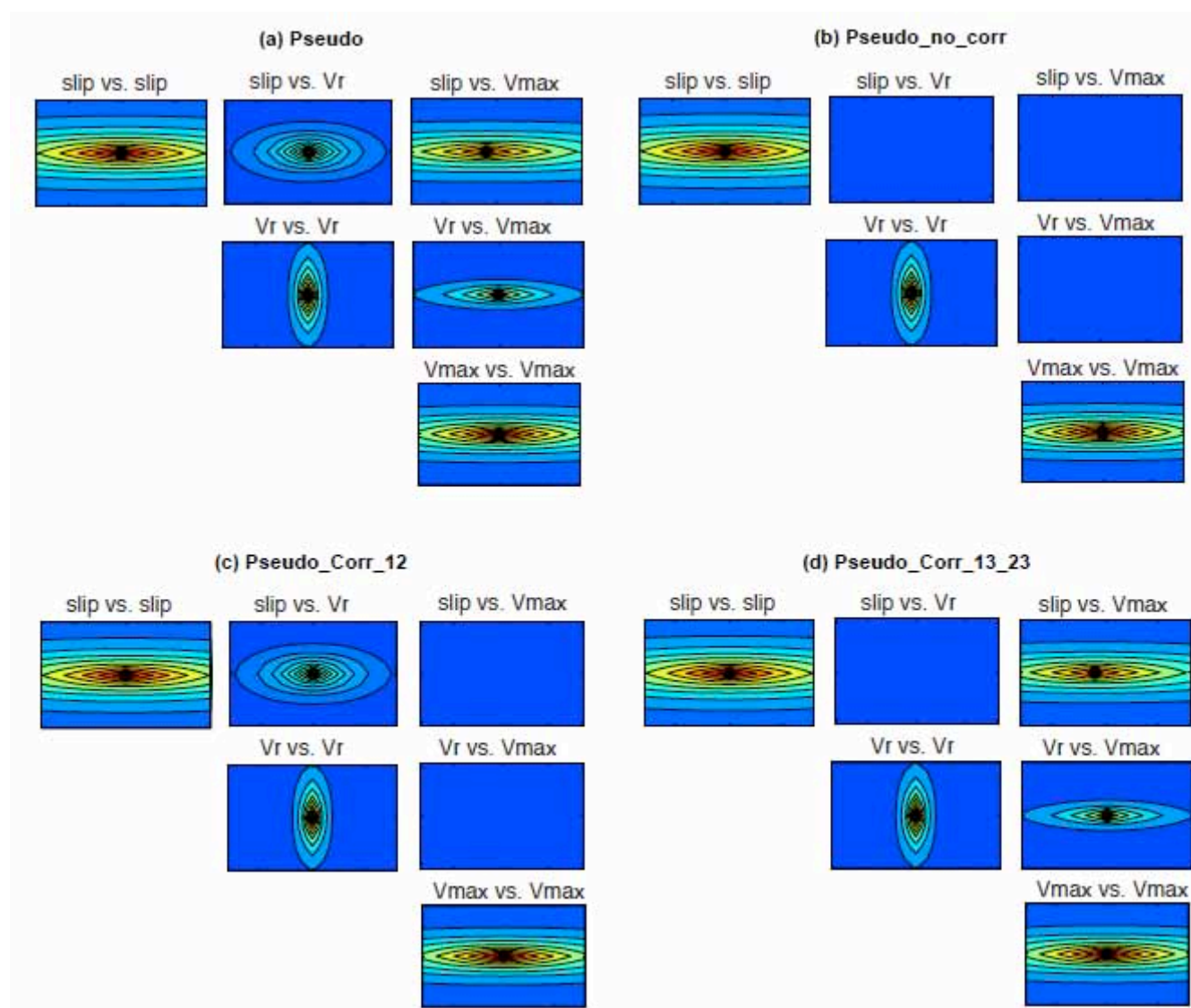


Figure 39. Perturbation of 2-point statistics. 3 off-diagonal blocks are perturbed sequentially (Song et al. 2013)

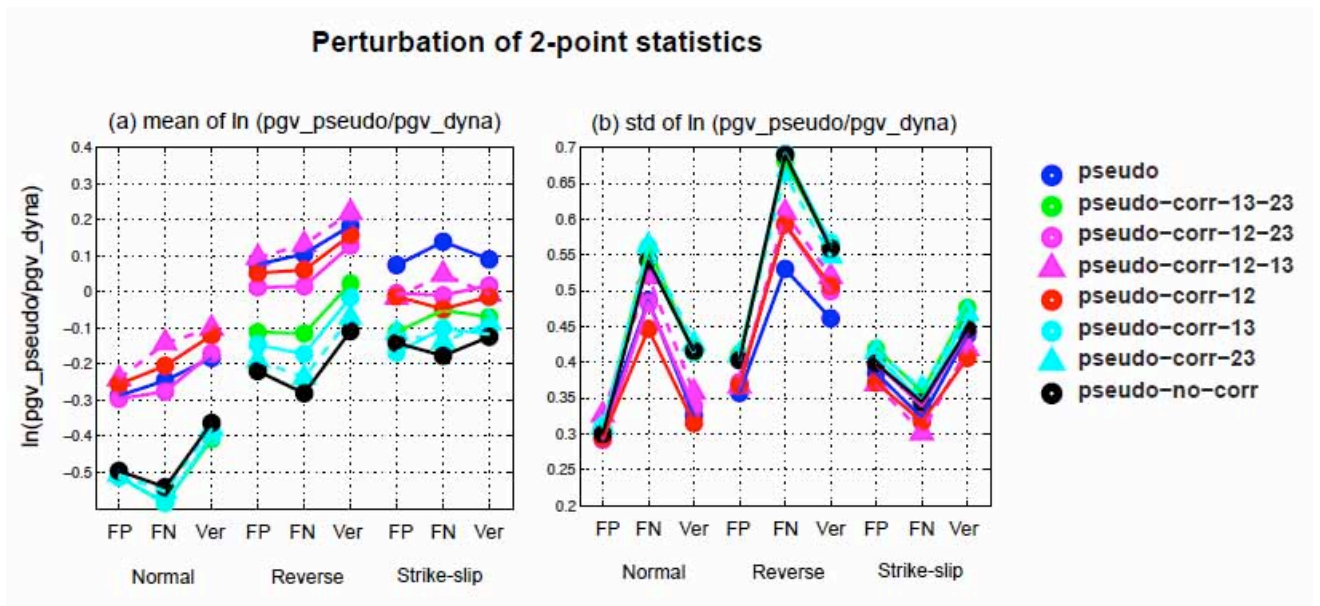


Figure 40. Comparison of pseudo-dynamically generated ground motions against dynamically generated ground motions after perturbing a certain element of 2-point statistics in pseudo-dynamic source models. (a) Mean of $\ln(\text{pgv_pseudo}/\text{pgv_dyna})$ for 168 stations, (b) Standard deviation of $\ln(\text{pgv_pseudo}/\text{pgv_dyna})$ for 168 stations. Mean and standard deviation are also averaged for 30 events (Song et al. 2013).

2.5 Case Studies

2.5.1 Broadband simulations of 2009 L'Aquila earthquake (AMRA team)

In near fault conditions unexpected large ground motion amplitudes associated with a rapid space gradient can be observed, due to the coupling of source effects (focal mechanism, directivity, up-dip propagation) and local scale wave reverberations related to topography, basins and/or regional scale structures. Moreover, high frequency peak acceleration is often observed on the vertical component of the seismic data in the presence of normal or reverse fault mechanisms. This was the case of the April 6, 2009, M_w 6.1, L'Aquila earthquake, where the complex ground motion pattern has produced the variability of the damage at the urban scale of L'Aquila city. Up to now, near fault effects on the ground motion are relatively poorly understood because of the limited amount of records in the fault vicinity. We aimed with this study to contribute to the investigation of the role of the source and the wave propagation at regional scale in the generation of the ground motion and its variability in the case test of the L'Aquila earthquake, for which we have, for the first time in Italy, a huge amount of records for both the mainshock and the aftershocks. These latter can be used as empirical Green's functions, improving the description of the elastic propagation at regional scale. For the aim we provided broadband simulations for the L'Aquila earthquake to be compared with real records. We fixed the rupture geometry, the focal mechanism, the hypocentral position and station distribution and we generated a large amount of strong motion records for several scenarios, obtained by changing the slip roughness, the rise time and the rupture velocity on the fault plane. We used coupled numerical-empirical Green's functions as a propagator. High-frequencies beyond the corner frequency of the Empirical Green's functions (EGFs) are stochastically introduced into the model. To be consistent with the low frequency part of the signal, we

used a kinematic source model of the L'Aquila earthquake. This was obtained by the inversion of local strong motion data up to 0.3 Hz. This kinematic model, however, poorly describes the waveform amplitude and shape even at low frequencies for the L'Aquila stations, where larger amplitudes seem to indicate a strong unravelled coupling of source effects with wave propagation and site. With the specific goal of better representing the strong motion data recorded at L'Aquila stations in a broader frequency range, we also used an inversion scheme, with a separated parametrization for the slip and the rupture velocity (Lucca et al., 2012) which is mainly aimed at fitting L'Aquila data at low-frequencies (up to 0.5 Hz) by the use of EGFs. The retrieved model is represented in Figure 41. We found a major slip patch between 5 and 10 km southwards of the hypocenter, which is responsible for the directivity effect observed south of the fault. We also found a smaller asperity in the upper part of the fault with slip as large as 50 cm and a third one nearby the surface, lower slip value (30 cm), which is responsible of the up-dip directivity observed at L'Aquila and GSA stations. Rupture times indicate a faster rupture in the upper part of the fault, in the initial stage of the rupture. The features of this model are consistent with the one provided by the other group (INGV) within this project (see Section 1.1), but exact location of asperities and rupture velocity values do not completely match, indicating a strong influence of slip parametrization and velocity structure on the final model. We then coupled this model with high frequency k^{-2} slip distributions obtained with a stochastic technique (Causse et al., 2009). Retrieved models were tested up to high frequencies (5-10 Hz) to provide the ground motion amplitude and its variability.

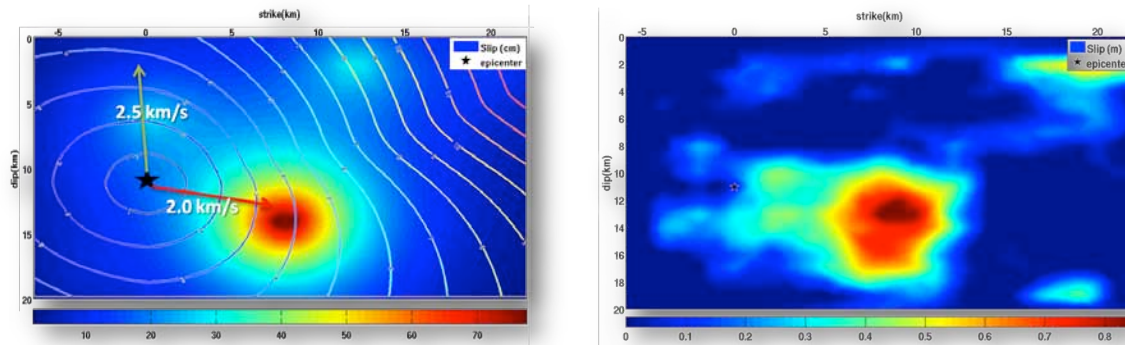


Figure 41: Retrieved slip model for the L'Aquila earthquake on the left. An example of a derived high-frequency model on the right panel, obtained by coupling the low frequency model with a k -2 slip distribution at short wavelengths.

For the broad band ground motion simulations, we needed to couple the source model with a reliable Green function up to high-frequency, in a complex medium like L'Aquila region. We then used Empirical Green's functions as high frequency propagators of the waves emitted by the rupture on the fault. Starting from a dataset of more than 400 aftershocks and foreshocks recorded between March 30, 2009 and April 30, 2009 by DPC-RAN and INGV networks, with a magnitude ranging between 2.5 and 4.8, we selected about 100 events to be used as EGFs. Selection of the functions was based on location, stress drop, magnitude and signal to noise ratio. For the hypocentral position we used the accurate double difference locations of Chiaraluce et al. (2012). Magnitude and stress drop were estimated from inversion of displacement spectra based on the ω^2 Brune model. Signal to noise ratio threshold was finally fixed to 10 in the frequency range of interest (0.4-10 Hz) in order to maintain high quality seismic data in a broad frequency range. In Figure 42 we plot the magnitude versus distance distribution of the selected aftershocks and scale laws for stress drop and radiated energy. The available focal mechanisms, as deduced by Chiaraluce et al. (2012), indicated for all the aftershock a rupture pattern similar to the one of the main event.

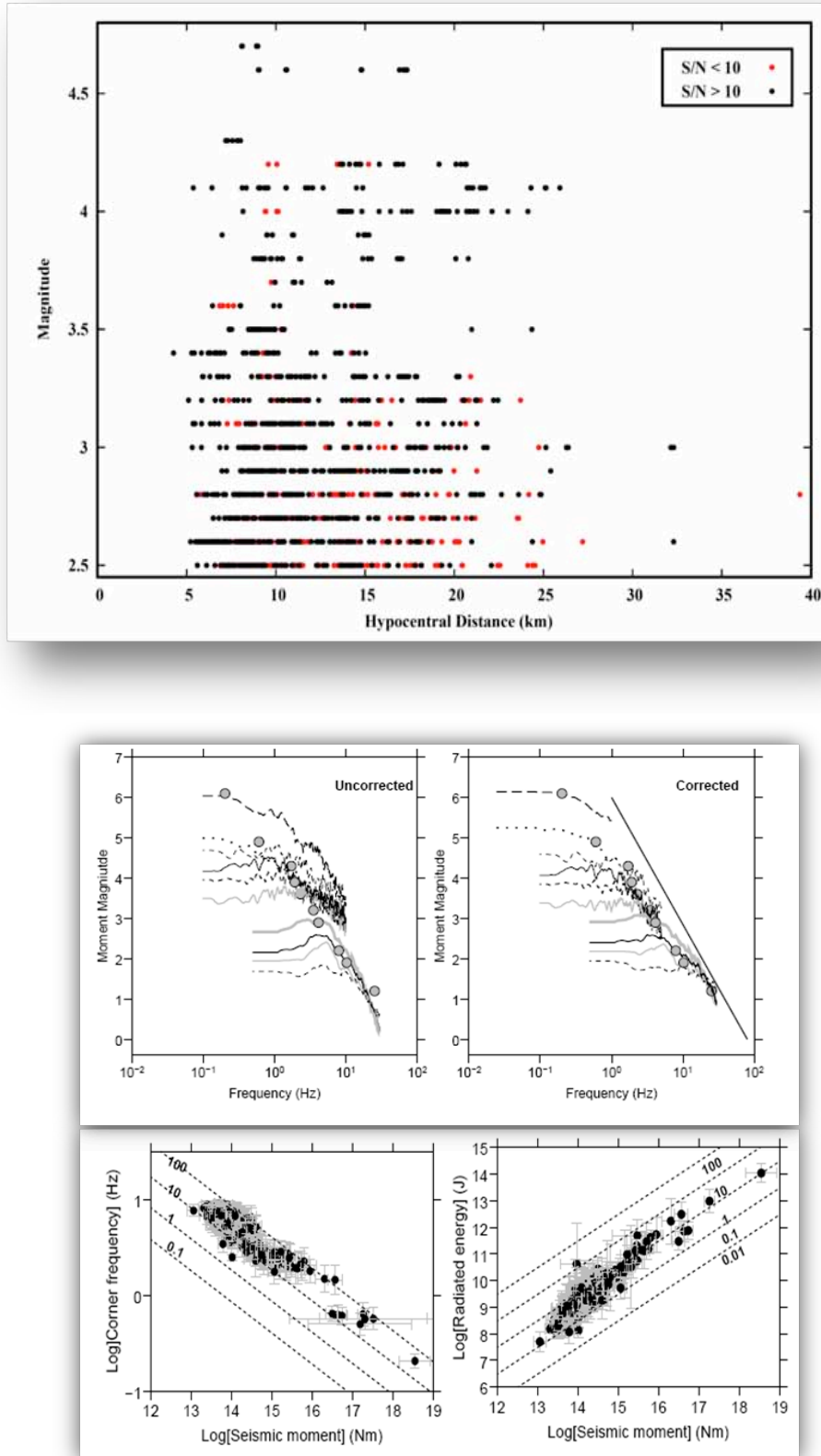


Figure 42: On the top magnitude vs distance distribution of selected aftershocks. On the bottom, corrected and uncorrected by the Q parameters spectra and scaling laws for corner frequency and radiated energy.

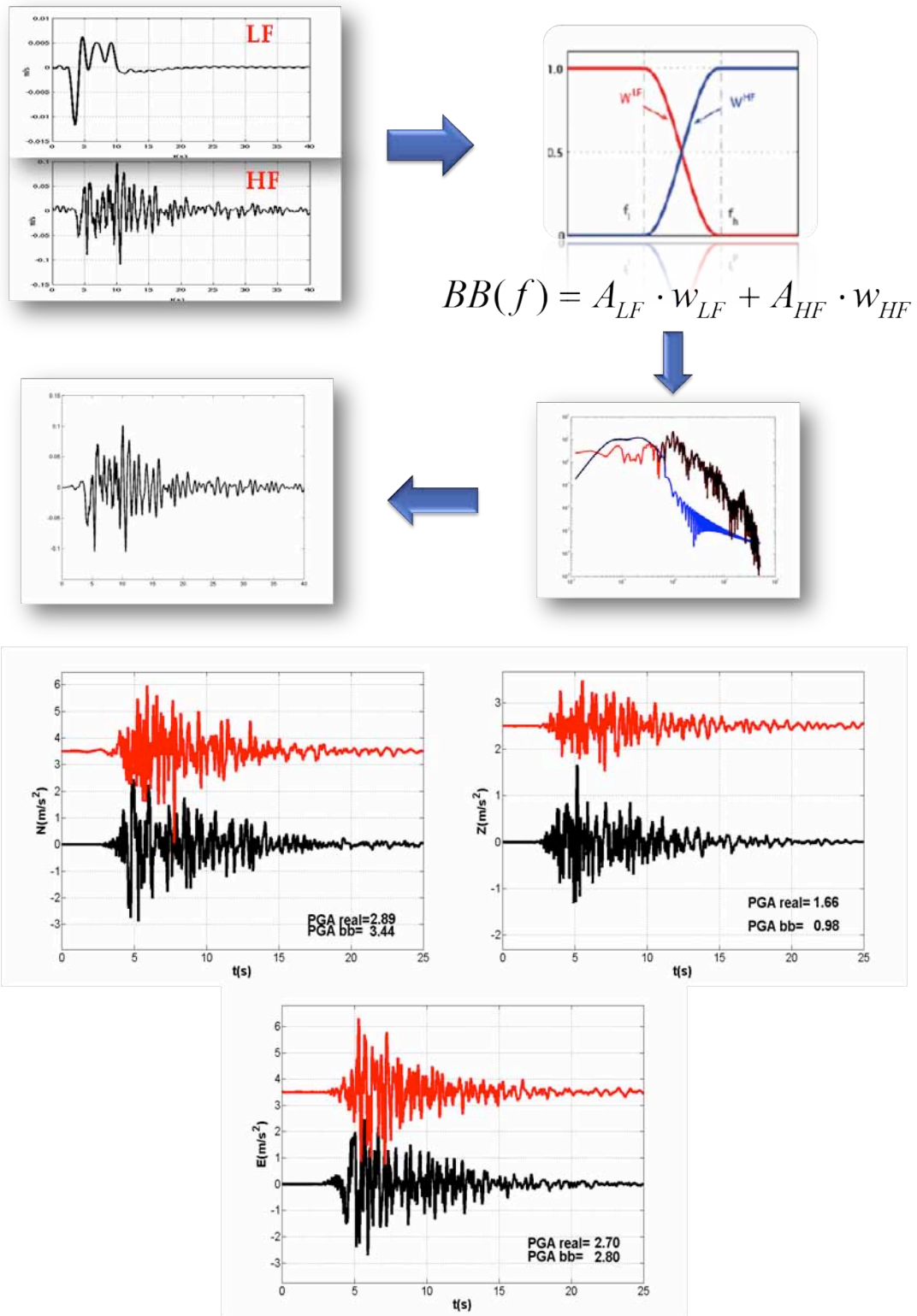


Figure 43: Broad-band ground motion strategy and simulations.

At low frequencies, where the signal to noise ratio is poor in the EGF, we computed 1D numerical Green's functions computed via a discrete wave-

number- finite-element method. Broadband signals are obtained coupling the low frequency part with high frequency simulations computed using EGFs and compared with real data both for near source AQ* stations and far source stations. An example for the station AQG is represented in Figure 43. Synthetic waveforms fit almost well the envelope, the duration and the amplitude of the real data, with the only exception of the first impulsive train which is indeed not well reproduced by this kinematic source model. To check the possibility to improve the low/intermediate frequency wave propagation we also replaced the 1D model with a 3D structure of L'Aquila basin. Numerical Green's function were computed with the spectral element method in this case. 3D features are particularly significant for the near source stations like AQU. As shown in Figure 44, there is a significant increase in amplitude for the intermediate frequencies with respect to the simulations obtained by a simple 1D propagation model.

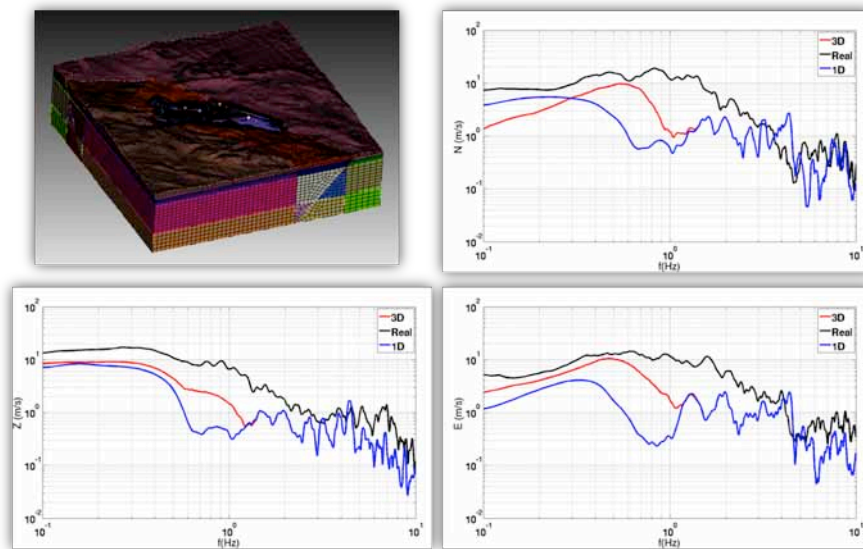


Figure 44: 3D geometry model for the L'Aquila region and comparison of Fourier spectra for the three components of AQU for 1D, 3D simulation and real records.

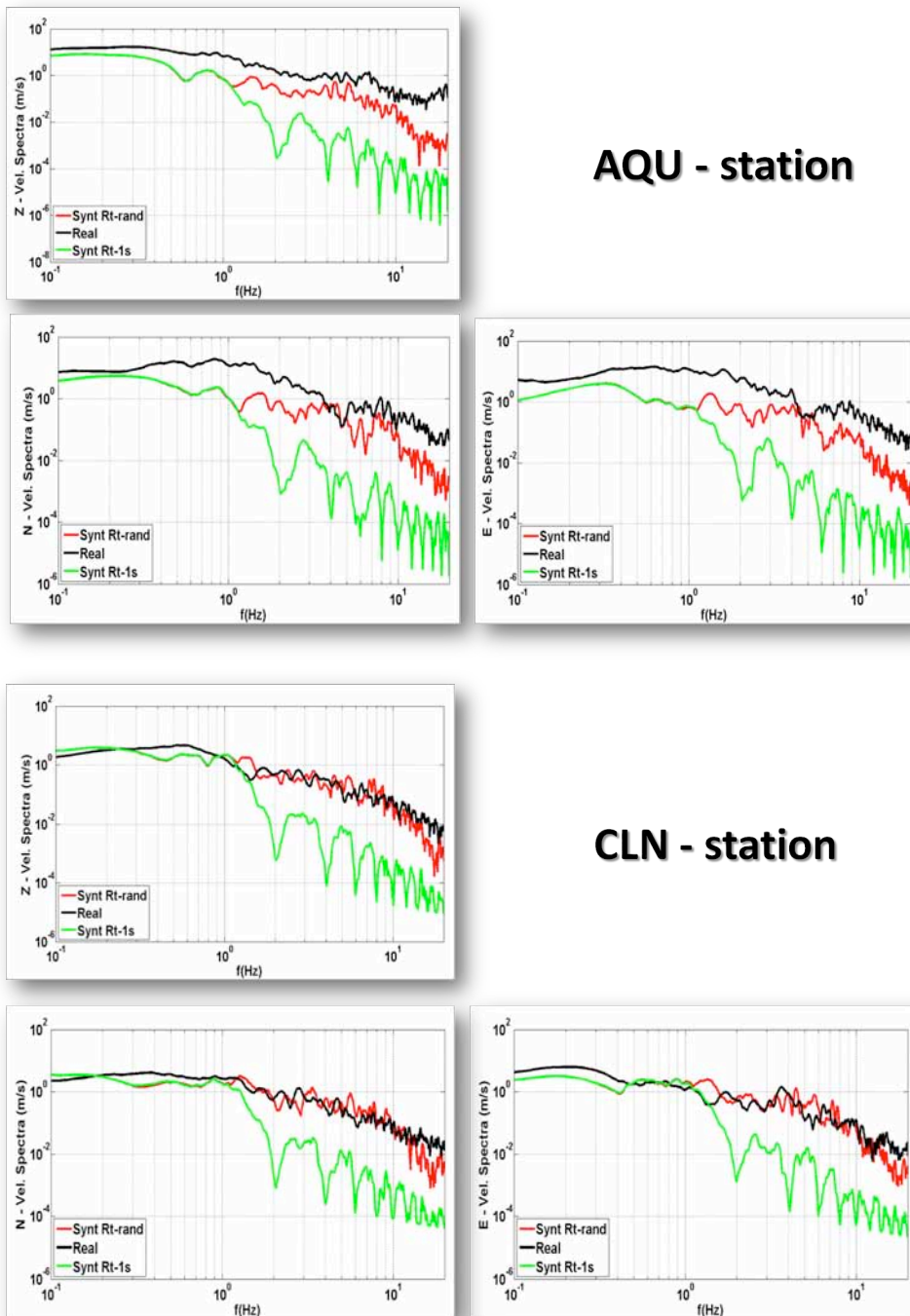


Figure 45: Velocity spectra for uniform (1s- green curve) and variable (0.1s to 1s-red curve) compared to real observations (black curve) for two stations.

After providing a source model coupling kinematic inversion results with a pure stochastic k-2 distribution, we computed broadband simulation up to high frequencies (5-10 Hz) to provide the ground motion amplitude and its variability at the basin and city scales. We also investigated the influence

of the source parameters and their distribution on the fault plane on the ground motion. We found that a primary role is played by the variability of the rise time on the fault. Specifically the synthetic spectrum at high frequency well fit the real one when the rise time rapidly changes in a broad interval (0.1s to 1s). Figure 45 shows the comparison between real and synthetics data in terms of velocity spectra: synthetic spectra were obtained with 1s rise time (green line) and variable rise time (red line) respectively. Results are shown for the stations AQU, which is very close to the fault area, and CLN, which is about 50 km far from the epicenter. Finally we generated a large amount of synthetic spectra for the strong motion stations, changing the slip distribution at high frequency according to a k-2 model, and the empirical Green function, used as a propagator. We studied the variability of the simulations as compared to the real observations in terms of amplitude and response spectra. In Figure 46 we show an example for AQU and FMG stations. We found that for the far source station (FMG) the average estimate well describes the data both for the amplitude the response spectra, while real response spectra at L'Aquila station are larger than the average value of the simulations for almost all periods.

Conclusions

1. Near fault stations reveal complex waveforms that need a modelling coupling complex source effects with reliable propagation. For the L'Aquila case, low frequency source model needs to be coupled with a 3D modelling of the basin to retrieve the right frequency content in the low/intermediate range (0.5-1Hz).
2. As for the source parameters, the rise time variability plays the major role in controlling the high frequency spectrum of the simulation. This variability can be directly linked to the high frequency behaviour of the model. Changes in the slip roughness play a secondary role.

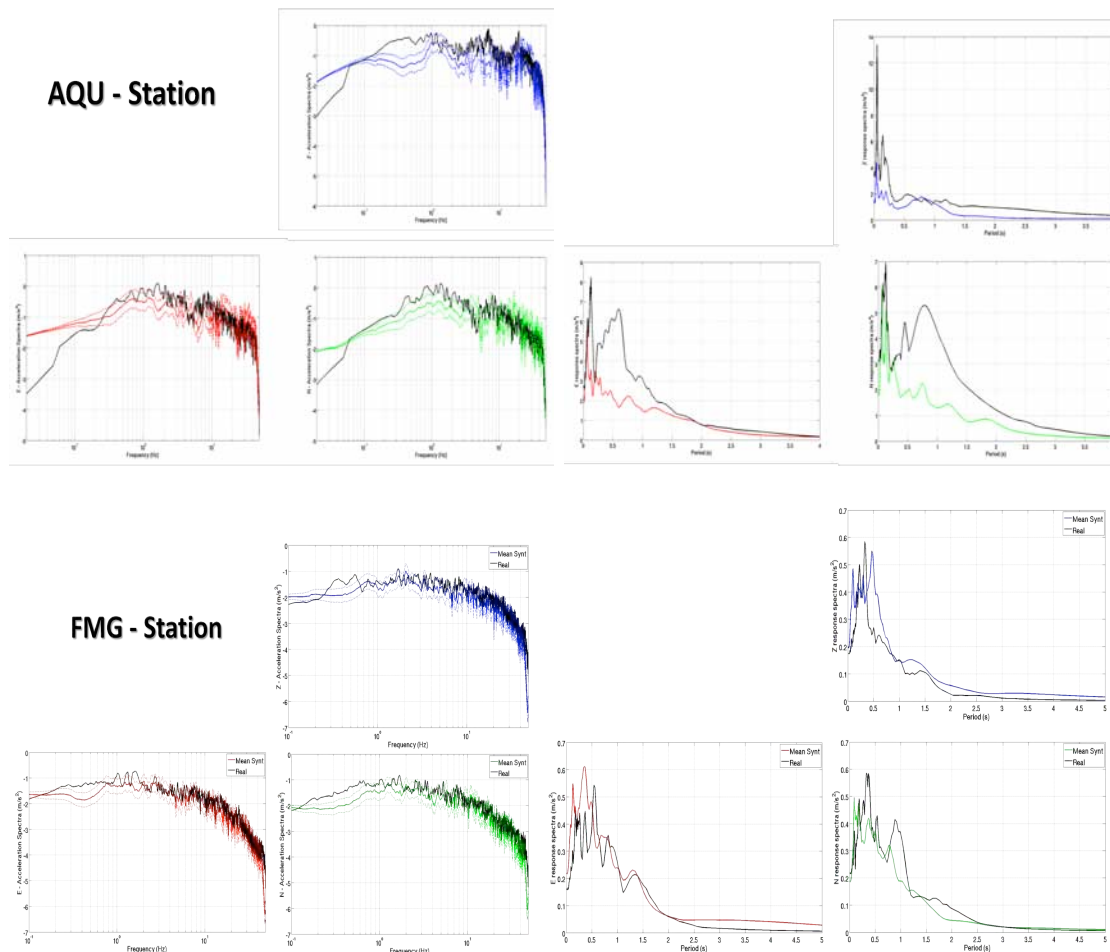


Figure 46: Simulated Fourier and response spectra for two stations compared to real data (black curve)

3. Selection of EGF is a critical point for correct modelling of the ground motion. Changing the EGF can lead to changes in the Fourier and response spectra of one order of magnitude in near fault at some frequencies.
4. Far field data are well constrained by the average model. Fourier spectrum sigma is less than one order of magnitude. In near fault, some frequencies appear underestimated and the sigma in the Fourier spectrum is larger than one order of magnitude.

2.5.2 Intra-event ground motion variability of the 2009 L'Aquila earthquake (INGV team)

This study is focused on the identification of the spatial variability of the ground motion parameters in relation to the heterogeneities of the source. We know that the accurate evaluation of a ground motion intensity measure for future earthquakes is necessary to inform earthquake-engineering decision. One widely adopted strategy is the probabilistic approach that uses the ground motion predictive equations to assess a ground motion intensity measure. Nevertheless at present the available empirical models are not able to comprehensively predict the high spatial heterogeneity of the observed ground motion. One key issue is related to the fact that the contribution of each explanatory variable to the ground motion variability is still unclear. In this framework we investigated the ground motion variability through a posteriori analysis of a well instrumented past earthquake, the 2009 L'Aquila, central Italy, M_w 6.1 (Scognamiglio et al., 2010; Herrmann et al., 2011) earthquake. As explained before (see Section 1.1), the joint inversion of strong motion, GPS and DInSAR data allowed us to image the coseismic rupture history on the fault plane (Figure 47, Cirella et al., 2012).

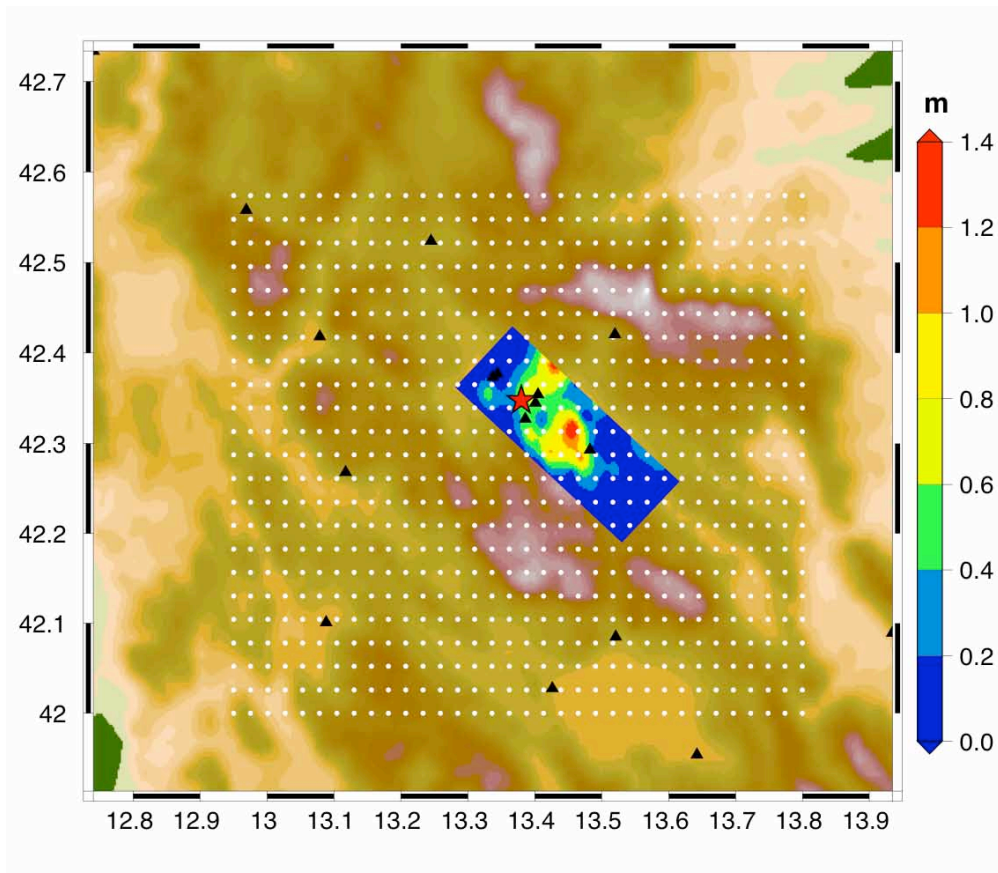


Figure 47 Inverted model of the 2009 L'Aquila earthquake. Slip distribution is in palette. Black dots represents the 800 sites of the virtual grid adopted in this study. Black triangles display real station positions.

Model and Assumptions

In order to quantify the source parameters contribution to the ground motion variability we fixed the rupture velocity field, retrieved by the inversion (see Figure 4a in Section 1.1) and the seismic moment ($M_0 = 3.5 \times 10^{18} \text{Nm}$) to model scenarios for a single fault plane (the same of the 2009 L'Aquila earthquake) on a 'virtual' grid (800 sites, displayed in Figure 47) of observers around the fault. We varied the slip distribution (36 models, Figure 48) and the nucleation position (15 points, Figure 48) by considering a heterogeneous rupture time distribution for each nucleation point. Each slip distribution is obtained by varying the position of one slip patch on the fault by using a self-similar slip distribution ($k=2$, Herrero and Bernard, 1994).

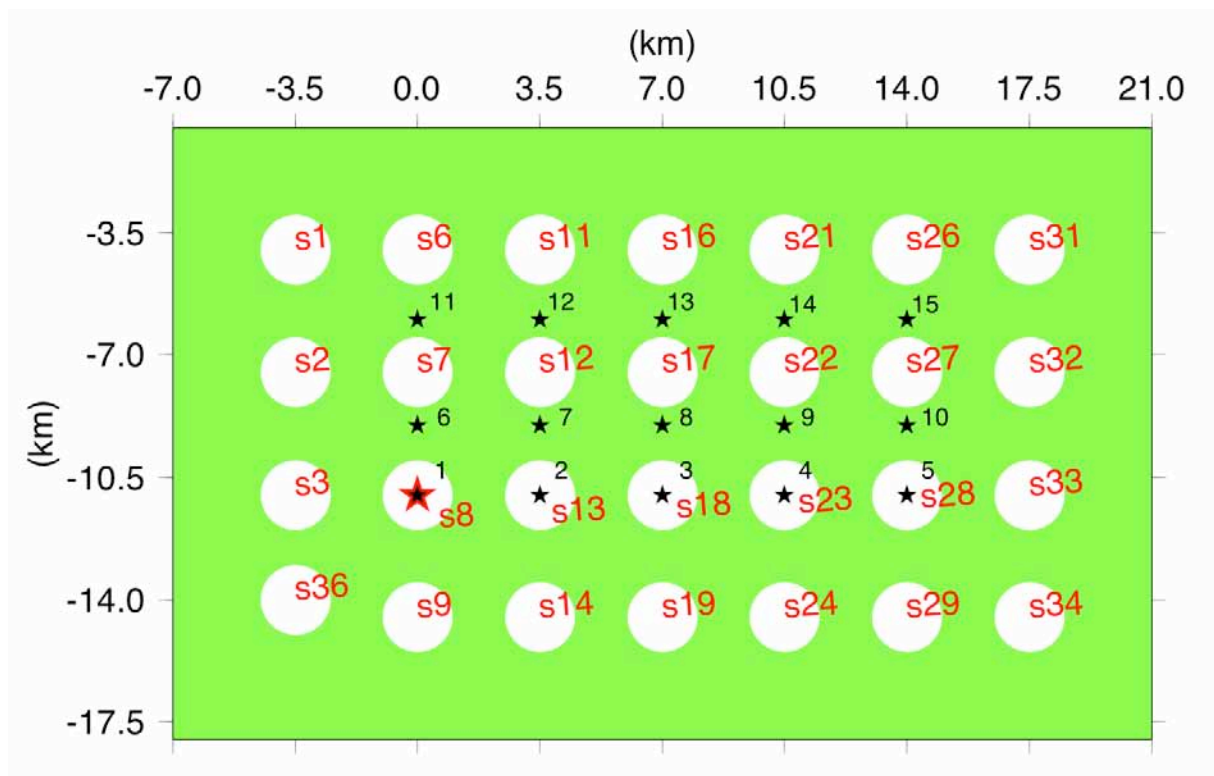


Figure 48 Scheme of the slip distributions considered in this study. White circles show the 36 slip patch positions; black stars displays the 15 nucleation positions. The nucleation position of the L'Aquila mainshock is highlighted in red.

We compute synthetic displacement time histories, up to 1 Hz, by using a discrete wave-number/finite element technique (Spudich and Xu, 2003). The amount of models guarantees the statistical consistency of the dataset. From those sets of scenarios we extracted several ground motion parameters: PGD, PGV, SA at different oscillator periods.

Ground Motion Variability

We studied the variability of the peak ground displacement (PGD) for both synthetics and real waveforms. The huge quantity of synthetic data allows the definition of a mean value and standard deviation for PGD. Based on the variability obtained by changing the combination of slip patch position and nucleation points, we compared the variability resulting from the simulations with the recordings of the L'Aquila mainshock (Figure 49).

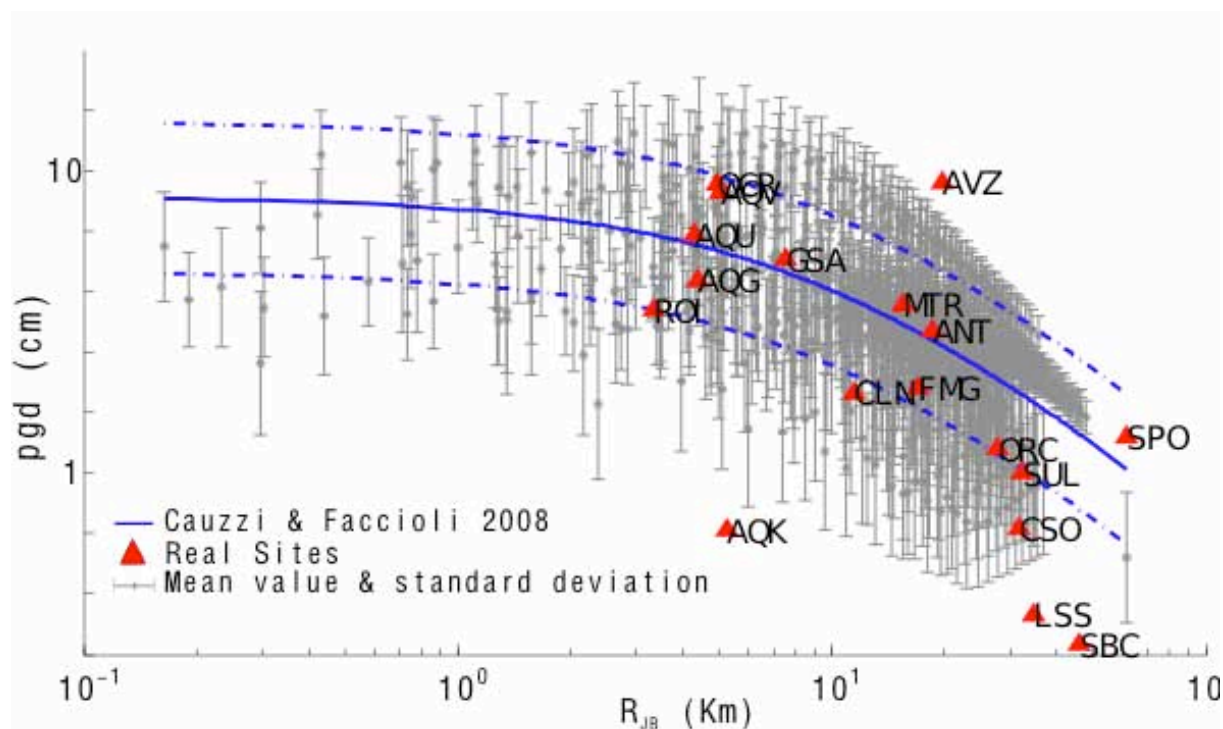


Figure 49 Intra-event variability obtained by varying nucleation point and slip distribution. Blue lines show the Cauzzi and Faccioli GMPE; red triangles are real recordings.

The prediction based on the amount of scenarios is consistent for distances shorter than 10 km. For comparison, a ground motion predictive equation is also superimposed in blue (Cauzzi and Faccioli, 2008). The variability predicted by the GMPE is in agreement with real data with the exception of a few cases who are overestimated.

Single Source Parameters Contribution to Ground Motion Variability

The single station PGD variability features a log-normal distribution. From this distribution is it possible to extract significant moments: i.e. mean (to use in predictive equations), or maximum (for strategical structures). Figure 50 shows the contribution of the nucleation position (number from 1 to 15) and slip (number from 1 to 36) to the PGD distribution at a given station (587). In the selected case maximum values of PGD are obtained for nucleation points 4, 8, 10 and for slip distribution 16, 21, 31.

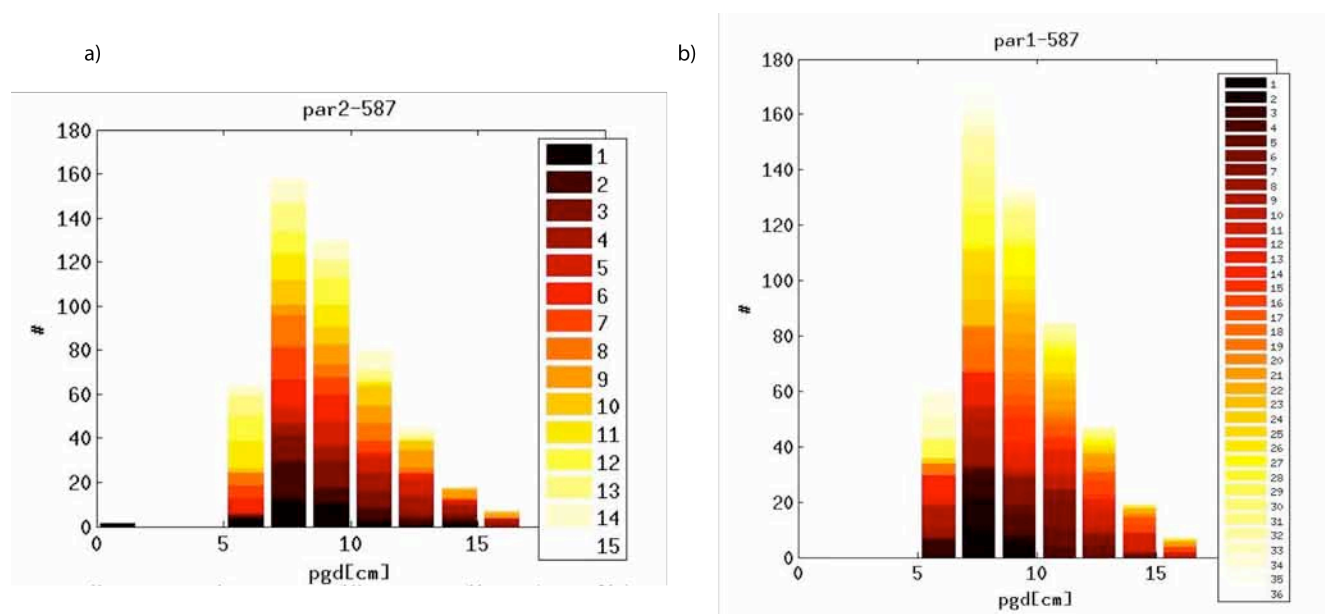


Figure 50 Contribution of single source parameters to PGD variability at one station. a) contribution of the nucleation position; b) contribution of the slip distribution.

This sensitivity analysis to kinematic parameters describing the source process, is useful to investigate how the variation of the source parameters affect the variability of ground motion prediction. In particular the relative position of the patch of slip respect to the hypocenter location could strongly influence the ground motion variability. The obtained results show how the position of the main patch of slip relative to the nucleation position on the fault plane is significant for the ground motion analysis also at low-intermediate frequency; moreover, it seems that the L'Aquila earthquake may not be intended as the *worst-case* scenario (Spagnuolo et al., 2013).

2.5.3 Stochastic Finite Fault Ground Motion Simulation of the 2009 L'Aquila Earthquake (METU team)

On 6th April 2009, an earthquake of M_w 6.1 (Herrmann et al., 2011) occurred in central Italy, close to the town of L'Aquila. Although the earthquake is considered to be a moderate-size event, it caused extensive damage to the surrounding area. The event is identified with significant

directivity effects: high amplitude, short-duration motions are observed at the stations that are oriented along the rupture direction, whereas low-amplitude, long-duration motions are observed at the stations oriented in the direction opposite to the rupture. The complex nature of the earthquake combined with its damage potential brings the need for studies that assess the seismological characteristics of the 2009 L'Aquila mainshock. Within this work package, METU team along with other researchers (Ugurhan et al., 2012) studied the event using an improved approach for stochastic finite fault modeling based on a dynamic corner frequency approach (Motazedian and Atkinson, 2005). In this study, 21 strong-ground-motion stations within an epicentral distance of 100 km are selected as the simulation sites (see Figure 51 for the map of the study area and the entire set of stations that recorded the mainshock).

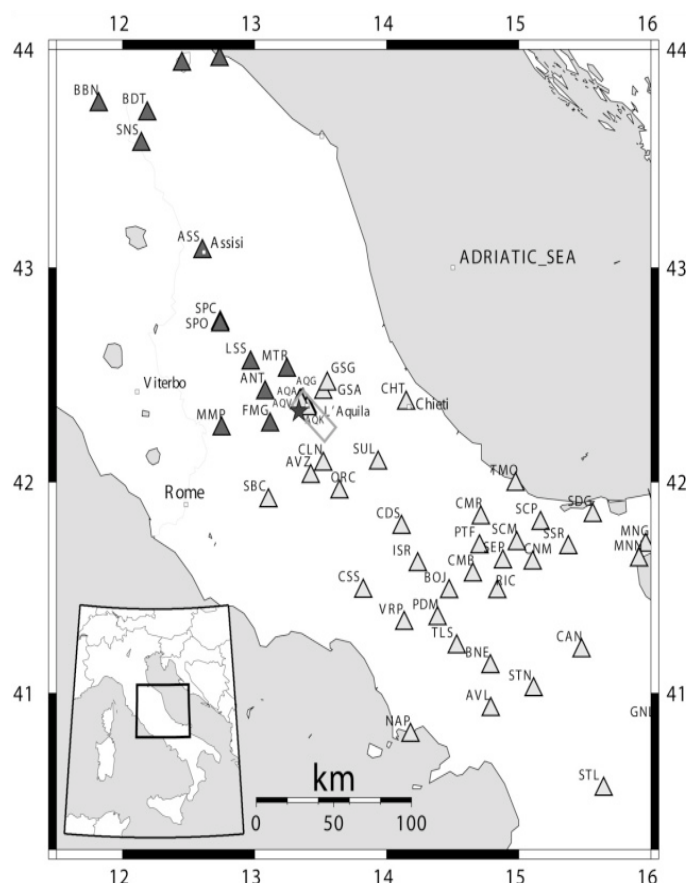


Figure 51. Map showing the regional setting of 2009 L'Aquila earthquake. The fault plane and the epicenter are indicated with rectangle and star, respectively. Triangles show the strong ground motion stations that recorded the mainshock. The gray triangles indicate the stations located in the NW of the epicenter (in the backward directivity direction) is indicated by gray colored triangles while the white-colored triangles indicate the stations located in the SE of the epicenter (in the forward directivity direction).

Stochastic strong ground motion simulations require well-defined source, path and site effects within the region of interest in order to generate reliable results. Due to the trade-off between the source, path and site filters, it is essential to start the simulations with well-resolved model parameters. The source and attenuation parameters used in this study have been chosen among the several recent models published after the 2009 L'Aquila earthquake. In this study, we test finite-fault source and slip distribution models by Cirella *et al.* (2009) and Scognamiglio *et al.* (2010). In this study we use two recent attenuation models by Bindi *et al.* (2009) and Malagnini *et al.* (2010) which are obtained using strong motion and weak-motion data set, respectively. With several combinations of the input parameters, we finally formed and tested 4 alternative models as shown in Table 5. Figure 52 and 53 displays respectively the Fourier Amplitude spectra and time histories of the acceleration records in comparison with the synthetics at twelve selected stations.

Table 5. Finite-fault model parameters for alternative models used for the 2009 L'Aquila earthquake simulations

Parameters	Model 1(*)	Model 2 (†)	Model 3 (‡)	Model 4 (§)
Fault orientation (strike & dip)	133°–54°	133°–54°	139°–48°	139°–48°
Fault dimensions	28 × 17.5 km	28 × 17.5 km	26 × 16 km	26 × 16 km
Moment magnitude	6.2	6.2	6.2	6.2
Depth of the top of fault plane	0.5 km	0.5 km	0.85 km	0.85 km
Subfault dimensions	2 × 2 km	2 × 2 km	2 × 2 km	2 × 2 km
Stress drop	150 bar	92 bar	150 bar	92 bar
Crustal shear wave velocity (β)	3200 m/s	3200 m/s	3200 m/s	3200 m/s
Crustal density	2800 kg/m ³	2800 kg/m ³	2800 kg/m ³	2800 kg/m ³
Rupture velocity	0.8 β	0.8 β	0.9 β	0.9 β
Pulsing area percentage	50%	50%	50%	50%
κ_0	0.035	0.035	0.035	0.035
Duration model	Malagnini <i>et al.</i> (2010)	Malagnini <i>et al.</i> (2010)	Malagnini <i>et al.</i> (2010)	Malagnini <i>et al.</i> (2010)
Attenuation model, $Q(f)$	140 $f^{0.25}$	59 $f^{0.56}$	140 $f^{0.25}$	59 $f^{0.56}$
Geometric spreading	$r^{-1.1}$ $r < 10$ km $r^{-0.7}$ $10 \leq r < 30$ km $r^{-0.5}$ $r \geq 30$ km	r^{-1} , $r < 50$ km	$r^{-1.1}$ $r < 10$ km $r^{-0.7}$ $10 \leq r < 30$ km $r^{-0.5}$ $r \geq 30$ km	r^{-1} , $r < 50$ km
Windowing function	Saragoni and Hart(1974)	Saragoni and Hart(1974)	Saragoni and Hart(1974)	Saragoni and Hart(1974)
Local amplification	Boore and Joyner (1997)	Boore and Joyner (1997)	Boore and Joyner (1997)	Boore and Joyner (1997)

*Cirella *et al.* (2009) and Malagnini *et al.* (2010).

†Cirella *et al.* (2009) and Bindi *et al.* (2009).

‡Scognamiglio *et al.* (2010) and Malagnini *et al.* (2010).

§Scognamiglio *et al.* (2010) and Bindi *et al.* (2009).

Among the alternative models, Model 1 yields the smallest misfits in terms of peak ground motion parameters and Fourier amplitudes. However, we observe that the directivity effects cannot be entirely simulated with the synthetics regardless of the model used. To observe the attenuation of the synthetics; we compare the results from Model 1 and Model 2 with existing GMPEs in Figure 54.

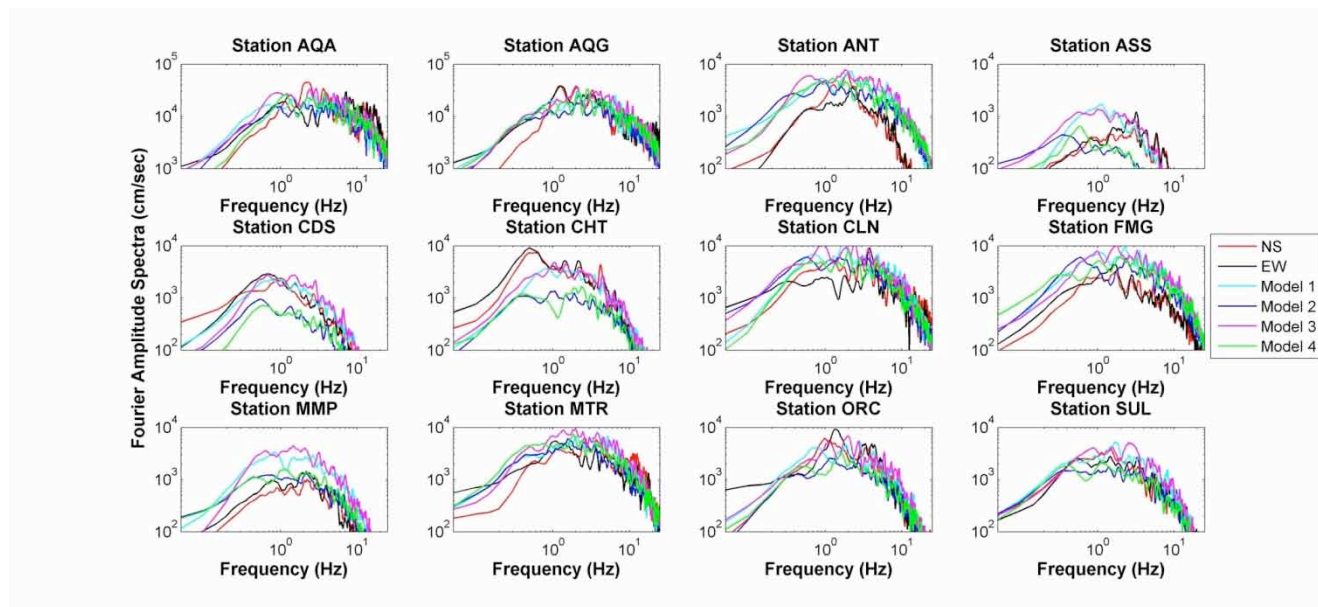


Figure 52. Fourier amplitude spectra at ten selected stations that recorded the 2009 L’Aquila earthquake in comparison with the synthetic ground motions obtained using alternative models.

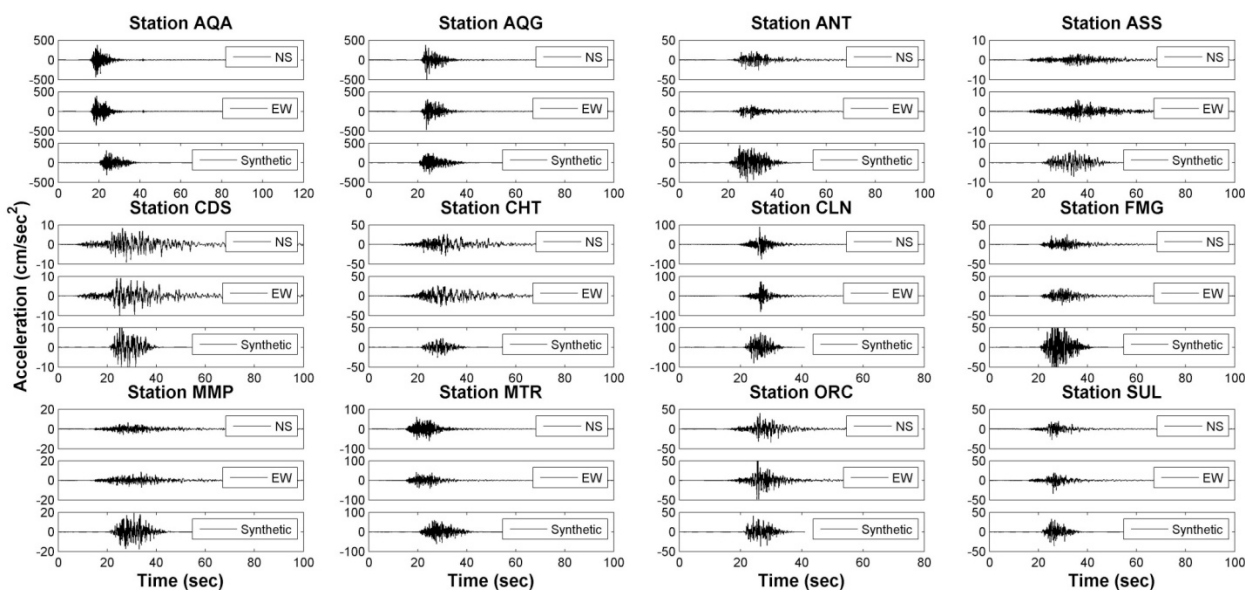


Figure 53. Acceleration time history plots at ten selected stations that recorded the 2009 L’Aquila earthquake in comparison with the synthetic ground motions

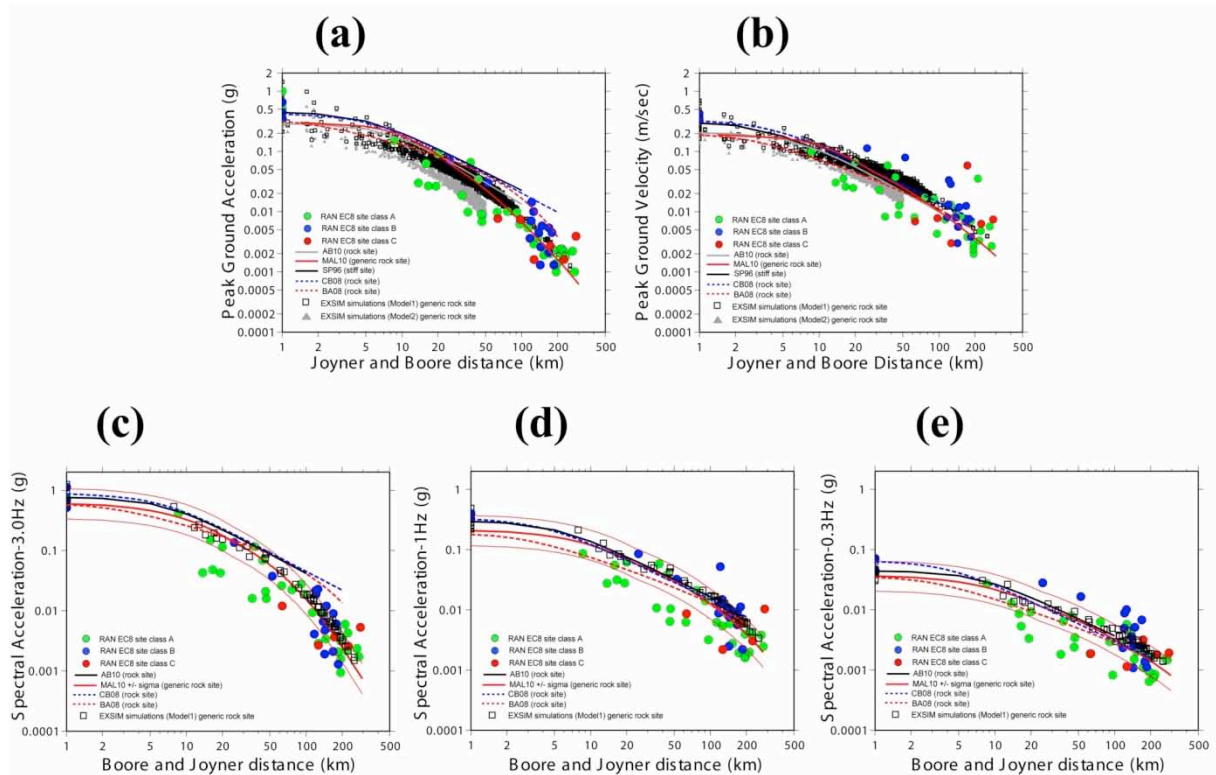


Figure 54. Comparison of the attenuation of synthetics and observed recordings with GMPEs by SP96, BA08, CB08, AB10 and MAL10 in terms of (a) PGA, (b) PGV, (c) %5 damped SA at $f=0.3$ Hz, (d) %5 damped SA at $f=1$ Hz and (e) %5 damped SA at $f=3$ Hz. In the case of (a) PGA and (b) PGV terms comparisons are done between the observed and simulated records that performed for generic rock site class both at the 1326 dummy stations includes the near-field records and the RAN network of strong motion stations (inside the 200 km distances). For the case of SA (%5 damped) at 0.3, 1.0 and 3.0 Hz case comparisons are made only between the observed and simulated records that performed for generic rock site class for the RAN network of strong motion stations.

Next, to assess the directivity effects in the simulated records, we study station pairs which have similar Joyner-Boore distances but oriented in opposite directions with respect to rupture propagation. Figure 55 shows 5% damped acceleration response spectra of the recordings at selected stations along with simulation results. It is evident that there are significant differences in the response spectra of station pairs in terms of amplitudes. Due to the attenuation phenomena, distance is an important factor affecting the amplitudes. But these differences are not due to distance effects since the station pairs have similar distances from the fault plane. An alternative reason for amplitude differences is the local site conditions. In order to overcome this problem, the station pairs are chosen to be of the same site class. Indeed, except station GSA which is

classified as of type B class, the majority of the stations used in the comparisons are of type A class. Therefore, the station pairs are chosen such that the stations have similar propagation and site effects. Based on this discussion, the differences (if any) in the spectra of station pairs are most probably due to the directivity effects. The forward stations, indicated with red lines are shown to have larger amplitudes. It is clear that the synthetic spectra of station pairs have similar amplitudes except the spectra at FMG and GSA stations. From the spectra of other station pairs, it is observed that whether the station is oriented in the rupture direction or opposite to the rupture direction does not make a significant difference in terms of synthetic spectral accelerations for intermediate to far field distances. A similar conclusion is obtained from analyses of observed versus synthetic peak ground motion parameters (PGA and PGV) at stations located in the forward and backward directions.

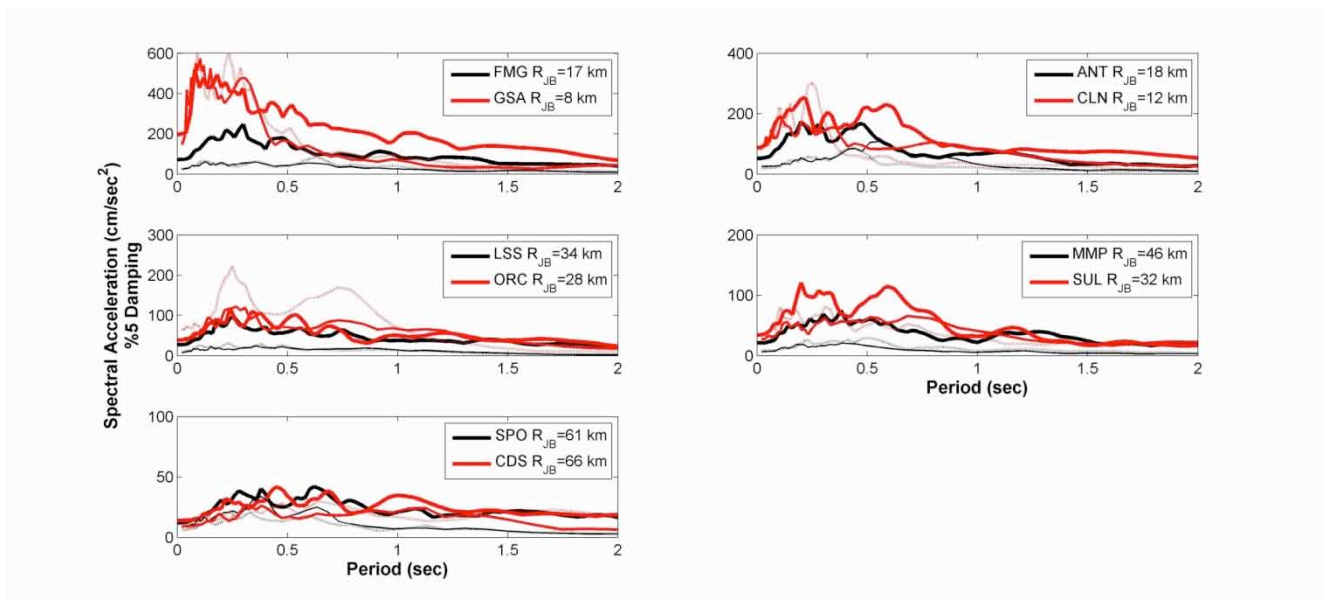


Figure 55. Comparison of response spectra curves of equal distant stations. The thin solid line shows the NS component, dashed line shows the EW component of the observed recordings. The thick solid line represents for the synthetic records. Forward stations are shown with red color whereas backward stations are shown with black color.

In the light of these observations, we conclude that with stochastic finite-fault models are mostly limited in terms of simulating the directivity

effects. Simulation algorithms that can employ more complex models of the source mechanism could yield more realistic results. We finally compare the spatial distribution of shaking intensity in L'Aquila region with the simulated ground motion distribution. Figure 56.a displays the intensity distribution within 9° - 15° E longitudes and 39° - 45° N latitudes. In Figure 56.b, a closer inspection is performed by displaying the intensity distribution within 13° - 13.8° E longitudes and 42° - 42.6° N latitudes. In both figures, the distribution is obtained from "Did You Feel It?" project and is given in terms of MCS scale. In Figure 56.c, the intensity distribution obtained from the site survey conducted in the meizoseismal area (Camassi *et al.*, 2009) is given, also in MCS scale. From both the "Did You Feel It?" data and the site survey we observe that the maximum intensities occur on and around the fault plane as expected. There is also an enhancement of higher intensities in the fault-normal direction consistent with the directivity phenomena. We note that recently Ameri *et al.* (2011) showed that forward directivity effects influenced the microseismic intensity distribution in the near source area of the 2009 L'Aquila earthquake and directivity-induced amplification effects are observed. Next, to compare these intensity distributions with the simulated PGA and spectral acceleration (SA) distributions, we display the synthetic PGA and SA for $T=0.25$ and $T=0.5$ sec within 13° - 13.8° E longitudes and 42° - 42.6° N latitudes in Figures 56.d-f. We note that approximately 40% and 50% of the building stock in L'Aquila is comprised of 2-3 and 4-6 storey buildings, respectively, which have fundamental periods corresponding to the selected values of $T=0.25$ and $T=0.5$ sec (Liel and Lynch, 2009). In Figures 56.e and 56.f, the spectral accelerations corresponding to these periods are observed to reach extremely high values at close distances from the fault plane. We note that this asymmetrical distribution of high SA values combined with possible local soil amplifications resulted in the widespread building damage observed in L'Aquila.

We further assessed the distribution of damage by computing the

expected PGA values from an MCS-PGA correlation proposed by Faenza and Michelini (2010) which is given as:

$$I_{MCS} = 1.68 + 2.58 \log PGA \quad (2.2)$$

We input the MCS intensities of site survey results into Equation (2.2) and obtain the corresponding PGA values shown in Figure 56.g.

We observe that Figures 56.b to 56.d are consistent with each other in terms of spatial distribution around the fault. Certainly there are variations since the "Did You Feel It?" data is not as well-resolved as either the site survey or the simulations. Especially the site survey results are far more localized and highly-resolved around the fault area. Still, there is consistency in these spatial distributions shown in Figures 56.b-56.f. In Figure 56.g, a more localized PGA distribution is observed than that in Figure 56.d. This is certainly expected because the empirical relationship by Faenza and Michelini (2010) uses the MCS data from site surveys shown in Figure 56.c. Finally, we conclude that in general the spatial distribution of the intensities correlate well with the spatial distribution of the synthetic PGAs and SAs around the fault area. Both the intensity and the ground motion parameters take their highest values on the fault plane in the NW-SE direction.

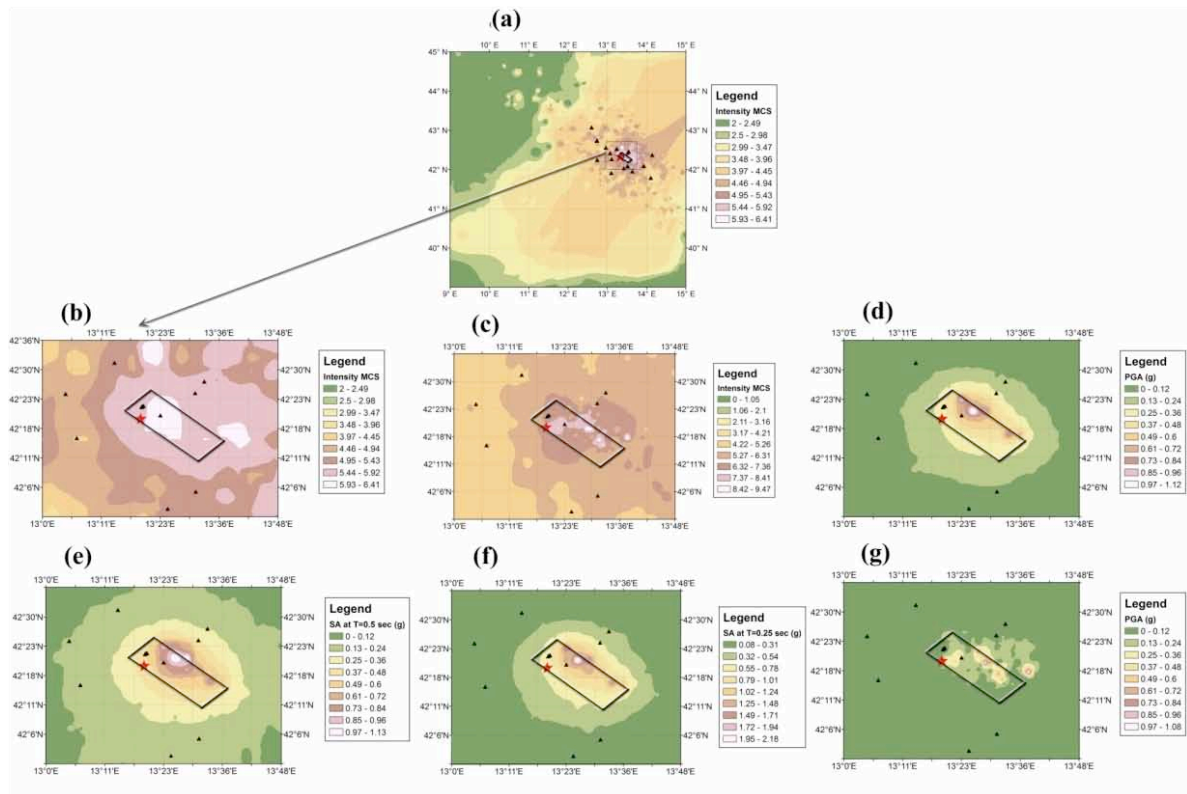


Figure 56. (a) Shaking intensity distribution obtained from Did You Feel It? Project – Large Scale (b) Shaking intensity distribution obtained from Did You Feel It? Project – Small Scale (c) Shaking intensity distribution obtained from site survey results (d) Spatial distribution of PGA values of synthetic ground motions (e) Spatial distribution of SA values of synthetic ground motions at $T=0.5$ sec (f) Spatial distribution of SA values of synthetic ground motions at $T=0.25$ sec (g) Spatial distribution of PGA values obtained from a regional MCS-PGA relationship by Faenza and Michelini (2010)

Conclusions

Our results suggest that the high frequency ground motion in the study region decay faster when compared to the average trends described by national and global GMPEs. The discrepancy obtained with the predictions by both GMPEs and ground motion simulations and observations are observed to be also dependent on the source directivity which is significantly pronounced in the 2009 L'Aquila earthquake. This effect was recognized by the analysis of the instrumental and macroseismic data (Akinci *et al.*, 2010; Chioccarelli and Iervolino, 2010; Pino and Di Luccio, 2009). Therefore, the azimuthal variations are further tested in terms of peak ground motion intensity parameters. Moreover, the spatial

distribution of PGA and SA values of the synthetics are compared with the shaking intensity distributions obtained from Did You Feel It? project and site survey (Faenza *et al.*, 2009; Camassi *et al.*, 2009) results. Further comparisons are made in terms of PGA values obtained from an empirical MCS-PGA conversion relation.

In this study, we demonstrated the importance of choosing the critical region-specific source and attenuation parameters and their influence on the simulated ground motions. Finally, despite the limitations of the method in simulating the directivity effects, it is observed that a stochastic finite-fault model is an effective tool for estimating the peak ground motion parameters of near-to-intermediate field ground motions. Advanced source models taking into account dynamic effects of rupture propagation may lead to improvements in the simulation results, and future detailed investigation of local soil conditions, may be used to minimize the uncertainty due to the site amplifications. Finally, the results obtained in this study may be combined with low-frequency simulations of the mainshock radiation, in order to obtain broadband seismograms.

The results shown in this contribution can be found in the following paper: B. Ugurhan, A. Askan, A. Akinci and L. Malagnin (2012). Strong Ground Motion Simulations of the 2009 L'Aquila Earthquake, Italy, *Bulletin of the Seismological Society of America*, Vol. 102, No. 4, pp. 1429–1445.

2.5.4 Broadband (HIC Model) Ground motion Simulation of the 2009 L'Aquila earthquake (METU team)

Near-fault strong-ground motions (0.1–10 Hz) recorded during the (M_w 6.1) 2009 L'Aquila earthquake exhibit great spatial variability. Modeling the observed seismograms allows linking distinct features of the observed wavefield to particular source and propagation effects and provides insights on strong motion complexity from this moderate magnitude event. We adopt a hybrid integral-composite approach based on a k^2 kinematic rupture model, combining low-frequency coherent and high-frequency incoherent source radiation and providing ω^2 source spectral

decay. We show that most of the observed complexity can be explained when properly combining site specific and finite-fault effects. In particular, we test the effects of the rupture delay of the largest asperity, rupture velocity values, small-scale slip distribution and local site response. In this study we use the same fault plane and mechanism as defined in Gallovič and Zahradník, (2011), i.e., a rectangular fault plane 20 km long and 15 km wide having a strike of 140° and dipping 50° toward south-west. The rake angle is -90° (pure normal-fault mechanism) and the hypocentral depth is 9 km. We constrain the basic features of the kinematic rupture model according to the low-frequency inversion performed in Gallovič and Zahradník, (2011): namely 1) the approximate location of the two main asperities, 2) the time delay of the southeastern asperity rupture, and 3) the decrease of rupture velocity in the shallow parts of the fault. The final HIC source model used to calculate synthetic seismograms up to 10 Hz is reported in Figure 57. The rupture time distribution is obtained assuming two rupture velocities (as marked also in Figure 57) and a nucleation point corresponding to the instrumental hypocenter. As suggested by the slip inversion, a rupture delay of the southern asperity by approximately 3s is also included in the model. Although the low-frequency inversion suggests that the shallower subsources ruptured with a lower velocity than the deeper ones, the results show poor sensitivity to rupture velocity values. For this reason we test different values and set the final rupture velocity in the bottom and top part of the fault equal to $V_r=3$ km/s and $V_r=2$ km/s, respectively. Note that these values roughly correspond to 85% of the average shear-wave velocity at the relative depths. The final slip distribution is obtained constraining the positions of the three largest subsources (at level $n=2$), that are characterized by the largest seismic moment. In particular, one of them is placed "above" the hypocenter and the other two are set in the southern bottom part of the fault. At levels higher than 2, the remaining 60 subsources are randomly distributed over the fault plane following the defined number-size distribution, composing random high-wavenumbers details of the slip distribution. Finally, the

stress drop of the whole event is set to 100 bars based on estimates by Bindi et al. (2009) and on comparison between observed and synthetic high-frequency level of the Fourier amplitude spectra. We note that, since the main features of this model are retrieved by the low-frequency inversion, the success of the broadband modeling depends on whether or not the observed high-frequency ground motions are affected/controlled by the low-frequency source features.

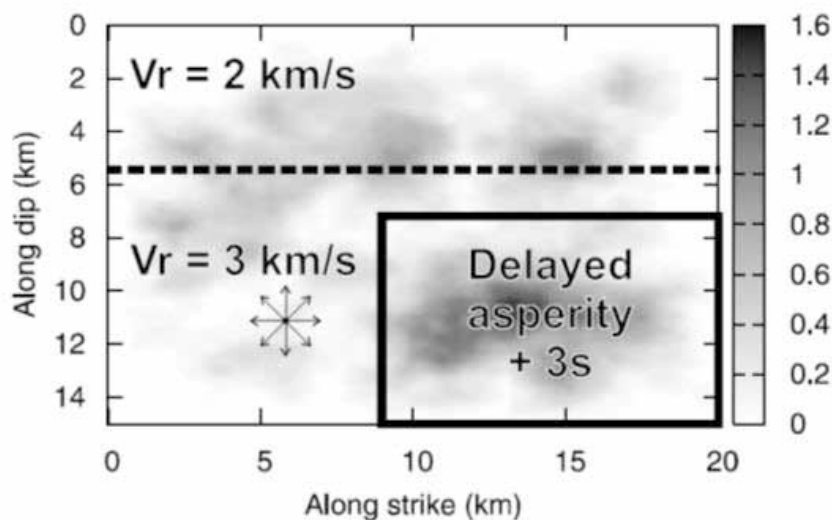


Figure 57. Kinematic rupture model used in the simulations. The final k-squared slip distribution composed of slip contributions from the fractal subsources is mapped by gray tones. The rupture velocity (V_r) values used in the top and bottom part of the fault as well as the location of the delayed asperity are illustrated. The outward vectors indicate the rupture nucleation point. The positions of the three largest subsources (at level $n=2$) centers are: (8,6), (12,11) and (15,11).

The HIC method allows for relatively fast ground-motion simulations, thus we performed a large number of trial calculations with the aim to obtain the “best fit” with recorded data. The sensitivity of the results to the local site response, rupture velocities, slip distribution at high wavenumbers, rupture delay of second asperity and cross-over frequency between the integral and composite approaches is investigated. Figure 58 displays an overview of the modeling results for this model, showing comparison of synthetic and observed acceleration and velocity time histories for 11 selected stations (to visualize the locations of these stations please see Section 2.5.3).

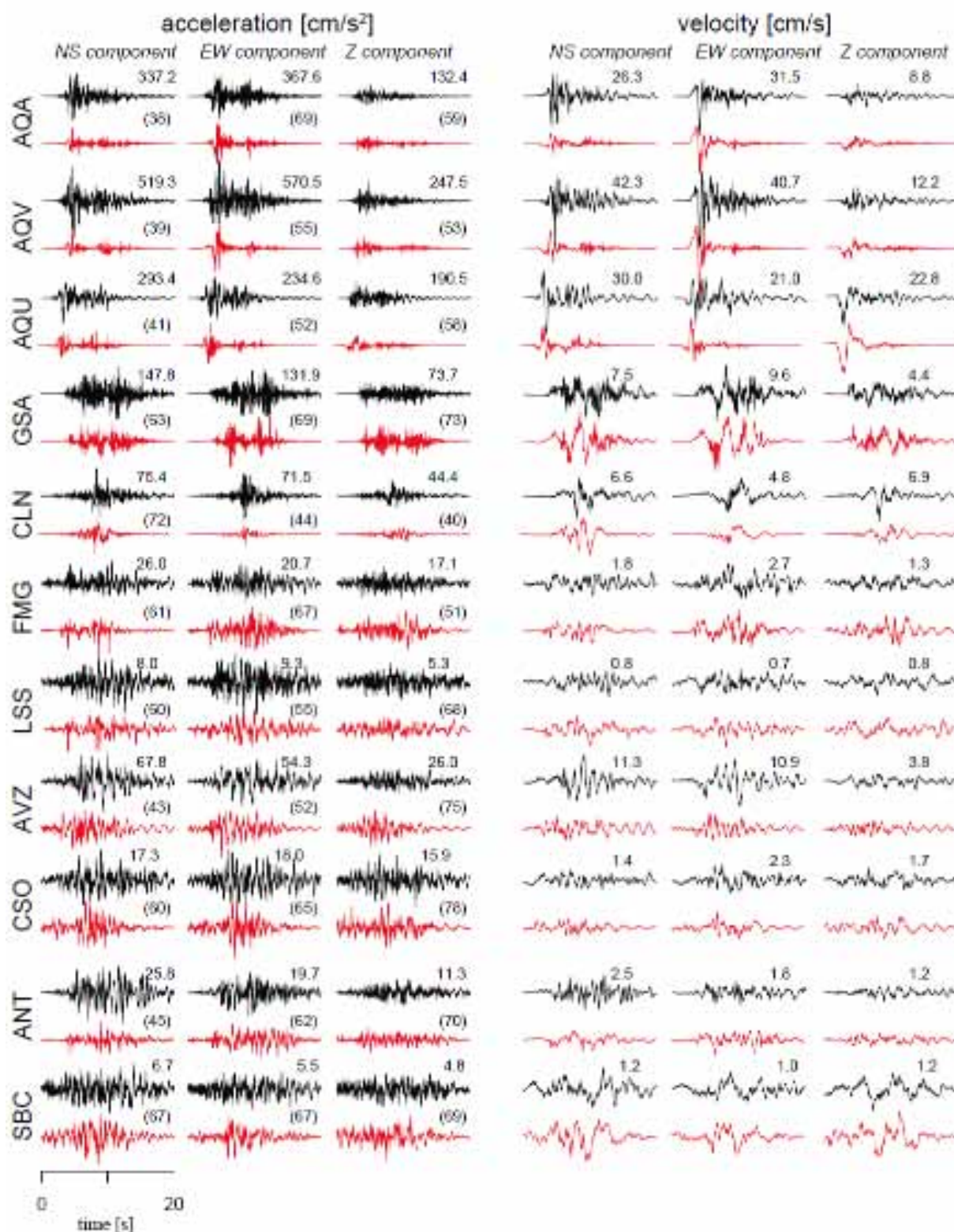


Figure 58. Comparison of recorded (black) and simulated (red) broadband three-component ground acceleration (left) and velocity (right) waveforms at eleven selected sites (indicated in Figure 57) for the L'Aquila earthquake. North-South, East-West and vertical components are shown. The recorded and simulated motions for each station are scaled to the maximum value listed above each pair of waveforms. The numbers between brackets are the goodness-of-fit score. Waveforms are band-pass filtered between 0.1 and 10 Hz.

In general, the synthetics match well the observed waveforms, despite the simplicity of the propagation models and the lack of site response for the most of the stations. The duration of the strong motion phase is well reproduced as well as the acceleration and velocity peak values. Concerning near fault sites (AQ_ stations), the synthetics show the characteristic velocity pulses with amplitude similar to the observed ones, at least on one component. However, an underestimation in the amplitudes and a lack of some high-frequency phases is noticed on the horizontal components (particularly on the North-South one), suggesting that more complex effects related to the presence of Aterno valley or details of source rupture model could affect the ground motion at these sites. Next, the sensitivity of the simulations with respect to 1D soil models, delayed asperity, slip distribution a high wavenumbers, and cross-over frequency band is investigated; following important conclusions are drawn (the related set of figures can be found in Ameri et al., 2012):

- the introduction of the site-specific soil profile into calculation of the Green's function allows to better evaluate the site effects, taking implicitly into account the incoming wavefields with proper incident angles at the base of the profile. Synthetic acceleration and velocity seismograms and acceleration FAS, calculated including versus not including the 1D soil profiles are observed. The most dramatic effect is observed at station AVZ where the FAS are increased 5-10 times over a broad frequency band. Accordingly, the velocity and acceleration wavefields are also enhanced, however, by a smaller factor. The large amplifications of the FAS are also due to the modeling of later phases generated by the wave propagation in the shallow layers, resulting in longer duration of the simulated records. The large amplification and duration lengthening at AVZ station are caused by the thick soft sediments of the Avezzano Plain over which the station is located.

At the other stations, the effect of the adopted 1D soil profile is lower. The durations are more or less preserved. The shape of velocity synthetics is only slightly modified. These differences are related to features not included in the adopted model, such as 3D crustal effects and/or additional complexities of the source model. The latter might be related to rupture propagation effects that we substitute in our model by the delay of the second asperity (see next point). Equally, there might be some slip complexities in the upper part of the rupture not resolved by the inversion. However, any such conclusions would have to rely on more precise Green's functions, taking into account, e.g., all possible reverberations of the complex 3D valley in the area;

- the effect of a delayed asperity is studied by comparing the best fit model simulation and a simulation where the delayed asperity is not considered. The effect of the delayed asperity is largest at CLN and partially at CSO and GSA stations. Indeed, at CLN, the model without the asperity delay exhibits a strong pulse at the beginning of the waveform, which is not present in the observed data. It is interesting to note that due to the position of CLN station respect of the fault, the energy-time distribution is mainly controlled by the rupture time of the stronger SE asperity. Finally, the broadband modeling confirms the significance of the rupture delay of the deeper asperity;
- to study the sensitivity of slip distribution a high wavenumbers, we studied the effect of 6 (random) different realizations of the slip distributions, obtained by using different seeds in the random generator, on the ground acceleration and velocity simulated at AQA and GSA stations. As expected, the effect is stronger at AQA that is closer to the fault rupture, being sensitive to the details of the slip distribution. The ground motion amplitudes around 0.7-1 Hz are remarkably affected (mostly due to varying position of level 3 and 4 subsources) and, for some slip distributions, the

velocity pulse amplitude decreases substantially. Examining alternative models, we note that the larger low-frequency spectral content is somehow related to the amount of slip “above” the hypocenter and toward the northwestern termination of the fault plane. At GSA station the six slip distributions produce less ground motion variations;

- the cross-over frequency range in the HIC model is optional and it divides the low-frequency (coherent/deterministic) and high-frequency (incoherent/stochastic) parts of the simulated wavefield. Use of higher cross-over frequency range allows modeling the long-period pulses in velocity records observed at the closest stations by means of the integral approach. At AQU and AQA stations, the arrival of the observed waveforms starts with a distinct onset and a strong directivity pulse. Both the onset and the pulse are better explained when the higher cross-over frequency range is considered (i.e. 1.5 – 2 Hz). This means that the very close stations require the wavefield to arrive coherently up to the relatively high frequencies of 2Hz. On the other hand, at GSA and CLN stations, located in the up-dip and along-strike rupture propagation directions, respectively, a better fit is obtained with the lower cross-over frequency range (i.e. 0.15–0.6 Hz). At these stations, the integral part of the model produces too large low-frequency amplitudes due directivity effects that are not equally observed in the recorded FAS. Simulations show that the use of higher cross-over frequency range allows modeling the long-period pulses in velocity records observed at the closest stations by means of the integral approach. The lower frequency range for the further stations suggests that a purely deterministic modeling of rupture directivity is not suitable in this case, and that the stochastic (composite) approach is needed in almost the whole frequency band.

The HIC broadband modeling yielded strong conclusions not only to earthquake physics but also to ground-motion simulations for hazard analyses and earthquake engineering applications. In summary, it is shown that purely composite and/or stochastic models without the possibility of modeling the coherent low-frequency wavefield by the integral approach would meet difficulties when explaining the near-source directivity pulses observed at AQ_ stations. Correct modeling of pulse-type records is of great relevance to structural engineering because their seismic demand and spectral shape are different with respect to ordinary records and can generate much higher damage.

The results shown in this contribution can be found in the following paper: G. Ameri, F. Gallovič and F. Pacor (2012). Complexity of the Mw6.3 2009 L'Aquila (central Italy) earthquake: 2. Broadband strong motion modeling, *Journal of Geophysical Research*, VOL. 117, B04308, doi:10.1029/2011JB008729, 2012.

2.5.5 Broadband (HIC Model) Ground Motion Simulation of the 2011 Van Earthquake (METU team)

On October 23, 2011, Mw 7.1 earthquake occurred in Eastern Turkey, close to Van and Erciş towns, causing more than 600 casualties and a widespread structural damage. The earthquake ruptured a 60-70 km long NE-SW fault with a thrust mechanism, in agreement with regional tectonic stress regime. Within this work, METU team along with other researchers (Galovič et al., 2013) studied the fault process of the event and the recorded ground motions using different sets of data. Regional records (0.005-0.010 Hz) are used to constrain the centroid-moment-tensor solution. Near-regional data, 100-200 km from the fault, are used for relocation of the hypocenter and, in the frequency range 0.05-0.15 Hz, for inversion of the rupture propagation by two methods: multiple point-source model (ISOLA) and Multiple Finite-Extent (MuFEx) source model. MuFEx provides also estimate of the model uncertainty, which is quite large due to unfavorable station distribution. We arrive at several

plausible scenarios (equally well fitting the observed data including GPS co-seismic displacements) with different styles of the rupture propagation. A few alternative source models are used for broadband (0.1-10Hz) ground motion simulations by means of the Hybrid Integral-Composite (HIC) source model. Only models comprising source complexities, such as a delayed rupture of shallow asperities, enable explanation of the acceleration record at the only available near-fault station, which exhibits a long duration and two prominent wave groups. These complex rupture models are used to simulate the ground motion in the near-fault area, specifically, at Van and Erciş, where records of the mainshock were missing, providing reasonable agreement with the observed spatial distribution of damage. In this study we used freely available data from several repositories. Broad-band seismograms were acquired from Orfeus and from the International Institute of Earthquake Engineering and Seismology (IIEES) of Iran. Strong motion records were available from the National Strong Motion Network of Turkey (TR-KYH), operated by the Turkish Earthquake Research Department (AFAD) and from the Iran Strong Motion Network (ISMN) (Figures 59 and 60).

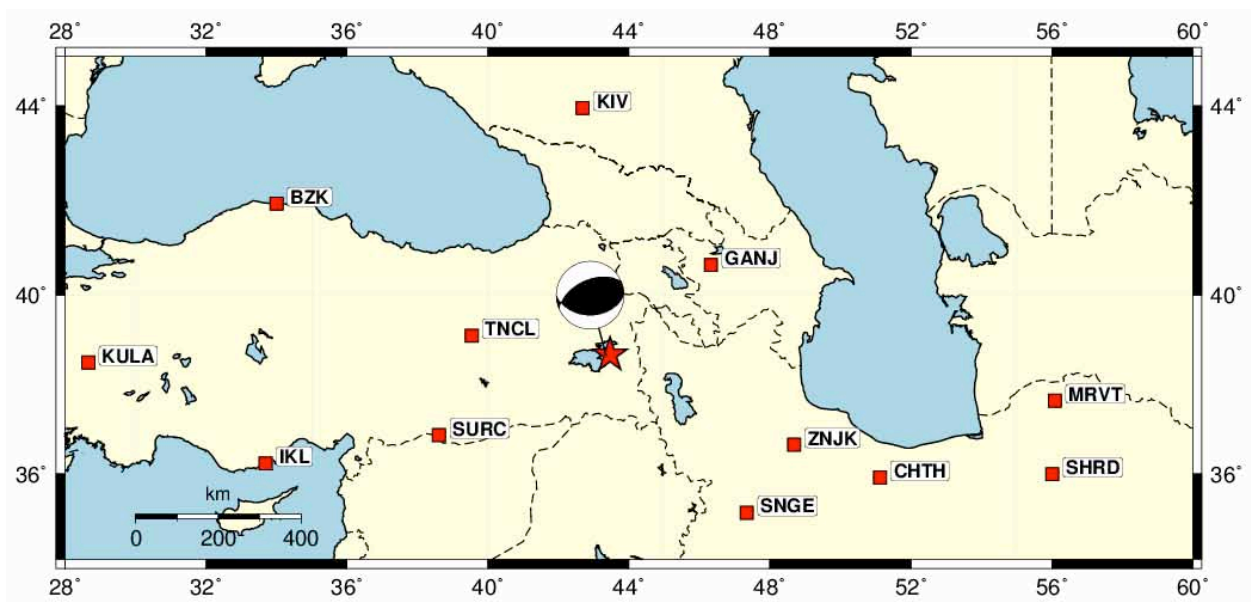


Figure 59. Map of the area with the CMT solution (beachball) calculated for the 2011 Van earthquake using regional broad-band seismograms in the frequency range 0.005-0.010 Hz. The used stations are shown by squares.

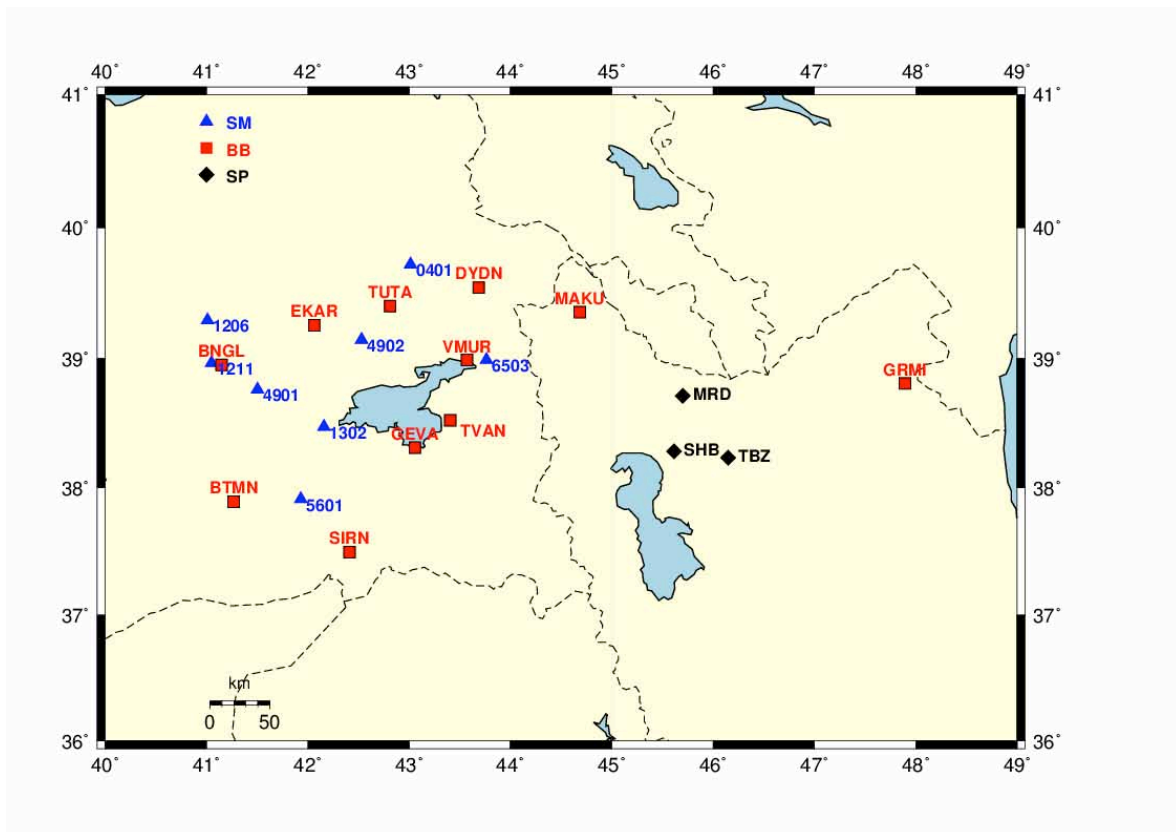


Figure 60. Near-regional strong-motion(SM), broad-band (BB) and short-period(SP) stations used in this study.

Our study of the event started with hypocenter relocation, CMT analysis by means of the full-waveform inversion using the ISOLA package, and the multiple-point source inversion. The latter is then extended to the inversion of the event considering multiple finite-extent (MuFEx) source model, grid-searching for possible values of parameters of the subsources, namely nucleation times, nucleation point positions and rupture velocities. Due to the unfavorable station locations (stations situated at large distances and almost exclusively in a single quadrant), the uncertainty of the source model is very large. We present three selected models to illustrate a broad variability in possible rupture propagation in Figure 61. For the details of the related source inversions, please see Section 1.3.

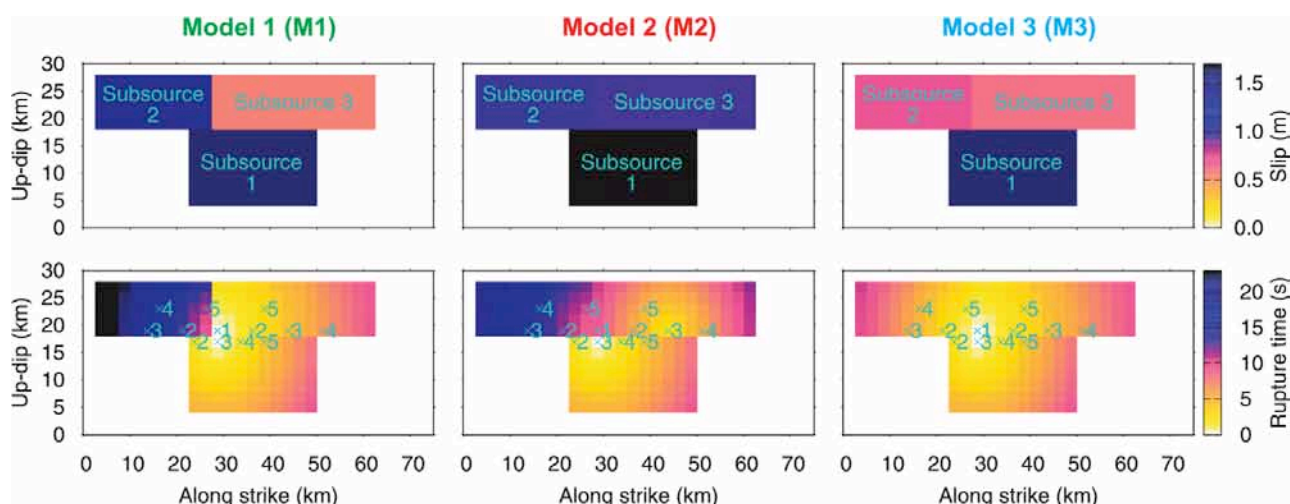


Figure 61. Three alternative Multiple Finite-Extent source models almost equally well fitting the data of near-regional strong motion stations

Then we developed a broadband strong-motion model based on the inverted fault model and simulate strong ground motions using the Hybrid Integral-Composite (HIC) source model. In this approach (Galovič and Brokešová, 2007), the rupture process is represented by overlapping subsources with fractal number-size distribution (the number of subsources decreases linearly with increasing subsource size). Note that here the term 'subsource' does not have the same meaning as in the MuFEx modeling. Assuming the constant stress-drop scaling, the subsources compose a slip distribution with k^{-2} decay at high wavenumbers k . In the low-frequency part of the modeling we use the representation theorem (hence integral approach). For high-frequencies, each of the subsources is considered as a point source radiating from its center a Brune's pulse with corner frequency and seismic moment given by the size of the subsource (composite approach). This way, the non-realistic directivity of the integral approach at high frequencies is diminished. Further, to reduce the effect of the radiation pattern, we assume $\pm 30\%$ variations of the subsource focal mechanism. The low- and high-frequency wavefields are cross-over combined at 0.5Hz. We impose the position of the largest subsources of the HIC model at places roughly corresponding to the subsources considered in the MuFEx source analysis. The other (smaller) subsources are distributed randomly over the fault

plane. The same slip-distribution model is complemented with three different examples of the rupture propagation. We consider the three cases of MuFEx models M1-3 (see above and in the bottom panels of Figure 61) with the rupture velocity of 3km/s. In addition, in model M4 we consider the same uniform style of rupture propagation as for M3 (radial rupture propagation at 3 km/s) but with the rupture velocity of 2 km/s; this was done to test the effect of a slow rupture velocity on the results. The first objective of the broadband simulations is the modeling of the Muradiye records (Station coded as 6503 on Figure 60). This station is extremely important because it is the only station located close to the causative fault and thus it can be used to assess the validity of HIC source model.

In the frequency band considered in this step the local site effects can have a large influence on the wave propagation and thus their appropriate consideration significantly affects the quality of modeling at a specific station. For this reason, we approximate the local site response of Muradiye station by including a soil profile specific for this station. The results of the modeling of Muradiye records by including or not including the local site response are presented in Figure 62 for source model M1. In the time domain, peak acceleration values are enhanced twice with almost no change in duration when the site specific structure is included in the simulation. In Fourier domain the site effect increases spectral amplitudes in a broad frequency band, and mostly for $f > 0.5$ Hz, improving significantly the fit with observed spectra. We note that there are still some differences between the observed and simulated horizontal Fourier spectra around 1 Hz. Such differences could be ascribed to site effects not captured by the adopted soil profile. This hypothesis is supported by the empirical amplification function based on horizontal-to-vertical spectral ratios (H/V) calculated by Akansel et al., 2013 considering mainshock and some aftershocks recorded at Muradiye station. Indeed, the H/V-based amplifications provide mean amplitudes of more than a factor of 3 (and a notable dispersion) for frequencies slightly below 1 Hz. Nevertheless, the

use of the site-specific soil profile at Muradiye represents a clear improvement in the modeling and thus it has been used in the following calculations at the station.

Figure 63 compares the modeling results for the Muradiye station with observed data for the 4 selected rupture models. The comparison is presented in terms of acceleration and velocity waveforms and acceleration Fourier amplitude spectra. In particular, Models M3 and M4 with simple rupture propagation are characterized by relatively short duration of waveforms when compared to the observed data (both in acceleration and velocity). Moreover, most of the energy is released in the first 10 seconds of the seismograms. On the other hand, the observed seismograms are characterized by longer duration, with their peak amplitudes (both in acceleration and velocity) located not at the beginning of the records but rather in the central part (around 15 seconds after the onset). Only models M1 and M2, including late rupture of the NE asperity (n.2 in MuFEx analysis in Figure 61) are able to explain those late wave packages observed in the recordings. Recall that these models were revealed only by grid-searching all model parameter values in the MuFEx source inversion.

In Fourier domain, models M1, M2 and M3 explain equally well the spectral amplitudes. Thus the overall frequency content of the waveforms at Muradiye station is not particularly affected by the style of the rupture propagation. Only model M4, characterized by the same circular rupture style of model M3 but with a much smaller rupture velocity, provides small amplitudes compared to the observed ones.

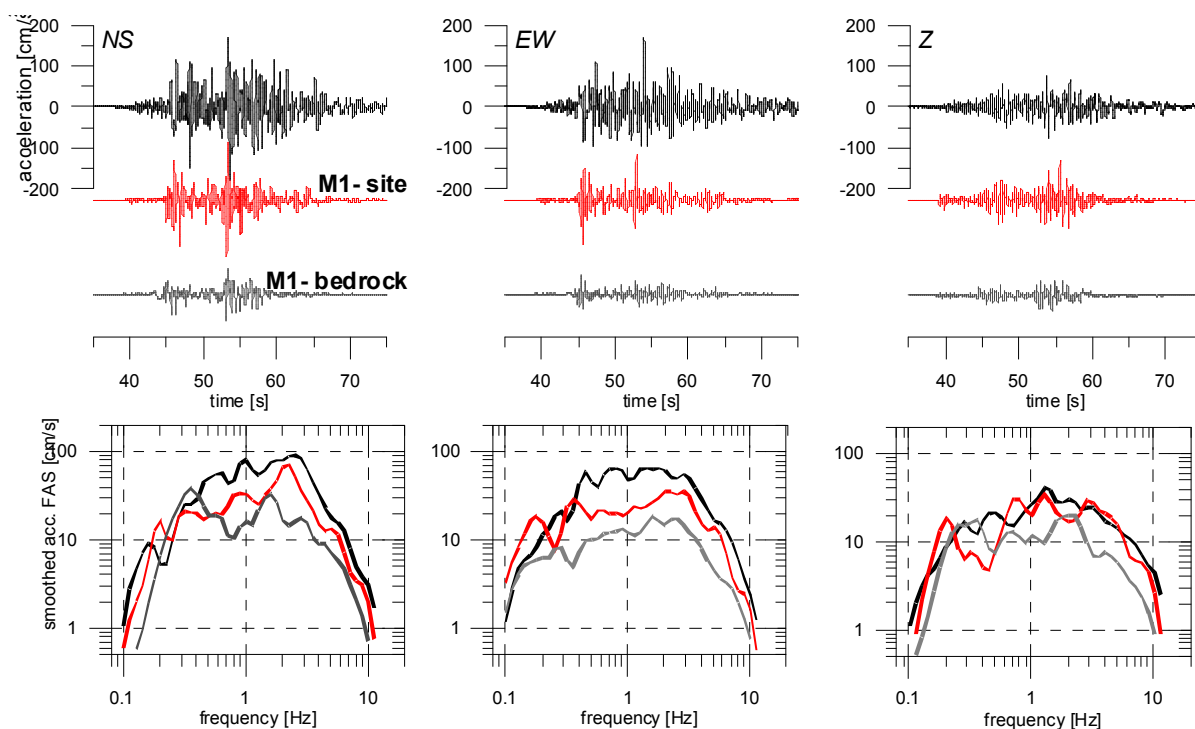


Figure 62. Modeling results at Muradiye (6503) station, including or not the local soil profile in the calculations. Observed 3-component acceleration time series and smoothed acceleration Fourier amplitude spectra are compared with simulated ones for soil and bedrock site conditions. The results are presented for source model M1.

In terms of modeling of the Muradiye records the results clearly suggest that models M1 or M2 are successful, being able to adequately explain the amplitude levels and temporal characteristics (duration and number of wave packages) of the observed seismograms.

We showed that the long duration of the closest Muradiye station, consisting of two-three distinct wave packages in the observed accelerometric record, can be reproduced only when models with complex rupture propagation (such as a delayed rupture of shallow asperities) is considered. Using the HIC modeling technique validated by means of the Muradiye records, next we simulate bedrock ground motions at a dense grid of virtual receivers in the epicentral region, up to 50 km from the fault. We adopted three of the source models presented in the previous section, excluding model M4 that clearly provided a worse fit at Muradiye. The results are presented in terms of peak ground velocity (PGV) and peak ground acceleration (PGA) maps in Figure 64. The maximum values on the maps reach approximately 1g in PGA and 1.2m/s in PGV. All the

maps are characterized by two distinct spots of high values above the fault that are related to the two subsurface asperities in the HIC model.

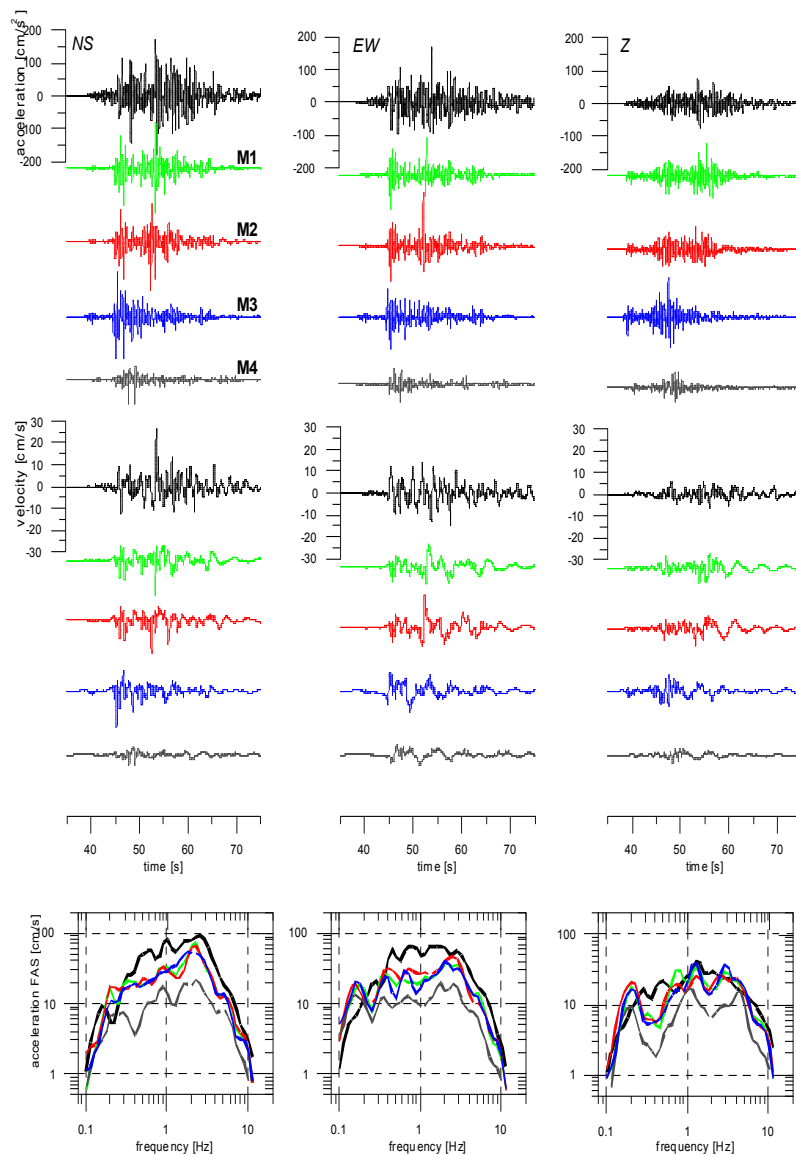


Figure 63. Modeling of Muradiye records using several rupture models.

The strength of the eastern spot, however, differs from one scenario to another, depending on the timing of the rupture evolution (i.e. details of the rupture propagation). In particular, smaller amplitudes of the eastern spot are obtained with model M2 characterized by a late rupture of both shallow subsources.

The spatial distribution of PGA from the models resembles the spatial extent of the distribution of damage in adobe masonry buildings

obtained from a detailed site survey (Figure 65). Indeed, the damage is localized in two spots towards the NE and SW of the epicenter. It is known from previous studies (e.g., Erberik, 2008) that vulnerability of wall-bearing masonry structures correlates with PGA mostly due to their short fundamental periods.

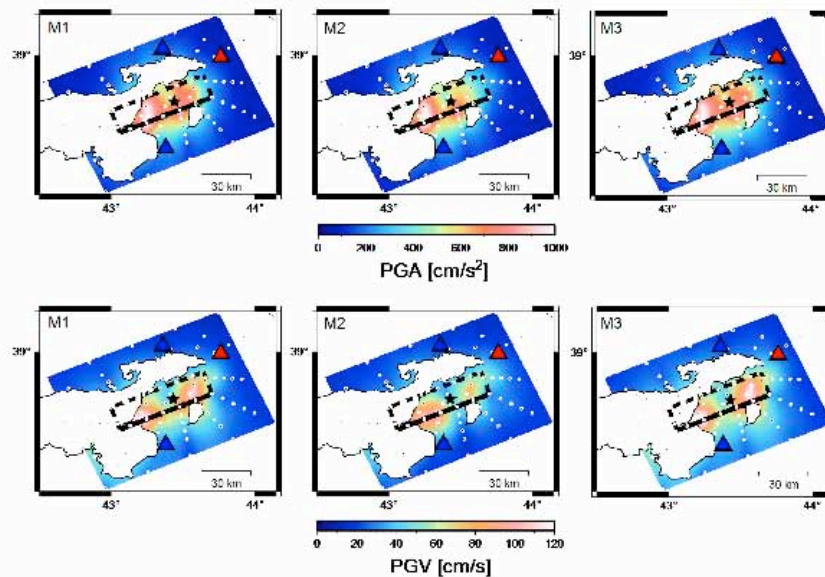


Figure 64. PGA (top) and PGV (bottom) maps calculated using models M1, M2 and M3 at a grid of virtual receivers (dots) on at the surface situated up to 50 km from the fault. The geometric mean of horizontal components is used. The epicenter (star), fault (rectangle), MURA station (eastern triangle) and Van and Erciş cities (southern and northern blue triangles, respectively) are shown. Site effects are not taken into account.

Conclusions

- The unfavorable station locations (stations situated at large distances and almost exclusively in a single quadrant), the uncertainty of the source model were very large which is believed to significantly affect the results of the ground motion simulations.
- Three selected models were used to illustrate a broad variability in possible rupture propagation.

- We show that the long duration of the closest Muradiye station, consisting of two-three distinct wave packages in the observed accelerometric record, can be reproduced only when models with complex rupture propagation (such as a delayed rupture of shallow asperities) is considered.
- With the same source models we also performed bedrock ground motion estimates for the whole Van area, including seismograms simulated in Van and Erciş cities, where no instruments recorded the event. Despite the predictions suggest similar levels of ground motion, the observed structural damage in city of Erciş was larger than in Van. This difference could be attributed to different building properties in Van and Erciş or local site amplifications in Erciş. Resolving this apparent discrepancy remains a topic for future research.



Figure 65. Spatial distribution of damage in villages located within the meizoseismal area (symbols). Erciş and Van city centers are also shown in the figure along with the collapse ratios of a sample of surveyed buildings in the field. The earthquake impact ranges from the high damage and collapse ratios to slight or no damage. (For further details, please see Akansel et al., 2013.)

The results shown in this contribution can be found in the following paper: F. Gallovič, G. Ameri, J. Zahradník, J. Janský, V. Plicka, E. Sokos, A. Askan, M. Pakzad (2013). Fault process and broadband ground-motion simulations of the 23 October 2011 Van (Eastern Turkey) earthquake, *in press* at *Bulletin of the Seismological Society of America*.

2.5.6 Stochastic Finite Fault Ground motion Simulation of the 2011 Van earthquake: Mainshock and Aftershock Modeling (KOERI team)

Ground Motion Simulations for the 23 October 2011 Van, Eastern Turkey Earthquake Using Stochastic Finite Fault Approach

METHODOLOGY

The stochastic approach (Hanks and McGuire 1981; Boore 1983) is one of the most powerful methods for simulating the ground motions at frequencies in the range [0.5-20 Hz] of engineering interest. The stochastic finite fault model developed by Beresnev and Atkinson (1997,1998a,b) overcomes the limitation of conventional point-source modeling, by including properties of a large source such as fault geometry and slip inhomogeneity. The total ground motion at the observation point is obtained by summing up the contribution of each sub-fault with an appropriate delay time. Motazedian and Atkinson (2005) introduced the dynamic corner frequency concept to reduce the sub-fault size dependency of estimated ground motions and to conserve the total radiated energy. Further modifications and improvements proposed by Boore (2009) include the scaling of high-frequency motions on the integral of the squared acceleration spectrum rather than the integral of the squared velocity spectrum and removing the truncation of the sub-fault time series. In addition, this modified version uses the inverse of the corner frequency of each sub-fault for the duration of the sub-fault motions. In this study, the simulations have been performed based on the dynamic corner frequency approach using the modified stochastic finite-source program EXSIM (Extended Earthquake Fault Simulation) (Boore 2009).

INPUT

Strong Motion Data

The main event was recorded by 22 strong ground motion stations operated by National Strong Motion Network of the Disaster and

Emergency Management Presidency (AFAD, see <http://kyh.deprem.gov.tr/indexen.htm>) as well as 11 acceleration stations operated by the Iranian Strong Motion Network (ISMN 2011). In this study, twenty recording stations, located in the epicentral distance range from 38 km to 224 km, are utilized in order to calibrate and validate simulation input parameters. Figure 66 shows the location of the recording stations, as well as the epicenter and projection of fault plane. The maximum amplitudes of this earthquake are recorded at station 6503 (Muradiye), where processed peak ground accelerations (PGA) are 178 cm/sec^2 and 169 cm/sec^2 for the North-South (N-S) and East-West (E-W) components respectively. The peak ground velocities (PGV) are obtained as 24 cm/sec and 15 cm/sec in N-S and E-W directions, respectively. Table 6 lists the detailed information on the strong ground motion stations, average shear wave velocities, V_{s30} (m/sec), of few stations, Joyner-Boore distances (R_{jb} , closest distance to surface projection of the fault plane; Joyner and Boore 1981), processed PGAs of each horizontal component and maximum PGV.

Source Effects

The main input parameters which are required to model source effects are fault geometry, slip distribution, rupture velocity, and stress drop. The finite-fault source model adopted in this study corresponds to the rupture of earthquake fault along the NE-SW direction with a reverse mechanism as suggested by Hayes (2011). The fault plane is confirmed by aftershock distribution information. The N-W dipping plane has strike, dip and rake angles of 241° , 51° and 58° , respectively. Figure 66 shows the orientation of the fault projection on the regional topography. The dimensions of the fault length and width are taken as 72 km and 46 km that are consistent with the finite fault solution of Hayes (2011). To investigate the effects of different source models on the variation of the ground motion levels in regional scale, we adopted another slip model which is proposed by Altiner et. al (2013) as shown in Figure 67. The rupture model of the Hayes (2011) is obtained by using teleseismic broadband waveforms from Global

Seismic Network (GSN) where one high slip patch with maximum amplitude of 4m is located near the hypocenter; whereas Altiner et.al (2013) derived the geodetic slip model based on the near-field GPS measurements, which shows the same moment magnitude (M_w 7.1) as the teleseismic model, but has a shallower depth of the major slip asperity than the teleseismic one.

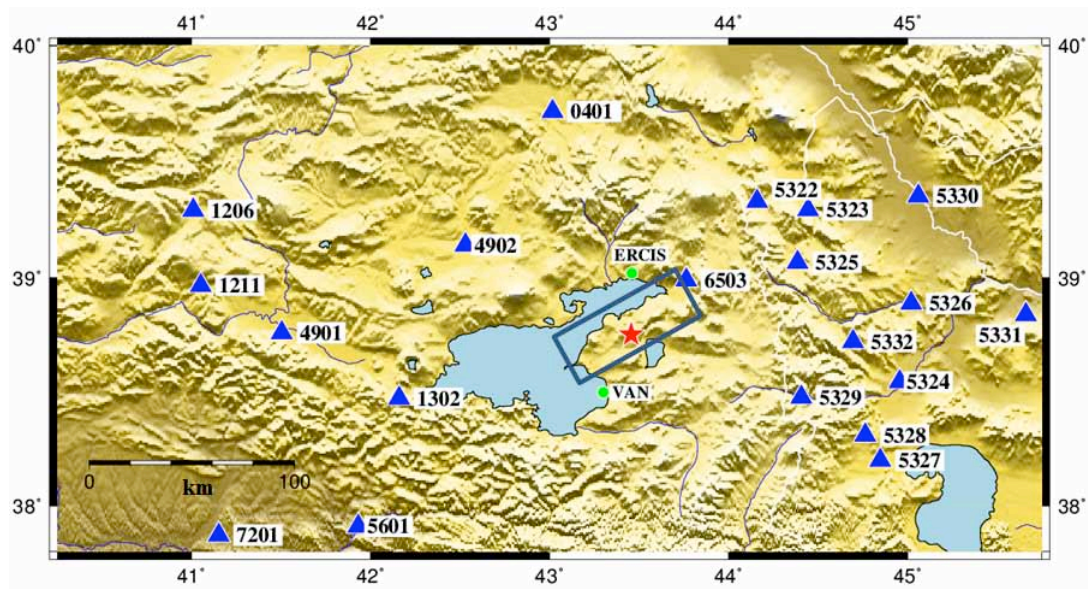


Figure 66 Location of the 20 strong ground motion stations utilized in the simulations are indicated by triangles. Epicenter of the mainshock is denoted with star on the projection of the fault plane.

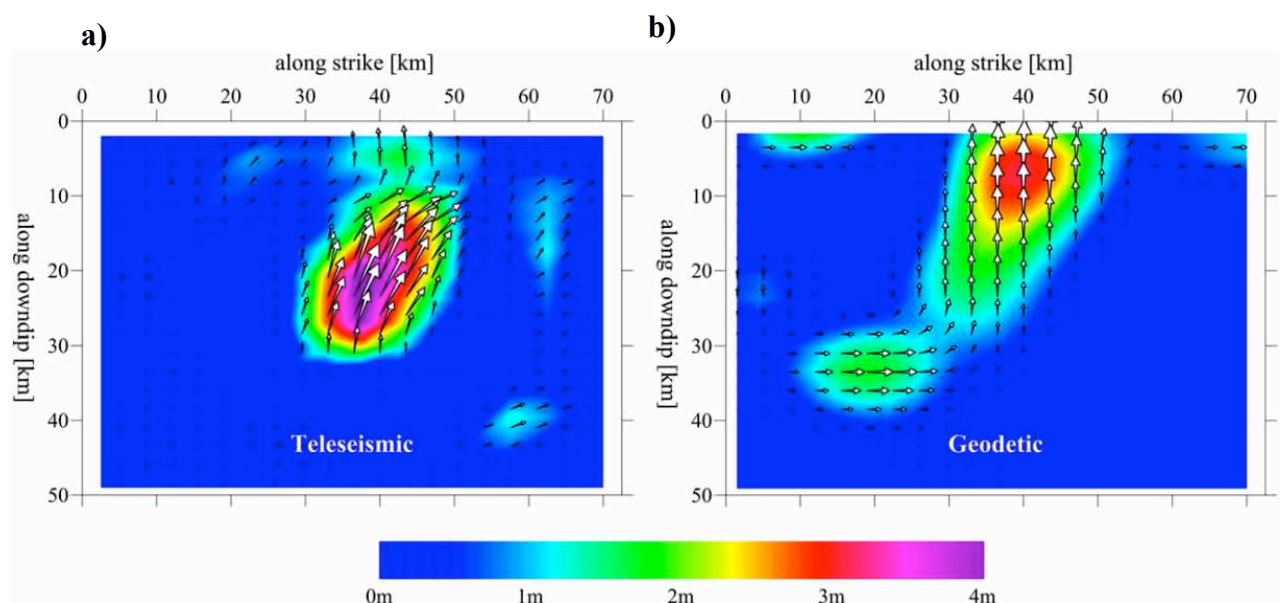


Figure 67 a) Teleseismic fault slip distribution (Hayes 2011); b) geodetic slip distribution (Altiner et al. 2013). The fault geometry of the both models are same (strike= 241° and dip= 51°). The slip amplitudes are shown in color. The motion direction of the hanging wall relative to the footwall is indicated by small arrows (from Altiner et al. 2013).

Table 6 Information on the strong ground motion stations used in the simulations of Van Earthquake (Mw 7.1) and processed ground motion values.

Station name	Station code/ operator	Lat. °N	Long. °E	Site ClassV s30 (m/s)	Repi (km)	PGA, N-S (cm/s ²)	PGA, E-W (cm/s ²)	Max PGV (cm/s)
Agri- Merkez	0401 (AFAD)	39.71	43.02	295	114	18.4	13.8	6.3
Bingol- Karliova	1206 (AFAD)	39.29	41.01	-	220	7.5	8.1	4.8
Bingol- Solhan	1211 (AFAD)	38.96	41.05	463	210	4.6	4.2	2.8
Bitlis- Merkez	1302 (AFAD)	38.47	42.16	-	117	89.5	102.3	9.2
Muş Merkez	4901 (AFAD)	38.76	41.50	315	169	10.3	6.9	2.7
Mus- Malazgirt	4902 (AFAD)	39.14	42.53	311	91	44.5	55.8	12.6
Siirt Merkez	5601 (AFAD)	37.91	41.93	-	163	9.9	9.2	5.7
Van- Muradiye	6503 (AFAD)	37.75	39.33	-	38	178.6	169.0	23.6
Batman - Merkez	7201 (AFAD)	37.87	41.15	450	224	8.3	8.6	3.9
Avagiq	5322 (ISMN)	39.33	44.16	-	89	25.8	13.7	5.7
Makoo	5323 (ISMN)	39.29	44.45	-	105	24.2	9.0	2.2
Khoy	5324 (ISMN)	38.55	44.96	-	132	12.2	5.6	2.9
Siah- Cheshmeh	5325 (ISMN)	39.06	44.39	-	88	68.9	30.3	17.8
Qareziaod din	5326 (ISMN)	38.89	45.02	-	136	13.9	8.3	3.1
Salmas1	5327 (ISMN)	38.20	44.85	-	135	21.8	7.4	5.5
Seylab	5328 (ISMN)	38.31	44.76	-	124	7.3	6.3	2.4
Qotoor	5329 (ISMN)	38.48	44.41	-	88	17.2	9.6	1.9
Pol Dasht	5330 (ISMN)	39.35	45.06	-	154	12.5	6.2	2.9
Hadi Shahr	5331 (ISMN)	38.84	45.66	-	191	10.3	7.6	2.8
Kelvans	5332 (ISMN)	38.72	44.69	-	107	9.7	6.2	1.9

Path Effects

In the stochastic method, the path effects are modeled by multiplication of geometrical spreading and an-elastic attenuation functions in the frequency domain (Boore 2003) as expressed in Equation 2.3:

$$P(R, f) = G(R) \exp[-\pi f R / Q(f) \beta] \quad (2.3)$$

Where, $G(R)$ is the distance dependent geometrical spreading function, $Q(f)$ is the frequency dependent quality factor, β is the shear-wave velocity of the crust, f is the frequency, and R is the hypocentral distance.

In order to estimate the S-wave attenuation relation (Q_s) using the spectral decay method (Anderson and Quaaas 1988; Castro and Cruz 2005; Safarshahi et al. 2013; among others) for the 23 October 2011 Van earthquake data, acceleration recordings at distances $r < 250$ km with the frequency range of 1-20 Hz are examined. The functional form for the average frequency-dependent quality factor is found as $Q_s = 90f^{0.88}$. However, as will be discussed further in this section, the synthetic results using derived attenuation model ($90f^{0.88}$) are not fitted well with the observations at high frequencies. Therefore, we have tried an alternative frequency dependent quality factor, which is based on the tomography model for Lg crustal attenuation within the Turkish Plateau (Zor et al. 2007). The alternative model suggests the average Q_0 value as ~ 100 in which the lateral variations of frequency dependent parameter are changed between $0.4 \sim 0.6$. We adopted the functional form of attenuation model as $Q(f) = 100f^{0.5}$ in our simulations (Zor et al. 2007; Akinci and Antonioli 2013). The station-based simulations are performed by using our optimum input parameters for two different quality factors and compared the bias values in terms of PGAs, PGVs, FAS and SA. $Q(f) = 90f^{0.88}$ and $Q(f) = 100f^{0.5}$ are referred to herein as Model 1 and Model 2, respectively. The performance assessment of our model has been achieved by calculating the PGA, PGV, SA residuals [\log_{10} (observed/simulated)] at each station. Figure 68 shows the residuals of PGA, PGV and SA plotted versus the R_{jb} distance for both models and FAS residuals averaged over twenty stations at each frequency from 0.5 Hz to 25 Hz, giving a measure of the mean model bias. As a result, the $Q(f)$ model is adopted as

$100f^{0.5}$ that represents the amplitude decay adequately in the given distance range. In order to have a complete definition of path effect, the distance dependent duration model (Herrmann 1985; Atkinson and Boore 1995) is defined as shown in Equation 2.4:

$$T = T_0 + 0.1R \quad (2.4)$$

where T_0 is the source duration (equal to the reciprocal of the corner frequency) and R is the hypocentral distance.

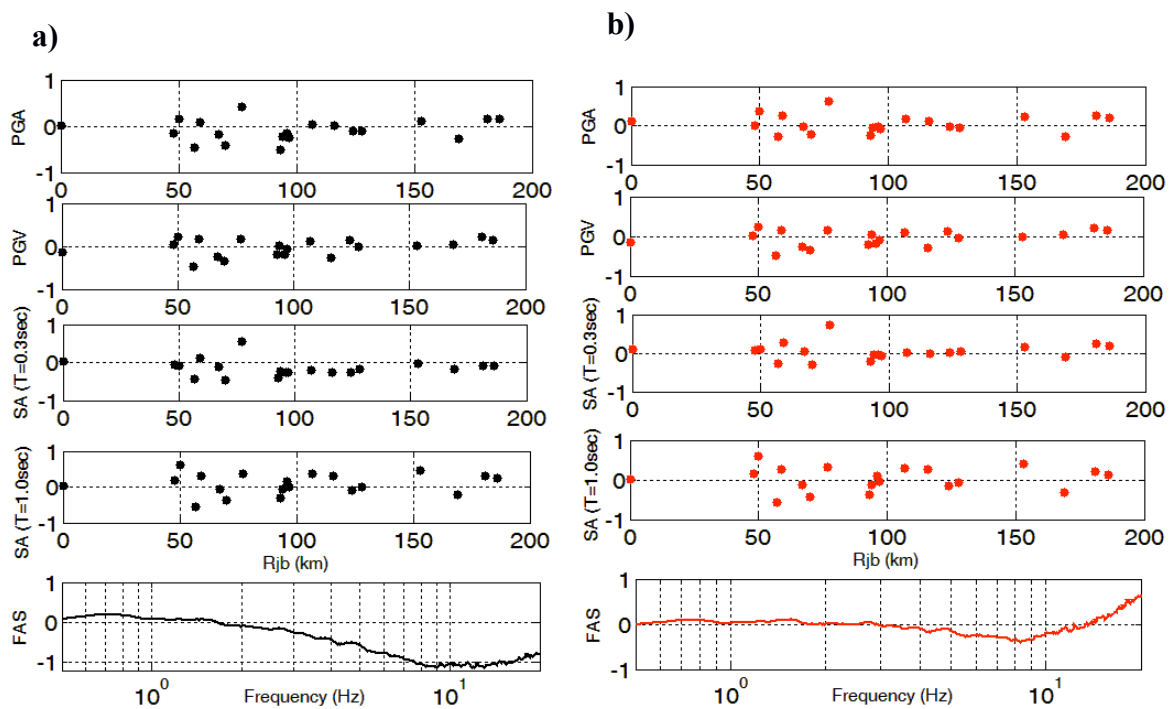


Figure 68 Comparisons of PGA, PGV and SA (at periods $T=0.3\text{sec}$ and $T=1.0\text{sec}$) residuals at each station versus R_{jb} distance, and FAS mean bias values in the frequency range of [0.5-20 Hz] for two different attenuation models **a)** $Q(f) = 90f^{0.88}$ **b)** $Q(f) = 100f^{0.5}$

Site Effects

Reliable estimation of the ground motion can be achieved by incorporating the site effects into the model properly. Site effects include the site

amplification function which mainly results from the impedance contrast between soil layers, and the diminishing function that is used to define path independent loss of energy, known as spectral decay parameter, $e^{-\pi f \kappa}$. Based on the HVSR results (Akinci and Antonioli 2013) and the available average V_{S30} parameters, we considered the AFAD stations as 'generic soil' sites. On the other hand, most of the ISMN stations do not show a distinct peak, yet spectral ratios follow a flat amplitude trend indicating the absence of site effects and that these sites can be generalized as 'rock'. Therefore, we grouped the stations into two categories as rock and soil.

Generic rock amplification factors (Boore and Joyner 1997) are adopted for the ISMN stations; whereas generic soil amplification factors are used for AFAD stations. The spectra are also attenuated by the kappa operator, which controls the path-independent high-frequency decay of the spectra (Anderson and Hough 1984). The derived vertical component kappa value of mainshock data is adopted, $\kappa_0=0.045$ which is less affected by the variation of shear wave velocity of near-surface deposits (Motazedian 2006).

The station-based simulation results and performance of our model show that the average site effect is reasonably estimated at most of the recording stations. Figure 68b shows the performance and bias values of our best model. Finite-fault parameters of our so-called best-model are listed in Table 7.

Table 7 Finite fault modeling parameters used in the simulations of 23 October 2011, Van Earthquake.

Parameters	Parameter Value
Fault orientation (Strike/Dip)	241°/51°
Depth of upper edge of	0.41

fault (km)	
Fault length and width (km)	72x46
Sub-fault dimensions (km)	4x4
Moment magnitude	7.1
Stress drop (bars)	70
Crustal shear wave velocity (km/s)	3.2
Crustal density (g/cm ³)	2.8
Rupture velocity (km/s)	0.8 x (shear wave velocity)
Attenuation, Q(f)	$Q(f) = 100f^{0.50}$
Geometric spreading	$1/R$ ($R \leq 100\text{km}$) $1/R^{0.5}$ ($R > 100\text{ km}$)
Duration Model	$T_0 + 0.01R$
Kappa	0.045
Windowing-function	Saragoni-Hart
Crustal amplification	-
Site amplification	Generic rock/soil amplification factors
Pulsing percentage	50
Slip Distribution	USGS Slip Model (Hayes 2011)

Spatially Distributed Ground Motion Intensity Measures

Spatial distributions of the simulated ground motions are obtained by using optimum model parameters in the study area. Our region of interest is divided into approximately 2500 grids with a size of 5 km x 5 km covering an area of [37.8-39.5°N, 42.0-45.0°E]. The time domain simulations carried out for each grid are utilized to generate PGA and PGV maps as shown in Figure 69. Generic soil site conditions are considered for the whole region to incorporate the site effect, thus only the variation of the source effect is taken into account for all simulations. Simulation results of Model 2 indicate ground motions reaching acceleration levels of 800 cm/sec² and velocities up to 100 cm/sec in the epicenter region for generic soil conditions. The area with accelerations larger than 400 cm/s² and velocities larger than 50 cm/s coincides with the surface projection of those parts of the fault plane where an asperity is evident. PGA and PGV

maps of the Model 2 shows similarity in terms of their distribution patterns which are extended along the southwest direction with the highest amplitudes localized around the epicenter region. PGA and PGV values of Model 1 are lower than those of Model 2, which mainly results from the location of the slip patches. Maximum accelerations and velocities are estimated in the range of 700-750 cm/sec² and 80-90 cm/sec, respectively in Model 1, and they are approximately 15% lower than those estimates of Model 2. Unlike Model 2, the area with large PGAs and PGVs of Model 1 extends toward the north-west direction, and the PGV values are more scattered than the PGAs over the fault area. PGA values of 400cm/sec² estimated in Model 2 cover a larger area as compared to Model 1. This can be associated with the patch having small slip amplitudes located at a depth of 35km. Field survey results indicate that the most of the damages occurred in Van city center and Ercis district which are located at approximately same distances of 30km from the epicenter. The building stock in the Van city center and its districts (e.g. Ercis) comprise low-to-mid rise RC buildings up to 8-10 stories with approximate fundamental periods of $\sim T=1.0$ sec; as well as the masonry and adobe structures up to 2-3 floors with periods of $\sim T=0.3$ sec. As the building stocks of Van and Ercis can be considered as similar, greater damage observed in Ercis may be attributed to hanging wall effect or possible local soil amplification in that region. It may be concluded that the spatial distributions of the ground motion intensity measures of Model 1 show better correlation with the observed damage distributions in the region in terms of level and spatial extent of the ground motions.

a)

b)

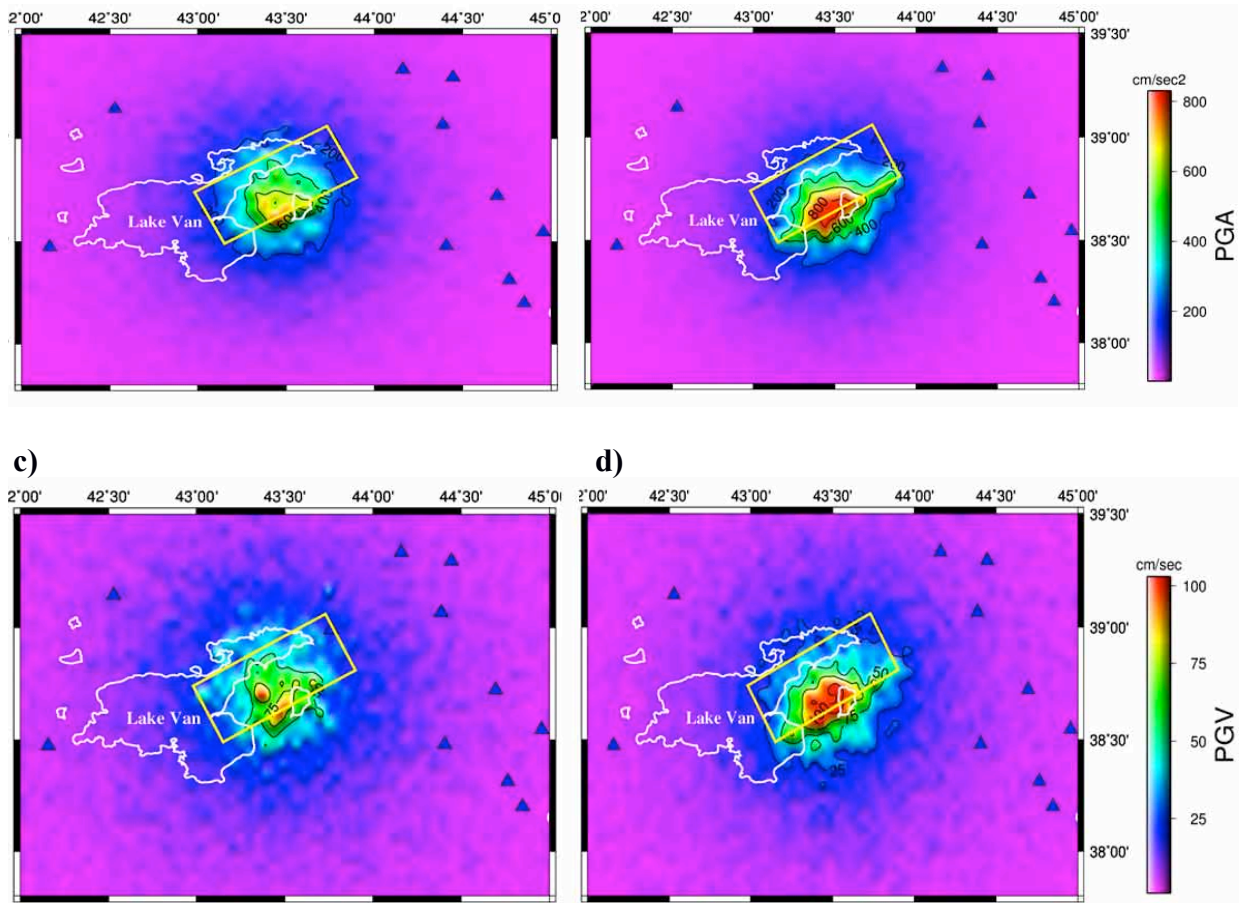


Figure 69 Spatial distribution of synthetics a) PGAs of Model 1 b) PGAs of Model 2 c) PGVs of Model 1 d) PGVs of Model 2.

Comparison with ground motion prediction equations

In order to verify the applicability of the simulation results, we compare the synthetic PGAs and PGVs of Model 1 and Model 2 with the median $\pm 1\sigma$ estimations of selected ground motion prediction equations for generic soil site with $V_{s30}=310\text{m/sec}$ and reverse fault conditions. We implement the GMPEs by Boore and Atkinson (2008), Akkar and Bommer (2010) and Akkar and Cagnan (2010). They are abbreviated as BA08, AB10, and AC10, respectively in this study. BA08 prediction equation is one of the Next Generation Attenuation (NGA) models, which is based on global ground motion database. AB10 model is developed for Europe, Middle East and the Mediterranean Region, and AC10 model is derived from the recently compiled Turkish strong-motion database. PGA and PGV levels estimated by median values of GMPEs and standard deviations of AC10

are plotted with respect to R_{jb} distances in Figure 70 together with the synthetic results and observations. Median estimations by BA08 and AB10 in fact provide an upper limit for synthetic PGAs of Model 1 where most of the synthetics fall in the region between the $\pm 1\sigma$ lines of AC10 ground motion prediction equation. Lower bound of both model estimates is similar, but upper bound of Model 2 exceeds the standard deviation limit of AC10 model at distances smaller than 5 km. Overall, our simulation results are overestimated by the median values of BA08 and AB10 ground motion prediction equations, but they show good agreement with the median $\pm 1\sigma$ estimations of AC10 model.

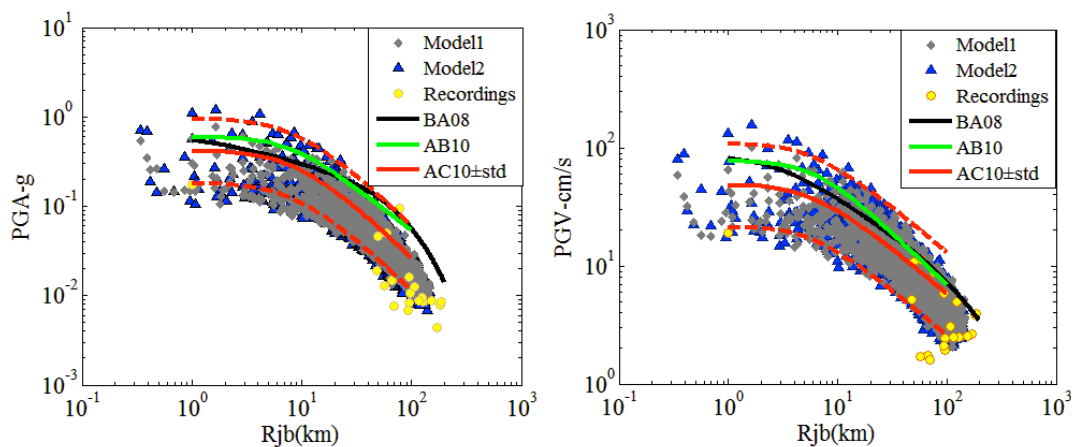


Figure 70 Comparison of Model 1 and Model 2 synthetics with GMPEs by BA08, AB10 and AC10 in terms of PGA and PGV. The GMPEs are for generic soil site conditions with $V_{s30}=310\text{m/s}$ and reverse type mechanism. Geometric mean values of recordings are also shown in the plots.

Conclusions

The stochastic finite fault method is a practical tool to understand the ground motion characteristics and distributions particularly in the near fault regions where real recordings are insufficient. This method requires region-specific input parameters in order to reproduce the realistic earthquake ground motions in the frequency range of engineering interest. In the present study, stochastic ground motion simulations of the 23 October 2011 Van Eastern Turkey earthquake (Mw 7.1) have been performed by using finite fault approach. It is noted that the modeling of the main input parameters of source, path, and site effects are crucial to

obtain reliable simulation results. The calibration of the input parameters is achieved by using misfit functions between peak ground motion and spectral values of the observations and synthetics. In the context of constraining path effect, the frequency dependent Q -model is calculated from the real recordings of the mainshock. The results indicate that the derived average attenuation model $Q(f) = 90f^{0.88}$ is compatible with the previous studies which have been proposed for the Eastern Anatolian and Iranian Plateau. However, regional attenuation model of $Q(f) = 100f^{0.5}$ (Zor et al. 2007) is adopted in our simulations as it shows a more reasonable match at the high frequency part of observed spectra. It should be emphasized that further detailed investigations on region-specific attenuation model may better represent heterogeneous characteristics of the regional crustal structure. Site effects are incorporated into our model using generic amplification factors on the basis of available soil information. Spectral kappa parameter is calculated from the mainshock data.

Our so called best model performed well with satisfactory mean bias values in the frequency range of 0.5-20 Hz. Moreover, peak ground motion and spectral values show no significant residual trend with distance. Despite the limitation of the method for incorporating the directivity effect and inadequate representation of the soil conditions at the individual stations, distributions of residuals show good agreement between synthetics and observations. The validated optimum parameters are then used to estimate ground motion intensity measures over the area of interest that gives an insight into the spatial distribution of the peak ground motions and spectral values particularly in the near fault region. Source-induced variability of the ground motion is examined by adopting two different slip models on regional extent. It is observed that the location of asperity has a significant effect on the ground motion amplitudes and shaking distribution patterns over the fault area.

The applicability of synthetic results has been verified by comparing the

synthetic PGAs and PGVs of both source models with the median $\pm 1\sigma$ values estimated by ground motion prediction equations of Boore and Atkinson (2008), Akkar and Bommer (2010) and Akkar and Cagnan (2010). The results indicate that synthetics are overestimated by the median values of BA08 and AB10 ground motion prediction equations, whereas they show good agreement with the median $\pm 1\sigma$ values of the AC10 model which is derived from Turkish strong motion database. Simulated results are also compatible with the observed damage distributions in the region. We have observed that the spatial distribution of synthetics using the slip model of Hayes (2011) shows better correlation with the observed damage distribution in terms of level and spatial extent of the ground motions.

Stochastic Finite Fault Ground motion Simulation of the 9 November 2011 ($M_w=5.6$) Van-Edremit Earthquake

Earthquake Information and Input Model Parameters

The $M_w=5.6$ earthquake that occurred on 9 November 2011 in the province of Van, 17 days after the first one, is used as another case study to perform stochastic simulations in our modeling region. This earthquake caused heavy damage in the city of Van and in the Edremit sub-province, which is located 16 km southwest of Van city center. Although the earthquake is considered to be a moderate magnitude event, high ground motion amplitudes within 20 km of the epicenter are recorded. Hypocenter locations, depth and magnitude estimations of the earthquake are reported by various institutions as shown in Table 8. Focal mechanisms assessed by moment tensor solutions indicate that this earthquake had a strike-slip mechanism and ruptured along the NNW-SSE direction. Following the first Van earthquake on 23 October 2011, Department of Earthquake Engineering of Bogazici University's Kandilli Observatory and Earthquake Research Institute (DEE-KOERI, 2011b) deployed eight strong motion stations to monitor the regional aftershock activity. Four of the

stations were installed in the city of Van. Remaining four was deployed in the town of Ercis, which had suffered the most damage and loss of life in the first event. One station in each town was located on a stiff soil or a rock site to be used as the reference station. Three stations were installed in the flat urban area (DEE-KOERI, 2011b). The Van-Edremit earthquake of 9 November 2011 was registered by the DEE-KOERI network, as well as by the AFAD stations. Altogether six stations operated by DEE-KOERI and five stations operated by AFAD recorded the Van-Edremit earthquake and are thus used in its simulation. No detailed site information is available for the DEE-KOERI stations. We classify them as rock or soil sites, based on regional geology, whether they are located on alluvial deposits (soil sites) or travertine deposits (stiff/rock sites). The maximum amplitudes are recorded at VNKEA Station, where processed PGAs are 262cm/s^2 and 200cm/s^2 for the E-W and N-S components respectively. PGVs are obtained as 35.0 cm/s and 21.8 cm/s in E-W and N-S directions, respectively. Information on station properties and processed data are given in Table 9. The stations are indicated in Figure 74.

Table 8. Hypocenter locations, depth and magnitude estimations of various institutions for the 9 November 2011 Van-Edremit ($M_w=5.6$) Earthquake

Date/Time	2011/11/0 9 21:23:21 Local	2011/11/0 9 19:23:33 GMT	2011/11/0 9 19:23:33 GMT	2011/11/0 9 19:23:33 GMT	2011/11/0 9 19:23:33 GMT
Institutions	KOERI ¹	USGS ²	EMSC ³	GFZ ⁴	AFAD ⁵
Latitude	39.429 N	38.429 N	38.42 N	38.41N	38.45 N
Longitude	43.234 E	43.229 E	43.29 E	43.35 E	43.26 E
Depth	5 km	5 km	6 km	23 km	8 km
Magnitude	5.6 (M_L)	5.6 (M_w)	5.6 (M_w)	5.6 (M_w)	5.6 (M_L)

¹ Kandilli Observatory and Earthquake Research Institute.

² United States Geological Survey.

³ European-Mediterranean Seismological Centre.

⁴ German Research Centre for Geosciences.

⁵ Turkish Prime Ministry – Disaster and Emergency Management Presidency.

Table 9. Information on the strong ground motion stations used in the simulation of 9 November 2011 Van-Edremit Earthquake (Mw=5.6) and processed peak values.

Station	Latitude °N	Longitude °E	Site Class Vs30 m/s	Rjb km	PGA E-W cm/s ²	PGA N-S cm/s ²	PGV E-W cm/s	PGV N-S cm/s
Bitlis(1302)	38.47	42.15	-	103.7	5.9	3.9	0.4	0.4
Muradiye(6503)	38.99	43.76	293	67.1	9.5	13.4	1.3	1.1
Malazgirt(4902)	39.14	42.53	311	102.4	3.5	3.3	0.9	0.7
Merkez (6501)	38.50	43.40	363	7.1	244	144.3	27.3	17.4
Edremit (6510)	38.41	43.26	rock site	5.2	102	65.4	13.4	14.7
VNS	38.55	43.32	rock site	8.8	95	81.4	10.6	13.9
VNKEA	38.50	43.39	soil site	4.8	262	200	35.0	21.8
ERSFB	38.99	43.45	stiff soil	58.4	9.9	6.9	0.9	0.5
ETR	39.01	43.35	soil site	59.5	12.5	16.2	1.8	1.7
ERKRY	39.03	43.35	soil site	62.1	11.6	11.9	1.9	1.4
ERISF	39.02	43.34	soil site	60.4	11.0	11.2	1.8	1.6

We assess the fault dimensions by Leonard (2010) and adopt a fault geometry that is 9 km long and 6 km wide. Several institutes (KOERI, USGS, EMSC, GFZ, AFAD) provide various epicenter locations. KOERI, USGS and EMSC report epicenters located approximately 3, 5 and 13km to the northwest of Edremit station; whereas AFAD centered it 3km northeast of the same station. According to the GFZ solution, the epicenter is located 9 km to the east of the Edremit Station. To fix the location of the epicenter for our study, we perform simulations by using the solutions of each institute and compare the results with the near-fault station recordings. Among all trials, GFZ epicenter provides a better match

of synthetics and observations at near fault stations. For all epicenters except the one by GFZ, we overestimate ground motions at Edremit, VNS and Merkez stations. Hypocentral depth estimates of various institutions varied between 5km to 23km. Although GFZ reported the hypocentral depth at 23km, we assume that the earthquake occurred at a shallow depth (between 5km to 8km) as reported by other institutes. In our model, we locate the hypocenter at the south end of the fault, 3 km down the dip. The hypocenter location is constrained on the fault plane. We test two different upper edge of the fault depths, 2 km and 5 km. The strike is 180° , dip is 90° , and the average rake is 14° . Sub-fault dimensions are chosen as 1 km x 1 km. A random slip distribution on fault plane, assigned by the EXSIM program, is assumed in all simulations.

The input parameters for the simulation of the Van-Edremit Earthquake are specified on the basis of the finite-fault parameters of 23 October 2011, Van Earthquake discussed in previous sections. Similar path effect and site amplification factors are assumed. We test plausible scenarios with varying rupture speed, stress drop and fault depths to obtain the best model for this particular earthquake. The adopted parameters for rupture speed, stress drop and top depth of fault are taken as 2.24 km/s, 70bars and 2.0km, respectively.

Station-based Simulations

We present the N-S and E-W accelerations and average (geometric mean) FAS between 1 Hz-25 Hz of 8 out of 11 recording stations and their simulated counterparts. The comparison of near fault stations and distant stations are shown in Figure 71 and Figure 72, respectively. Among the near fault stations, Edremit, Merkez, VNS and VNKEA, synthetic PGAs representing stations Merkez and VNKEA underestimate the observations as shown in Figure 71. These stations located in the rupture direction of the fault plane within the epicentral distances of about 5 km have similar waveforms.

Significant pulses in the velocity time histories and high amplitudes in the

long-period portion of the acceleration spectra of these stations imply the forward directivity effects (DEE-KOERI, 2011a), which cannot be fully developed by the implemented model. The overestimation in the Edremit and VNS stations might be ascribed to soil amplification factors, because these stations are located on stiff rock. It is known that inadequate representation of the soil amplification factors affect the ground motion levels both in time and frequency domain. A comparison of selected four distant stations which are located at about 60 km are presented in Figure 72. The peak ground motion values of synthetics and the recordings are in agreement with each other. Yet the duration of the synthetics are significantly underestimated and FAS are slightly overestimated in the high frequency part. This can probably be attributed to the effect of basin generated surface waves judged from the velocities and displacements of the Ercis station records (DEE-KOERI, 2011a).

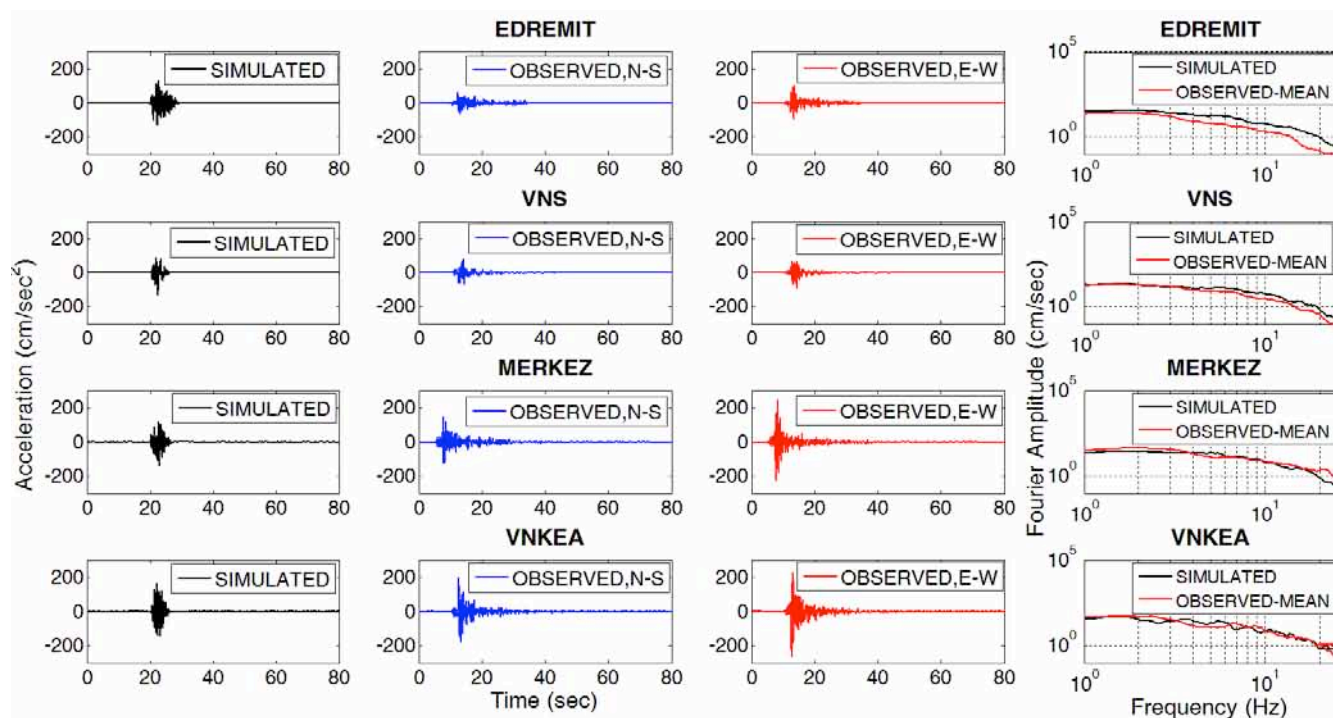


Figure 71 Comparison of acceleration time histories and FAS of synthetics with the near field station recordings of 9 November 2011 Van-Edremit (Mw=5.6) Earthquake.

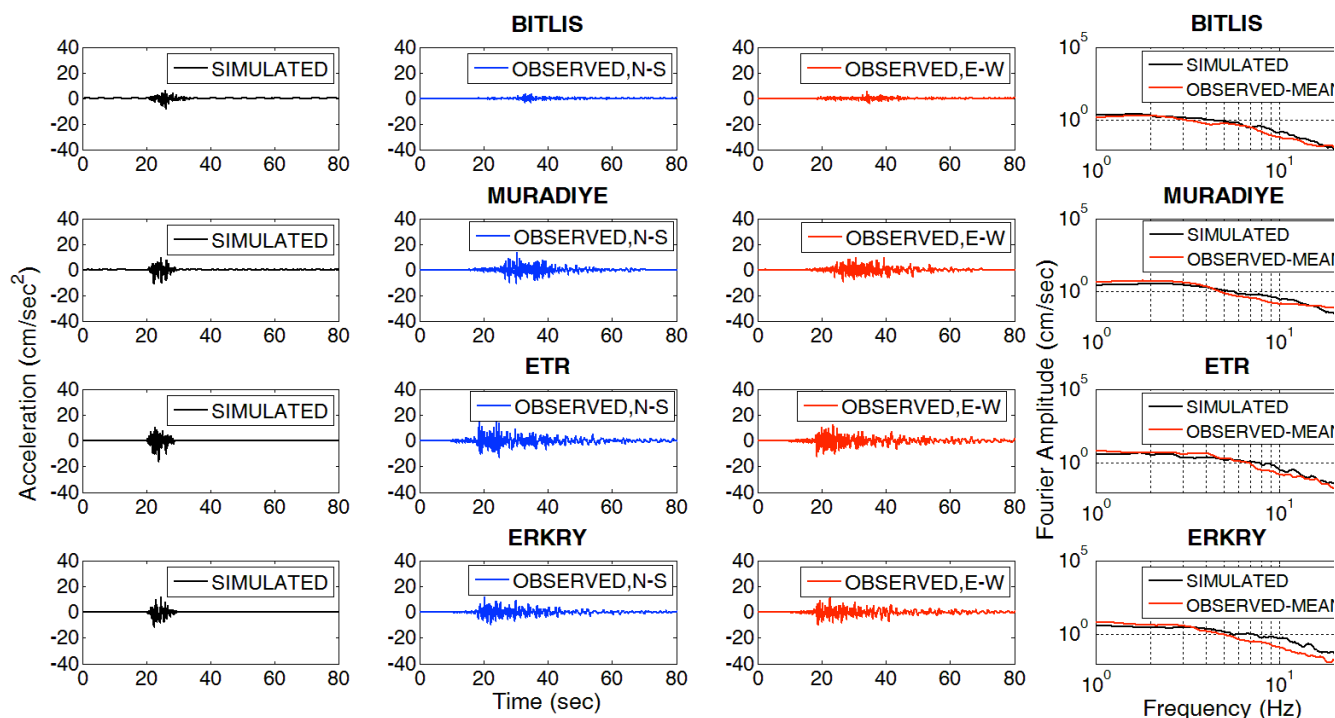


Figure 72 Comparison of acceleration time histories and Fourier amplitude spectra of synthetics with the far-field station recordings of 9 November 2012 Van-Edremit (Mw=5.6) Earthquake

Response spectra of simulated and average (geometric mean) observed ground motions in the frequency band 1.0–25 Hz are compared in Figure 73. The trend and level of the synthetics are reasonably matched with the recorded values at most of the stations. Merkez and VNKEA stations (close to each other) located along the forward rupture direction have maximum SA amplitudes (approximately 500 cm/s^2) with a strong peak at 2.5 Hz. We observe that general shape of the synthetic response spectrum at VNS station is in close agreement with the recording except the clear overestimation above 5 Hz. This may be the result of generic soil site amplification factors that we assumed for the stiff soil/rock ground motion stations as well. There exists large discrepancies between simulated and observed spectra at Edremit Station, which is located about 7 km west of the rupture initiation point. The response spectrum of this station has a fall-off after its peak value at 2 Hz and simulated spectra overestimate the values in the whole frequency range.

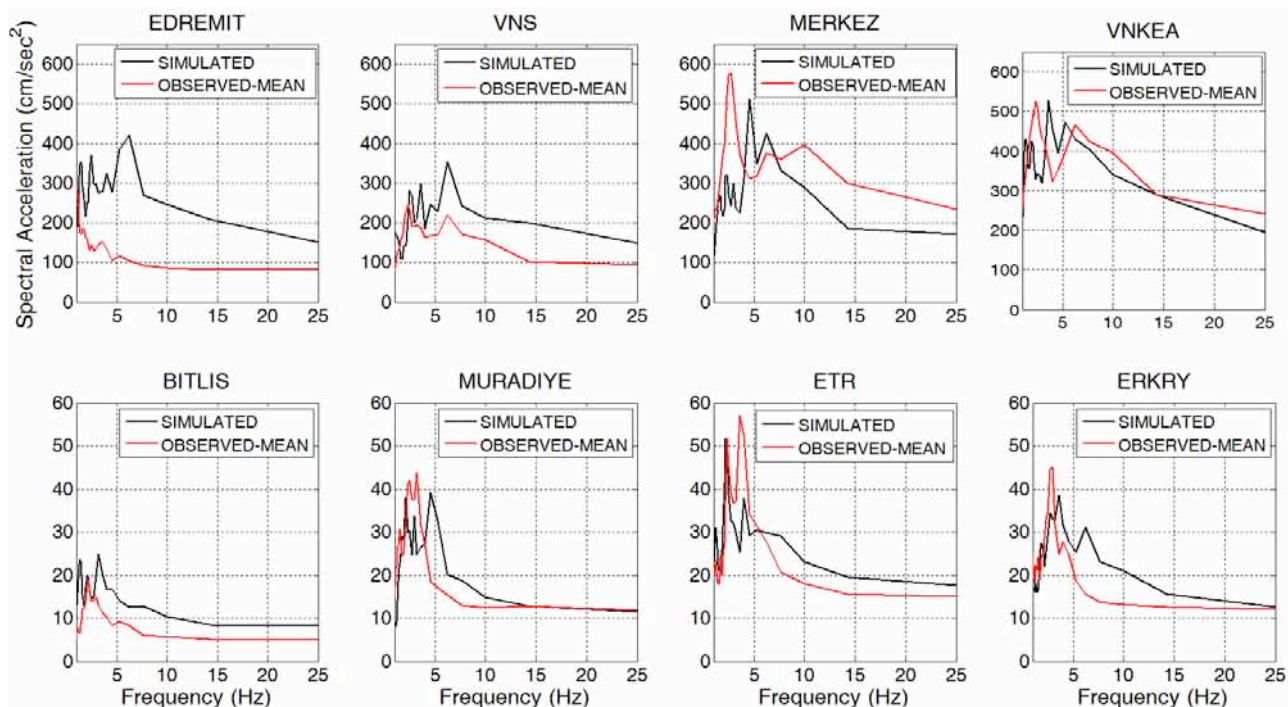


Figure 73 Comparison of simulated and observed average (geometric mean of two horizontal components) response spectra at eight selected stations that recorded the 9 November 2012 Van-Edremit (Mw=5.6) Earthquake.

Spatial Distributions of Synthetics

The spatial distribution of PGAs and PGVs are obtained by performing grid-based simulations in a region of 170km (East-West) and 130 km (North-South) using calibrated input parameters. The area covers approximately 8200 phantom stations with a grid size of 2 km x 2 km. The spatial distributions of PGA and PGV and station locations are shown in Figure 74. Simulation results indicate ground motions reaching acceleration levels of 300 cm/s^2 and velocities up to 30 cm/s for generic soil conditions. The highest ground motion levels are reached in the vicinity of the fault plane and in an area within the 30 km of the epicentral region where the source dominates. The shape of this region is not symmetrical around the fault. It widens slightly towards N-E. Verification of the simulation results are achieved by comparing the synthetic PGAs and PGVs of our model with the median $\pm 1\sigma$ values estimated by the GMPEs of Boore and Atkinson (2008), Campbell and Bozorgnia (2008) and Akkar and Bommer (2010). In addition, we compare our analysis results with the peak ground motions estimated by the ShakeMap interpolation scheme. Peak ground motions

are shown as functions of closest distance to the rupture surface in Figure 75. The PGA level of the regional synthetics shows good agreement with the observations. As with the observed PGAs, they fall between the median- 1σ line of the AkB(10) GMPE and are generally below the median of all GMPEs. We predict that the peak values estimated by the ShakeMap approach are not well calibrated for this earthquake. The comparison of ShakeMap results with GMPEs, recorded data and our simulations are shown in Figure 75.

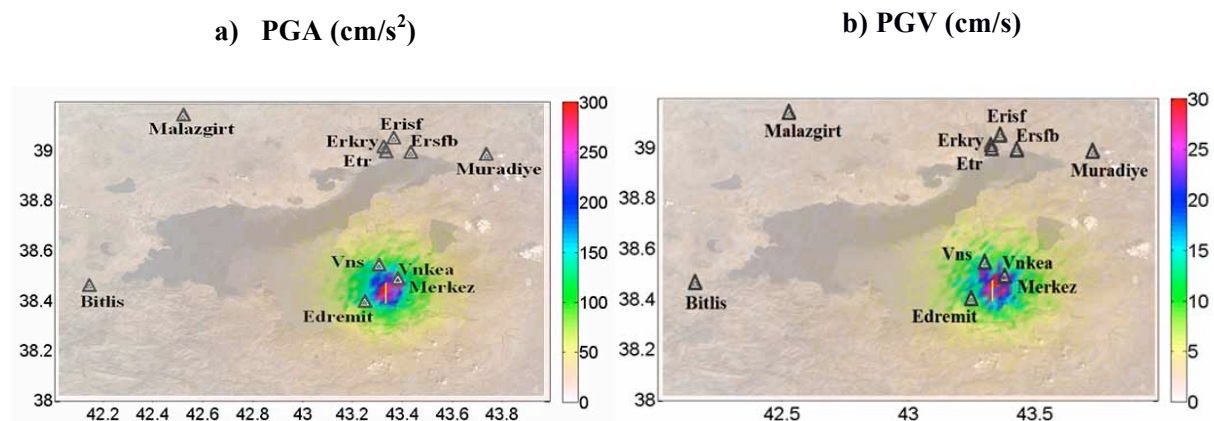


Figure 74 Spatial distribution of synthetic a) PGAs and b) PGVs of 9 November 2011 Van-Edremit ($M_w=5.6$) earthquake.

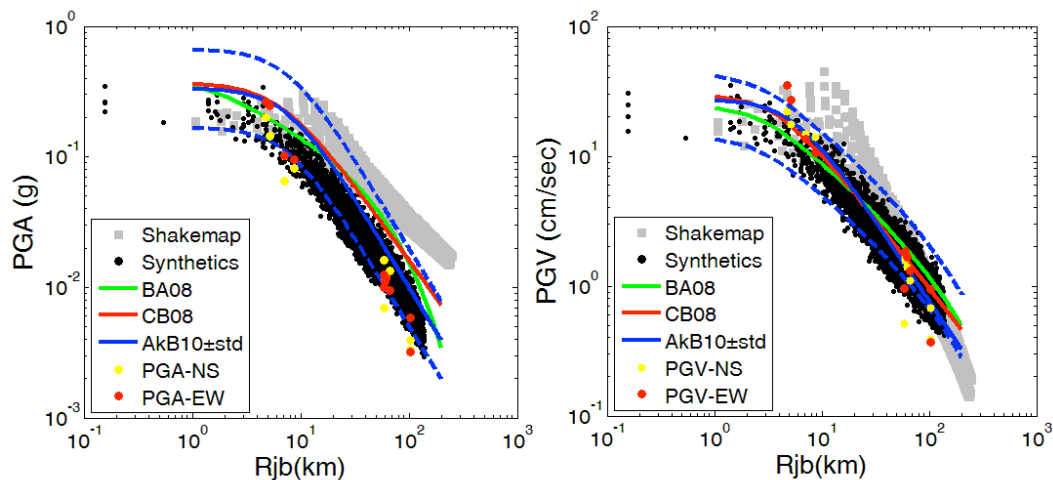


Figure 75 Comparison of the synthetics and observed recordings with GMPEs by BA08, CB08, AkB10 in terms of PGA and PGV. ShakeMap data of the Van-Edremit ($M_w=5.6$) earthquake by USGS (2011) are also used in the comparisons. The GMPEs are for generic soil site conditions with $V_{s30}=310\text{m/s}$ and strike-slip mechanism.

2.5.7 Low and High Frequency Ground motion Simulation of the 1999 Kocaeli earthquake (KOERI)

Introduction

With the aim of obtaining a low and high frequency wave field generated by the 1999 M_w 7.4 Kocaeli earthquake both long period deterministic and high frequency stochastic simulations have been carried out. Kinematic simulations studied the long period part of the frequency band with Finite Difference Method, whereas the high frequency part was simulated with stochastic finite fault modeling based on a dynamic corner frequency approach.

FINITE DIFFERENCE KINEMATIC SIMULATION OF THE 1999 KOCAELI EARTHQUAKE

Methodology

The major steps of the study were:

- Create a 3D velocity model of the Kocaeli region.
- Validate the model with recent small earthquakes in the Marmara Sea.
- Simulate the 1999 Kocaeli earthquake with various existing source models.
- Study the effects of source parameters on resulting ground motion distributions.

3D velocity model

The previous version of the 3D velocity model of the Marmara Sea and Kocaeli regions that was developed after the 1999 earthquake has been updated with recent data. Some examples of the profiles that were used in this study are presented in Figure 76 and Figure 77. The 3D velocity model of Eastern Marmara region is given in Figure 78. Two aftershocks of the 1999 earthquake (23.8.1999 $M_{3.71}$ in the Cınarcık Basin and 24.8.1999 $M_{3.43}$ in the Izmit Bay) as well as a more recent event (20.1.2011 $M_{4.3}$ on the southern coast of Izmit Bay) have been used for

the validation of the velocity model. Some comparisons of the simulated and observed time histories are presented in Figure 79.

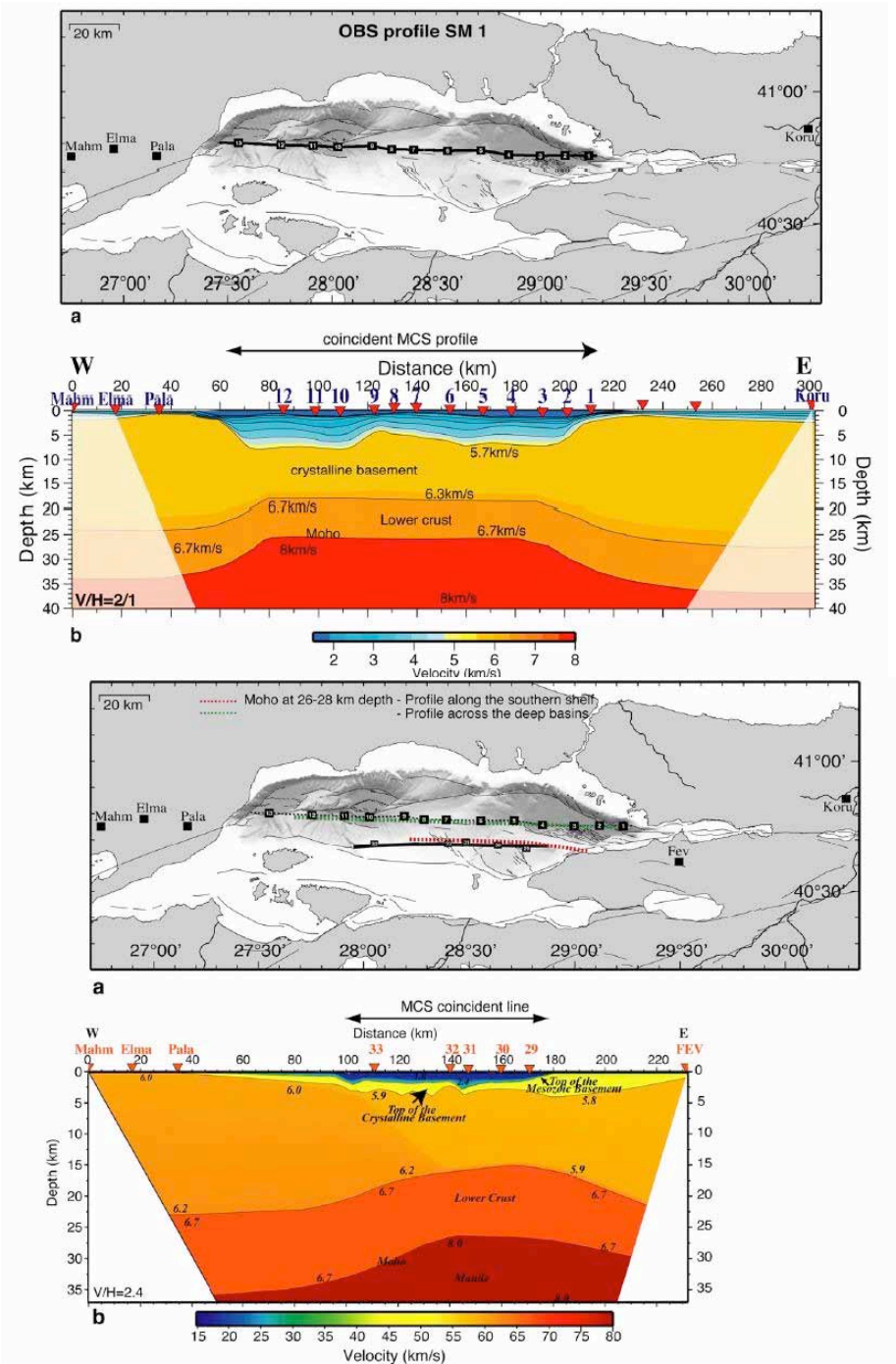


Figure 76. Sample profiles of Marmara Sea obtained from Becel et al. (2009)

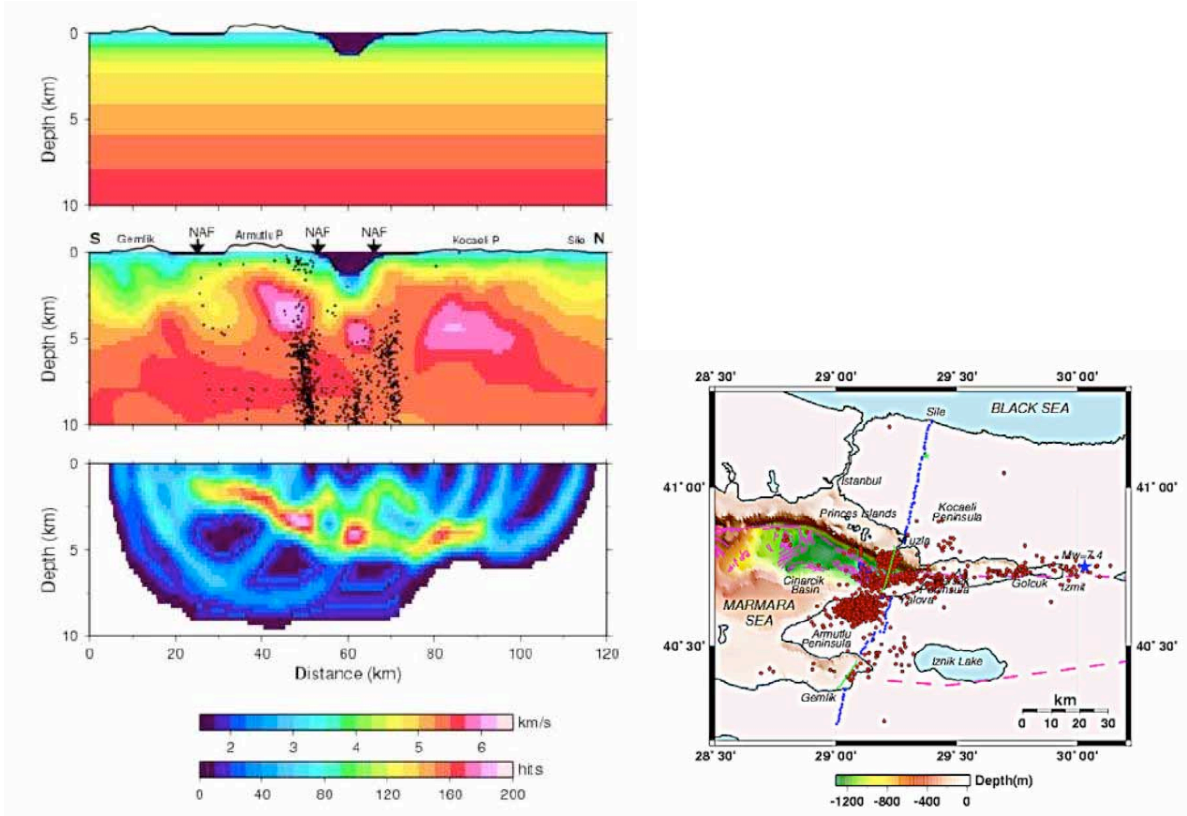


Figure 77. Sample profiles of Eastern Marmara obtained from Karabulut et al. (2002)

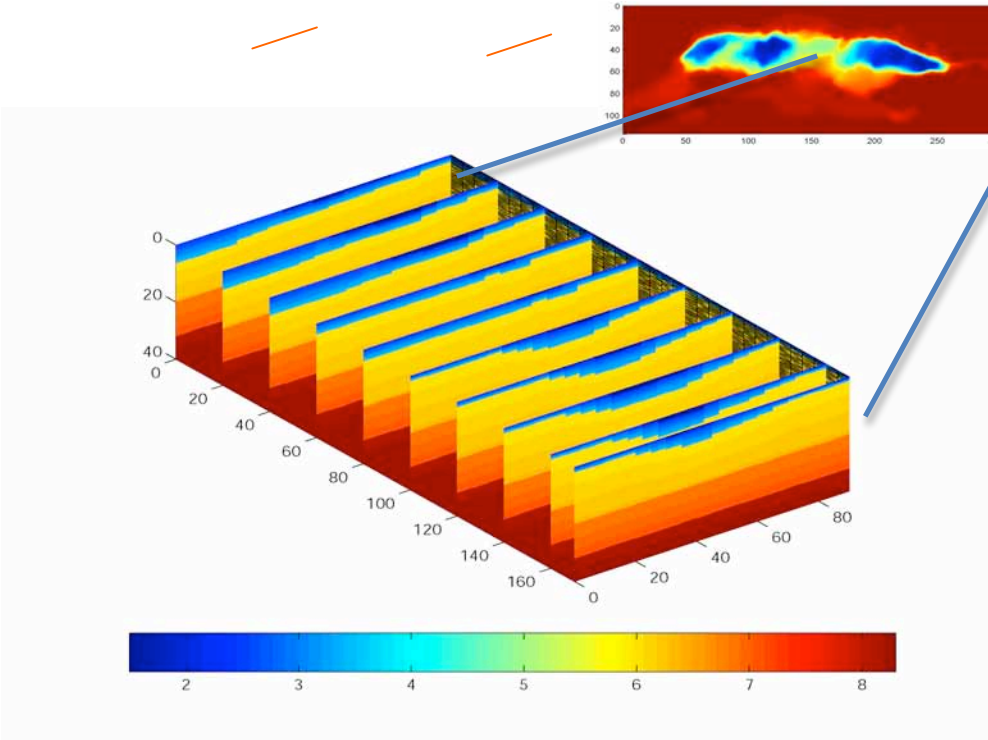


Figure 78. 3D velocity model of Eastern Marmara Region

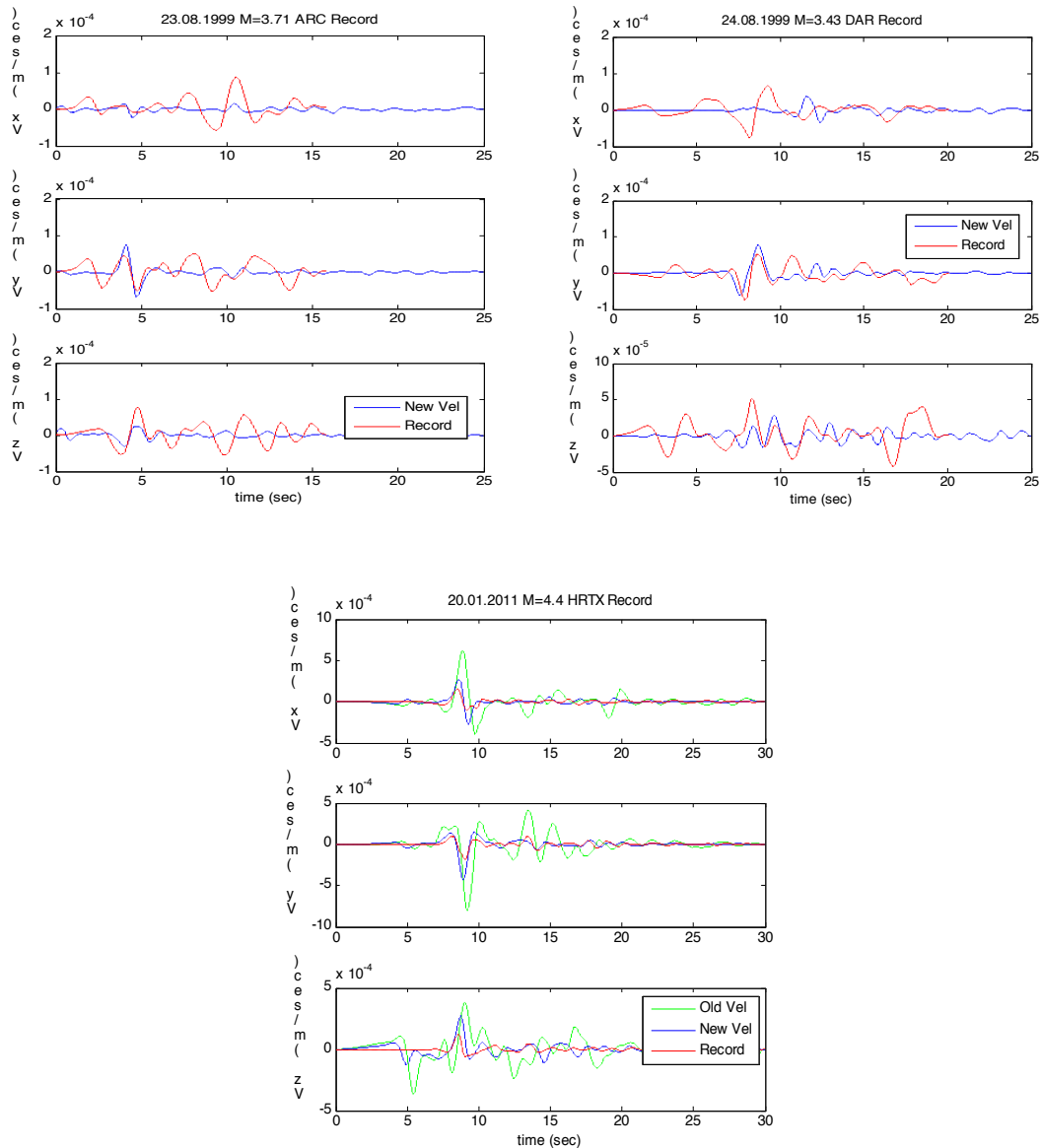


Figure79. Comparisons for the calibration events

Simulation of the main event

Four rupture models of the 1999 Kocaeli main shock are used in the simulations. The models are: Yagi and Kikuchi (2000), Segikuchi and Iwata (2002), Delouis et al. (2002) and Bouchon et al. (2002). The comparison of observed and simulated time histories at the IZMIT (close to the epicenter) and ATS (west of Istanbul) stations are presented in Figure 80 and Figure 81 respectively.

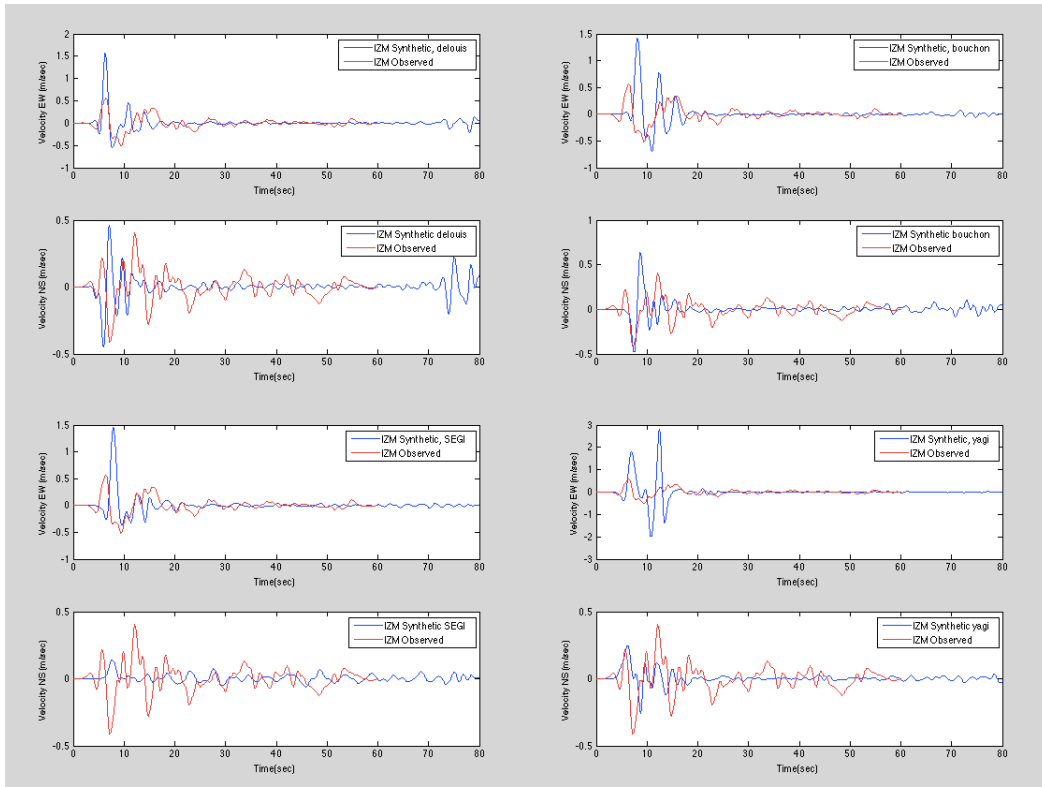


Figure 80. Simulated and observed velocities in the IZMIT station with the four source models

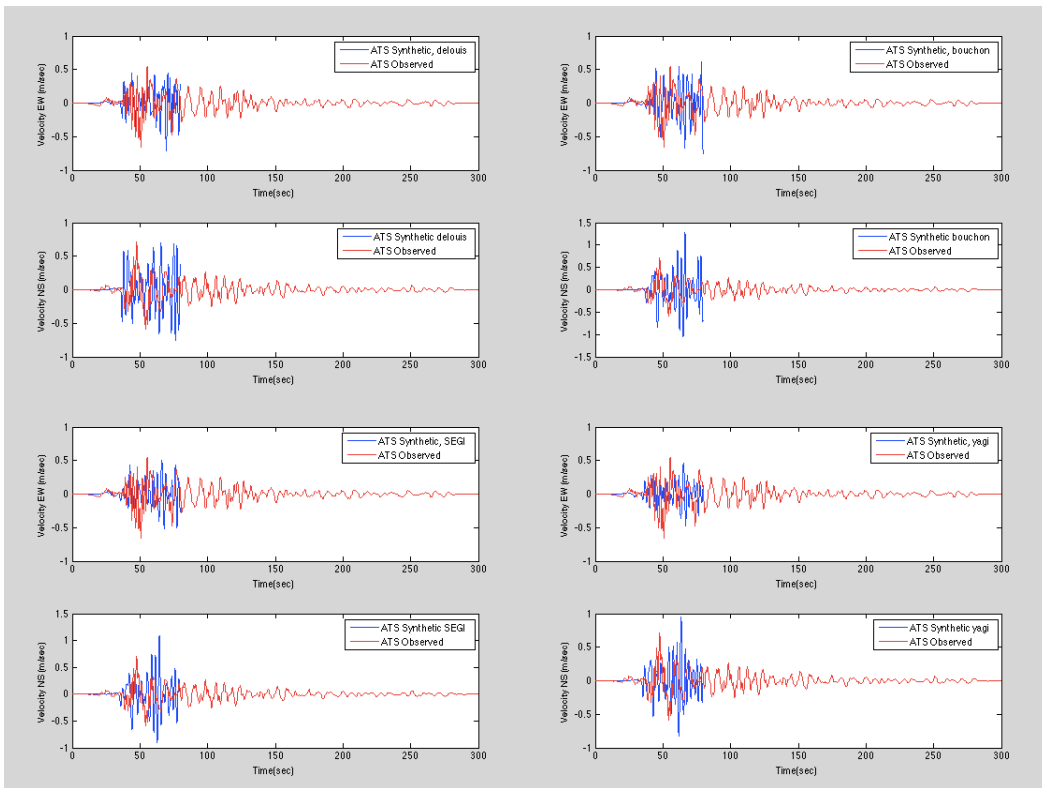


Figure 81. Simulated and observed velocities in the ATS station with the four source models

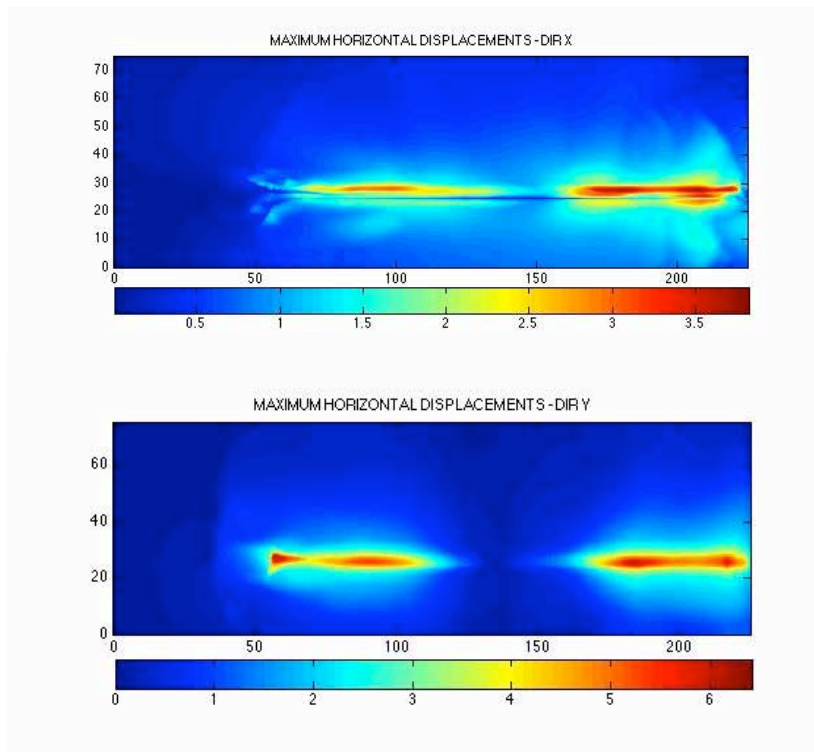


Figure 82. Fault parallel and fault normal peak displacements obtained for the model of Bouchon et al. (2002)

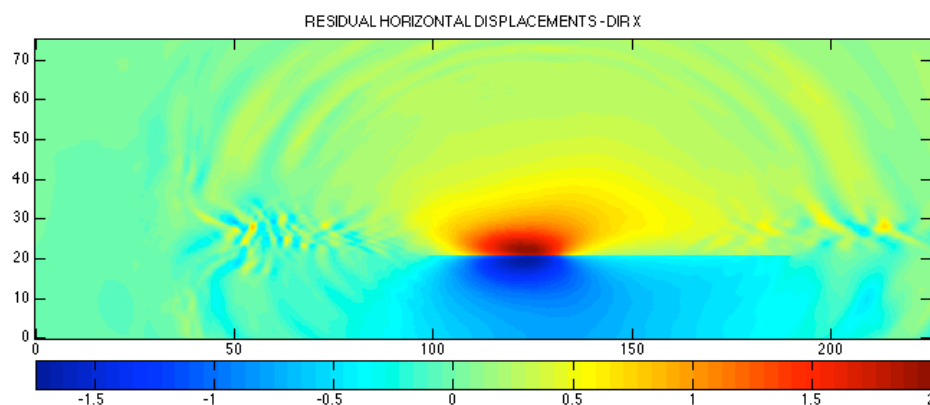


Figure 83. Permanent displacements in the fault parallel direction obtained for the model of Yagi and Kikuchi (2000)

STOCHASTIC MODELING OF THE 1999 KOCAELI EARTHQUAKE

Simulation Methodology and Modeling Parameters

Stochastic finite fault modeling based on a dynamic corner frequency approach is used to generate synthetic records for a specified region by defining the input parameters of the seismic source, wave propagation

Where, n is the number of stations used in simulations and $A_i(f)$ is the acceleration spectrum of the i^{th} station. This model misfit function is minimized in the frequency range of 0.25–25 Hz. Using a stress drop of 70 bars and a shear wave velocity of 3.4 km/sec in our model minimizes the overall modal bias. By using the calibrated model parameters, we obtain simulated acceleration time histories and Fourier Amplitude Spectra for all recording stations. Figure 85 and Figure 86 show comparisons of synthetic ground motions with North-South and East-West components of observed ground motions at selected stations for rock and soil sites respectively. Smoothed Fourier amplitude spectra of simulated and average observed ground motions are also compared in the same figures. A good agreement between the simulated and observed ground motions is obtained both in time and frequency domains. This suggests that calibrated model parameters can be used in the regional ground motion simulation of the selected regional area for 1999 Kocaeli (Mw 7.4) earthquake. Calibrated finite fault parameters are listed in Table 10.

Table 10. Finite-fault parameters used in the simulations of 1999 Kocaeli Earthquake.

Parameters	Parameter Value
Fault orientation (Strike/Dip)	90°/90°
Depth of upper edge of fault (km)	0
Fault length and width (km)	110x20
Sub-fault dimensions (km)	5x5
Moment magnitude	7.4
Stress drop (bars)	70
Crustal shear wave velocity (km/sec)	3.4
Crustal density (g/cm ³)	3.0
Rupture velocity (km/sec)	0.8 x (shear wave velocity)
Attenuation, Q(f)	Q(f)=180f ^{0.45}
	1/R (R ≤ 30km)
	1/R ^{0.4} (30 < R < 60km)
Geometric spreading	1/R ^{0.6} (60 ≤ R < 90km)
	1/R ^{0.8} (90 ≤ R < 100km)
	1/R ^{0.5} (R ≥ 100 km)
Duration Model	T ₀ +0.07R
Kappa	0.04(average rock)
	0.06 (NEHRP D -site class)
Windowing -function	Saragoni -Hart
Crustal amplification	Average rock(for soil sites)
Site amplification	NEHRP D (Boore and Joyner, 1997)
Pulsing percentage	50
Slip Distribution	Bouchon, 2002

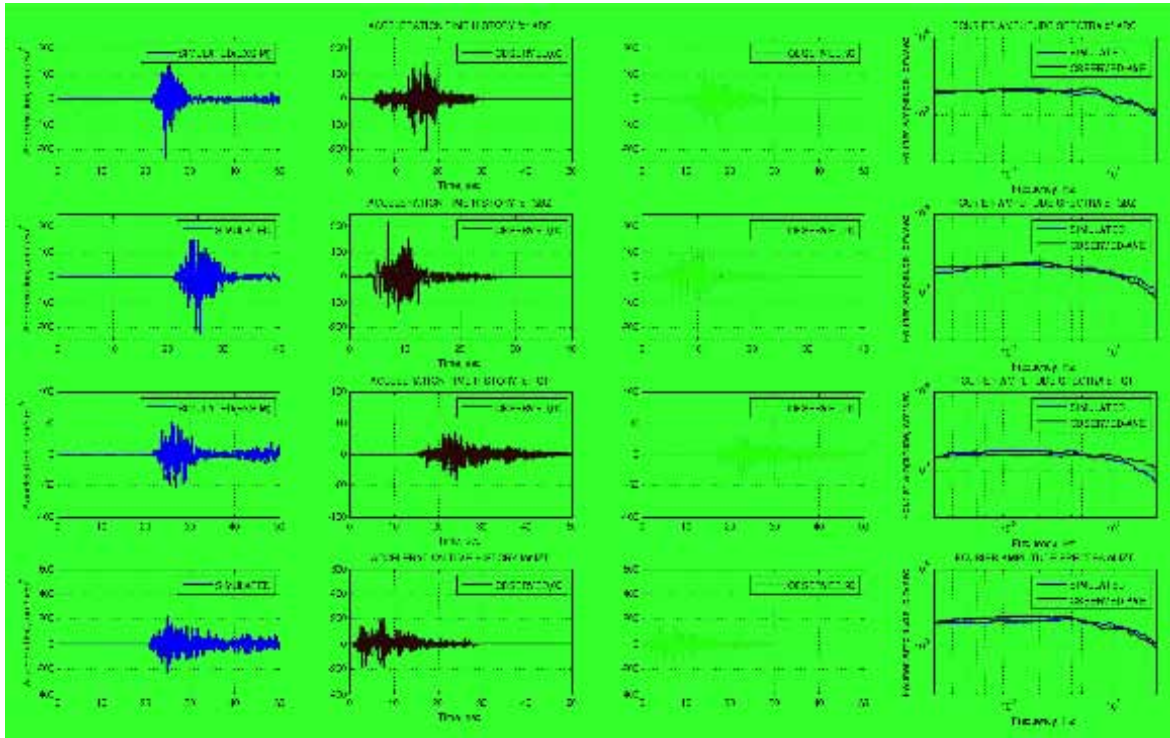


Figure 85. Comparisons of waveforms and Fourier spectra of synthetics with those of selected rock stations for 1999, Kocaeli Earthquake.

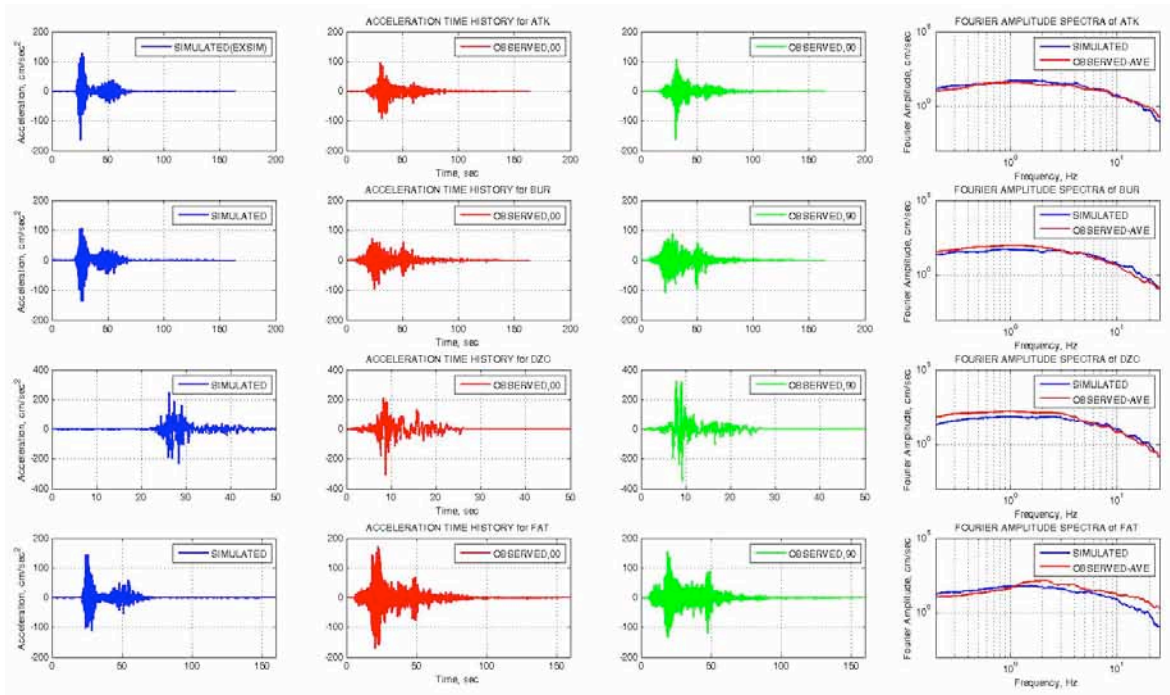


Figure 86. Comparisons of waveforms and Fourier spectra of synthetics with those of selected soil stations for 1999, Kocaeli Earthquake.

Comparison of grid-based synthetics with ground motion prediction equations

Validated model parameters were used in order to obtain spatial distribution of the synthetics in our study area. PGAs and PGVs of station recordings and simulation results are compared with the median $\pm 1\sigma$ of the Next Generation Attenuation (NGA) Models for generic rock site conditions, represented with a $V_{s30}=620\text{m/s}$ in Figure 87. We implemented the ground motion prediction equations of Abrahamson and Silva (2008), Boore and Atkinson (2008), Campbell and Bozorgnia (2008), and Chiou and Youngs (2008); these models are abbreviated as AS08, BA08, CB08, and CY08, respectively. We see that the simulated PGAs are in good agreement with the median estimation of the GMPEs, whereas synthetic PGVs are underestimated by the attenuation models for all distance range. It is noted that the simulated PGAs attenuated faster at large distances than the simulated PGVs.

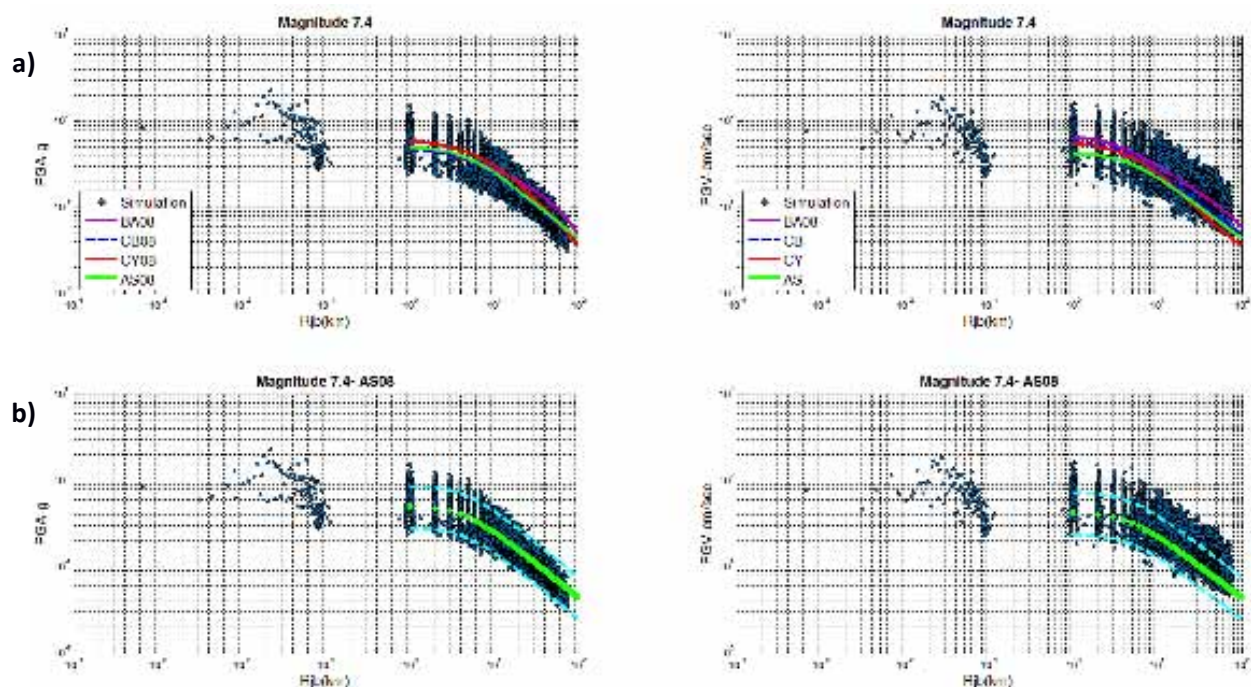


Figure 87. a) Comparison of synthetics with median estimations of GMPEs by BA08, CB08, CY08, AS08 in terms of PGAs and PGVs. b) Comparison of synthetics with median $\pm 1\sigma$ estimations of GMPE by AS08.

3. Scattering and Locale Site Effects

3.1 Spatial Variability of the Ground motion and its effect on the Structural Behavior based on NERA Argostoli experiment (ISTerre team)

The term “spatial variation of seismic ground motions” denotes the differences in the amplitude, phase and frequency content of seismic motions recorded over extended areas but even within the dimensions of a structure. At few tens of meter scale, such spatial variability may indeed have important effect on the response of extended lifelines such as bridges, pipelines, communication systems, dams because of the spatially variable contributions applied at different supports of the structure. The spatial variability of the ground motion can be mainly divided in three categories: the spatial coherency (difference in amplitude and phase at local scale), the spatial correlation (difference in amplitude at local and regional scale) and spatial variation (variation of amplitude at large scale). Spatial coherency models that include both the change in phase and amplitude have been investigated extensively by Zerva (2009) according to who the variation of ground motion depends on frequency and inter-station distance; therefore the coherence function is widely used to characterize spatial variability of ground motion. Despite that a very large number of coherency models were derived over the last four decades, these models rely on the analysis of a limited number of earthquakes (a few tens events at most) recorded at rather few array sites (station spacing ranging between 0.2 to 4 km), (Liao, 2006; Zerva, 2009), restricting the use of the actual coherency models to the sites where they were developed. Assessment of spatial correlation of peak ground motions and spectral acceleration has also become an issue of further investigation in the recent years. Indeed, development of reliable and well calibrated parametric models that describe the spatial correlation of ground

motion is of main importance in order to improve shake-maps, probabilistic seismic and risk hazard for spatially distributed infrastructures and site-specific ground motion prediction (e.g. Wald D.J et al., 2005; Goda and Hong, 2008; Harmandar, 2009). However, till now, the research of the spatial correlation of the ground motion was performed mainly in large scale (station spacing of several kilometers). Therefore to know whether the existing spatial correlation models can be extrapolated to relatively shorter separation distances as well as the effect on the structural behavior are still open issues. Despite the several efforts that have been done during the recent years, there are still scientific gaps and open issues in the comprehension of the spatial variability of the ground motion and even more on its effect on the structural behaviour. Within NERA JRA1-JRA3, a seismological experiment took place in from September 2011 to April 2012 in the high seismicity area of the island of Cephalonia in Greece (see NERA Deliverable 11.4 (2012) for additional information). Some of the main goals were to understand the key parameters that locally control the ground motion spatial variability and amplification, to derive coherency models and to study its dependency on earthquake magnitude and azimuth and to develop engineering-oriented models that allow incorporating basin topography effects in seismic design. Here, we focus on the analysis and quantification of the importance of the ground motion variability in Argostoli basin by means of a spatial correlation approach applied to earthquakes recorded by the very dense array installed in the center of Argostoli basin (Figure 88). This dense array consists of 21 Guralp CMG40T velocimeters (eigen period of 30 s) connected to Taurus (Nanometrics) belonging to the French mobile national seismological pool SISMOB. Seismometers are distributed on concentric circles of 5 m, 15 m, 40 m and 80 m radius around the reference station (Figure 88).

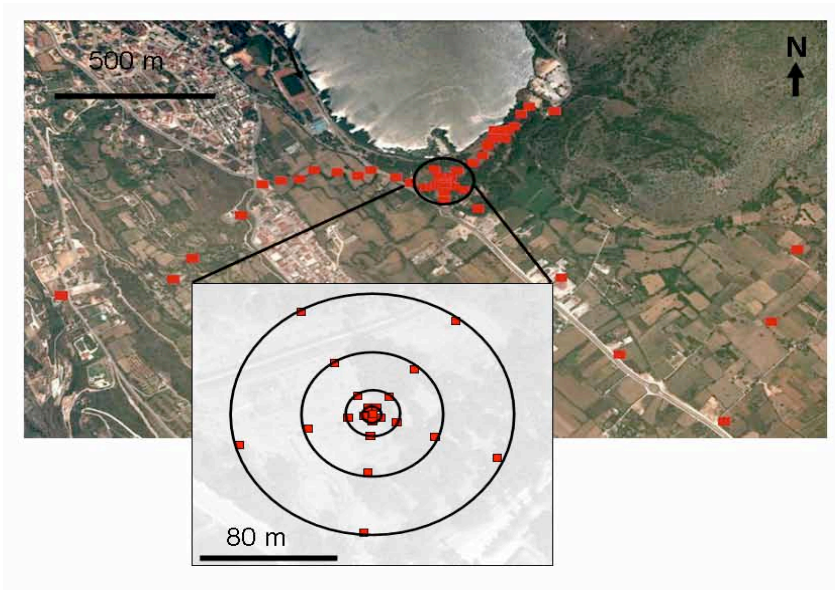


Figure 88: Location of seismological stations in the Argostoli basin (red markers) and zoom on the dense array layout.

During the period of 7 months that recordings have been done, more than 3000 local and regional events, with $M \geq 2.0$, occurred in the broader Aegean area. The earthquake catalog was built combining the EMSC-CSEM catalog (www.emsc-csem.org) and the Greek National catalog (NOA; www.noa.gr). Magnitudes are thus not completely homogeneous and correspond either to Local Magnitude (M_L) or to Moment Magnitude (M_w). Events with epicentral distance less than 80 km were relocated by ITSAK and the Observatory of Thessaloniki. From these 3000 events, 405 were considered for the present study for their very high signal to noise ratio. For all these events, velocities were differentiated or integrated to obtain acceleration and displacement, respectively; and Peak Ground Acceleration (PGA) as well as response spectra considering a 5% damping were computed. Figure 89 indicates distribution of magnitude and peak ground acceleration (PGA) as a function of epicentral distance for the 405 selected events. It is noticeable that the majority of the recorded events occurred within a 3 to 100 km epicentral distance with magnitude ranging between 1.5 and 3.5.

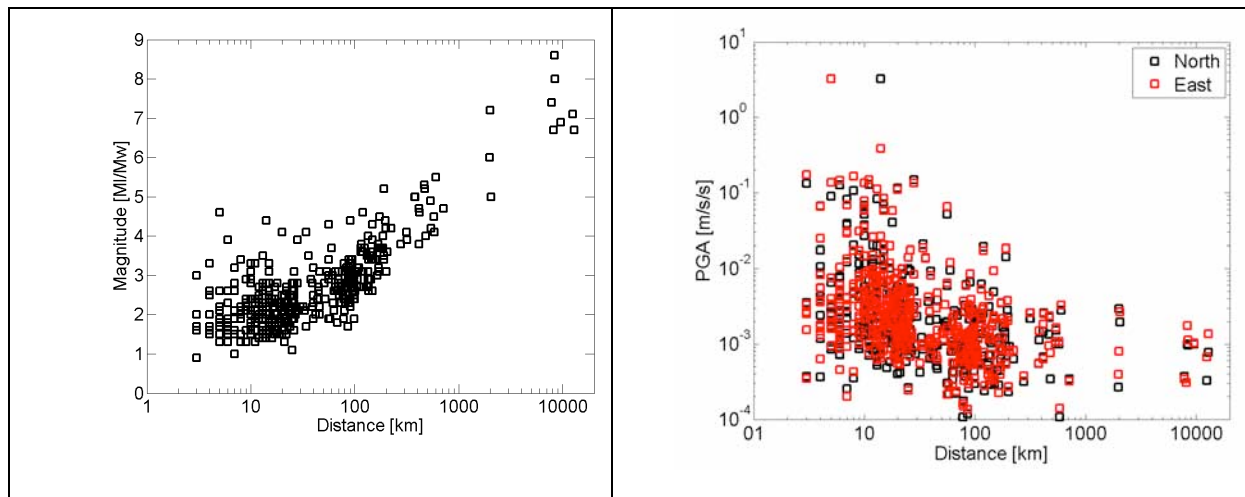


Figure 89: (left) Magnitude as a function of epicentral distance (km); (right); Peak Ground Acceleration (PGA) for the East and North component as a function of epicentral distance. Recordings of the seismological station locate din the center of the Argostoli basin is considered.

In order to investigate and quantify the aleatory (random) variability of single-site ground motion for the site of Argostoli, the procedure of Al Atik et al. 2010, was followed. An empirical ground motion prediction equation generally has the form:

$$Y = f(X_{es}, \theta) + \Delta \quad (3.1)$$

where Y is the natural logarithm of the observed ground motion parameter, $f(X_{es}, \theta)$ is the ground motion model, X_{es} is the vector of explanatory parameters (e.g magnitude, distance, style of faulting, site conditions), θ is the vector of model coefficients and Δ is a random variable describing the total variability of the ground motion. Δ is usually decomposed into between-events variability, ΔB , and within-event variability, ΔW , which are zero-mean, independent, normally distributed random variables with standard deviations τ and ϕ , respectively. The between-events residual (also called inter-event residual or event term), δB_e , represents the average shift of the observed ground motion from an individual earthquake, e , from the population median predicted by the ground motion model (GMPEs). The within-event residual (also called intra-event residual), δW_{es} , is the misfit between an individual observation at station s from the

earthquake-specific median prediction, which is defined as the median prediction of the model plus the between event term for earthquake e . The between-events and within-event standard deviations of the ground motion represent the earthquake-to-earthquake variability and record-to-record variability respectively. The within-event and between-events residuals are uncorrelated, so the total standard deviation of the ground-motion model, σ , can be written as (Al Atik et al., 2010):

$$\sigma = \sqrt{\varphi^2 + \tau^2} \quad (3.2)$$

According to Wailing's (2009) classification, the dataset of Argostoli is a site-specific dataset which contains multiple recordings at one site from earthquakes located in different source regions and can be used to estimate the systematic and repeatable site-specific effects. Due to lack of GMPEs for the area of Argostoli the calculated median values were predicted by all the recordings that are available. In order to estimate the σ_{ss} which is the aleatory variability of single-site ground motion, it is necessary to decompose it to the single-station within-event standard deviation, φ_{ss} , and the standard deviation of the between-events standard deviation, τ , according to the equation:

$$\sigma_{ss} = \sqrt{\varphi_{ss}^2 + \tau^2} \quad (3.3)$$

The natural logarithm of Peak Ground Acceleration (PGA) is the intensity measure that is used for the computations. In the absence of reliable GMPE for the area, the standard deviation of the between-events residuals τ was not estimated. However, the single-station within-event standard deviation φ_{ss} was calculated using the available recordings. The φ_{ss} is the standard deviation of $\delta W S_{es}$ which can be calculated using the equation:

$$\delta W S_{es} = \delta W_{es} - \delta S S_s \quad (3.4)$$

In equation 3.4, δW_{es} corresponds to the within-event residual at station s for an earthquake e and $\delta S_2 S_s$ is the site-to-site residual for site s considering several earthquakes (Al Atik et al., 2010). Due to the non-uniform spatial distribution of the stations, a weight was used for each station for the computation of the residuals. This weight corresponds to the surface around each station defined by Voronoi cells.

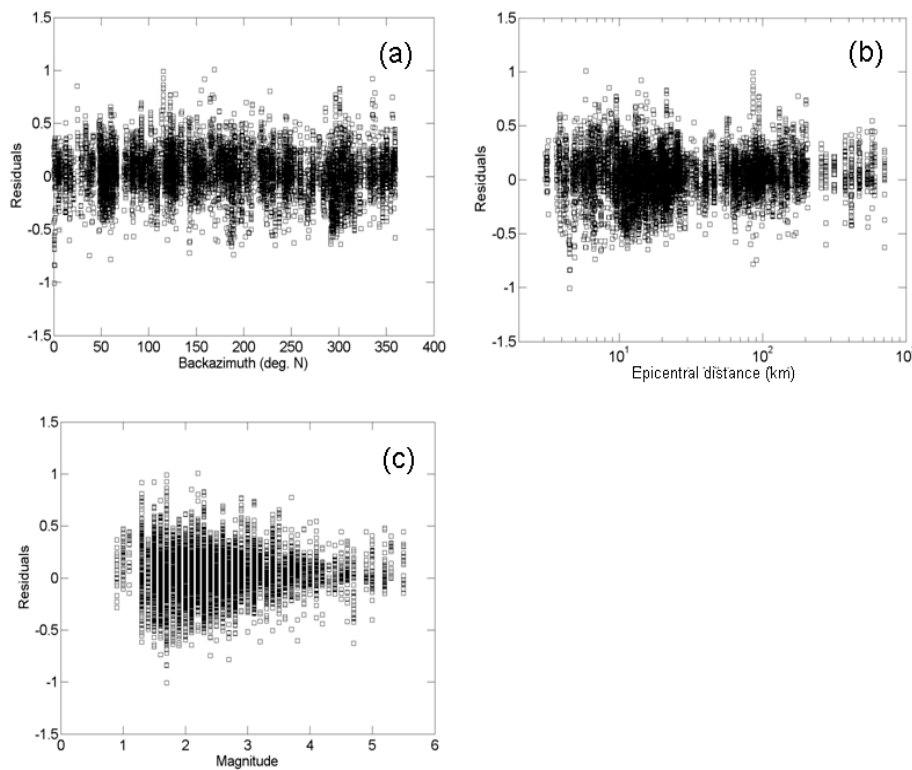


Figure 90. Within-event residuals (δW_{es}) as a function of event back-azimuth (a), epicentral distance (b) and magnitude (c). East component of the recorded acceleration is used.

Computed within-event residuals δW_{es} do not exhibit any strong dependency on back-azimuth and epicentral distance. On the contrary, there is a slight increase of residuals with lower magnitudes, which may be due to imprecise earthquake location as already observed in other datasets (Rodriguez-Marek et al., 2011). The derived value of the single-station within-event standard deviation for both horizontal components is 0.2. The standard deviation value obtained on the small scale network of

Argostoli is half the classical single-station within-events standard deviation of 0.45 obtained on large scale datasets (Al Atik et al., 2010; Rodriguez-Marek et al., 2011). This is due to the fact that the classical values are mainly controlled by large scale regional within events variations (e.g. path to path) and not by short-scale variations. Here, the computed value represents rather the ground motion site-specific spatial variability. Although and can not be strictly compared, a value of about 0.2 clearly indicates that the variation in natural logarithm of PGA within a small area (about 20000 square meters here) is not negligible compared to the expected variation of natural logarithm of PGA at any single station from GMPE studies. Following the same procedure by calculating the residuals for the natural logarithm of spectral amplitude (lnSA) for different values of period, instead of PGA, an increase in the standard deviation values with the increase of frequency (decrease of period) is observed. For the case of frequencies lower than the 1.8 Hz resonance frequency of the site the standard deviation is not zero which suggests wave propagation effects produced by heterogeneities outside the basin. Future work will focus on comparing the observed site-specific spatial variability with the ones observed at other dense arrays (e.g. SMART1, Chiba), especially by comparing the standard deviation of the residuals as a function of inter-station spacing.

Table 11. Standard deviation of residuals when considering spectral amplitudes (lnSA) for various periods

Period (s)	φ_{SS}	
	North	East
0.05	0.27	0.27
0.1	0.23	0.21
0.2	0.18	0.18
0.5	0.17	0.15
1	0.13	0.14

3.2 Statistical Analyses of the Kappa Factor of Soils: Application on the Marmara Dataset (METU team)

One approach to model the high-frequency attenuation of spectral amplitudes of S-waves is to express the observed exponential decay in terms of Kappa (k) factor. Kappa is a significant parameter used for identifying the high-frequency attenuation behaviour of ground motions as well as one of the key parameters for stochastic strong ground motion simulation method. There is not yet a systematic investigation of the Kappa parameter based on the recently-compiled Turkish ground motions. Within NERA- JRA3- WP13, we examined a strong ground motion dataset from Northwestern Turkey with varying source properties, site classes and epicentral distances. We manually computed k from the S-wave portion of each record and we studied both horizontal and vertical kappa values. We used traditional regression techniques to describe the (potential) relationships between kappa and selected independent variables such as the site class, distance from the source or magnitude of the event. No significant statistical dependency on magnitude is found in the analyses. We express the initial findings of a regional k model for Northwestern Turkey as a function of site class and epicentral distances. The dataset we used consists of 174 records (522 components) measured at 15 different strong motion stations from 142 earthquakes with magnitudes $3.0 < M_w < 6.0$ in Northwestern Turkey. Events with magnitudes lower than $M_w = 3.0$ are rejected for corner frequency issues that could complicate the kappa computations. The near-field datasets from the 1999 Kocaeli ($M_w = 7.4$) and Düzce ($M_w = 7.2$) earthquakes are also not included here due to the local site amplification effects and possible nonlinearity at the soft soil sites which both could lead to issues in kappa estimations. Due to space limitations, it is not possible to display information regarding all 142

events used, however, Table 12 gives a summary in terms of three magnitude bins and shows the number of events and records per each magnitude bin. Figure 91 shows the epicenters of the events and locations of the strong ground motion stations used in this study. Figure 92 displays the magnitude- epicentral distance distribution of the records analyzed herein. We note that the regional database we gathered originally has slightly more data than those employed herein however, for reliable kappa calculations; we selected only the records with clear S-wave arrivals and no signal-to-noise problems. We use the epicentral distances to study distance-dependency of kappa and only employ the records within 200 km epicentral distance.

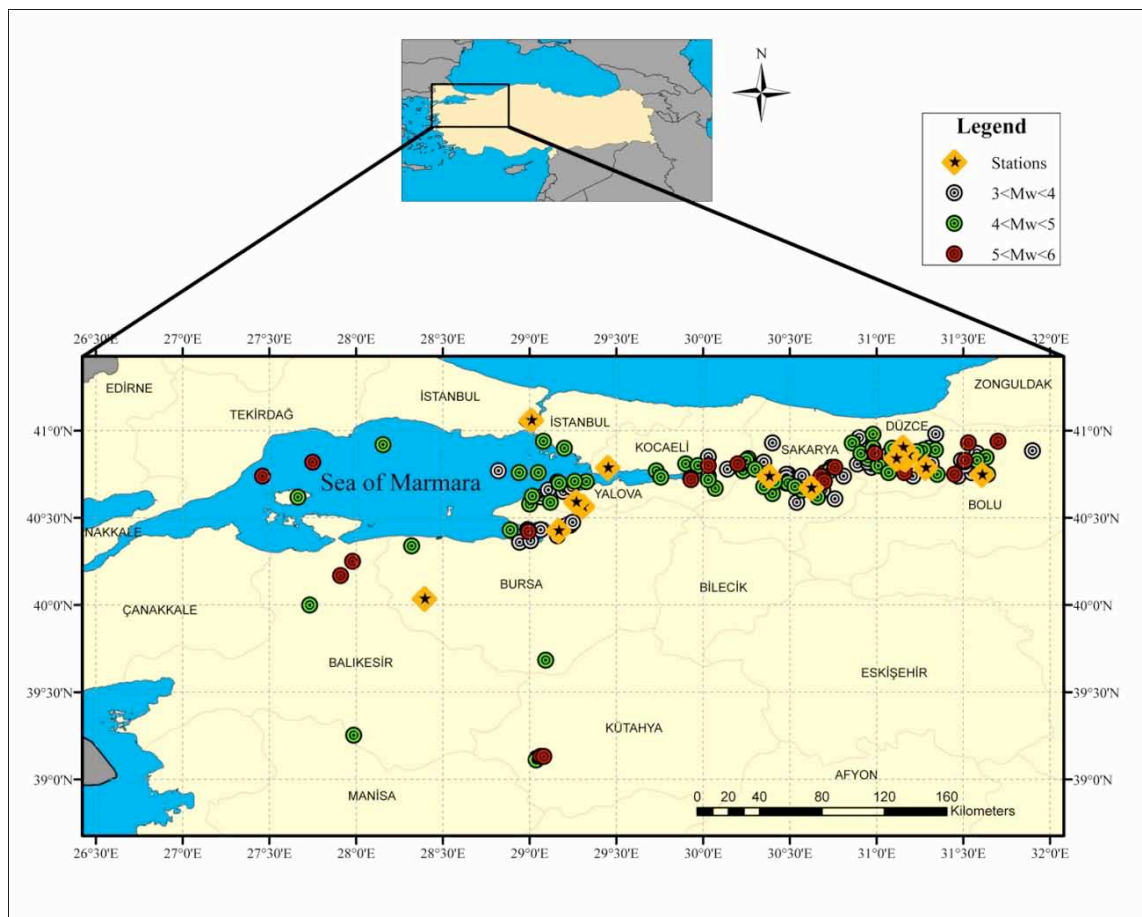


Figure 91. Locations of the earthquakes and strong ground motion stations used in this study

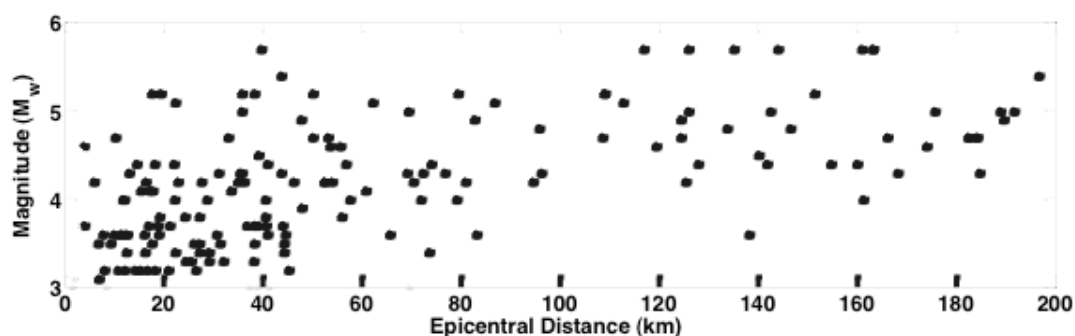


Figure 92. Magnitude-epicentral distance distribution of the records used in this study

Table 12. Magnitude ranges of the earthquakes used in this study with the number of events and records per each magnitude bin

Magnitude (Mw)	Bins	Number of Events	Number of Records (Number of Components) from these Events
3.0-4.0		60	70 (210)
4.0-5.0		61	74 (222)
5.0-6.0		21	30 (90)
Total		142	174 (522)

In majority of the previous work on kappa, only horizontal values are assessed in detail, however for several purposes it is essential to study the variation in kappa values computed from each of the three components of a single record. One important application of vertical kappa values is the stochastic ground motion simulations where the site amplifications are represented with empirical H/V curves. In addition, any clear difference in horizontal and vertical kappa values could augment the observations on the site-class dependency of the kappa parameter. Thus, we compute three separate kappa values for each record to observe the differences between the vertical and horizontal values. To assess the variations in the two horizontal kappa values per record, Figure 93 displays the ratios of kappa estimates from NS

components to that of EW components. Despite severe discrepancies at some distances, the y-intercept of straight line fit to the ratios is around 1.0. Thus, from this point onward in this study, we average the two horizontal kappa values to yield a single κ_h for each record. This averaging assumes that the direction of incoming waves does not affect kappa value or an isotropic near surface earth material. We then evaluated the horizontal and vertical components of kappa at each site. Figure 94 shows the distance-dependency of these kappa values.

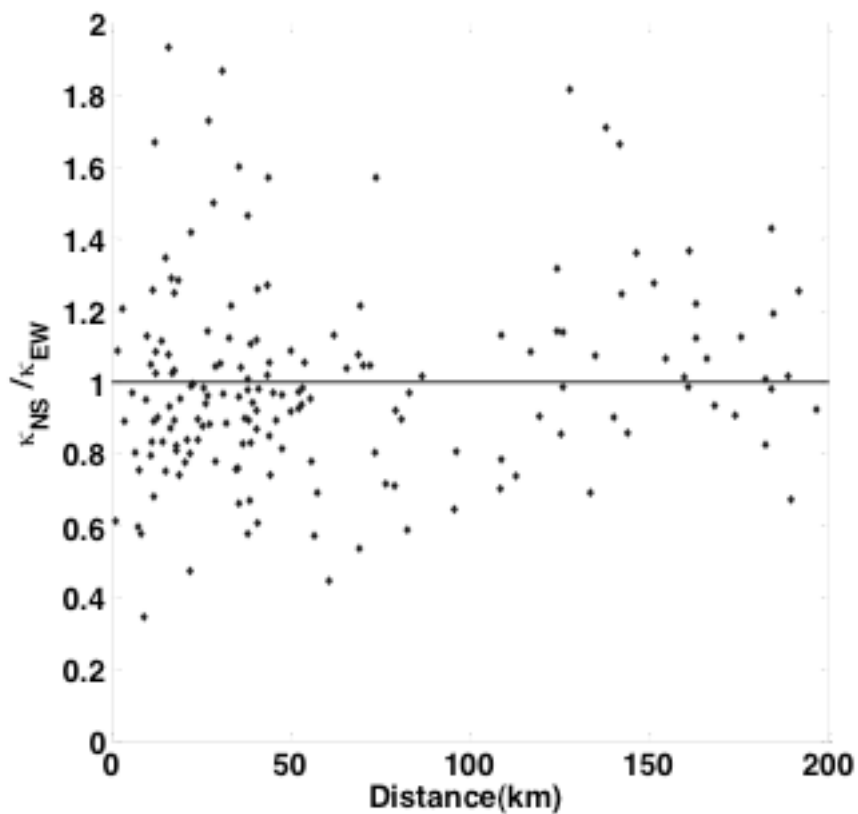


Figure 93. Variation of the ratio of two horizontal kappa values (κ_{NS}/κ_{EW}) with epicentral distance

Finally, we proposed an initial kappa model for the study region. In order to better understand and quantify the relation between the input and output variables in the Northwestern-Turkey kappa dataset, we performed multivariate linear regression (MVLRL) analyses. Initially, we performed Shapiro-Wilk test to check whether the data is normally distributed or not. The results indicate that the data is normally distributed. We then took the variables "distance", "site conditions" and "magnitude" as the dependent variables to correlate them with the calculated values of horizontal and vertical kappas. However, the P values obtained from t-test indicate that kappa does not vary linearly with magnitude at 5% significance level. We therefore did not include the magnitude in regression analyses.

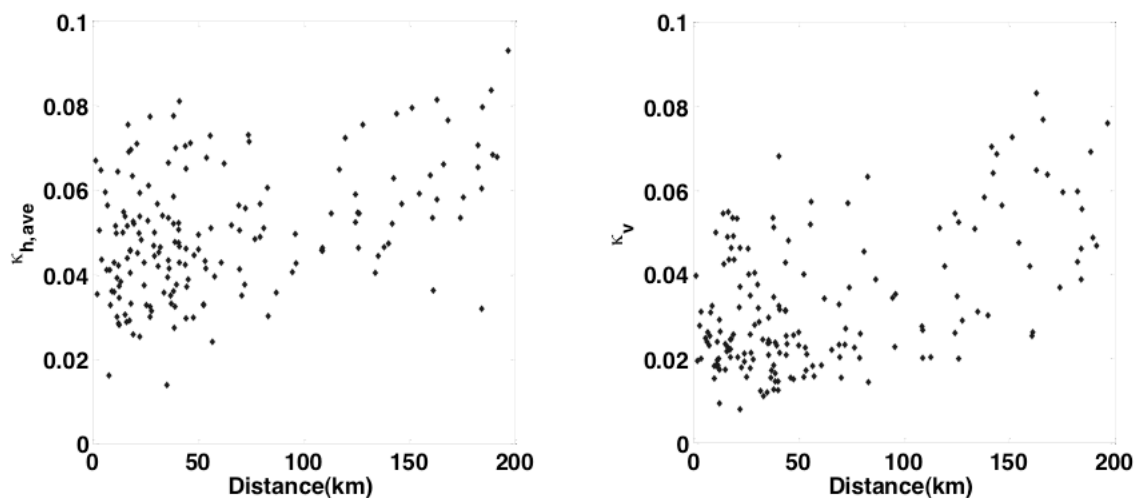


Figure 94. Variation of the (a) average horizontal and (b) vertical kappa values with epicentral distance.

We later used Variance Inflation Factors (VIFs) to investigate the multicollinearity among distance and site conditions. The VIF values obtained from the analyses indicate that these variables are not collinear and

can be reliably used in the regression analysis. Finally, as site conditions in this database take only two distinct values (Site C and Site D), we introduce dummy variables to properly take them into account in the regression analyses. The general form of the proposed relationships is as follows:

$$\kappa(R, \text{Site Class}) = \kappa_{0,C} \cdot \text{Site C} + \kappa_{0,D} \cdot \text{Site D} + C_R \cdot R \quad (3.5)$$

where R is the epicentral distance, Site C is 1 if the site class is C and 0 otherwise, Site D is 1 if the site class is D and 0 otherwise, C_R is the regional slope, $\kappa_{0,C}$ and $\kappa_{0,D}$ are the zero-distance kappa values for site C and D soils, respectively. In previous studies, it is expressed that while κ_0 is a station-specific value, C_R is related to the regional attenuation properties. We note that similar to many previous studies, a linear model in terms of distance is used herein. This assumption is justified for our dataset as observed from the distance distributions of kappa shown in Figures 94.a and 94.b. In this study, in order to avoid the tendency of the residuals to show a non-uniform pattern when compared with the predicted values at some regions (known as "heteroscedasticity"), we have used the Huber-White sandwich estimators in linear regression analysis to estimate the standard errors and make them robust. The results of the linear regression analyses for the horizontal and vertical kappa, respectively are given as:

$$\kappa_h = 0.03774 \times \text{Site C} + 0.04546 \times \text{Site D} + 0.0001321 \times R \quad (3.6)$$

$$\kappa_v = 0.01498 \times \text{Site C} + 0.02706 \times \text{Site D} + 0.0001881 \times R \quad (3.7)$$

where the parameters R , Site C and Site D are as defined in Equation (3.5). Expectedly, equations 3.6 and 3.7 yield higher κ_0 values for softer soil sites than those for stiffer sites. In addition, κ_h is greater than κ_v at all distances for both site conditions.

To evaluate the goodness of fit in the predictions, the coefficient of determination, R^2 values are computed as 0.2346 and 0.4141 for equations 3.6 and 3.7, respectively. The low values of R^2 indicated by the regression analyses are attributed to the nature of the data with large scatter. Figure 95 displays the predicted versus computed kappa values for the horizontal and vertical components for the entire dataset.

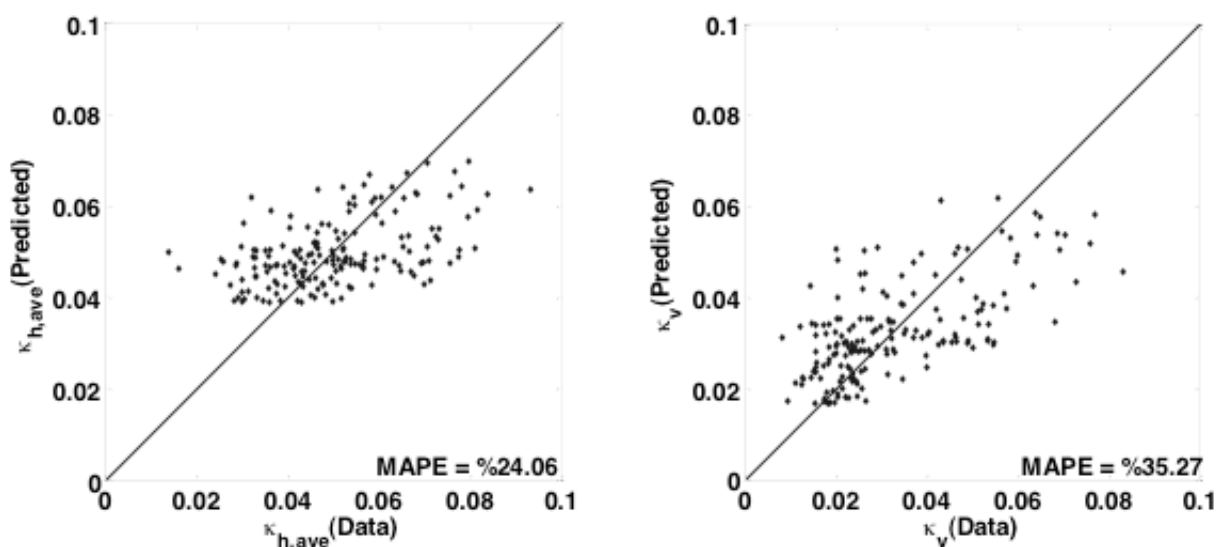


Figure 95. Comparison of predicted κ_h (left panel) and predicted κ_v (right panel) versus corresponding computed (data) values for the entire dataset.

Conclusions

In summary, within the project, we investigated the kappa parameter computed from 174 records (522 components) measured at 15 different strong motion stations from 142 earthquakes with magnitudes $3.0 < M_w < 6.0$ in Northwestern Turkey. The effects of magnitude, site class and distance on kappa values are investigated for both the horizontal and vertical components. A regional model is also presented for future use in stochastic simulations and GMPE adjustments. Based on 5% confidence interval, t-tests indicate no linear relation of kappa on

earthquake magnitude for the dataset employed. However, site class influences the computed kappa values significantly. Our numerical results for zero-distance kappa values are consistent with the worldwide data and the previous findings from smaller datasets in the same region. Following are important points to be tackled in further studies:

- The effect of magnitude on kappa is not found statistically significant for the database studied herein. However, for the future studies with more near-fault data, it is possible to focus on the scatter of the near-field kappa values and treat them separately for potential source effects.
- The objective of this study was to construct a regional model. However, for further studies, authors aim to compare kappa values from different regions from Turkey which could give better insight to the origins of kappa.
- It is possible to develop models that employ single-station kappa values for site classification purposes. As of today, there are still strong motion stations in Turkey where the local site conditions are not well known with neither a Vs30 value nor a site class assigned. If a reliable relationship between site classes and kappa can be established, it could be potentially used to assess the site class of a station as well as to adjust ground motions. Such a study could not be formed herein as the stations that have records from more than 10 events are limited in number.
- Finally, these analyses should be considered as an initial step for systematic analyses for kappa estimates in Turkey. The METU team is currently making progress toward better explaining the potential factors affecting kappa with advanced data modeling techniques on larger databases.

The results shown in this contribution can be found in the following paper: A.Askan, F.N. Sisman and O. Pekcan, A Regional Near-Surface High Frequency Spectral Attenuation (Kappa) Model for Northwestern Turkey (2013), submitted to Soil Dynamics and Earthquake Engineering.

3.3 Assessment of Nonlinear Dynamic Building Response to Simulated Ground Motions (METU team)

The fundamental purpose of this study is to provide insights into the nonlinear dynamic behavior of typical frame structures to real records of a particular event versus the corresponding synthetic records. The key question here is whether the seismologically “acceptable” synthetic ground motion records can be used for earthquake engineering purposes without any prior scaling or modification of the records. We also investigate if the misfits in terms of seismological measures (such as Fourier Amplitude Spectrum) between the real and simulated records correspond to consistent differences in engineering demand parameters. This study and similar research are particularly useful for evaluating synthetics in terms of engineering performance measures in regions with scarce strong ground motion records. In this study, real and simulated acceleration records of the 2009 L’Aquila earthquake (M_w 6.1) are employed for the nonlinear dynamic analyses of buildings. This event occurred in central Italy, very close to the L’Aquila town, on a NW–SE trending normal fault (Cirella et al., 2009; Gallovic and Zahradník, 2012). Despite its moderate size, the 6 April 2009 L’Aquila earthquake caused significant structural damage in the near-fault area. The mainshock was recorded at 14 strong motion stations within 50 km epicentral distance. The large variability of ground motion amplitudes around the fault plane is attributed to a combination of source and wave propagation effects (Ameri et al., 2012). Most of the near-fault stations were located on sites with class A according to EC08, however at some stations on softer soils, local site effects were pronounced. To use in nonlinear time history analyses of the buildings, we employ records from 7 selected stations from the near-fault area, 4 out of which are located on site-class A. Figure 96 displays the map of the meizoseismal region with the epicenter, fault plane and the locations of the selected stations. Table 13 lists further information regarding the

locations and site classes of these stations. In two recent papers by members of the project team (Ameri et al., 2012 and Ugurhan et al., 2012), the horizontal records at these stations are simulated using two different simulation techniques: Hybrid Integral Composite method (Galovič and Brokešová, 2007) and Stochastic Finite-Fault method (Motazedian and Atkinson, 2005). From this point onward, we name the synthetic records from HIC method as SYN1 set and the latter as SYN2 set. We note that there are 2 SYN1 components and only 1 SYN2 component per record. Obtained from SYN1 and SYN2 record sets, at every station we have a total of 3 simulated and 2 real horizontal components which sum up to 35 records at 7 stations used as input ground motions for dynamic analyses of the selected frames. We note that the synthetic and real records are not scaled or modified by any means other than baseline corrections and filtering between 0.1 and 10 Hz. We note that the two alternative simulation methods are performed in two independent studies thus identical source or path models were not employed. Hence, it might not seem valid or fair to compare these synthetics with each other. However, these models use different but consistent model parameters. Also, we compare them against the real records and not directly with each other. In addition, the entire focus of this study is to evaluate synthetic records (that are generated independently and are seismologically acceptable to a certain extent) from the earthquake engineering point of view.

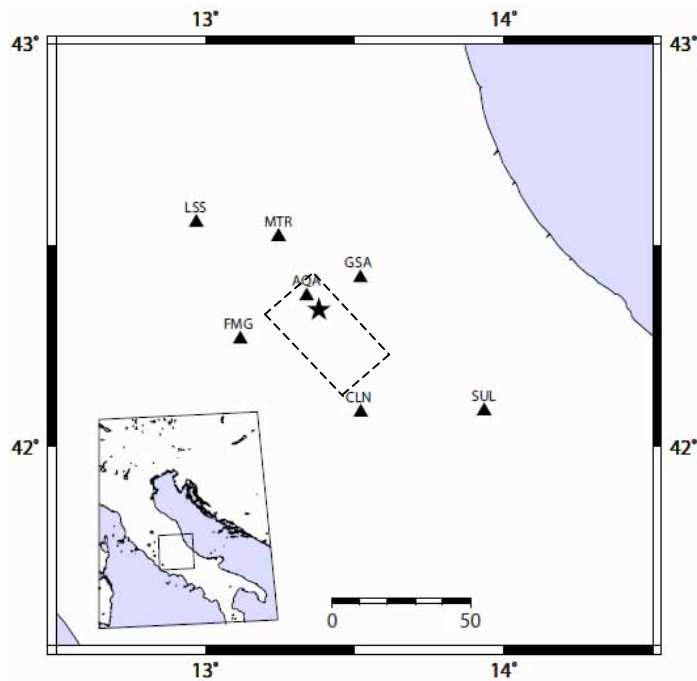


Figure 96. Map showing the fault plane and epicenter of 2009 L'Aquila earthquake with the locations of the selected stations

Table 13. Information on the strong motion stations that recorded the 2009 L'Aquila earthquake

Station Code	Station Name	Site Class (EC08)	R_{EPI} (km)	R_{JB} (km)	PGA (cm/s²)
AQA	V. Aterno-F. Aterno	B	4.6	0	435.39
CLN	Celano	A	31.64	11.69	88.47
FMG	Fiamignano	A	19.32	17.07	26.32
GSA	Gran Sasso	B	18.05	7.86	146.62
LSS	Leonessa	A	39.02	33.68	9.61
MTR	Monte reale	A	22.35	14.48	61.37
SUL	Sulmona	C	56.53	32.23	33.61

Before we present nonlinear analyses, we check the differences between the real and synthetic records at the selected stations. We quantify frequency/period-dependent misfits for each frame between the synthetic

and the real records in terms of the Fast Fourier Amplitude Spectra (FAS) and elastic response spectra with 5% damping (RS) as follows:

$$Misfit_{FAS} = \frac{1}{n_f} \sum_{f=1}^{n_f} \left| \log \frac{FAS_{syn}(f)}{FAS_{obs}(f)} \right| \quad (3.8)$$

$$Misfit_{RS} = \frac{1}{n_T} \sum_{T=1}^{n_T} \left| \log \frac{RS_{syn}(T)}{RS_{obs}(T)} \right| \quad (3.9)$$

where for each frame n_f and n_T are the number of discrete frequencies and periods in the selected period-band used in the FFT and response spectrum computations, respectively. For each frame we have considered a period-band separately with respect to the fundamental period of that frame as follows: the lower value of the period-band is selected with respect to the highest modal frequency of the considered frame (20% of the first fundamental period), and the upper period band is selected with respect to the nonlinearity effects in increasing of the period of each frame after dynamic analysis (120% of the first fundamental period). Nonlinear time history analysis (NLTHA) is a step by step analysis of the dynamic response of a structure under a loading that is a function of time, which in this case is a ground motion record. For this study, NLTHA involves the numerical solution to MDOF equation of motion under the horizontal-components of the real and synthetic motions presented in the previous section. The corresponding differential equation of motion is given as follows:

$$\mathbf{M}\ddot{\underline{u}} + \mathbf{C}\dot{\underline{u}} + \mathbf{K}(\underline{u})\underline{u} = -\mathbf{M}\ddot{\underline{u}}_g \quad (3.10)$$

where \underline{u} is the nodal displacement vector, \mathbf{M} is the mass matrix, \mathbf{C} is the damping matrix, $\mathbf{K}(\underline{u})$ is the nonlinear stiffness matrix as defined by the nonlinear material models and $\ddot{\underline{u}}_g$ is the ground acceleration vector. We select three two-dimensional, regular and symmetric reinforced concrete (RC) frames to model building structures for NLTHA. The frame set is

particularly selected to yield a uniform distribution of fundamental periods and to represent typical RC buildings from worldwide. Frame 1 (F3S2B) is a 3 story-2 bay frame with story height of 3 meters. Frame 2 (F4S3B) is a 4 story-3 bay frame with story height equal to 2.7 meters, and finally frame 3 (F8S3B) is a 8 story-3 bay frame with a 3.96 meters story height. Among these, frames F3S2B and F4S3B are selected from the existing structures located in Turkey while frame F8S3B is designed using the Uniform Building Code-1982 in California (Kadaş, 2008; Yılmaz, 2007). Numerical modeling of the frames is carried out by the use of OPENSEES software that employs finite elements for discretization and solution of the equation of motion. Two-dimensional modeling is preferred due to the symmetry of the frames. To compare the nonlinear dynamic response of the frames, for each record maximum displacement of each story is computed (see Figures 97, 98, and 99). The main objective of this study is to investigate whether the nonlinear responses of building structures to synthetic records from alternative simulations are consistent with the “real” response (which is defined as the response from the corresponding real record). Another fundamental question of interest is whether the measured period-dependent misfits in terms of ground motions (FAS in this case) and SDOF response indicators (RS) correlate with differences between the real and synthetic nonlinear responses of the frames. For this purpose, we define a misfit measure for differences in nonlinear response (NR) under real and synthetic motions. The NR misfit is expressed in terms of average of maximum story displacement ratios as follows:

$$Misfit_{NR} = \frac{1}{n_s} \sum_{s=1}^{n_s} \left| \log \frac{NR_{syn}(s)}{NR_{Obs}(s)} \right| \quad (3.11)$$

where n_s is the total number of stories in the frames. A comparison of the misfits in terms of ground motions and story displacements (Figures 97-99) leads to the following conclusions given below.

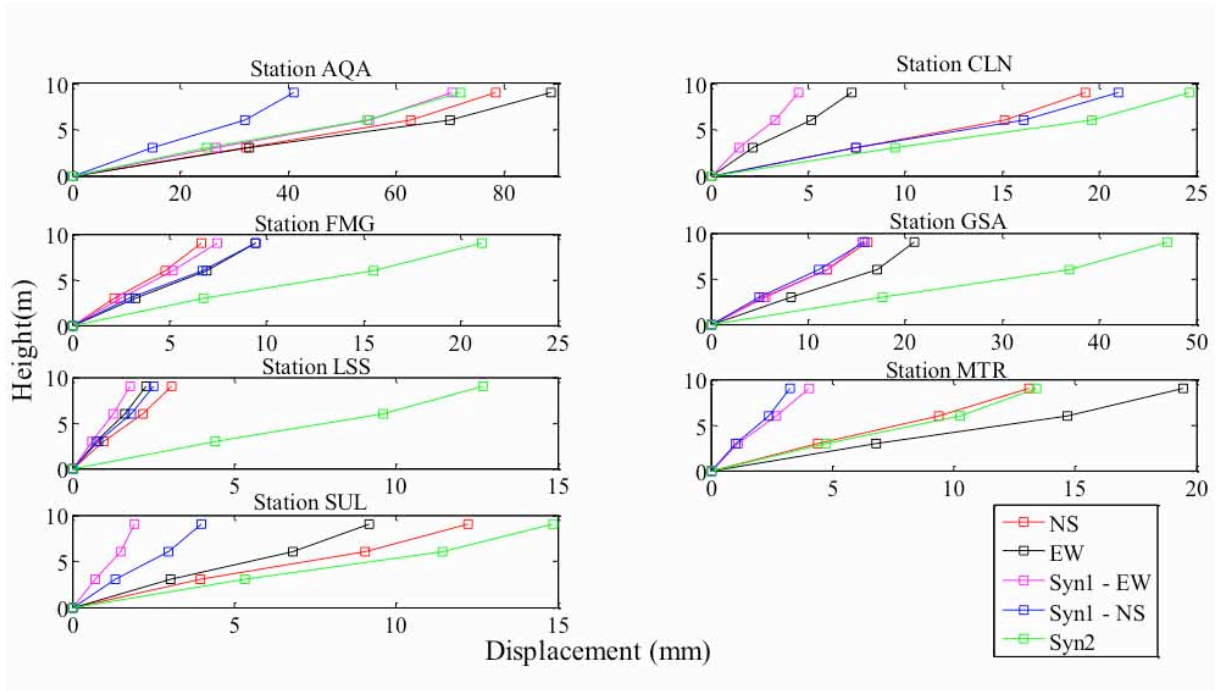


Figure 97. Distribution of maximum story displacements for Frame 1 (F3S2B) due to the real and synthetic records at the selected stations.

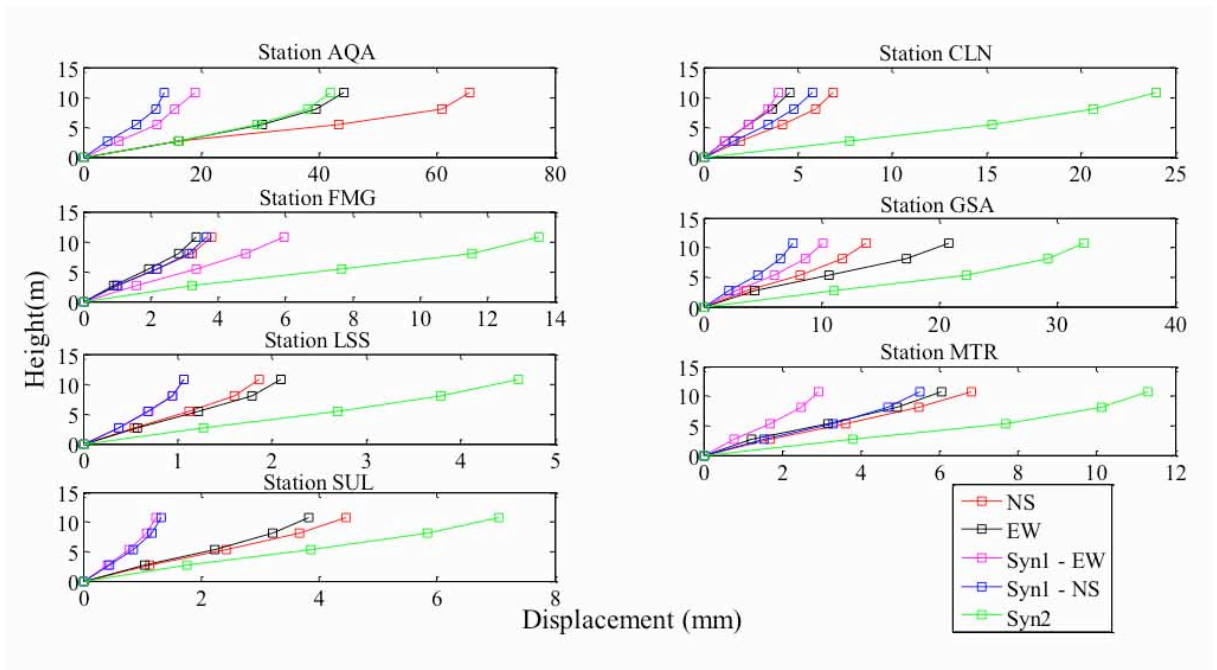


Figure 98. Distribution of maximum story displacements for Frame 2 (F4S3B) due to the real and synthetic records at the selected stations

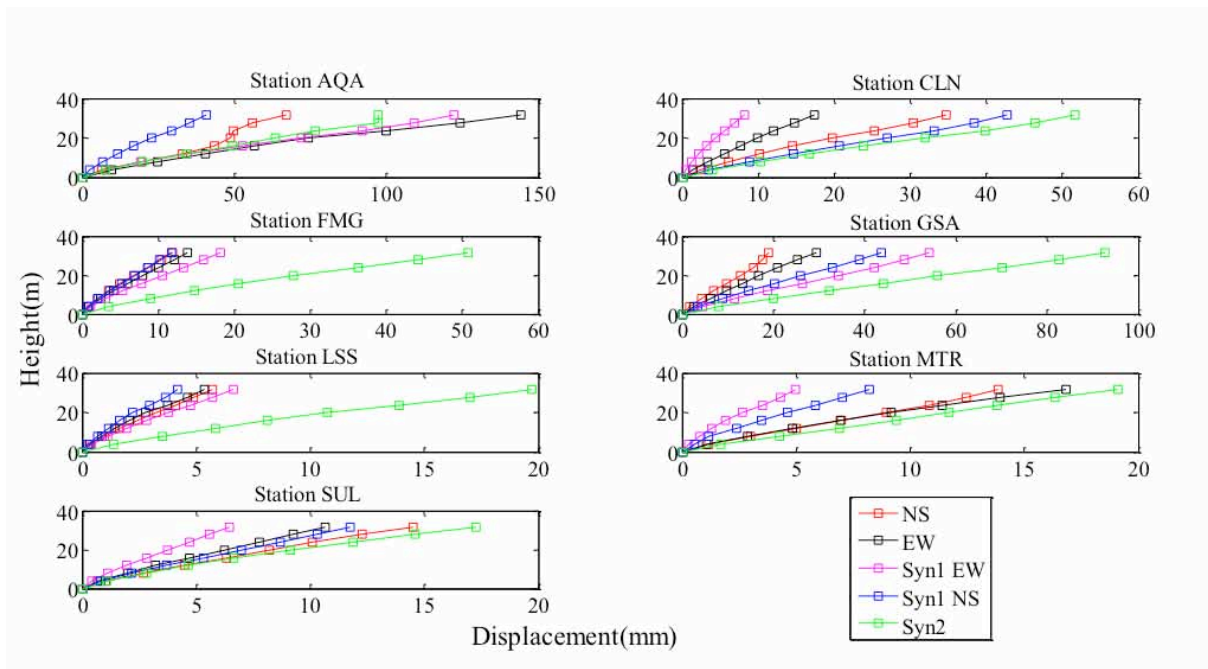


Figure 99. Distribution of maximum story displacements for Frame 3 (F8S3B) due to the real and synthetic records at the selected stations

Conclusions

Through the numerical experiments conducted in this study, we have drawn the following conclusions:

- Among the two simulation methods used in this work, for most of the stations the Stochastic Finite-Fault model yields more conservative results because of overestimation of the nonlinear response. On the other hand, Hybrid Integral Composite method mostly provides accurate results as it covers the broadband frequency range. However, due to some frequency bands where the synthetics are not close to the real amplitudes, the response under the simulated record from HIC method does not always match the real response closely. Therefore, when a poor fit is obtained from a seismological point of view (e.g., MTR and SUL for HIC model) a similar outcome is observed from the engineering point of view.
- In general, misfits obtained in terms of the ground motion parameters (i.e. RS and FAS) are in agreement with those obtained for dynamic response of the frames. Among RS and FAS misfits, we

observed that RS misfits are mostly in better agreement with NR misfits.

- It is generally known that the match between a target response spectrum (real record in this case) and a synthetic response spectrum determines the fit between the linear elastic response under real and synthetic records. Our numerical results indicate that for all cases even when nonlinear behavior is more likely, period-dependent SDOF indicators of goodness of fit between the real and synthetic records match MDOF behavior of those real frame structures. Thus, SDOF-based misfits that cover the fundamental period range of the frames describe the nonlinear response sufficiently.
- The match between the Fourier Amplitude Spectrum of the real and synthetic record around the frequencies that correspond to the fundamental period of the structure governs the nonlinear response. Thus, it is important to simulate realistic amplitudes over the entire broadband frequency range of interest for earthquake engineering purposes in order to cover all types of buildings with a range of fundamental periods.
- For this specific case, simulated records that seismologically satisfy a certain goodness of fit criterion yield nonlinear responses that are acceptable when compared to the real responses (in terms of story displacements).
- Finally, synthetic records that reasonably overestimate the nonlinear response could be conservatively used for seismic design and assessment purposes.

The results shown in this contribution can be found in the following paper: S. KarimZadeh, A. Askan, A. Yakut, G. Ameri (2013). Assessment of synthetic ground motion records obtained from alternative simulation techniques in nonlinear time history analyses of multi-story frame buildings: A case study, submitted to *Bulletin of the Seismological Society of America*.

3.4 Modeling of Spatial Variation of Ground Motion: A case study for Istanbul (KOERI team)

INTRODUCTION

The estimation of strong ground motion is vital for the evaluation of the shakemaps. Empirical data; i.e. earthquake records, are the primary source of information in the characterization of strong ground motion. However, the lack and scarcity of accelerometers necessitate the use of synthetic ground motions. In the shakemaps, ground motion prediction equations (GMPEs) are used to detect the peak ground motion parameters at locations with no ground motion recordings. Estimated parameters are modified using the bias-adjustment and site-dependent coefficients. A state-of-art algorithm based on combination of observed ground motions and intensities with estimated peak ground motions is implanted to ShakeMap (Worden et al., 2010). Highly vulnerable mega-cities and urban areas have attracted significant attention in recent years. Realistic assessment of ground motion properties in urban scale asks for dense strong ground motion arrays. No matter how dense strong motion arrays are, as in many cases, such as Istanbul, the building and population densities are so high that we need to develop approaches, or improve existing ones, for rational damage estimation. Stochastic approaches are often used in earthquake engineering to simulate seismic ground motion. The conditional simulation is a physical way to generate spatially variable ground motions. The conditional simulation of random fields permits the use of predefined time histories. In other words, it deals with the simulation of the full random field that has limited number of recorded information, using the same recorded data (Wang *et al.*, 2003). Generally, the conditional simulation can be performed using the Kriging method.

The Kriging method was developed by Krige (1966) in solving the ore evaluation problem. Its applications can be found in Krige (1966) and Journel and Huijbregts (1978). Kriging methodology provides the best linear unbiased estimate built on data of a stochastic field. Vanmarcke and Fenton (1991), Vanmarcke *et al.* (1993) applied the Kriging method to conditional simulation problems in earthquake engineering. Hoshiya (1994), Hoshiya and Maruyama (1994), Hoshiya (1995) modified the conditional simulation method using Kriging method by considering the corresponding error covariance matrix; and Shinozuka and Zhang (1996) used orthogonality property in kriging method to improve the conditional simulation. The geometric mean of peak ground accelerations (PGAs) are estimated based on an interpolation technique of data obtained from strong motion stations. The spatial distribution of PGAs is analyzed by geo-statistical analysis. A new numerical technique based on Kriging method is developed with the aim of interpolation of PGAs using information obtained from geo-statistical analysis. A dense array is needed to develop, to test, and to apply the method, effectively. The proposed method is independent of region, event, and past or future data. It relies on data obtained from a certain earthquake to estimate regional distribution of PGAs for the same event. The Istanbul Earthquake Rapid Response and Early Warning System (IERREWS) that includes 100 rapid response and 10 early warning stations provides an ideal platform to present the new numerical technique.

ARRAY AND DATA DESCRIPTION

In Istanbul Earthquake Rapid Response and Early Warning System (IERREWS) 110 strong motion recorders are installed throughout the city. Out of these, 100 stations provide ground motion information for the preparation of a building damage map immediately after an earthquake for rapid response purposes. The other ten stations are located on the

shoreline as close as possible to the Great Marmara Fault to provide on-line information for early warning purposes. All stations consist of external, tri-axial (three orthogonal axis), force-balance (servo) type accelerometers, recorders, timing and communication modules (Erdik *et al.*, 2003). Distribution of 100 stations can be seen in Figure 100. The inter-station distances of the IERRS stations vary between 0.67 km and 56 km. Since the deployment of the IERRS in 2001, a series of moderate and small earthquakes have been recorded. In this study, seven of them are used. The locations of chosen events are shown in Figure 101. Their source properties are summarized in Table 14. The magnitudes of chosen earthquakes range from 3.1 to 5.2. Minimum epicentral distances vary between 1 and 101 km, and maximum epicentral distances change between 16 and 130 km (Table 14). Source mechanisms are dominantly strike-slip for the first six earthquakes. The seventh earthquake has a dominantly normal mechanism (<http://www.koeri.boun.edu.tr/sismo/map/en/index.html>). The geometric mean peak ground accelerations (PGAs) recorded during the seven earthquakes are shown in Figure 102. The acceleration traces are baseline-corrected and butter-worth fourth order filtered using the filter range detected by Fourier amplitude spectrum and signal to noise ratio. PGA at a station is then computed as the geometric mean of two horizontal PGAs. They vary between 0.01 m/s^2 and 0.37 m/s^2 . The number of triggered stations and their geographical distribution depend on earthquake magnitude, epicentral location, distance, and site conditions. The epicentral locations of events associated with data presented in Figure 102 can be seen in Figure 101. Modified Kriging method is used for the estimation of PGAs conditional upon the measured records of the IERRS. In this connection, PGA is estimated for each IERRS station that has triggered data from an earthquake, using the methodology outlined in Figure 103.

RESULTS, DISCUSSION AND CONCLUSIONS

Based on the newly developed methodology to estimate the PGA distribution by interpolating data obtained from strong motion stations, we essentially attempted to characterize the spatial variation of PGA and to use it to estimate PGA at places with no recordings using a statistical approach. We relied on the Kriging method for this purpose. The proposed methodology has the potential to predict PGA closer to observed. The methodology is developed for the assessment of strong ground motion distribution in urban context. A methodology for the interpolation of measured ground motion of discrete array stations to be used in the bias adjustment of the theoretical shake map assessments with the empirical ground motion measurement (PGA) is a natural follow-up of the investigations. Peak ground accelerations at Istanbul Rapid Response stations estimated using the modified kriging method are compared with observed ground motion. Several tests were conducted to assess the performance of modified kriging method in estimation of ground motion distribution in Istanbul. The estimated and recorded PGAs were compared showing that the results obtained by the proposed method were found to be within one geometric standard deviation ranges. It was also concluded based on analyses on the four control groups that the methodology is not significantly sensitive to site and distance correction for our cases. Thus it was decided not to apply any distance and site correction. As more data from this array or similar arrays are available with a wider magnitude range for further development and verification of the methodology, it will be possible to study distance and site dependence in more detail. The estimated and observed values were then compared with the values calculated by GMPEs. The results from GMPEs are biased with a magnitude correction to minimize the misfits between GMPEs and observations. Also, the correlation coefficients for the biased results of GMPEs are considered. In general the GMPEs underestimated observed and estimated PGAs. It was observed that among GMPEs Akkar and Bommer (2010) model

produced values closest to observed and estimated PGAs. The proposed method was used to compute PGA at the phantom stations. The computed PGAs were compared with the values computed by RRMMap software of the Istanbul Earthquake Rapid Response system that uses spline interpolation. It was observed that with the modified kriging methodology it is possible to synthetically produce ground motion values at phantom locations. When compared with the results by the RRMMap algorithm, our results were found to be too smaller (Figure 104). The estimations by our methodology were in line with the observations in terms of amplitude and trend (Figure 104). The biased spatially-correlated estimates by Akkar and Bommer (2010) model and by the modified kriging method agreed also in terms of distribution character and amplitude of PGA, although Akkar and Bommer (2010) naturally could not estimate zones of higher PGAs that can be seen in many earthquakes and can not be explained by site effects only. The current weakness of the methodology is that it does not cover the regions with no observed data. This weakness can be avoided by using biased spatially-correlated GMPEs. It is developed for regions with dense arrays and requires records within six kilometers of a point where the PGA is to be estimated. It should be noted that six kilometers are chosen within the framework of this work. This figure can be higher or lower depending on the number of available stations. The methodology's dependency on dense arrays seems to be a disadvantage considering the approach taken in ShakeMap applications and the GMPEs. However the spatially estimated ground motion values as close as possible to the observed data is important for damage estimations in highly populated urban regions. We expect that more cities will host dense arrays in coming years.

Table 14. Source properties of the earthquakes recorded by IERREWS
(<http://www.koeri.boun.edu.tr/sismo/default.htm>)

No.	Eq	Date	Latitude N	Longitude E	GMT	M _L	M _d	Number of recording stations	Maximum Epicentral Distance (km)	Minimu Epicent Distanc (km)
1	Güzelyalı	19/09/2003	40.8498	29.2867	00:51	3.1	3.2	16	16	1
2	Yalova	16/05/2004	40.6957	29.3222	03:30	4.3	4.2	72	58	14
3	Güzelyalı	24/06/2004	40.8676	29.2683	13:28	3.2	3.2	14	23	1
4	Marmara Sea	29/09/2004	40.7797	29.0200	15:42	4.0	-	86	34	14
5	Kuşgölü	20/10/2006	40.2635	27.9843	21:15	-	5.2	43	130	101
6	Gemlik	24/10/2006	40.4240	28.9947	17:00	-	5.2	47	70	52
7	Çınarcık	12/03/2008	40.6210	29.0110	20:52	4.8	-	54	50	30

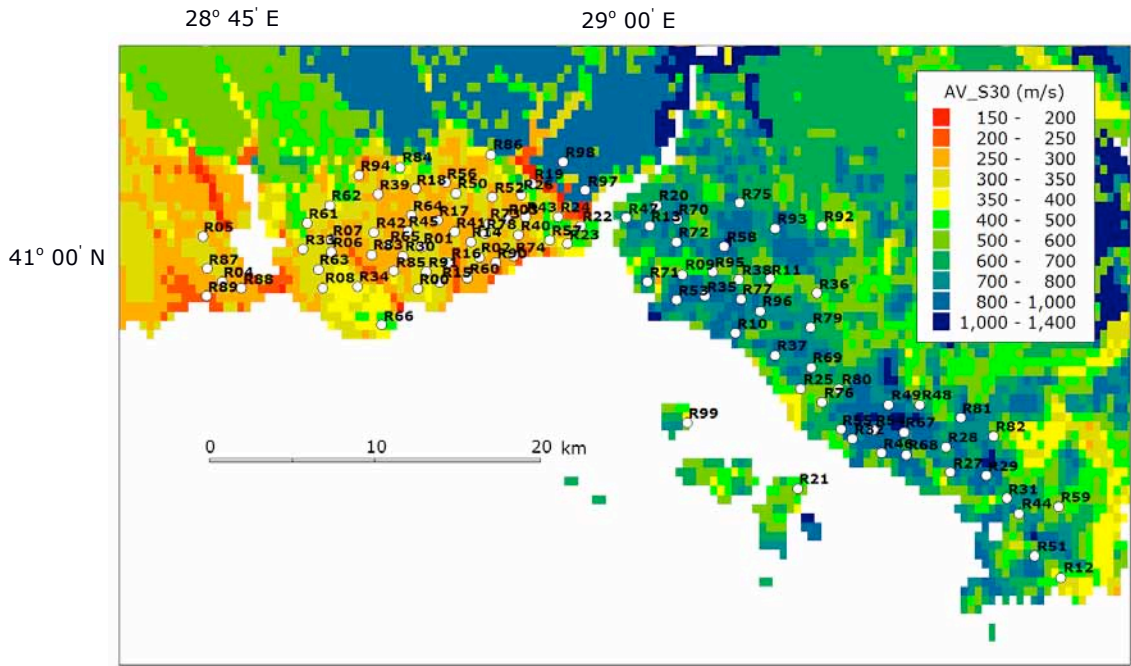


Figure 100. Configuration of urban stations in the Istanbul Earthquake Rapid Response and Early Warning System (IERREWS) and Istanbul site classification map based on Vs30 (OYO, 2007 and 2009).

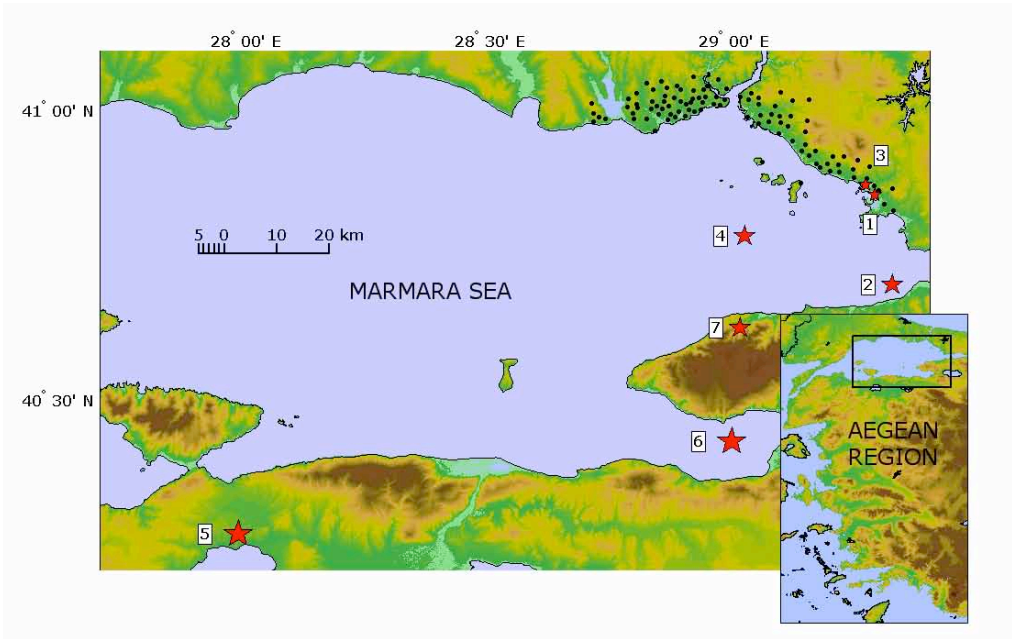


Figure 101. Locations of the selected events recorded by the Istanbul Earthquake Rapid Response and Early Warning System (IERREWS).

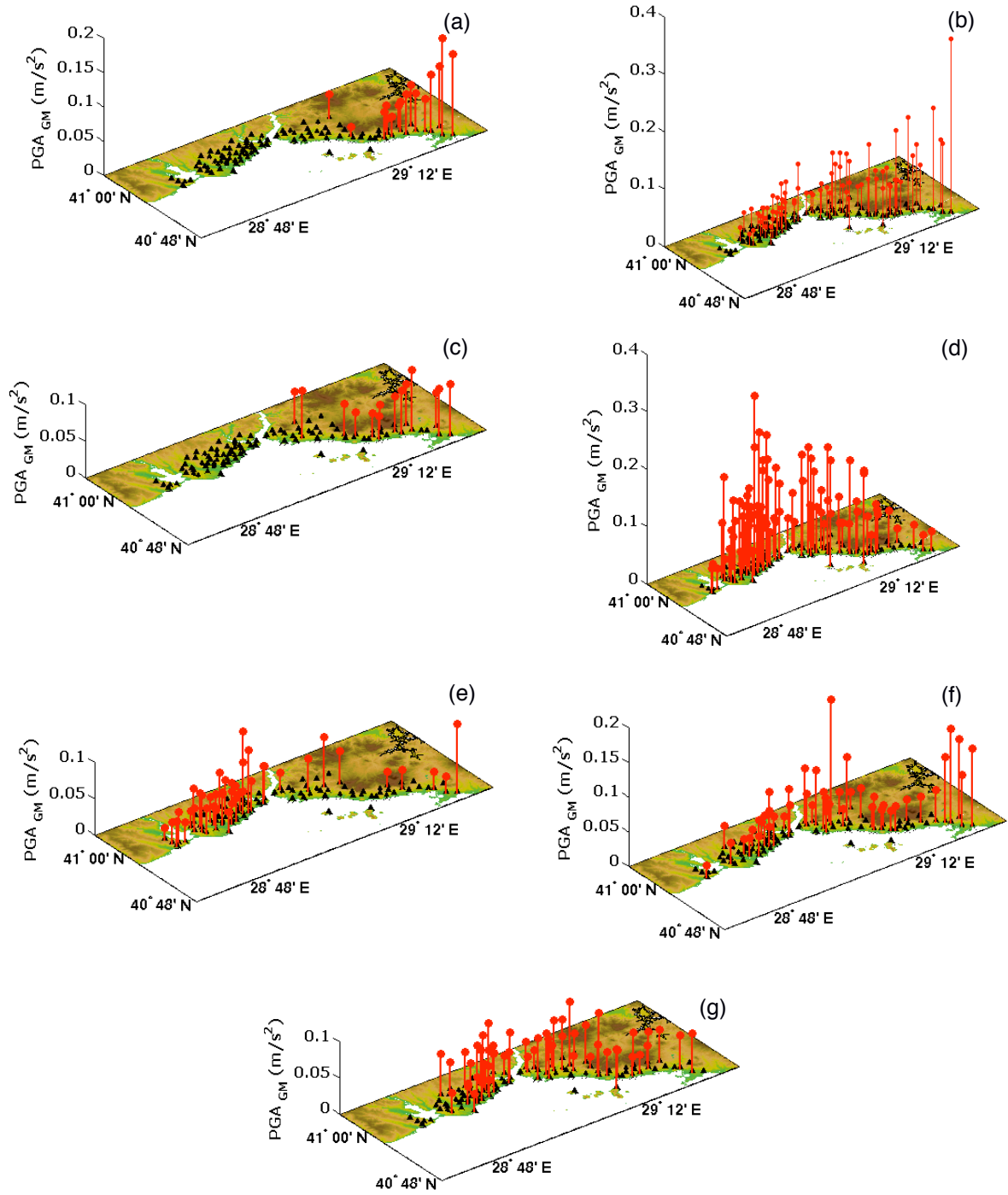


Figure 102. Peak ground accelerations for the geometric mean of the horizontal components at each Rapid Response System station triggered during the a) September 19, 2003 earthquake, b) May 16, 2004 earthquake, c) June 24, 2004 earthquake, d) September 29, 2004 earthquake, e) October 20, 2006 earthquake, f) October 24, 2006 earthquake, and g) March 12, 2008 earthquake.

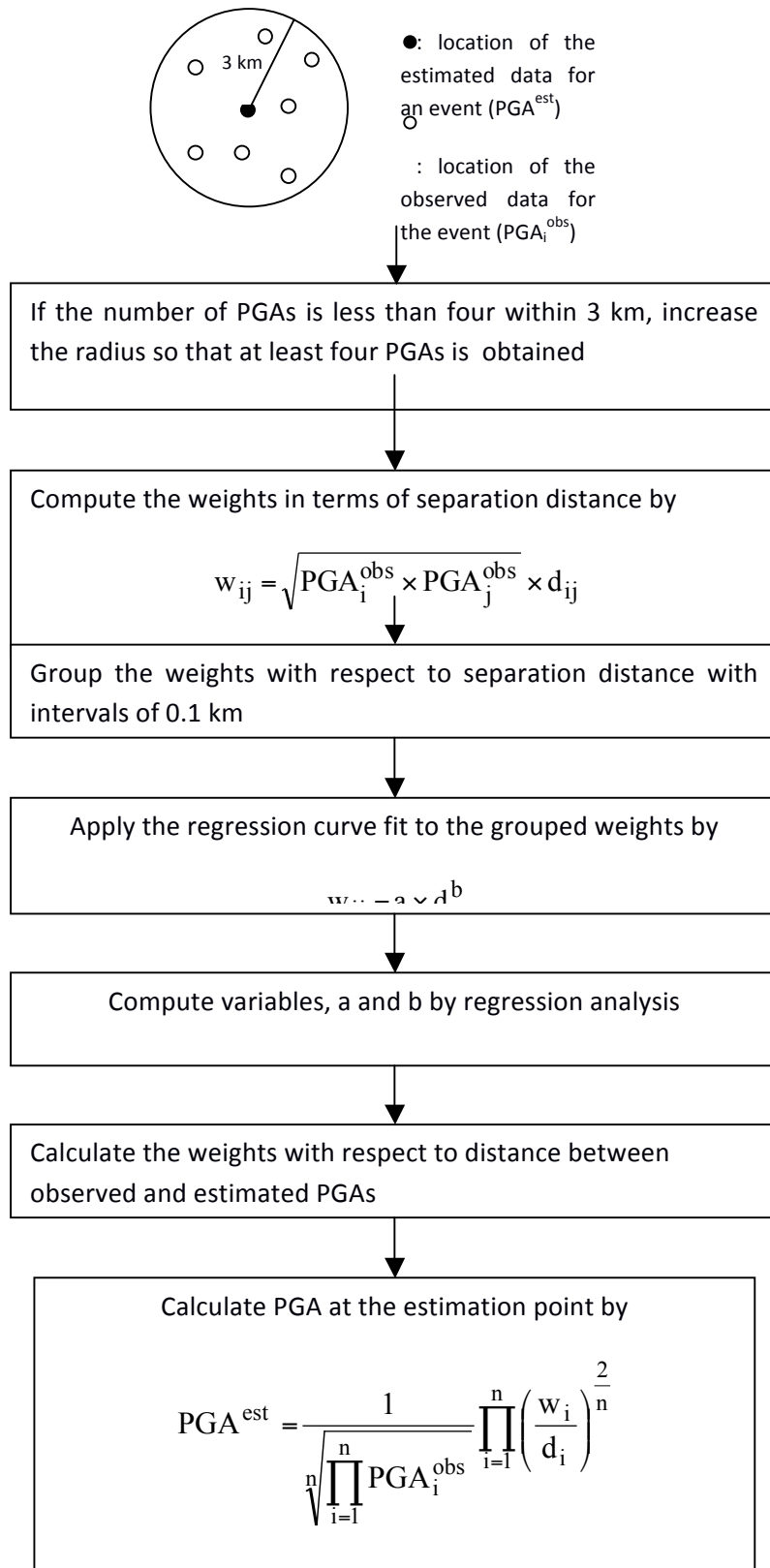


Figure 103. Procedure of the modified kriging method.

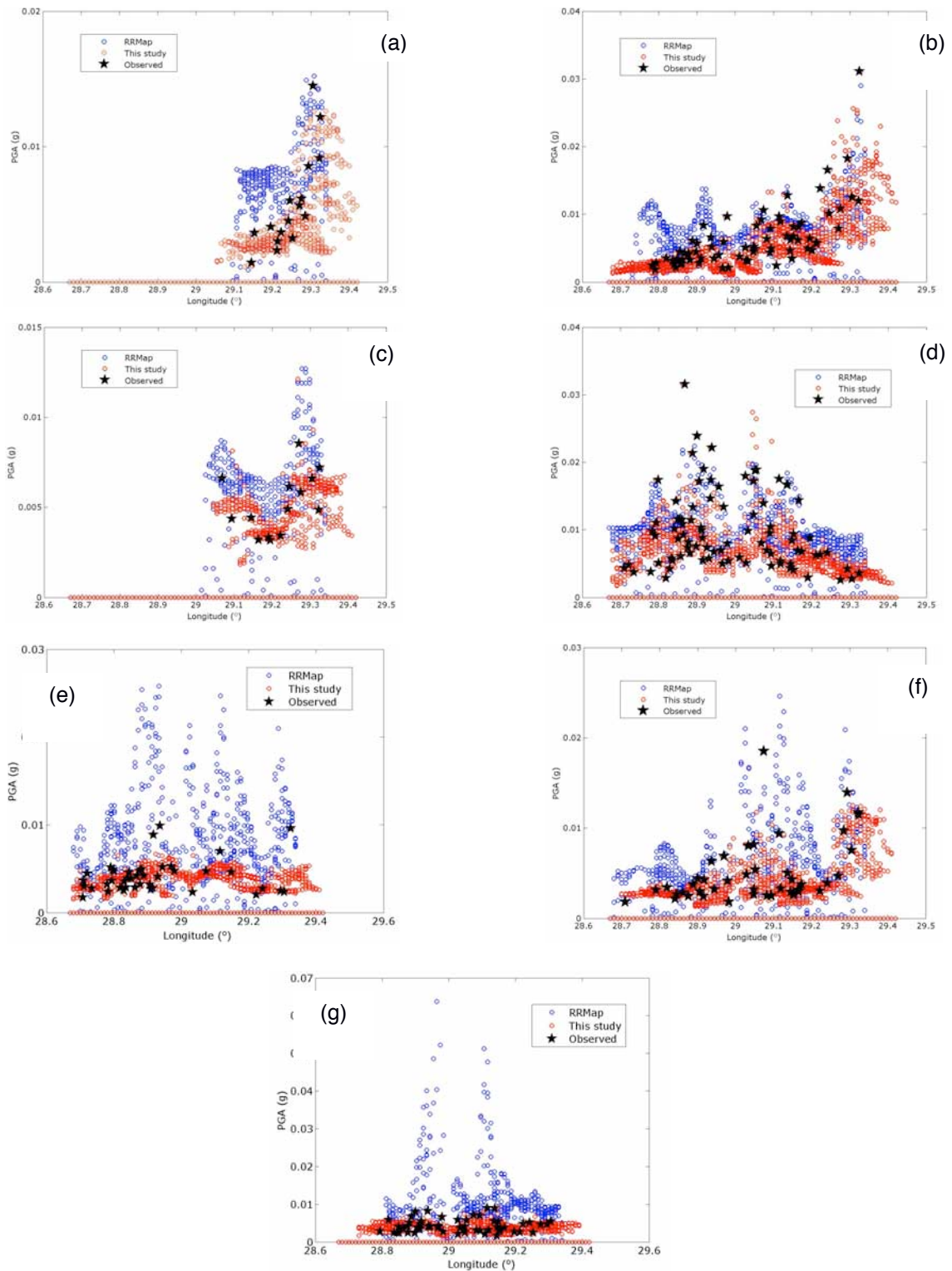


Figure 104. Comparison of PGA of the observed data (black stars) with PGA obtained by this study (red circles) and PGA obtained by RRMMap software (blue circles) at each phantom station using the data triggered during (a) the September 19, 2003 earthquake, (b) the May 16, 2004 earthquake, (c) the June 24, 2004 earthquake, (d) the September 29, 2004 earthquake, (e) the October 20, 2006 earthquake, (f) the October 24, 2006 earthquake, and (g) the March 12, 2008 earthquake.

3.5 Development of Coherency Models (KOERI)

INTRODUCTION

A large number of studies confirmed that the correlation of seismic ground motion decreases as the frequency and the separation distance between the stations increase. For the quantification of the variability of seismic ground motion, Schneider et al. (1990) used Fourier amplitude spectra; Abrahamson and Sykora (1993) relied on the acceleration response spectra; Joyner and Boore (1981) examined the dependence of peak horizontal acceleration and velocity on moment magnitude, distance and recording site geology. Abrahamson (1988) studied the relationship between the intra-event variation of peak ground acceleration (PGA) and earthquake magnitude. Kawakami and Mogi (2003) analyzed the spatial intra-event variability of PGAs as a function of separation distance. The study of Field et al. (1997) addressed the variability of pseudo-velocity response spectra. Evans et al. (2003) repeated the analysis by using pseudo-spectral velocity (PSV) response spectra as a function of inter-station distance. On the other hand, coherency is commonly used to describe the spatial variation, since previous studies have shown that the spatial variation of strong ground motion is strongly dependent on frequency (Loh et al., 1982; Smith et al., 1982; McLaughlin, 1983; Harada, 1984; Abrahamson, 1985). Modeling of the spatial variability of seismic ground motion is important for the design of aboveground and buried structural systems where multiple-support excitation needs to be considered. Spectral representation method (Rice, 1944; Shinozuka, 1972); AR (auto-regressive), MA (moving-average), and ARMA (auto-regressive-moving-average) models (Conte et al. 1992; Ellis and Cakmak, 1991; Mignolet and Spanos, 1992; Spanos and Mignolet 1992; Shama, 2007); local average subdivision method (Fenton and Vanmarcke, 1990); covariance matrix decomposition (Hao et al., 1989, Zerva and Katafygiotis, 2000); envelope functions containing random phase variability (Abrahamson, 1992); and coherency function approximation by a Fourier series (Ramadan and Novak,

1993b; Ramadan and Novak, 1994) are some of the methods used for the simulation of spatially variable strong ground motion. This study has two foci: (1) derivation of a coherency model for Istanbul that can be used in the simulati

on of spatially variable ground motion needed for the design of extended structures; and (2) constitution of a simulation scheme that generates ground motion compatible with the prescribed design response spectrum and consistent with the prescribed coherency function. The coherency model is derived based on data of six events recorded by Istanbul Earthquake Rapid Response System (IERRS) stations.

DEFINITION OF COHERENCY

The spatial variability of ground motion is generally characterized using the notions of correlation and coherency. Characterization of phase variability in time is correlation; in frequency domain it is coherency. The frequency domain description is used because of its mathematical convenience in random vibration analysis. Matsushima (1977); Abrahamson (1990); Harichandran (1991); and Zerva and Zervas (2002) are some of the authors who studied the variation in frequency domain. The normalized cross-power spectrum, namely the coherency function $\gamma_{xy}(\omega)$, between two accelerograms recorded at two stations x and y is given as follows:

$$\gamma_{xy}(\omega) = \frac{S_{xy}(\omega)}{\sqrt{S_{xx}(\omega)S_{yy}(\omega)}} \quad (3.12)$$

in which $S_{xy}(\omega)$ is the cross-power spectral density between stations x and y , $S_{xx}(\omega)$ is the power spectral density at station x and $S_{yy}(\omega)$ is the power spectral density at station y . Coherency is a complex number. The absolute value of the coherency, called as lagged coherency and commonly used in engineering applications, removes the effects of simple inclined plane wave propagation (Abrahamson et al., 1991).

ARRAY AND EARTHQUAKES

The Istanbul Earthquake Rapid Response System (IERRS) that includes 100 strong motion stations provided data for the estimation of coherency values. All stations consist of external, tri-axial (three orthogonal axes), force-balance (servo) type accelerometers, recorders, timing and communication modules (Erdik *et al.*, 2003). The inter-station distances of the IERRS stations vary between 0.67 km and 56 km. Since the deployment of the IERRS in 2001, a series of moderate and small earthquakes have been recorded. In this study, six of them are used. Their source properties are summarized in Table 15. The magnitudes of chosen earthquakes range from 3.1 to 5.2. Minimum epicentral distances vary between 1 and 101 km, and maximum epicentral distances change between 16 and 130 km (Table 15). Source mechanisms are dominantly strike-slip for the first five earthquakes. The sixth earthquake has a dominantly normal mechanism (<http://www.koeri.boun.edu.tr/sismo/map/en/index.html>).

EVALUATION OF COHERENCY VALUES

Coherency values for the six events recorded by IERRS are calculated using a code written in MATLAB for different distance bins. The term 'distance' denotes station separation distance. The coherency values are calculated using the data from east-west (EW); north-south (NS); radial (R); and transversal (T) directions considering both 11- and 15- point hamming windows. Seven distance bins are used. The bins are: Less than 2.0 km; 2.0-2.5 km; 2.5-3.0 km; 3.0-3.5 km; 3.5-4.0 km; 4.0-4.5 km; and 4.5-5.0 km. The coherencies are averaged in each distance bin. In Figure 106, the computed average coherency values are illustrated for different directions and smoothing window lengths for the September 29, 2004 earthquake. As it is expected, coherency values decrease with the increase of separation distance. EW component has higher coherency at about 3 Hz for the separation distance less than 2 km (Figure 105a). the coherencies are arranged with

respect to the earthquake source, in other words, direction of the wave propagation by separating them into R and T components, to investigate any dependency the coherency may have on them. There was no relation between wave propagation direction and the coherency for data triggered by six earthquakes. In Figure 106; (a), (b), (c), (d), (e), and (f) demonstrate the coherency values for distance bins for the September, 19 2003; May 16, 2004; September, 29 2004; October 20, 2006; October 24, 2006; and March 12, 2008 earthquakes, respectively. Totally, 332 recorded data triggered by Istanbul Earthquake Rapid Response System (IERRS) are used. The coherency values are calculated for 9837 pairs. As it can be seen in Figure 107, magnitude dependence of coherency for frequency-distance behavior is not clear. The main reason is that the number and location of the recorded data vary from earthquake to earthquake. In Figure 106b and Figure 106c, the variation of coherencies with respect to distance and frequency is clearly displayed. This can be attributed to higher number of recording stations in these two earthquakes. High coherencies (0.8) are detected around the region of 1.5-3 km and 0-3 Hz except for September 19, 2003 (Figure 106a) and November 20, 2006 earthquakes (Figure 106b). Generally, coherency values are higher than 0.6 at the frequencies less than 5 Hz. Coherency values are approximately 0.65 at the zone of 2-4 Hz and 1.5-2.8 km (Figure 106b, c, e, f).

DEVELOPMENT OF COHERENCY MODEL

The decay of the coherency with respect to frequency, estimated based on IERRS data, is approximately exponential (Figure 105). Several formulae involving exponential terms have been developed and tested to reach the expression:

$$|\tilde{\alpha}(d, f)| = a_1 e^{(a_2 - a_3 \sqrt{f})d} + (1 - a_1) e^{(-a_4 - a_5 f^2)d^2} \quad (3.13)$$

Regression analyses are done for six earthquakes separately. The results are listed in Table 16. The last column of Table 16 represents the results of the regression analysis carried out using the whole data set that includes all coherency values from six earthquakes. It is seen that five parameters, a_1 , a_2 , a_3 , a_4 , and a_5 , are close to each other for every event and whole data set.

The logarithmic residuals of these earthquakes are plotted in Figure 107 for seven separation distance bins. Each distance bin in Figure 107 includes the combined coherency values from six earthquakes. The residuals are calculated as logarithmic distance of observed and estimated coherency values. The mean residuals vary between +0.2 and -0.2. No systematic trends can be observed in the residuals. They show no dependency on the frequency or the distance bin. The coherency model developed for Istanbul can be seen in Figure 108 for distances of 100m, 300m, 500m, 1000m, 3000m, and 5000m. It is developed using data from earthquakes having magnitudes smaller than 5.2 and is better resolved for the distance bins of less than 2.0 km; 2.0-2.5 km; 2.5-3.0 km; 3.0-3.5 km; 3.5-4.0 km; 4.0-4.5 km; and 4.5-5.0 km.

SIMULATION OF SPATIALLY VARIABLE GROUND MOTION

The objective herein is to generate earthquake ground motion for a finite array of ground surface stations, including the reference station. They need to be compatible with a prescribed design response spectrum at a reference station and their coherencies have to be consistent with the target coherency function. First, target response spectrum compatible earthquake ground motions are simulated using code RSPATCH2005 (Abrahamson, 1998; Hancock et al., 2006). Then, they are used to generate the ground motion that produce coherencies in agreement with the target coherency function following Shama (2007). The coherency compatible simulation methodology is used to simulate an accelerogram at station R85 that is located at 1.82 km from the record at station R00 obtained during the October 3, 2010 earthquake with a local magnitude of 4.4. The recorded ground motion has a

sampling rate of 200 Hz. In Figure 109a the reference record at R00 is displayed at the top row. The simulated ground motions, at 1.82 km distance from the reference data are compared with the observed data shown in red in Figure 109. Besides the fact that simulated accelerations are consistent with those of the observed record, ground velocity and displacement time histories are also in good agreement with observed data. It is observed that the Fourier amplitude spectrum of simulated ground motion is consistent with the observed ground motion at 1.82 km for the frequencies less than 10 Hz (Figure 109d). The acceleration response spectra of the simulated motion presented in Figure 109e slightly underestimates the observed response spectrum. The coherency values are computed by using reference data and simulated data for a station located 1.82 km away from the reference point. The target coherency spectrum at 1.82 km separation distance is plotted in Figure 109. The computed coherencies using reference and simulated data are compared with the target coherency spectrum. It is shown that the computed coherency values are in good agreement with that of the target coherency model.

CONCLUSIONS

The spatial variability of earthquake ground motion can be important for the response of linear lifelines such as bridges, pipelines, communication systems, and should preferably be accounted for in their design. The derived empirical coherency function for Istanbul in terms of frequency and separation distance correlates well with the observed data recorded by IERRS as indicated by the residuals. The model can be used for the assessment and simulation of spatially variable ground motion in Istanbul. Additionally a procedure is developed to generate earthquake ground motions that are compatible with given target response spectrum, as per Hancock et al. (2006), and that have coherencies consistent with the coherency model generated for Istanbul using the model derived by Shama (2007). The procedure was tested for two separation distances, 0.5km and 1.82km. The

agreement between the simulated and reference ground motions was found satisfactory for both cases.

Table 15. Source properties of the earthquakes recorded by IERRS

(<http://www.koeri.boun.edu.tr/sismo/default.htm>)

No	Eq.	Date	Latitude N	Longitude E	GMT	M _L	M _d	Number of recording stations	Max. Epicentral Distance (km)	Min.n Epicent Distan (km)
1	Güzelyalı	19/09/2003	40.8498	29.2867	00:51	3.1	3.2	16	16	1
2	Yalova	16/05/2004	40.6957	29.3222	03:30	4.3	4.2	72	58	14
3	Marmara Sea	29/09/2004	40.7797	29.0200	15:42	4.0	-	86	34	14
4	Kuşgölü	20/10/2006	40.2635	27.9843	21:15	-	5.2	43	130	101
5	Gemlik	24/10/2006	40.4240	28.9947	17:00	-	5.2	47	70	52
6	Çınarcık	12/03/2008	40.6210	29.0110	20:52	4.8	-	54	50	30

Table 16. Regression coefficients for data recorded by IERR

	2003.09.19 earthquake	2004.05.16 earthquake	2004.09.29 earthquake	2006.10.20 earthquake	2006.10.24 earthquake	2008.03.12 earthquake	All data
a₁	0.5298	0.4813	0.5620	0.4708	0.4702	0.5023	0.5130
a₂	0.0253	0.0867	0.4155	0.0777	0.1071	0.1320	0.0781
a₃	0.0170	0.0399	0.0263	0.0446	0.0398	0.0517	0.0380
a₄	0.3795	0.1925	0.1444	0.3081	0.2137	0.1926	0.2643
a₅	0.0067	0.0233	0.0409	0.1000	0.0248	0.0302	0.0301

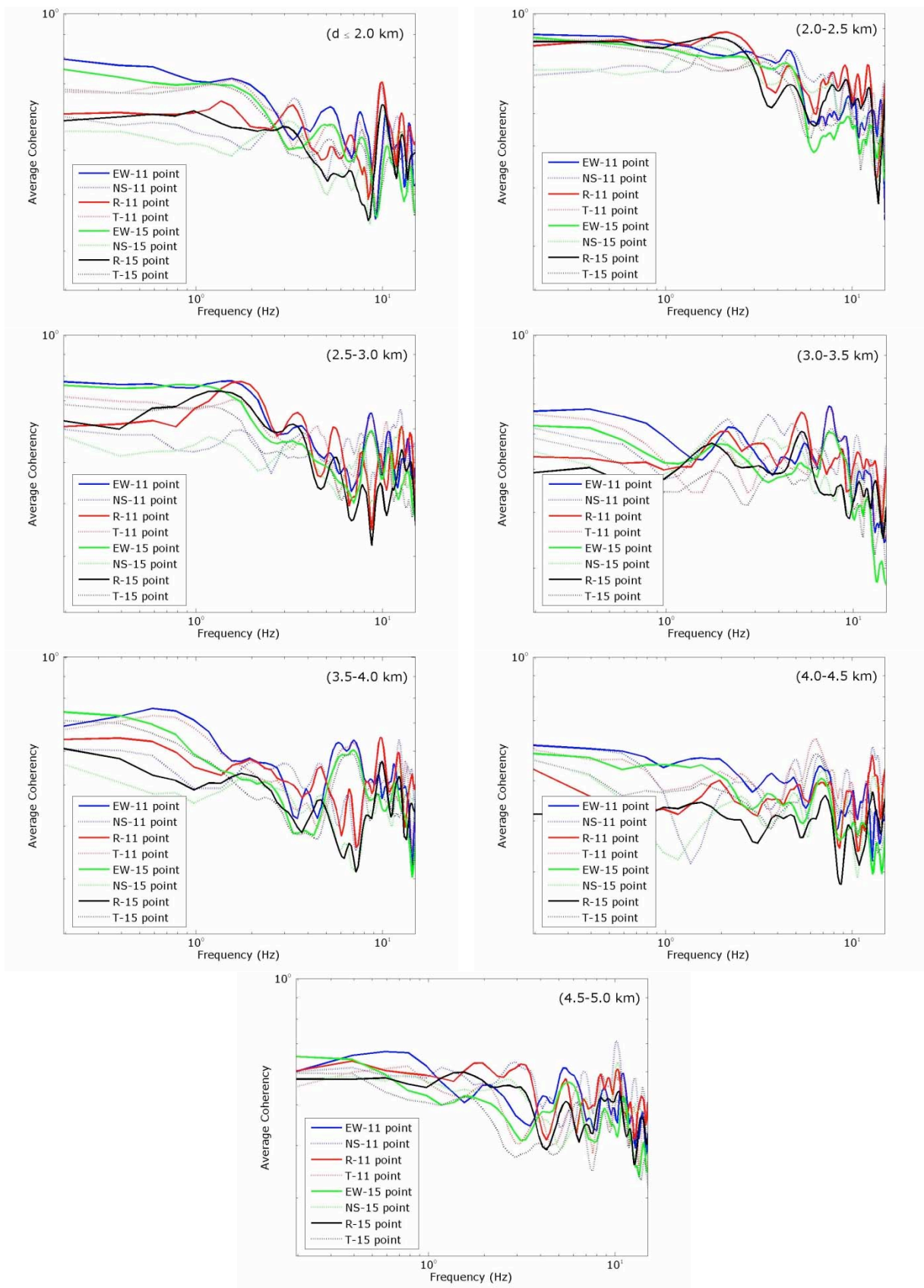


Figure 105. Average coherency values of distance bins with respect to direction and smoothing window length –September 29, 2004 earthquake

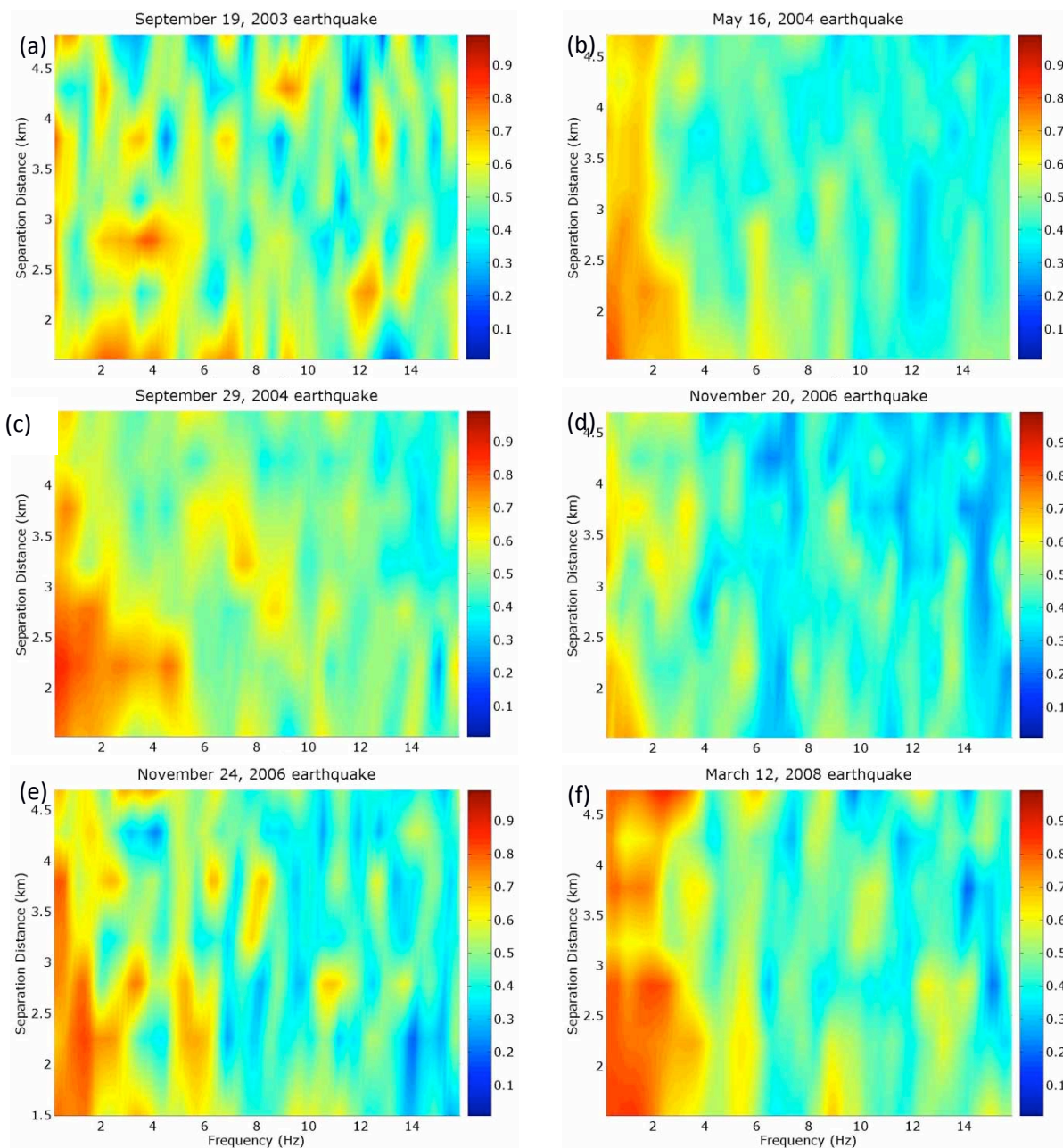


Figure 106. Coherency values for distance bins and average coherency values in the EW direction (11-point): (a) September, 19 2003 earthquake; (b) May 16, 2004 earthquake; (c) September, 29 2004 earthquake, (d) October 20, 2006 earthquake, (e) October 24, 2006 earthquake, (f) March 12, 2008 earthquake

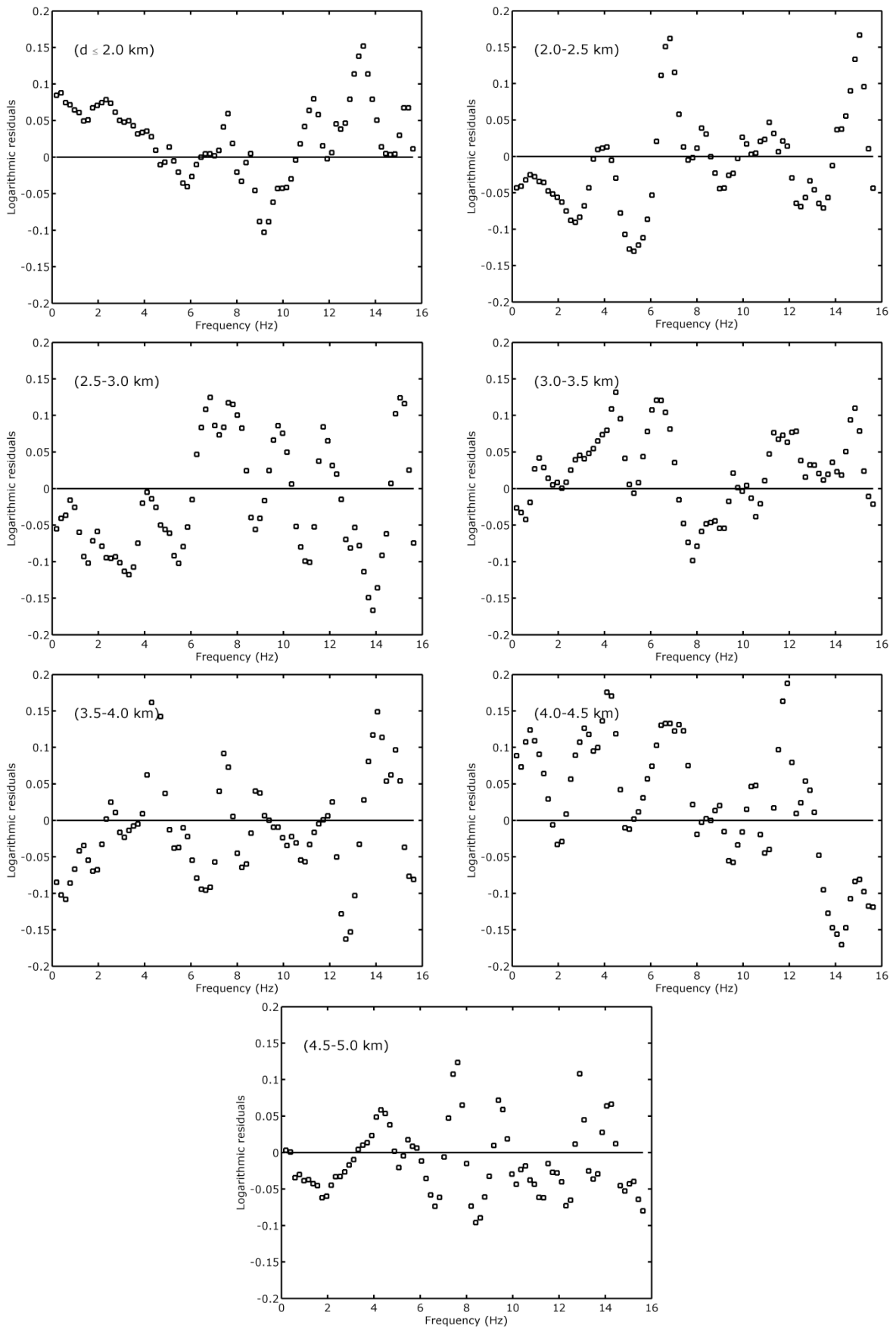


Figure 107. Residuals of the coherency model for each distance bin

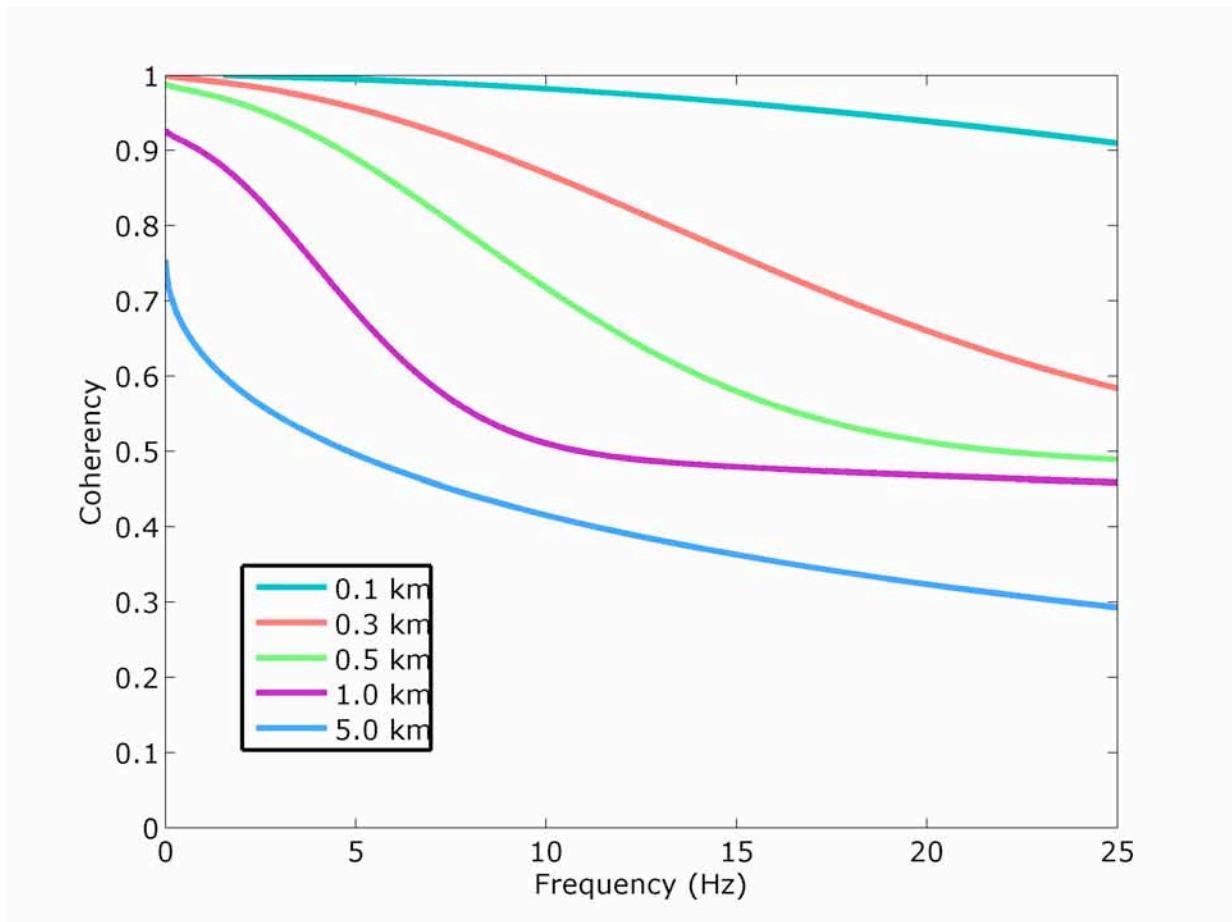


Figure 108. Decay of coherencies with respect to frequency for different station separation distances

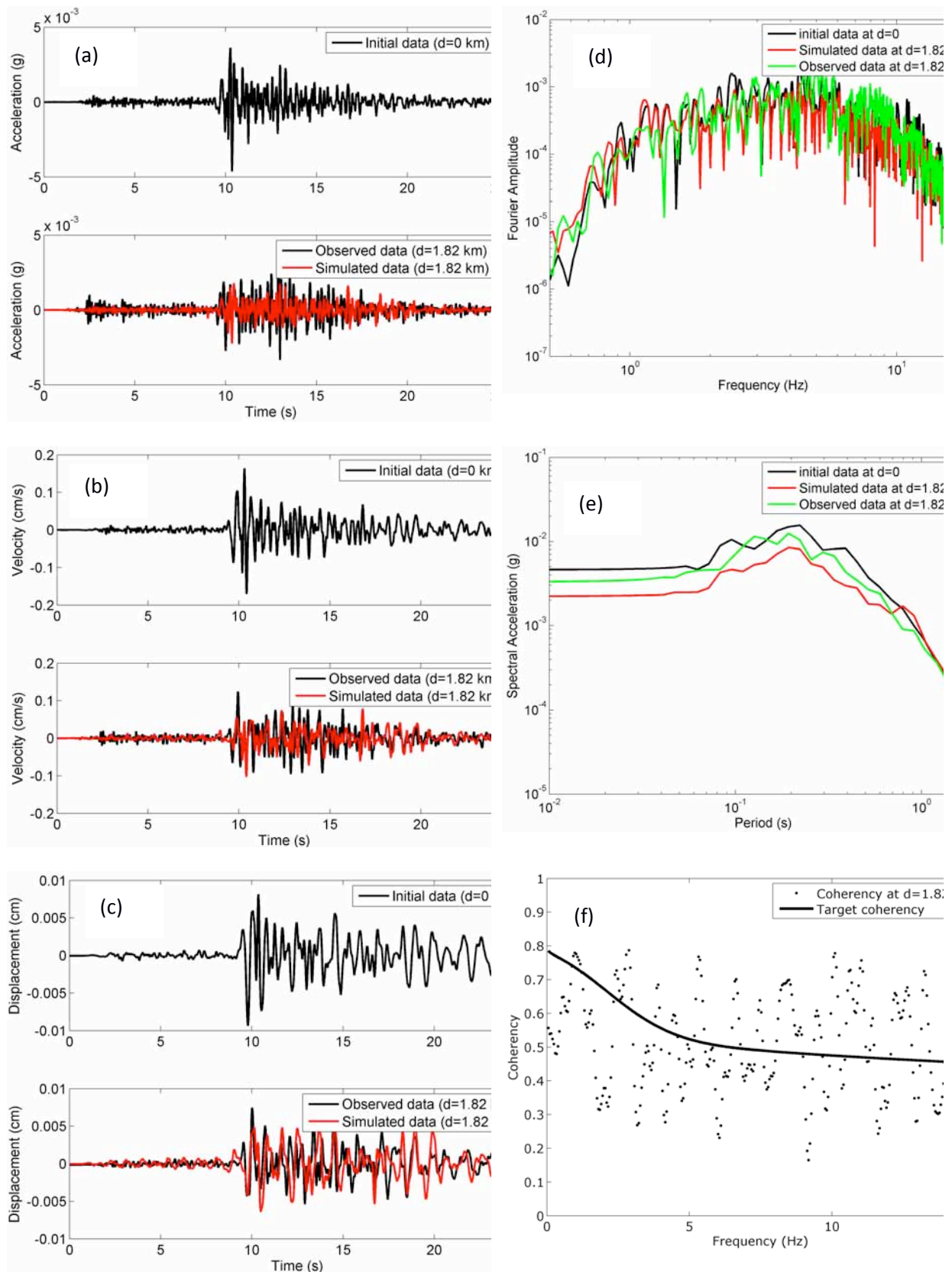


Figure 109. Comparison of time histories of reference station with observed and simulated data at $d=1.82$ km: (a) Acceleration, (b) Velocity, (c) Displacement, (d) Fourier amplitude spectrum, (e) Response spectrum, (f) Coherency spectrum

4. Conclusions

In summary, within the project we investigated the relative contribution of source, local sites and scattering effects to ground motion. Below we report the main results and conclusions in synthetic bullet-style list.

Following are the main conclusions we can draw from our analysis of the source:

- we have analyzed the magnitude and distance dependency of sigma, through numerical ground-motion simulations. Our results suggest that the PGV variability: (1) decreases with distance for small magnitudes and (2) decreases with magnitude at short distances from the source (for details see Section 2.1);
- our results indicate that fracture energy, static and dynamic stress drop, and apparent stress drop tend to increase with magnitude. The epistemic uncertainty due to uncertainties in kinematic inversions remains small ($\phi \sim 0.1$ in \log_{10} units), showing that kinematic source models provide robust information to analyze the distribution of average dynamic source parameters (for details see Section 2.2);

In particular, our results from the study of the 2009 L'Aquila earthquake suggest that:

- near fault stations reveal complex waveforms that can be reproduced only taking into account complex source effects and reliable propagation. For the L'Aquila case, in fact, low frequency source model needs to be coupled with a 3D modelling of the basin to retrieve the right frequency content in the low/intermediate range (0.5-1Hz), (for details see Section 2.5.1);
- as for the source parameters, the rise time variability plays the major role in controlling the high frequency spectrum of the simulation. This variability can be directly linked to the high frequency behavior of the model. Changes in the slip roughness play

- a secondary role (for details see Section2.5.1);
- when using EGF approach, the selection of EGF is a critical issue for correct modelling of the ground motion. Changing the EGF can lead to changes in the Fourier and response spectra of one order of magnitude in near fault at some frequencies (for details see Section2.5.1);
 - far field data are well constrained by the average model. Fourier spectrum sigma is less than one order of magnitude. In near fault, some frequencies appear underestimated and the sigma in the Fourier spectrum is larger than one order of magnitude (for details see Section2.5.1);
 - high frequency ground motion in the study region of the 2009 L'Aquila earthquake decays faster when compared to the average trends described by national and global GMPEs. The discrepancy between predictions by both GMPEs and ground motion simulations and observations are found to be also dependent on the source directivity, which is significantly pronounced for the 2009 L'Aquila earthquake (for details see Section2.5.3);
 - we demonstrated the importance of choosing the critical region-specific source and attenuation parameters and their influence on the simulated ground motions. Despite the limitations of the method in simulating the directivity effects, it is observed that a stochastic finite-fault model is an effective tool for estimating the peak ground motion parameters of near-to-intermediate field ground motions. Advanced source models taking into account dynamic effects of rupture propagation may lead to improvements in the simulation results, and future detailed investigation of local soil conditions may be used to reduce the uncertainty due to the site amplifications. Finally, the results obtained in this study may be combined with low-frequency simulations of the mainshock radiation, in order to obtain broadband seismograms (for details see Section2.5.3);
 - the cross-over frequency range in the HIC model divides the low -

frequency (coherent/deterministic) and high-frequency (incoherent/stochastic) parts of the simulated wavefield. Use of higher cross-over frequency range allows modeling the long-period pulses in velocity records observed at the closest stations by means of the integral approach. The lower frequency range for the further stations suggests that a purely deterministic modeling of rupture directivity is not suitable in this case, and that the stochastic (composite) approach is needed in almost the whole frequency band (for details see Section 2.5.4);

- the HIC broadband modeling of the 2009 L'Aquila earthquake, yielded strong conclusions not only to earthquake physics but also to ground-motion simulations for hazard analyses and earthquake engineering applications. It is shown that purely composite and/or stochastic models without the possibility of modeling the coherent low-frequency wavefield by the integral approach would meet difficulties when explaining the near-source directivity pulses observed at AQ_ stations. Correct modeling of pulse-type records is of great relevance to structural engineering because their seismic demand and spectral shape are different with respect to ordinary records and can generate much higher damage (for details see Section 2.5.4).

We have developed a suite of rupture dynamic simulation to evaluate ground-motion variability generated by earthquakes in the range of magnitude $5.5 < M_w < 7.0$, with a particular focus on extreme ground motion acceleration exceeding 1g. A total of 360 source models for strike, reverse and normal faulting with buried and surface rupturing features as well as depth and non-depth dependent stress parameterization have been generated and their resulting near-field ground-motions have been examined. This diversity of rupture models creates a broad range of scenarios for evaluating near-source ground motion variability and for

identifying the causes for extreme ground motion. From this analysis (for details see Section 2.3) emerges that:

- surface rupturing events predict stronger ground motion than buried rupture, with the strongest for surface rupturing models with non-depth dependent stress;
- in general, simulated ground motion are consistent with GMPE's at distance greater than 5km, but not at short distance. The consistent saturation, very close to the source, of ground motion quantities as predicted by GMPE is not obvious in our calculations, rather, there are significant ground-motion reductions near the source, particularly for buried faults, and considerable variability for surface rupturing earthquakes;
- there is an increased variability in the near-field considering all the rupture models;
- extreme ground motion appear to be correlated with faulting that breaks the free-surface with the strongest for strike-slip rupture;
- we found ground motion at some stations very near to the source that exceed the gravity acceleration at frequencies range 1.0 to 2.5Hz, those extreme ground motions resemble the ground motion recorded during the 2011 M_w 6.3 Christchurch, New Zealand earthquake that occurs at such as frequency range.

Following are the main conclusions we can draw from our analysis of the scattering and local site effects:

- we investigated the *kappa* parameter computed from 174 records (522 components) measured at 15 different strong motion stations from 142 earthquakes with magnitudes $3.0 < M_w < 6.0$ in Northwestern Turkey. The effects of magnitude, site class and distance on *kappa* values are investigated for both the horizontal and vertical components. A regional model is also presented for

future use in stochastic simulations and GMPE adjustments. Based on 5% confidence interval, t-tests indicate no linear relation of *kappa* on earthquake magnitude for the dataset used. However, site class influences the computed *kappa* values significantly. Our numerical results for zero-distance *kappa* values are consistent with the worldwide data and the previous findings from smaller datasets in the same region (for details see Section3.2);

- the effect of magnitude on *kappa* is found to be statistically not significant for the database studied herein. However, in future studies with more near-fault data, it will be possible to focus on the scatter of the near-field *kappa* values and treat them separately for potential source effects (for details see Section3.2).

Through the numerical experiments conducted in the study of nonlinear dynamic building response to simulated ground motions, we can draw the following conclusions:

- among the two simulation methods used, for most of the stations the Stochastic Finite-Fault model yields more conservative results because of overestimation of the nonlinear response. On the other hand, Hybrid Integral Composite method mostly provides accurate results as it covers the broadband frequency range. However, due to some frequency bands where the synthetics are not close to the real amplitudes, the response under the simulated record from HIC method does not always match the real response closely. Therefore, when a poor fit is obtained from a seismological point of view, a similar outcome is observed from the engineering point of view (for details see Section3.3);
- in general, misfits obtained in terms of the ground motion parameters (i.e. RS and FAS) are in agreement with those obtained for dynamic response of the frames. Among RS and FAS misfits, we

observed that RS misfits are mostly in better agreement with NR misfits (for details see Section3.3);

- it is generally known that the match between a target response spectrum (real record in this case) and a synthetic response spectrum determines the fit between the linear elastic response under real and synthetic records. Our numerical results indicate that for all cases, even when nonlinear behavior is more likely, period-dependent SDOF indicators of goodness of fit between the real and synthetic records match MDOF behavior of those real frame structures. Thus, SDOF-based misfits that cover the fundamental period range of the frames describe the nonlinear response sufficiently (for details see Section3.3);
- the match between the Fourier Amplitude Spectrum of the real and synthetic record around the frequencies that correspond to the fundamental period of the structure governs the nonlinear response. Thus, it is important to simulate realistic amplitudes over the entire broadband frequency range of interest for earthquake engineering purposes in order to cover all types of buildings with a range of fundamental periods (for details see Section3.3);
- for the specific case of the 2009 L'Aquila earthquake, simulated records that seismologically satisfy a certain goodness of fit criterion yield nonlinear responses that are acceptable when compared to the real responses (in terms of story displacements), (for details see Section3.3);
- synthetic records that reasonably overestimate the nonlinear response could be conservatively used for seismic design and assessment purposes (for details see Section3.3).
- The spatial variability of earthquake ground motion can be important for the response of linear lifelines such as bridges, pipelines,

communication systems, and should preferably be accounted for in their design. The coherency models developed in this work (for details see Section 3.5) show that:

- empirical coherency function for Istanbul in terms of frequency and separation distance correlates well with the observed data recorded;
- the obtained model can be used for the assessment and simulation of spatially variable ground motion in Istanbul. Additionally, a procedure is developed to generate earthquake ground motions that are compatible with given target response spectrum, and that have coherencies consistent with the coherency model generated for Istanbul. The procedure was tested for two separation distances, 0.5km and 1.82km. The agreement between the simulated and reference ground motions was found satisfactory for both cases.

References

- Abrahamson, N.A., 1985. Estimation of Seismic Wave Coherency and Rupture Velocity Using the SMART-1 Strong Motion Array Recordings. EERC Report No. EERC/UCB/85-02, Earthquake Engineering Research Center, University of California.
- Abrahamson, N.A., 1988. Statistical Properties of Peak Ground Accelerations Recorded by the Smart 1 Array. *Bulletin of the Seismological Society of America* 78, 26-41.
- Abrahamson, N.A, Schneider, J.F., Stepp, J.C., 1990. Spatial Variation of Strong Ground Motion for Use in Soil-Structure Interaction Analyses. *Proceedings of Fourth U.S. National Conference on Earthquake Engineering*, Palm Springs, California.
- Abrahamson, N.A., 1992. Generation of Spatially Incoherent Strong Motion Time Histories. *Proceedings of Tenth World Conference on Earthquake Engineering*, Madrid, Spain.
- Abrahamson, N.A., Sykora, D., 1993. Variations of Ground Motions Across Individual Sites. *Proceedings of the Fourth DOE Natural Phenomena Hazards Mitigation Conference*, 9192-9198, Atlanta, Georgia.
- Akansel, V., G. Ameri, A. Askan, A. Caner, B. Erdil, Ö. Kale, and D. Okuyucu (2013). The 23 October 2011 Mw 7.0 Van (Eastern Turkey) Earthquake: Interpretations of Recorded Strong Ground Motions and Post Earthquake Conditions of Nearby Structures, in press at *Earthquake Spectra*.
- Akinci A., L. Malagnini and F. Sabetta (2010). Characteristics of the strong ground motions from the 6 April 2009 L'Aquila earthquake, Italy, *Soil Dyn Earthquake Eng.*, **30**, 320-335.
- Akinci A, Antonioli A (2013) Observations and stochastic modelling of

strong ground motions for the 2011 October 23 M_w 7.1 Van, Turkey earthquake. *Geophys J Int* 192(3):1217–1239

Akkar, S., and J. J. Bommer (2010). Empirical Equations for the Prediction of PGA, PGV and Spectral Accelerations in Europe, the Mediterranean Region and the Middle East, *Seismological Research Letters*, **81**, 195-206.

Akkar S, Cagnan Z (2010) A local ground-motion predictive model for Turkey and its comparison with other regional and global ground-motion models. *Bull Seismol Soc Am* 100:2978–2995

Al Atik L, Abrahamson N, Bommer JJ, et al, The Variability of Ground-Motion Prediction Models and Its Components, *Seismological Research Letters* 794-801, Volume 81, Number 5, doi: 10.1785/gssrl.81.5.94.

Altiner Y, Söhne W, Güney C, Perlt J, Wang R, Muzli M (2013) A geodetic survey of the 23 October 2011 Van, Turkey earthquake. *Tectonophysics* 588:118–134

Ameri, G., D. Bindi, F. Pacor, and F. Galadini (2011). The 2009 April 6, Mw 6.3, L'Aquila (central Italy) earthquake: Finite-fault effects on intensity data, *Geophys. J. Int.* 186, 837–851.

Ameri G., F. Galovic and F. Pacor (2012). Complexity of the Mw6.3 2009 L'Aquila (central Italy) earthquake: 2. Broadband strong motion modeling, *Journal of Geophysical Research*, VOL. 117, B04308, doi:10.1029/2011JB008729, 2012.

Anderson JG, Hough SE (1984) A model for the shape of the Fourier spectrum of acceleration at high frequencies. *Bull Seismol Soc Am* 74:1969–1993

Anderson JG, Quaas R (1988) The Mexico earthquake of September 19, 1985-Effect of magnitude on the character of strong ground motion: An example from the Guerrero, Mexico strong motion network. *Earthq Spectra* 4:635–646

Anderson, J. G., and J. N. Brune (1999). Probabilistic seismic hazard assessment without the ergodic assumption. *Seismological Research Letters* 70 (1), 19–28.

Andrews, D. J., (1999), Test of two methods for faulting in finite-difference calculations, *Bull. Seismol. Soc. Am.*, 89(4), 931-937.

Asano, K., T. Iwata, and K. Irikura (2005), Estimation of source rupture process and strong ground motion simulation of the 2002 Denali, Alaska, earthquake, *Bull. Seismol. Soc. Am.*, 95, 1701–1715, doi:10.1785/0120040154.

Askan A., F.N. Sisman and O. Pekcan, A Regional Near-Surface High Frequency Spectral Attenuation (Kappa) Model for Northwestern Turkey (2013), submitted to *Soil Dynamics and Earthquake Engineering*.

Atkinson GM, Boore DM (1995) Ground-motion relations for eastern North America. *Bull Seismol Soc Am* 85:17–30

Baumann C. and L.A. Dalguer (2013), Evaluating the Compatibility of Dynamic-Rupture- Based Synthetic Ground Motion with Empirical GMPE. *Bull. Seismol. Soc. Am.* In review

Becel, A., Laigle, M., de Voogd, B., Hirn, A., Taymaz, T., Galve, A., Shimamura, H., Murai, Y., Lepine, J.C., Sapin, M., Ozalaybey, S., 2009. Moho, crustal architecture and deep deformation under the North Marmara Trough, from the SEISMARMARA Leg 1 offshore-onshore reflection-refraction survey. *Tectonophysics* 467, 1–21.

Beresnev I, Atkinson GM (1997) Modeling finite-fault radiation from the ω n spectrum. *Bull Seismol Soc Am* 87:67–84

Beresnev I, Atkinson GM (1998a) FINSIM—a FORTRAN program for simulating stochastic acceleration time histories from finite faults. *Seism Res Lett* 69:27–32

Beresnev I, Atkinson GM (1998b) Stochastic finite-fault modeling of

ground motions from the 1994 Northridge, California, earthquake. I. Validation on rock sites. *Bull Seismol Soc Am* 88:1392–1401

Berryman, K (2011), A tale of two earthquakes – the Christchurch sequence of 2010-2011, Proc. G-Ever1 Conference, Tsukuba, march 2011.

Bianchi, I., C. Chiarabba, and N. Piana Agostinetti, (2010), Control of the 2009 L'Aquila earthquake, central Italy, by a high-velocity structure: A receiver function study, *J. Geophys. Res.*, 115, B12326, doi: 10.1029/2009JB007087.

Bindi, D., F. Pacor, L. Luzi, M. Massa and G. Ameri (2009). The Mw 6.3, 2009 L'Aquila earthquake: source, path and site effects from spectral analysis of strong motion data, *Geophys. J. Int.* **179**, 1573-1579.

Boore DM (1983) Stochastic simulation of high-frequency ground motions based on seismological models of the radiated spectra. *Bull Seismol Soc Am* 73:1865–1894

Boore DM, Joyner W (1997) Site amplification for generic rock sites. *Bull Seismol Soc Am* 87:327–341

Boore DM (2003) Prediction of ground motion using the stochastic method. *Pure Appl Geophys* 160:635–676

Boore, D. M., Lamprey, J.W. and Abrahamson, N. A., (2006). Orientation-Independent Measures of Ground Motion. *Bulletin of the Seismological Society of America*, Vol. 96, No. 4A, pp. 1502–1511, August 2006, doi: 10.1785/0120050209.

Boore DM, Atkinson GM (2008) Ground motion prediction equations for the average horizontal component of PGA, PGV, and 5%-damped PSA at spectral periods between 0.01 s and 10.0 s. *Earthq Spectra* 24:99–138

Boore DM (2009) Comparing Stochastic Point-Source and Finite-Source Ground-Motion Simulations: SMSIM and EXSIM. *Bull Seismol Soc Am* 99:3202–3216

Borcherdt RD (1994) Estimates of site-dependent response spectra for design (methodology and justification). *Earthquake Spectra* 10(4):617–653

Borcherdt RD (2002) Empirical evidence for acceleration-dependent amplification factors. *Bull. Seis Soc Am.* 92(2):761–782.

Bouchon, M. (1981). A simple method to calculate Green's functions for elastic layered media, *Bull. Seismol. Soc. Am.* 71, 959-971.

Bouchon, M., (1997), The state of stress on some faults of the San Andreas system as inferred from near-field strong motion data, *J. Geophys. Res.*,102(B6), 11731-1744.

Bouchon, M., M.N. Toksoz, H. Karabulut, M.P. Bouin, M. Dietrich, M. Aktar, and M. Edie (2002). Space and time evolution of rupture and faulting during the 1999 Izmit (Turkey) earthquake, *Bull. Seism. Soc. Am.*, 92 (1), 256-266.

Camassi, P. Galli, A. Tertulliani, Castenetto, A. Lucantoni, D. Molin, G. Naso, E. Peronace, F. Bernardini, V. Castelli, A. Cavaliere, E. Ercolani, S. Salimbeni, D. Tripone, G. Vannucci, L. Arcoraci, M. Berardi, C. Castellano, S. Del Mese, L. Graziani, I. Leschiutta, A. Maramai, A. Massucci, A. Rossi, M. Vecchi, R. Azzaro, S. D'Amico, F. Ferrari, N. Mostaccio, R. Platania, L. Scarfa, T. Tuva, L. Zuccarello, S. Carlino, A. Marturano, P. Albinì, A. Gomez Capera, M. Locati, F. Meroni, V. Pessina, C. Piccarreda, A. Rovida, M. Stucchi, G. Buffarini, S. Paolini, V. Verrubbi, M. Mucciarelli, R. Gallipoli, M.S. Barbano, I. Cecic, M. Godec, (2009). *Macroseismic investigation: method, earthquake parameters, open questions, (L'indagine macrosismica: metodologia, parametri del terremoto, questioni aperte, in Italian)*, IUSS Press, Progettazione Sismica.

Campbell, K. W., and Y. Bozorgnia (2008). NGA ground motion model for the geometric mean horizontal component of PGA, PGV, PGD and 5% damped linear elastic response spectra for periods ranging from 0.01 to

10 s, *Earthquake Spectra* **24**, 139–172.

Castro RR, Ruiz-Cruz E (2005) Stochastic modeling of the 30 September 1999 Mw 7.5 earthquake, Oaxaca, Mexico. *Bull Seismol Soc Am* 95:2259–2271

Castro, R. R., Pacor, F., Franceschina, G., Bindi, D., Zonno, G., and Luzi, L. (2008). Stochastic strong motion simulation of the Mw 6 Umbria–Marche earthquake of September 1997: Comparison of different approaches, *Bull. Seismol. Soc. Am.* 98, 662–67.

Causse M., Chaljub E., Cotton F., Cornou C. and Bard P. (2009); New approach for coupling k-2 and empirical Green's functions: application to the blind prediction of broadband ground motion in the Grenoble basin, *Geophys. J. Int.* , 79 (3): 1627-1644. doi: 10.1111/j.1365-246X.2009.04354.x.

Causse, M., L.A. Dalguer, P.M Mai (2012). Fracture energy scaling in dynamic models of past earthquakes as a constraints for physics-based ground-motion simulation. *Proceedings of the 15th World Conference on Earthquake Engineering*, Lisbon, Portugal.

Causse M., L.A. Dalguer, P.M Mai (2013). Variability of Dynamic Parameters Inferred from Kinematic Models of Past Earthquakes, accepted at *Geophysical Journal International*.

Cauzzi C, Faccioli E (2008), "Broadband (0.05 s to 20 s) prediction of displacement response spectra based on worldwide digital records", *Journal of Seismology* , 12, pp 453-475

Cheloni, D., N. D'Agostino, E. D'Anastasio, E. A. Avallone, S. Mantenuto, R. Giuliani, M. Mattone, S. Calcaterra, P. Gambino, D. Dominici, F. Radicioni and G. Fastellini, (2010), Coseismic and initial post-seismic slip of the 2009 Mw 6.3 L'Aquila earthquake, Italy, from GPS measurements, *Geophys. J. Int.*, 181, 3, 1539-1546, doi: 10.1111/j.1365-

246X.2010.04584.x.

Chen, Y.-H., and C.-C. P. Tsai (2002). A new method for estimation of the attenuation relationship with variance components. *Bulletin of the Seismological Society of America* 92 (5), 1,984–1,991.

Chiarabba, C., A. Amato, M. Anselmi, P. Baccheschi, I. Bianchi, M. Cattaneo, G. Cecere, L. Chiaraluce, M. G. Ciaccio, P. De Gori, G. De Luca, M. Di Bona, R. Di Stefano, L. Faenza, A. Govoni, L. Improta, F. P. Lucente, A. Marchetti, L. Margheriti, F. Mele, A. Michelini, G. Monachesi, M. Moretti, M. Pastori, N. Piana Agostinetti, D. Piccinini, P. Roselli, D. Seccia, and L. Valoroso, (2009), The 2009 L' Aquila (central Italy) Mw 6. 3 earthquake: Main shock and aftershocks, *Geophys. Res. Lett.*, 36, L18308, doi:10.1029/2009GL039627.

Chiaraluce, C. Chiarabba, P. De Gori, R. Di Stefano, L. Improta, D. Piccinini, A. Schagenhauf, P. Traversa, L. Valoroso and C. Voisin (2011); The 2009 L'Aquila (central Italy) seismic sequence, *Bollettino di Geofisica Teorica ed Applicata*, 52.

Chioccarelli, E., and I., Iervolino (2010). Near-source seismic demand and pulse-like records: A discussion for L'Aquila earthquake. *Earthquake Engng Struct. Dyn*, DOI: 10.1002/eqe.987.

Cirella A., Piatanesi A., Tinti E. and M. Cocco, (2008), Rupture process of the 2007 Niigata-ken Chuetsu-oki earthquake by non-linear joint inversion of Strong Motion and GPS data, *Geophys. Res. Lett.*, 35, L16306, doi:10.1029/2008GL034756.683.

Cirella, A., A. Piatanesi, M. Cocco, E. Tinti, L. Scognamiglio, A. Michelini, A. Lomax, and E. Boschi, (2009), Rupture history of the 2009 L'Aquila earthquake from non-linear joint inversion of strong motion and GPS data, *Geophys. Res. Lett.*, 36, L19304, doi:10.1029/2009GL039795.

Cirella A., Piatanesi A., Tinti E., Chini M. and M. Cocco (2012),

"Complexity of the rupture process during the 2009 L'Aquila, Italy, earthquake", *Geophysical Journal International*. 190, 607-621, doi:10.1111/j.1365-246X.2012.05505.x.

Cocco M., Tinti E., Marone C., and A. Piatanesi (2009), "Scaling of slip weakening distance with final slip during dynamic earthquake rupture", in: E. Fukuyama (Ed.), *Fault-zone Properties and Earthquake Rupture Dynamics*, International Geophysics Series, 94, Elsevier (2009), pp. 163–186.

Conte, J.P., Pister, K.S., Mahin, S.A., 1992. Non-Stationary ARMA Modeling of Seismic Ground Motions. *Soil Dynamics and Earthquake Engineering* 11, 411-426.

Cotton, F. and Campillo, M., Inversion of strong ground motion in the frequency domain: application to the 1992 Landers, California, earthquake. *J. Geophys. Res.*, 100:3961-3975, 1995.

Cotton, F., R. Archuleta, M. Causse (2013). What is sigma of stress drop ?, *Seismological Research Letters* 84, 42-48.

Coutant, O. (1989). Program of Numerical Simulation AXITRA. Research Reports LGIT. Université Joseph Fourier, Grenoble (in French).

Dalguer, L. A. & Mai, P.M., 2011. Near-Source Ground Motion Variability from M=6.5 Dynamic Rupture Simulations, 4th IASPEI /IAEE International Symposium, University of California, Santa Barbara, USA

Dalguer, L. A. & Mai, P.M., 2012. Prediction of near-source ground motion exceeding 1g at low frequencies (<2Hz) from Mw~6.5 deterministic physics-based dynamic rupture simulations, Proceedings of the 15th World Conference on Earthquake Engineering (15WCEE), Lisbon, Portugal

Day, S. M., G. Yu and D. J. Wald (1998) Dynamic stress changes during earthquake rupture, *Bull. Seismol. Soc. Am.*, 88, 512-522.

DEE-KOERI (2011a). November 9, 2011, Edremit-Van

earthquake, http://www.koeri.boun.edu.tr/depremmuh/depremraporlari/Van_Eq__09112011.pdf

DEE-KOERI (2011b). Department of Earthquake Engineering, Aftershock Deployment in Van and Erciř, http://www.koeri.boun.edu.tr/Haberler/Aftershock%20Deployment%20In%20Van%20and%20ErcIs_6_208.depmuh

Delouis, B., D. Giardini, P. Lundgren, and J. Salichon (2002). Joint inversion of InSAR, GPS, teleseismic, and strong-motion data for the spatial and temporal distribution of earthquake slip: Application to the 1999 Izmit mainshock, *Bull. Seism. Soc. Am.*, 92 (1), 278-299.

De Luca, G., E. Del Pezzo, F. Di Luccio, L. Margheriti, G. Milana, and R. Scarpa, (1998), Site response study in Abruzzo (central Italy): Underground array versus surface stations. *Journal of Seismology*, 2, 223–236.

Di Stefano R., C. Chiarabba, L. Chiaraluce, M. Cocco, P. De Gori, D. Piccinini and L. Valoroso, (2011), Fault zone properties affecting the rupture evolution of the 2009 (Mw 6.1) L'Aquila earthquake (Central Italy): Insights from seismic tomography. *Geophys. Res. Lett.*, 38, L10310, doi: 10.1029/2011GL047365.

Ellis, G.W., Cakmak, A.S., 1991. Time Series Modeling of Strong Ground Motion from Multiple Event Earthquakes. *Soil Dynamics and Earthquake Engineering* 10, 42-54.

Ellsworth W. and L. Chiaraluce, (2009), Supershear During Nucleation of the 2009 Mw 6.3 L'Aquila, Italy Earthquake. AGU Fall Meeting, San Francisco December 14 -18, 2009

Ely, G. P., S. M. Day, and J. B. Minster (2008). A support-operator method for viscoelastic wave modeling in 3D heterogeneous media, *Geophys. J. Int.* , 172, doi: 10.1111/j.1365-246X.2007.03633.x, 331-344

Ely, G., S.M. Day, and J-B. Minster (2009). Dynamic rupture models for the southern San Andreas fault, *Bull. Seism. Soc. Am.*, 100 (1), 131-150, doi:10.1785/0120090187.

EMERGEIO Working Group, (2010), Evidence for surface rupture associated with the Mw 6.3 L'Aquila earthquake sequence of April 2009 (central Italy), *Terra Nova*, 22, 43-51, 2010 doi: 10.1111/j.1365 3121.2009.00915.x.

Erberik, M. A. (2008). Generation of fragility curves for Turkish masonry buildings considering in-plane failure modes, *Earthquake Eng. Struct. Dynam.* 37, 387-405.

Erdik, M. (2006). Urban Earthquake Rapid Response and Early Warning Systems, *First European Conference on Earthquake Engineering and Seismology (a joint event of the 13th ECEE & 30th General Assembly of the ESC)*, Keynote lecture 4, Geneva, Switzerland.

Faenza L., and A. Michelini (2010). Regression analysis of MCS intensity and ground motion parameters in Italy and its application in ShakeMap, *Geophys. J. Int.* 180, 1138-1152.

Fenton, G.A., Vanmarcke, E.H., 1990. Simulations of Random Fields via Local Average Subdivision. *Journal of Engineering Mechanics* 116, 1733-1749.

Field, H.E., Hough, S.E., 1997. The Variability of PSV Response Spectra across a Dense Array Developed During the Northridge Aftershock Sequence. *Earthquake Spectra* 13, 2, 243-257.

Fukuyama, E. and R. Madariaga (1998) Rupture dynamics of a planar fault in a 3D elastic medium: Rate-and slip-weakening friction, *Bull. Seismol. Soc. Am.*, 88, 1-17.

Gallovič, F., and J. Brokešová (2007). Hybrid k-squared source model for strong ground motion simulations: Introduction, *Phys. Earth Planet. In.*

160, 34-50.

Gallovič, F., Zahradník, J. (2012). Complexity of the Mw6.3 2009 L'Aquila (Central Italy) earthquake: 1. Multiple finite-extent source inversion, *J. Geophys. Res.*, 117, B04307, doi: 10.1029/2011JB008709.

Gallovič F., G. Ameri, J.Zahradník, J. Janský, V. Plicka, E. Sokos, A. Askan, M. Pakzad (2013). Fault process and broadband ground-motion simulations of the 23 October 2011 Van (Eastern Turkey) earthquake, *in press* at *Bulletin of the Seismological Society of America*.

Goda, K., and H. P. Hong (2008). "Estimation of seismic loss for spatially distributed buildings", *Earthq. Spectra* 24, 889–910.

Gök, R., R. J. Mellors, E. Sandvol, M. Pasyanos, T. Hauk, R. Takedatsu, G. Yetirmishli, U. Teoman, N. Turkelli, T. Godoladze, and Z. Javakishvirli (2011). Lithospheric velocity structure of the Anatolian plateau–Caucasus–Caspian region, *J. Geophys. Res.* 116, B05303.

Hancock, J., Watson-Lamprey, J., Abrahamson, N.A., Bommer, J.J., Markatis, A., McCoy, E., Mendis, E. (2006). An improved method of matching response spectra of recorded earthquake ground motion using wavelets. *Journal of Earthquake Engineering*. 10:Special Issue I, 67-89.

Hancock, J., Bommer, J.J., Stafford, P.J. 2006. Numbers of Scaled and Matched Accelerograms Required for Inelastic Dynamic Analyses. *Earthquake Engineering and Structural Dynamics* 37, 1585-1607.

Hanks TC, McGuire RK (1981) The character of high frequency strong ground motion. *Bull Seismol Soc Am* 71:2071–2095

Hao, H., Oliveira, C.S., Penzien, J., 1989. Multiple-Station Ground Motion Processing and Simulation based on SMART-1 Array Data. *Nuclear Engineering Design* 111, 293-310.

Harada, T., 1984. Probabilistic Modeling of Spatial Variation of Strong Earthquake Ground Displacement. *Proceedings of Eighth World Conference*

on Earthquake Engineering, San Francisco, 605–612.

Harichandran, R.S., 1991. Estimating the Spatial Variation of Earthquake Ground Motion from Dense Array Recordings. *Structural Safety* 10, 219-233.

Harmandar, E., 2009. Spatial variation of ground motion, PhD thesis, Kandilli Observatory and Earthquake Research Institute, 162 pp.

Hayes G (2011) Finite Fault Model Updated Result of the Oct 23, 2011 Mw 7.1 Eastern Turkey Earthquake by Gavin Hayes, USGS NEIC. Available online at http://earthquake.usgs.gov/earthquakes/eqinthenews/2011/usb0006bqc/finite_fault.php (Last accessed June 2013)

Herrero, A. and P. Bernard (1994), A kinematic self-similar rupture process for earthquakes, *Bull. Seismol. Soc. Am.*, 84, 1216-1228.

Herrmann RB (1985) An extension of random vibration theory estimates of strong ground motion to large earthquakes. *Bull Seismol Soc Am* 75:1447–1453

Herrmann, R.B. Malagnini, L., and I. Munafo, (2011), Regional Moment Tensors of the 2009 L'Aquila Earthquake Sequence, *Bull. Seismol. Soc. Am.*, 101, No. 3, pp. 975-993.

Hoshiya, M. (1994). Conditional Simulation of Stochastic Field, in G. I. Schueller, M. Shinozuka, and J. T. P. Yao (editors), *Structural Safety and Reliability*, Balkema, Rotterdam.

Hoshiya, M. (1995). Kriging and Conditional Simulation of Gaussian Field, *Journal of Engineering Mechanics*, ASCE, **121**, 181-186.

Hoshiya, M., and O. Maruyama (1994). Stochastic Interpolation of Earthquake Wave Propagation", in G. I. Schueller, M. Shinozuka, and J. T. P. Yao (editors), *Structural Safety and Reliability*, Balkema, Rotterdam.

Ide, S. and M. Takeo, (1997), Determination of constitutive relations of fault slip based on seismic wave analysis, *J. Geophys. Res.*, 102(B12), 27379-27391.

Journel, A. G. and C. J. Huijbregts (1978). *Mining Geostatistics*, Academic Press, London, England.

Joyner, W.B., Boore, D.M., 1981. Peak Horizontal Acceleration and Velocity from Strong-Motion Records Including Records from the 1979 Imperial Valley, California, Earthquake. *Bulletin of the Seismological Society of America* 71, 2011-2038.

Karabulut, H., Bouin, M., Bouchon, M., Dietrich, M., Cournou, C., Aktar, M., 2002. The seismicity in the eastern Marmara sea after the august 17, 1999 Izmit earthquake. *Bull. Seism. Soc. Am.* 92, 387–393.

KarimZadeh S., A. Askan, A. Yakut, G. Ameri (2013). Assessment of synthetic ground motion records obtained from alternative simulation techniques in nonlinear time history analyses of multi-story frame buildings: A case study, submitted to *Bulletin of the Seismological Society of America*.

Kato, A., E. Kurashimo, N. Hirata, S. Sakai, T. Iwasaki and T. Kanazawa (2005), Imaging the source region of the 2004 mid-Niigata prefecture earthquake and the evolution of a seismogenic thrust-related fold, *Geophys. Res. Lett.*, 32, L07307, doi:10.1029/2005GL022366.

Kawakami, H., Mogi, H., 2003. Analyzing Spatial Intraevent Variability of Peak Ground Accelerations as a Function Of Separation Distance. *Bulletin of the Seismological Society of America* 93, 1079-1090.

Krige, D. G. (1966). Two-Dimensional Weighted Moving Average Trend Surfaces for Ore Evaluation, *Journal of the South African Institute of Mining and Metallurgy*, **66**, 13-38.

Leonard M (2010) Earthquake Fault Scaling: Self-Consistent Relating of

Rupture Length, Width, Average Displacement, and Moment Release. *Bull Seismol Soc Am.* 100:1971–1988

Liao, S., 2006. Physical Characterization of Seismic Ground Motion Spatial Variation and Conditional Simulation for Performance-Based Design, PhD Thesis, Department of Civil, Architectural and Environmental Engineering, Drexel University, Philadelphia, PA, 203 pp.

Liel A. B., and K. P. Lynch (2009). Vulnerability of Reinforced Concrete Frame Buildings And Their Occupants in the 2009 L'Aquila, Italy Earthquake, *Natural Hazards Center Report*, 213.

Loh, C.H., 1985. Analysis of the Spatial Variation of Seismic Waves and Ground Movements from SMART-1 Array Data. *Earthquake Engineering and Structural Dynamics* 13, 561–581.

Lucca E., G. Festa and A. Emolo (2012). Kinematic inversion of strong motion data using a Gaussian parameterization for the slip: application to the 2008 Iwate-Miyagi, Japan, earthquake, *Bull. Seism. Soc. Am.*, 102(6), 2685-2703.

Lucente F.P., Gori P.D., Margheriti L., Piccinini D., Bona M.D., Chiarabba C., N. Piana Agostinetti, (2010), Temporal variation of seismic velocity and anisotropy before the 2009 M_w 6.3 L'Aquila earthquake, Italy: *Geology*, 38, p. 1015–1018, doi: 10.1130/G31463.1.

Mai, P.M., and G.C. Beroza (2002). A spatial random-field model to characterize complexity in earthquake slip, *J. Geophys. Res.*, 107(B11), 2308, doi:10.1029/2001JB000588, 2002.

Malagnini, L., A. Akinci, K. Mayeda, I. Munafo', R.B. Herrmann, and A. Mercuri (2010). Characterization of Earthquake-Induced Ground Motion from the L'Aquila Seismic Sequence of 2009, Italy, *Geophys. J. Int.*, 184, 325-337 doi: 10.1111/j.1365-246X.2010.04837.x

Matsushima, Y., 1977. Stochastic Response of Structure due to Spatially

Variant Earthquake Excitations. Proceedings of Sixth World Conference on Earthquake Engineering, Vol. II, 1077-1082, Sarita Prakashan, Meerut, India.

McLaughlin, K.L., 1983. Spatial Coherency of Seismic Waveforms, Ph.D. Dissertation, University of California, Berkeley.

Michelini, A, Faenza, L, Lomax, A, and M. Cocco, (2009), Appraisal of the hypocentral location of the L'Aquila main shock. *Eos Trans. AGU*, 90(52), Fall Meet. Suppl., Abstract. AGU Fall Meeting, San Francisco December 14 □ 18, 2009.

Mignolet, M.P., Spanos, P.D., 1992. Simulation of Homogeneous Two-Dimensional Random Fields: Part I—AR and ARMA Models. *Journal of Applied Mechanics* 59, 260–269.

Motazedian, D., and G. M. Atkinson (2005). Stochastic finite-fault modeling based on a Dynamic Corner Frequency, *Bull. Seism. Soc. Am.* **95**, 995–1010.

Motazedian D (2006) Region-Specific Key Seismic Parameters for Earthquakes in Northern Iran. *Bull Seismol Soc Am* 96:1383–1395

Motions. *Journal of Engineering Mechanics* 119, 997–1016.

NERA Deliverable 11.4 (2012). Array measurements, Activity “Waveform modeling and site coefficients for basin response and topography”.

OYO Inc., Japan (2007). Production of Microzonation Report and Maps on European Side (South), Final report to Istanbul Metropolitan Municipality.

OYO Inc., Japan (2009). Production of Microzonation Report and Maps on Asian Side, Final report to Istanbul Metropolitan Municipality.

Pino, N.A. and F., Di Luccio (2009), Source complexity of the 6 April 2009 L'Aquila (central Italy) earthquake and its strongest aftershock revealed by elementary seismological analysis, *Geophys. Res. Lett.*, 36, L23305,

doi:10.1029/2009GL041331.

Pulido, N. and L. Dalguer, (2009), Estimation of the high-frequency radiation of the 2000 Tottori (Japan) earthquake based on a dynamic model of fault rupture: application to the strong ground motion simulation, *Bull. Seism. Soc. Am.*, 99 (4), 2305-2322, doi: 10.1785/0120080165.

Ramadan, O., Novak, M., 1994. Simulation of Multidimensional Anisotropic Ground Motions. *Journal of Engineering Mechanics* 120, 1773–1785.

Rice, S.O., 1944. Mathematical Analysis of Random Noise. *Bell System Technical Journal* 23, 3, 282–332.

Ripperger, J., Mai, P. M., Ampuero, J. -P. Variability of Near-Field Ground Motion from Dynamic Earthquake Rupture Simulations. *Bulletin of the seismological society of America*. Vol 98. No. 3, pp. 1207-1228, June 2008, doi: 10.1785/0120070076

Rodriguez-Marek, A., Montalva, G.A., Cotton, F. and F. Bonilla (2011). Analysis of Single-Station Standard Deviation Using the KiK-net data. *Bulletin of the Seismological Society of America*, doi: 10.1785/012010025.

Rodriguez-Marek, A., F. Cotton, F., N. Abrahamson, S. Akkar, L. Al-Atik, B. Edwards, G. Montalva and H. Mousad (2013). A model for single-station standard deviation using data from various tectonic regions, *Bull. Seismol. Soc. Am.*, in press.

Safarshahi M, Rezapour M, Hamzehloo H (2013) Stochastic Finite-Fault Modeling of Ground Motion for the 2010 Rigan Earthquake, Southeastern Iran. *Bull Seismol Soc Am* 103:223–235

Schneider, J.F., Abrahamson, N.A, Somerville, P.G., Stepp, J.C., 1990. Spatial Variability of Ground Motion from EPRI's Dense Accelerograph Array at Parkfield, California. *Proceedings of Fourth U. S. National Conf. on Earthquake Engineering, EERI, Palm Springs*, 375-384.

Scognamiglio, L., E. Tinti, A. Michelini, D. Dreger, A. Cirella, M. Cocco, S. Mazza, and A. Piatanesi (2010). Fast Determination of Moment Tensors and Rupture History: What Has Been Learned from the 6 April 2009 L'Aquila Earthquake Sequence, *Seismological Research Letters* 81, 6.

Sekiguchi, H., and T. Iwata (2002). Rupture process of the 1999 Kocaeli, Turkey, earthquake estimated from strong-motion waveforms, *Bull. Seism. Soc. Am.*, 92 (1), 300-311.

Shama, A., 2007. Simplified Procedure for Simulating Spatially Correlated Earthquake Ground Motions. *Engineering Structures* 29, 248-258.

Shinozuka, M., 1972. Monte Carlo Solution of Structural Dynamics. *Computers and Structures*, 2, 855-874.

Shinozuka, M. and R. Zhang (1996). Equivalence between Kriging and CPDF Method for Conditional Simulation, *Journal of Engineering Mechanics, ASCE*, **122**, 6, 530-538.

Smith, S.W., Ehrenberg, E., Hernandez, E.N., 1982. Analysis of the El Centro Differential Array for the 1979 Imperial Valley Earthquake. *Bulletin of Seismological Society of America* 72, 237- 258.

Sokos, E., and J. Zahradník (2008). ISOLA A Fortran code and a Matlab GUI to perform multiple-point source inversion of seismic data, *Computers & Geosciences* 34, 967-977.

Song S., A. Pitarka, and P. Somerville (2009). Exploring spatial coherence between earthquake source parameters, *Bull. Seism. Soc. Am.* 99, 2,564-2,571.

Song S., P. Somerville (2010). Physics-based earthquake source characterization and modeling with Geostatistics, *Bull. Seism. Soc. Am.* 100, 482-496.

Song S., and L.A. Dalguer (2013). Importance of 1-point statistics in earthquake source modeling for ground motion simulation, *Geophys. J.*

Int., 192, 1,255-1,270.

Song S., L.A. Dalguer, and P.M. Mai (2013). Pseudo-dynamic source modeling with 1-point and 2-point statistics of earthquake source parameters, *Geophys. J. Int.*, under revision.

Spagnuolo E., Cirella A., Piatanesi A., "Intra-event ground motion variability: Source Process of the 6th April 2009 L'Aquila, central Italy, Earthquake", in prep. for *Earthquake Spectra*.

Spanos, P.D., Mignolet, M.P., 1992. Simulation of Homogeneous Two-Dimensional Random Fields: Part II—MA and ARMA Models. *Journal of Applied Mechanics* 59, 270–277.

Spudich, P. and L. Xu, (2003), Software for calculating earthquake ground motions from finite faults in vertically varying media, in *International Handbook of Earthquake and Engineering Seismology*, Academic Press.

Sugiyama, Y (2007), 16 July 2007 Niigata-ken Chuetsu-oki earthquake; its characteristics, tectonic background and significance for active fault evaluation, *Eos Trans. AGU*, 88(52), Fall Meet. Suppl., Abstract T31G-01.

Tinti, E., P. Spudich, and M. Cocco, (2005a), Earthquake fracture energy inferred from kinematic rupture models on extended faults, *J. Geophys. Res.*, 110, B12303, doi: 10.1029/ 2005JB00364

Tinti E., E. Fukuyama, A. Piatanesi, M. Cocco (2005b) "A Kinematic Source Time Function Compatible With Earthquake Dynamics", 95 (4), 1211-1223, *Seismol. Soc. Am. Bull.*

Tinti E., Cocco M., Fukuyama E., and Piatanesi A., (2009) "Dependence of slip weakening distance (D_c) on final slip during dynamic rupture of earthquakes", *Geophys. Journal International*, 177, 1205-1220

Ugurhan B., A. Askan, A. Akinci and L. Malagnin (2012). Strong Ground Motion Simulations of the 2009 L'Aquila Earthquake, Italy, *Bulletin of the Seismological Society of America*, Vol. 102, No. 4, pp. 1429–1445.

Vallée, M., and M. Bouchon (2004). Imaging coseismic rupture in far field by slip patches, *Geophys. J. Int.* 156, 615-630.

Vanmarcke, E. and G. Fenton (1991). Conditioned Simulation of Local Fields of Earthquake Ground Motion, *Structural Safety*, 10, 247-264.

Vanmarcke, E. H., E. Heredia-Zavoni and G. A. Fenton (1993). Conditional Simulation of Spatially Correlated Earthquake Ground Motion, *Journal of Engineering Mechanics, ASCE*, 119, 11, 2333-2352.

Wald, D. J., B. C. Worden, V. Quitoriano, and K. L. Pankow (2005), "ShakeMap Manual: Users Guide, Technical Manual, and Software Guide, USGS Techniques and Methods", 12-A1, 128 p.

Walling, M. A. (2009). "Non-ergodic probabilistic seismic hazard analysis and spatial simulation of variation in ground motion. PhD diss., University of California, Berkeley"

Wang, J., A. Carr, N. Cooke and P. Moss (2003). A Simple Method for Stochastic Dispersion of Earthquake Waves, *Proceedings of Pacific Conference in Earthquake Engineering*, Paper no: 51, Christchurch, New Zealand.

Worden, C. B., Wald, D. J., Allen, T. I., Lin, K.-W., Garcia, D., and Cua, G. (2010). A revised ground-motion and intensity interpolation scheme for ShakeMap, *Bulletin of the Seismological Society of America.*, **100**, 6, 3083-3096.

Yagi, Y. and M. Kikuchi, Source rupture process of the Kocaeli, Turkey, earthquake of August 17, 1999, obtained by joint inversion of near-field data and teleseismic data, *Geophys. Res. Lett.*, Vol. 27, pp1969-1972, 2000.

Zahradník, J., and F. Gallovič (2010). Toward understanding slip inversion uncertainty and artifacts, *J. Geophys. Res.* 115, B09310.

Zerva, A., Katafygiotis, L.S., 2000. Selection of Simulation Scheme for the

Nonlinear Seismic Response of Spatial Structures. Proceedings of Fourth International Colloquium on Computation of Shell and Spatial Structures, Chania, Greece.

Zerva, A., Zervas, V., 2002. Spatial Variation of Seismic Ground Motions: An Overview. Applied Mechanics Review 55, 3, 271-297.

Zerva A., Spatial Variation of Seismic Ground Motion: Modeling and Engineering Applications, 2009 by Taylor ad Francis Group, LLC.

Zor E, Sandvol E, Xie J, Turkelli N, Mitchell B, Gasanov AH, Yetirmishli G (2007) Crustal attenuation within the Turkish Plateau and surrounding regions. Bull Seismol Soc Am 97:151–161